MICHAŁ HAPKA

POSZERZAJĄC MOŻLIWOŚCI DFT:
MODELOWANIE KOMPLEKSÓW ZŁOTA
ORAZ NIEKOWALENCYJNYCH ODDZIAŁYWAŃ
W UKŁADACH OTWARTOPOWŁOKOWYCH

WARSZAWA

2015

Michał Hapka

Expanding the predictive power of DFT:
modelling of gold complexes
and noncovalent open-shell interactions

A dissertation submitted in partial fulfillment of the requirements
for the degree of Doctor of Philosophy in Chemistry
Thesis supervisor prof. Grzegorz Chałasiński, D. Sc.
and Janusz Zachara, D. Sc.

Warszawa

2015

Acknowledgements

- First and foremost I would like to thank my advisors prof. Grzegorz Chałasiński and prof. Janusz Zachara for guidance and support during my studies.

- Special thanks to prof. Małgorzata Szczęśniak, Piotr Żuchowski, Łukasz Rajchel, Maciej Dranka and prof. Maciej Garstka for their enormous help.

- To my collegues at the Quantum Chemistry Lab UW, Department of Plant Anatomy and Cytology UW, Department of Metabolic Regulation UW and Department of Chemistry OU for *Unbearable Lightness of PhD Studies.*

Contents

Density Functional Theory (DFT) is one of the most popular first-principles approaches in modern quantum chemistry. The reason behind the tremendous success of DFT lies in the appealing combination of accuracy and favorable computational scaling it provides. Although the Kohn-Sham (KS) method [1] together with the versatile B3LYP exchange-correlation (xc) functional [2, 3] made DFT into a seemingly black box tool, there remains a plethora of yet-unresolved problems which state-of-the-art DFT has to confront [4–6].

One of the challenges comes from the rapid development of nanotechnology and supramolecular chemistry which requires a theory capable of treating large-scale systems involving atoms beyond the second row of the periodic table. Unfortunately, the application of DFT to such systems often amounts to a brute force screening for density functional approximations (DFAs) that best match the available experimental data. Clearly, the design and characteristic of new materials *via* DFT demands better understanding of the applicability of different DFAs.

A considerable effort made in this field regards developing DFT methods that properly account for both intermolecular electron correlation and electron delocalization [4, 7]. The aim of the presented Thesis is to address this challenge in two areas: 1) noncovalent intermolecular interactions, especially including open-shell species, 2) intermolecular interactions and optical response properties of gold complexes. In both areas a special attention will be given to the application of the optimally-tuned long-

range corrected (OT-LRC) xc functionals. This class of DFAs was designed specifically to allow for minimization of the delocalization error and has already been successfully applied in DFT treatment of materials relevant for organic electronics [6] and nonlinear optics [8].

The first part of the Thesis demonstrates our recent developments of the symmetry adapted perturbation theory based on DFT description of the monomers (DFT-SAPT). DFT-SAPT is a well-established perturbational approach which allows for calculations of noncovalent interactions [9]. Moreover, the dispersion energies from DFT-SAPT are frequently used in various DFT + dispersion (DFT-D) approaches [10–12] as training sets for *a posteriori* dispersion corrections.

The work on DFT-SAPT presented in this Thesis aimed at broadening the applicability of the method and extending SAPT to high-spin open-shell noncovalently bound systems. Two advances will be presented: i) introduction of the long-range corrected xc functionals in SAPT, leading to the LRC-SAPT approach [D1], ii) formulation of SAPT based on unrestricted Kohn-Sham (UKS) description of the monomers, SAPT(UKS) [D2]. Both LRC-SAPT and SAPT(UKS) were implemented and tested by me in the MOLPRO program [13].

The second part of the Thesis concerns the DFT description of model gold clusters and gold(I) compounds. Gold complexes are an excellent example of systems with numerous practical and potential applications which are modelled almost exclusively with DFT [14–16]. They pose a challenge for theory because of their shear number of highly correlated electrons, high density of states and relativistic effects [14]. The aim of the presented research was to develop a methodology allowing for a reliable DFT treatment of this class of compounds taking into account pitfalls rooted in fundamental deficiencies of the commonly used DFAs: delocalization error [7], the associated lack of derivative discontinuity [17] and inability to describe the long-range intermonomer correlation effects [4, 18]. Two aspects of gold chemistry were analyzed: i) intermolecular interactions within model Au clusters stabilized with ligands [D3], ii) optical absorption of small Au_n clusters themselves [D4]. Also presented is a joint experimental and theoretical work on the role of weak intermolecular interactions in gold(I) bisthiolates containing gold(I)-gold(I) dimers in an untypical spatial arrangement [D5].

The structure of the Thesis is as follows. The first two chapters serve as an introduction into the theoretical framework of the presented research. In Chapter 1 the basic

concepts of DFT are introduced, with special attention paid to the class of OT-LRC xc functionals. Next, a brief primer to SAPT is given in Chapter 2. The remaining chapters include my original works which I present into two parts. The first part - Chapters 3 and 4 - is focused on two novel theoretical developments introduced by me. In Chapter 3 the LRC-SAPT method is described. Chapter 4 is dedicated to the SAPT(UKS) approach. In the second part of the Thesis, enclosed in chapters from 5 to 7, several applications of DFT to gold complexes are reported. Chapter 5 is focused on a reliable DFT treatment of donor-acceptor interactions in gold-ligand systems. In Chapter 6 a study of UV absorption spectra of the selected Au_n ($n = 4, 6, 8, 12, 20$) clusters is presented. Finally, Chapter 7 is dedicated to my experimental synthetic work followed by theoretical analysis of three new gold(I) complexes and weak interactions stabilizing their conformation. The Thesis closes with brief summary in Chapter 8.

PART I:
Theory

Density Functional Theory: basic concepts

The foundation of DFT are the Hohenberg-Kohn (HK) theorems [19]. The first HK theorem states that the ground-state density of a system of interacting electrons in some external potential determines this potential uniquely up to a constant. This means that the ground-state density uniquely determines the Hamiltonian and thus all properties of the system. The second HK theorem introduces a variational principle [19, 20] that allows one to obtain the ground-state density by minimizing the following total energy expression:

$$
\begin{aligned}
E_{\text{tot}} &= \min_{\rho(\mathbf{r}) \to N} \left\{ \int v_{\text{ext}}(\mathbf{r}) \rho(\mathbf{r}) d^3\mathbf{r} + F[\rho] \right\} \\
&= \min_{\rho(\mathbf{r}) \to N} \left\{ V[\rho] + F[\rho] \right\}
\end{aligned}
\tag{1.1}
$$

where the minimization is performed within the space of all densities yielding N electrons and $F[\rho]$ stands for the universal (i.e. system-independent) functional of the density. Regrettably, not only does the explicit form of $F[\rho]$ remain unknown, but also there exist no straightforward approximations to it, mainly due to the difficulties in modelling of the kinetic energy functional.

1.1   The Kohn-Sham scheme

The practical approach to DFT follows an indirect scheme proposed by Kohn and Sham [1]. In the KS method one considers mapping the ground state of the physical interacting-electron system into the ground state of a fictitious system of noninteracting electrons that are subject to a common local (i.e., multiplicative) external potential, $v_{\mathrm{KS}}(\mathbf{r})$. The mapping is exact in a sense that solving a set of one-electron Schrödinger equations for the noninteracting system:

$$\left(-\frac{1}{2}\Delta_{\mathbf{r}} + v_{\mathrm{KS}}(\mathbf{r})\right)\varphi_i(\mathbf{r}) = \epsilon_i\varphi_i(\mathbf{r}), \tag{1.2}$$

where ϵ_i and φ_i are Kohn-Sham energies and orbitals, yields the density $\rho(\mathbf{r})$ calculated as a sum of over filled orbitals:

$$\rho(\mathbf{r}) = 2\sum_i \varphi_i(\mathbf{r})\varphi_i^*(\mathbf{r}) \tag{1.3}$$

which is the same as the density of the interacting system. In the KS method the total energy of the system (1.1) is recast as

$$E_{\mathrm{tot}} = \min_{\rho(\mathbf{r})\to N}\left\{V[\rho] + T_s[\rho] + J[\rho] + E_{xc}[\rho]\right\}, \tag{1.4}$$

where $T_s[\rho]$ denotes the kinetic energy of non-interacting fictitious particles, the external potential $v_{\mathrm{ext}}(\mathbf{r})$ in $V[\rho]$ is e.g.,the nuclear attraction potential

$$v(\mathbf{r}) = -\sum_{\alpha}^{\mathcal{N}} \frac{Z_\alpha}{|\mathbf{r} - \mathbf{R}_\alpha|}, \tag{1.5}$$

the Hartree functional $J[\rho]$ takes the form

$$J[\rho] = \frac{1}{2}\int\int \rho(\mathbf{r}_1)\rho(\mathbf{r}_2)d^3\mathbf{r}_1 d^3\mathbf{r}_2 \tag{1.6}$$

and $E_{xc}[\rho]$ is known as the exchange-correlation functional, which by (1.1) and (1.4) reads

$$E_{xc}[\rho] = F[\rho] - T_s[\rho] - J[\rho]. \tag{1.7}$$

Finally, the minimization of $E[\rho]$ with respect to $\rho(\mathbf{r})$ as in (1.4) gives the condition:

$$v_{\text{KS}}(\mathbf{r}) = v(\mathbf{r}) + j(\mathbf{r}) + v_{xc}(\mathbf{r}), \qquad (1.8)$$

with the Hartree local potential:

$$j(\mathbf{r}) = \int \rho(\mathbf{r}') \frac{1}{|\mathbf{r} - \mathbf{r}'|} d^3\mathbf{r}' \qquad (1.9)$$

and the exchange-correlation potential defined as:

$$v_{xc}(\mathbf{r}) = \frac{\delta E_{xc}[\rho]}{\delta \rho(\mathbf{r})}. \qquad (1.10)$$

1.2   The Generalized Kohn-Sham scheme

In 1996 Seidl *et al.* introduced the Generalized Kohn-Sham scheme, in which the real system is mapped onto any *interacting* model system which can be represented by a single Slater determinant [21]. Such mapping is realized by defining an energy functional of the orbitals constituting the Slater determinant of the model system, $S[\{\varphi_i\}]$, and expressing the energy of the system as

$$E_{\text{tot}} = \min_{\{\varphi_i\} \to N} \left\{ \int v_{\text{ext}}(\mathbf{r}) \rho(\mathbf{r}) d^3\mathbf{r} + S[\{\varphi_i\}] + R^s[\rho[\{\varphi_i\}]] \right\} \qquad (1.11)$$

where $R^s[\rho[\{\varphi_i\}]]$ is the "remainder" term and the minimization searches all unitary orbitals $\{\varphi_i\}$ yielding the density $\rho(\mathbf{r})$. Minimizing E_{tot} in an analogous manner to the KS scheme leads to the GKS equations:

$$\left(\hat{O}^S[\{\varphi_i\}] + v_{\text{ext}}(\mathbf{r}) + v_R(\mathbf{r}) \right) \varphi_i(\mathbf{r}) = \epsilon_i \varphi_i(\mathbf{r}), \qquad (1.12)$$

where $\hat{O}^S[\{\varphi_i\}]$ is a generally nonlocal, orbital-specific operator, $v_R(\mathbf{r}) = \frac{\delta R^s[\rho]}{\delta \rho(\mathbf{r})}$ denotes a "remainder" local potential. One should stress that while both KS and GKS mappings are formally exact [21], there exists only one map in the KS scheme, whereas in the GKS approach different maps are possible depending on the choice of $S[\{\varphi_i\}]$.

The hybrid functionals introduced by Becke [22] are well-known representants of the GKS scheme. Here $S[\{\varphi_i\}]$ is taken as the Slater-determinant expectation value of the

sum of the kinetic energy and a fraction of the electron-repulsion energy operator. In consequence, the $\hat{O}^S[\{\varphi_i\}]$ operator becomes the regular kinetic energy operator plus a fraction of the Fock operator $\hat{k}(\mathbf{r})$, and the same fraction of the Hartree $j(\mathbf{r})$ term. The approximate $v_R(\mathbf{r})$ is selected as the rest of the Hartree term, the fraction of the local exchange potential $v_x^{\mathrm{sl}}(\mathbf{r})$, and the correlation potential $v_c^{\mathrm{sl}}(\mathbf{r})$:

$$\left(-\frac{1}{2}\Delta_{\mathbf{r}} + v(\mathbf{r}) + \zeta\hat{k}(\mathbf{r}) + j(\mathbf{r}) + (1-\zeta)v_x^{\mathrm{sl}}(\mathbf{r}) + v_c^{\mathrm{sl}}(\mathbf{r})\right)\varphi_i(\mathbf{r}) = \epsilon_i\varphi_i(\mathbf{r}), \qquad (1.13)$$

where ζ is the fixed fraction of the Fock exchange, the action of a nonlocal Fock exchange is expressed as

$$\hat{k}(\mathbf{r})\varphi_i(\mathbf{r}) = -\sum_j \varphi_j(\mathbf{r}) \int d^3\mathbf{r}' \frac{1}{|\mathbf{r}-\mathbf{r}'|}\varphi_j^*(\mathbf{r}')\varphi_i(\mathbf{r}'). \qquad (1.14)$$

1.2.1 Range-separated functionals

Another interesting case of the GKS approach are the range-separated (RS) functionals, also known as Coulomb-attenuated or long-range corrected (LRC) functionals [23–25]. The range-separation (RS) scheme underlying the construction of these functionals is based on the splitting of the interelectronic repulsion operator $\omega(r) = \frac{1}{r}$ into long-range (LR) and short-range (SR) components:

$$\omega(r) = \omega^{\mathrm{LR}}(r) + \omega^{\mathrm{SR}}(r), \qquad (1.15)$$

with the LR part usually chosen so that it does not have a singularity at $r \to 0$. Most common choices are based on:
i) the Yukawa potential for SR, e.g., Ref. [26]:

$$\omega_{\mathrm{Y}}(r_{12}) = \underbrace{\frac{1-e^{-\omega r_{12}}}{r_{12}}}_{\mathrm{LR}} + \underbrace{\frac{e^{-\omega r_{12}}}{r_{12}}}_{\mathrm{SR}} \qquad (1.16)$$

ii) the error function[23, 27, 28] $\mathrm{erf}(x) = \frac{2}{\sqrt{\pi}}\int_0^x \exp(-t^2)dt$:

$$\omega_{\mathrm{erf}}(r) = \underbrace{\frac{1-\mathrm{erf}(\omega r)}{r}}_{\mathrm{SR}} + \underbrace{\frac{\mathrm{erf}(\omega r)}{r}}_{\mathrm{LR}} \qquad (1.17)$$
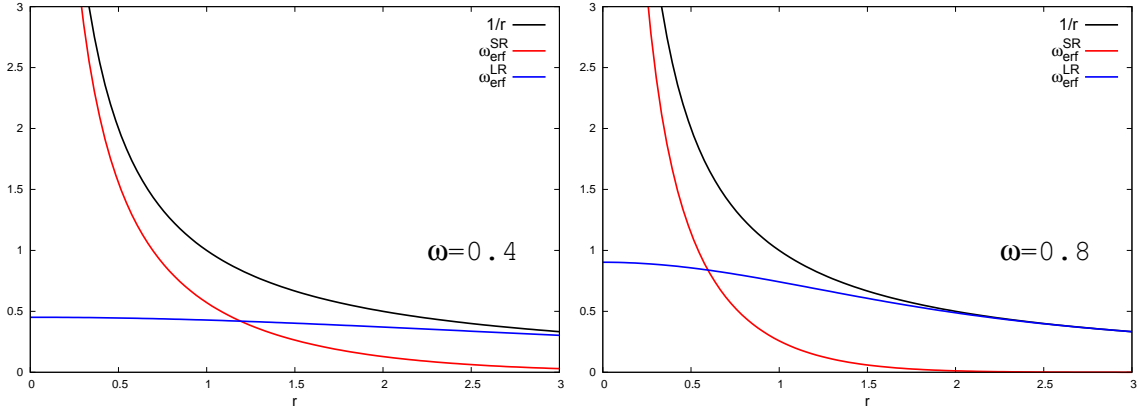
Figure 1.1: The illustration of the RS scheme based on the error function with different values of the ω parameter.

iii) the generalized error function ansatz referred to as the Coulomb-attenuating method (CAM) [24]:

$$\omega_{\text{CAM}}(r) = \underbrace{\frac{1 - [\alpha + \beta \text{erf}(\omega r)]}{r}}_{\text{SR}} + \underbrace{\frac{\alpha + \beta \text{erf}(\omega r)}{r}}_{\text{LR}}, \qquad (1.18)$$

with $\alpha \geq 0, \beta \geq 0, \alpha + \beta \leq 1$. $\omega \in (0, \infty)$ is the so-called range-separation parameter. In all the schemes the short-range terms decay to zero on a length scale of $\approx \frac{1}{\omega}$ (see Fig. 1.1), whereas the long-range term is non-singular and its limits at $r \to 0$ depend on the RS choice:

$$\omega_{\text{Y}}^{\text{LR}}(r) \xrightarrow{r \to 0} \omega; \quad \omega_{\text{erf}}^{\text{LR}}(r) \xrightarrow{r \to 0} \frac{2\omega}{\sqrt{\pi}}; \quad \omega_{\text{CAM}}^{\text{LR}}(r) \xrightarrow{r \to 0} \begin{cases} \frac{2\beta\omega}{\sqrt{\pi}}, & \alpha = 0 \\ \infty, & \alpha > 0. \end{cases} \qquad (1.19)$$

One should mention other applications of the RS scheme within DFT, e.g., combining DFT with the configuration interaction method (DFT + CI) [28] or constructing the RPA-based exchange-correlation functionals [29, 30].

The RS scheme applied in the LRC functionals allows for a different treatment of the SR and LR components of the GKS orbital equation. While the Hartree potential remains unchanged, i.e. the SR and LR parts are collected together, the partitioning is introduced in the exchange term: the SR exchange component is chosen as a standard local DFT potential, whereas in the LR component the full Hartree-Fock ("exact")

exchange is incorporated. The resulting equation takes the form:

$$\left(-\frac{1}{2}\Delta_{\mathbf{r}} + v(\mathbf{r}) + j(\mathbf{r}) + \hat{k}^{\mathrm{LR}}(\mathbf{r}) + v_x^{\mathrm{SR}}(\mathbf{r}) + v_c^{\mathrm{sl}}(\mathbf{r})\right)\varphi_i(\mathbf{r}) = \epsilon_i\varphi_i(\mathbf{r}), \quad (1.20)$$

where

$$\hat{k}^{\mathrm{LR}}(\mathbf{r})\varphi_i(\mathbf{r}) = -\sum_j \varphi_j(\mathbf{r}) \int d^3\mathbf{r}'\omega^{\mathrm{LR}}(|\mathbf{r}-\mathbf{r}'|)\varphi_j^*(\mathbf{r}')\varphi_i(\mathbf{r}') \quad (1.21)$$

and $v_x^{\mathrm{SR}}(\mathbf{r})$ is the SR semilocal exchange potential. In term of the GKS framework, $S[\{\varphi_i\}]$ in LRC functionals is a Slater-determinant expectation value of the sum of the kinetic energy and the long-range electron-repulsion energy operator $\omega^{\mathrm{LR}}(r)$. Therefore, the $\hat{O}^S[\{\varphi_i\}]$ operator has three parts: the usual kinetic energy operator, the LR fraction of the Fock operator and the Hartree term. The remainder potential is then a sum of the SR Hartree term, the local potential derived from the SR exchange term, and a standard correlation potential.

The inclusion of the Hartree-Fock exchange in the SR component of the DFT exchange is also possible. This approach leads to the so-called range-separated hybrid (RSH) or long-range corrected hybrid functionals [24]. Then, (1.21) is transformed into:

$$\left(-\frac{1}{2}\Delta_{\mathbf{r}} + v(\mathbf{r}) + j(\mathbf{r}) + (1-\zeta)\hat{k}^{\mathrm{LR}}(\mathbf{r}) + (1-\zeta)v_x^{\mathrm{SR}}(\mathbf{r}) + \zeta\hat{k}(\mathbf{r}) + v_c^{\mathrm{sl}}(\mathbf{r})\right)\varphi_i(\mathbf{r}) = \epsilon_i\varphi_i(\mathbf{r}). \quad (1.22)$$

Modelling of the long-range exchange energy in LRC functionals entirely *via* the orbital-dependent Hartree-Fock exchange assures the fixed asymptote of an exchange potential:

$$\hat{k}(\mathbf{r})\varphi_i(\mathbf{r}) \xrightarrow{r\to\infty} -\frac{1}{r}\varphi_i(\mathbf{r}), \quad (1.23)$$

which is in accordance with the exact theory [31]. Moreover, (1.23) holds irrespective of the applied ω. In contrast, local and semilocal correlation-energy functionals suffer from incorrect long-range behavior of $v_{xc}(\mathbf{r})$ [32] which leads to the poor description of KS virtual orbitals and eigenvalues. This in turn results in unsatisfactory second-order response properties [33–35] and wrong interaction energies in DFT-SAPT calculations [35–39].

The functional tuning procedure   The range-separation parameter ω is in general a system-dependent functional of the electron density [40–42]. In most cases, the ω value is simply fitted using a representative training set, however, there exist rigorous, nonempirical ways of choosing a systems-specific ω, the so-called optimal tuning procedures [41–43].

In the IP-tuning procedure [41, 44] one enforces the Koopmans' theorem so that the energy of the HOMO orbital, $\varepsilon_{\text{HOMO}}$, matches the negative of ionization potential (IP) as closely as possible. This is done by minimizing the following target function:

$$J_H^2(\omega) = \min_{\omega}(E(N-1;\omega) - E(N;\omega) + \varepsilon_{\text{HOMO}})^2, \qquad (1.24)$$

where $E(N;\omega)$ denotes the energy of an N-electron system for the specific ω value. Such a choice is justified as the Koopmans' theorem holds for exact KS and GKS theories [31]. The IP-tuning procedure automatically guarantees the proper limiting behavior of the electron density which should decay as $\rho(\mathbf{r}) \approx e^{-2\sqrt{2\text{IP}}r}$, whereas in both KS and GKS it decays as $\rho(\mathbf{r}) \approx e^{-2\sqrt{-2\varepsilon_{\text{HOMO}}}r}$ [31].

In the gap tuning approach one adjusts the ω value, so that both HOMO(N) of the neutral system corresponds to IP and HOMO($N+1$) of a negative ion corresponds to electron affinity (EA) [45]. A two-parameter (ω, α) target function has been proposed in the case of RSH functionals [46]. Recently, Modrzejewski *et al.* have proposed an alternative tuning paradigm [42]. The so-called global density-dependent (GDD) tuning procedure (ω_{GDD}) relates the optimal value of the range-separation parameter to the average distance between the outer electron and an exchange hole. It has been shown to yield comparable or better results with respect to other tuning schemes.

The tuning of LRC functionals is of importance for reliable prediction of properties that depend on the tail of the electron density, e.g. charge-transfer (CT) and Rydberg excitations [42, 43, 47], photoelectron spectra [46], HOMO-LUMO (HL) gaps [42, 48], electric field gradients at transition metal centers [49], polarizabilities [50] or hyperpolarizabilities [51, 52]. Nevertheless, the major drawback of the molecule-specific tuning approach is the lack of size consistency [41, 53]. Karolewski *et al.* reported size consistency errors up to several electron volts for diatomic molecules which disqualify the optimally-tuned LRC functionals (OT-LRC) for predictions of PES [53]. Finally, recent works by Garret *et al.* [54] and Whittleton *et al.* [55] have shown that the IP-tuning

approach may be inadequate for calculations of excitation energies and IPs in large molecules.

Although the success of OT-LRC functionals may be attributed to the correct form of the v_{xc} potential, a more comprehensive diagnostic, related to the xc functionals themselves, is in fact needed to fully grasp the physics underlying their behavior. As proposed by Yang *et al.* [7], such diagnostic may be based on examination of the delocalization error (DE), also known as many-electron self-interaction error (MSIE) [56].

1.3   Delocalization error in DFT

For an exact density functional the ground state energy of the system with a fractional number of electrons $N + \delta$, $0 \leq \delta \leq 1$ is given by [17, 57]:

$$E(N + \delta) = (1 - \delta)E(N) + \delta E(N + 1). \tag{1.25}$$

In other words, for any system, the total energy with respect to particle number is a series of straight lines (see Fig 1.2). Moreover, the derivative of the energy with respect to particle number is discontinuous at integer number of electrons. This simply corresponds to the slopes of the $(N-1, N)$ and $(N, N+1)$ segments being, by definition, equal to -IP and -EA, respectively. Importantly, the linearity should hold for both KS and GKS mappings [58].

The negative deviation of the $E(N)$ curve from the exact linear behavior is defined as the delocalization error. DE is present in local and semilocal functionals. As exemplified in Fig. 1.2, it results in spurious lowering of the energy for fractional charges, yielding unphysical partial charge anions as the most stable species. Similarly, the delocalized charge distributions will be favored over the localized ones [4]. One also defines the localization error, i.e. the concave behavior of the $E(N)$ curve, as observed in HF.

The optimal tuning procedures in LRC functionals may be viewed as a practical way of minimizing DE [43]. It should be stressed that the lack of DE results in proper asymptotic behavior of the xc potential, but *not vice versa* [D1]. In consequence, the asymptotic correction (AC) schemes improve upon some classes of excitations (Rydberg) and second-order response properties [33, 35], but fail for systems where DE is
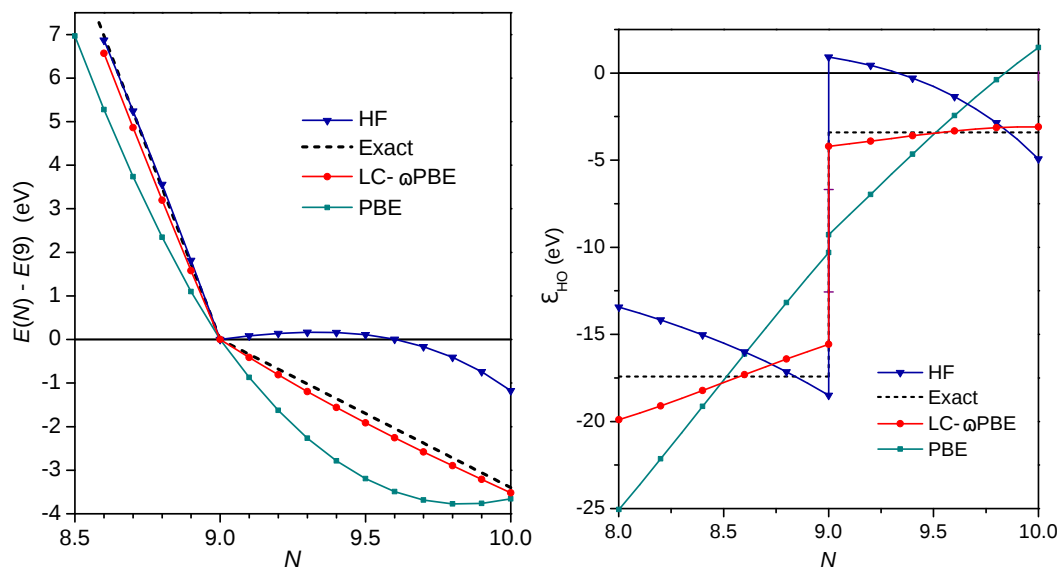
Figure 1.2: Total energy (left) and highest occupied orbital energy $\varepsilon_{\text{HOMO}}$ (right) of the F atom as a function of the electron number N. The energy is zeroed out at $N = 9$. The aug-cc-pV5Z basis set is used. The "exact" lines denote the experimental IP and EA. Reprinted by permission from Ref. [59].

large, e.g. symmetric ion radicals or extended molecular systems [50, 60].

1.4 Time-dependent DFT

A foundation of the time-dependent DFT (TDDFT) method was laid in the work of Runge and Gross [61] in which they proved a one-to-one correspondence between the external (time-dependent) single-particle potential, $v_s(\mathbf{r}, t)$, and the electronic density, $\rho(\mathbf{r}, t)$, for many-body systems evolving from a fixed initial state [61]. This theorem allowed for formulation of the time-dependent Kohn-Sham scheme (TDKS).

In TDKS one introduces an auxiliary system of noninteracting electrons subject to an external local potential $v_{\text{KS}}(\mathbf{r}, t)$. The Runge-Gross theorem applied to the noninteracting system guarantees that v_{KS} is unique. One then chooses the external potential such that the density of the Kohn-Sham electrons is equal to the density of the original interacting system. This means that the Kohn-Sham orbitals that are solution to the time-dependent Schrödinger equation:

$$i\frac{\partial}{\partial t}\varphi_i(\mathbf{r}, t) = \left[-\frac{\nabla^2}{2} + v_{\text{KS}}(\mathbf{r}, t)\right]\varphi_i(\mathbf{r}, t), \tag{1.26}$$

restore the density of the interacting system

$$\rho(\mathbf{r}, t) = \sum_i^{occ} |\varphi_i(\mathbf{r}, t)|^2. \tag{1.27}$$

The original derivation of TDKS was based on finding a stationary point of the quantum mechanical action integral:

$$A = \int_{t_0}^{t_1} dt \, \langle \Psi(t)|i\frac{\partial}{\partial t} - \hat{H}(t)|\Psi(t)\rangle \tag{1.28}$$

which for time-dependent systems is equivalent to solving the time-dependent Schrödinger equation. In this approach one arrives at the following form of $v_{\mathrm{KS}}(\mathbf{r}, t)$:

$$v_{\mathrm{KS}}(\mathbf{r}, t) = v_{\mathrm{ext}}(\mathbf{r}, t) + \int d^3\mathbf{r}' \frac{\rho(\mathbf{r}', t)}{|\mathbf{r} - \mathbf{r}'|} + v_{\mathrm{xc}}(\mathbf{r}, t) \tag{1.29}$$

where:

$$v_{\mathrm{xc}}(\mathbf{r}, t) = \frac{\delta A_{xc}[\rho]}{\delta \rho(\mathbf{r}, t)}, \tag{1.30}$$

and A_{xc} includes all nontrivial many-body parts of the action. The density-dependence of v_{xc} is nonlocal in both space and time, meaning that the potential at time t and position $\mathbf{r}$ may depend on the density at all previous times and all other positions. In other words, $v_{\mathrm{xc}}(\mathbf{r}, t)$ is in general a functional of the entire history of the density, the initial interacting wave function, and the initial Kohn–Sham wave function. Its explicit form is unknown, therefore approximating it is the fundamental challenge in TDDFT.

In standard TDKS calculations one employs the adiabatic approximation in which it is assumed that the xc potential reacts instantaneously and without memory to any temporal change of the charge density, i.e., v_{xc} does not depend on the history of the charge density. Although the adiabatic approximation is valid only for slow density variations in time, it is up until now the most successful approach in modern TDDFT [62, 63].

It is worth to mention, that the TDKS formulation based on (1.28) was diagnosed with two cardinal problems. First, (1.28) gives response functions that are symmetric in their time and space arguments, e.g. $f_{xc}(\mathbf{r}t, \mathbf{r}'t') = \frac{\delta v_{\mathrm{xc}}(\mathbf{r}, t)}{\delta \rho(\mathbf{r}', t')}$. This violates the causality principle which states that response functions should equal zero for $t < t'$ [64, 65].

Second, in order to derive the time-dependent Schrödinger equation from (1.28), one has to impose two boundary conditions: $\delta\Psi(t_0) = \delta\Psi(t_1) = 0$ on the variations of the wave function. The problem stems from the fact that in TDDFT these two variations are not independent: the variation $\delta\Psi(t)$ at times $t > t_0$ is entirely determined by the boundary condition $\delta\Psi(t_0) = 0$. The solution to both problems was first given in 1998 by van Leeuwen [66] who applied the Keldysh formalism [67] and formulated a new action functional which does not explicitly contain the time derivative operator $\partial/\partial t$. While the latter assures that no boundary appears when performing variations, the Keldysh time contour method allows one to avoid the causality problem. The Runge-Gross-Vignale action principle introduced in 2008 provided an alternative solution to restoring causality by imposing new boundary conditions to the variation of the Dirac-Frenkel action (1.28) [68].

The time-dependent GKS equation takes the form:

$$\left(-\frac{1}{2}\Delta_{\mathbf{r}} + v(\mathbf{r}, t) + j(\mathbf{r}, t) + v_{\text{loc}}(\mathbf{r}, t) + \hat{V}_{\text{nl}} \right)\varphi_i(\mathbf{r}, t) = i\frac{\partial\varphi_i(\mathbf{r}, t)}{\partial t}, \qquad (1.31)$$

where the nonlocal operator $\hat{V}_{\text{nl}}$ is equal to $\zeta\hat{k}(\mathbf{r})$ of (1.13) for regular hybrid functionals and $\hat{k}^{\text{LR}}$ of (1.21) for LRC functionals. $v_{\text{loc}}(\mathbf{r}, t)$ stands for all local-potential components of the applied hybrid functional.

The main area of TDDFT applications are the calculations of the excitation spectra and excited state properties by means of linear-response theory. For finite systems, discrete poles of the dynamic polarizability correspond to the actual transition frequencies, whereas the residues match oscillator strengths. Apart form the weak electrical field regime, TDDFT has also been successfully applied in the realm of strong, oscillating fields, e.g. atoms and molecules in laser beams of $10^{13} - 10^{16}$ W/cm^2 intensity [69–71].

Although broadly triumphant, TDDFT has several limitations. In his 2009 review [63], Casida identified four major problems of TDDFT: i-ii) underestimation of Rydberg and CT excitations, iii) the "scale up catastrophe" and iv) the failure to account for many-electron excitations. The first three of those issues were linked to the incorrect asymptotic behavior of the xc potential, persistence of the delocalization error and the absence of derivative discontinuity. The LRC functionals and optimal tuning procedures described in this Chapter were specifically designed to address the mentioned deficiencies.

Symmetry-adapted Perturbation Theory: basic concepts

The second part of the Thesis is focused on two developments in DFT-SAPT: i) application of OT-LRC functionals, ii) formulation of SAPT formalism based on unrestricted Kohn-Sham description of the monomers. Here we will briefly introduce basic concepts of SAPT which we will refer to in Chapters 3 and 4.

For a two-body system, the interaction energy is defined as:

$$E_{\text{int}} = E_{AB} - E_A - E_B, \tag{2.1}$$

where both energy of the dimer E_{AB} and energies of the A and B monomers are obtained within the Born-Oppenheimer approximation. Calculation of interaction energy directly from Eq. (2.1) is known as the supermolecular approach. Having the advantage of being relatively straightforward, the supermolecular method became a black-box tool for everyman's first-principles calculations. However, its disadvantages are the notorious basis-set superposition error (BSSE) [72] and implicit error-cancellation in Eq. (2.1).

An alternative approach to calculating intermolecular interactions is the perturbational method. As a BSSE-free method allowing for decomposition of the interaction energy in physically meaningful components, the perturbational method is a viable and popular tool. One should note, however, that it is in general more complex and computationally demanding than the supermolecular method, and therefore requires stepping

outside the comfort black-box zone.

2.1 Symmetry-adapted perturbation theory

The basic assumption of the perturbative methods is that the interaction energy is small with respect to total system energy. This leads to the following partitioning of the Hamiltonian:

$$
\begin{aligned}
\hat{H} &= \sum_{i \in AB} \left(-\frac{1}{2}\Delta_{\mathbf{r}_i} - \sum_{\alpha \in AB} \frac{Z_\alpha}{|\mathbf{r}_i - \mathbf{R}_\alpha|} \right) + \sum_{i \neq j \in AB} \frac{1}{r_{ij}} + \sum_{\alpha \neq \beta \in AB} \frac{Z_\alpha Z_\beta}{R_{\alpha\beta}} = \\
&= \hat{H}_A + \hat{H}_B + \hat{V} = \hat{H}_0 + \hat{V}.
\end{aligned} \tag{2.2}
$$

Thus, the monomer A Hamiltonian is:

$$
\begin{aligned}
\hat{H}_A &= \sum_{i \in A} \left(-\frac{1}{2}\Delta_{\mathbf{r}_i} - \sum_{\alpha \in A} \frac{Z_\alpha}{|\mathbf{r}_i - \mathbf{R}_\alpha|} \right) + \sum_{i \neq j \in A} \frac{1}{r_{ij}} + \sum_{\alpha \neq \beta \in A} \frac{Z_\alpha Z_\beta}{R_{\alpha\beta}} = \\
&= \sum_{i \in A} \hat{h}_A(\mathbf{r}_i) + \hat{V}_A^{ee} + V_A^{nn}.
\end{aligned} \tag{2.3}
$$

Based on (2.2) and (2.3) we find the form of the interaction operator:

$$
\hat{V} = \sum_{i \in A}\sum_{k \in B} \frac{1}{r_{ik}} - \sum_{i \in A}\sum_{\beta \in B} \frac{Z_\beta}{|\mathbf{r}_i - \mathbf{R}_\beta|} - \sum_{k \in B}\sum_{\alpha \in A} \frac{Z_\alpha}{|\mathbf{r}_k - \mathbf{R}_\alpha|} + \sum_{\alpha \in A}\sum_{\beta \in B} \frac{Z_\alpha Z_\beta}{R_{\alpha\beta}}. \tag{2.4}
$$

The total Hamiltonian is then assumed in the form:

$$
\hat{H} = \hat{H}_A + \hat{H}_B + \lambda\hat{V} = \hat{H}_0 + \lambda\hat{V}, \tag{2.5}
$$

where $\lambda \in \langle 0; 1 \rangle$ is a scaling parameter, such that $\lambda = 1$ restores the physical description of the system. Next, one assumes that the unperturbed Hamiltionian eigenfunctions are known:

$$
\begin{cases} \hat{H}_A \psi_A^0 = E_A^0 \psi_A^0 \\ \hat{H}_B \psi_B^0 = E_B^0 \psi_B^0 \end{cases}, \tag{2.6}
$$

and the dimer function is their product:

$$\psi^{(0)} = \psi_A^0 \psi_B^0. \tag{2.7}$$

Let us recast the Schrödinger equation using the reduced resolvent operator $\hat{R}_0$

$$\hat{R}_0 = \sum_{(n,m)\neq(0,0)} \frac{|\psi_A^n \psi_B^m\rangle \langle \psi_A^n \psi_B^m|}{E_A^0 + E_B^0 - E_A^n - E_B^m}, \tag{2.8}$$

to the convenient form:

$$\begin{cases} \Psi = \psi^{(0)} + \hat{R}_0(E_{\text{int}} - V)\Psi \\ E_{\text{int}} = \langle \psi^{(0)}|V\Psi\rangle \end{cases}. \tag{2.9}$$

and then expand the interaction energy and dimer's wavefunction in powers of λ:

$$\begin{cases} \Psi(\lambda) = \psi^{(0)} + \sum_{n=1}^{\infty} \lambda^n \psi^{(n)} \\ E_{\text{int}}(\lambda) = \sum_{n=1}^{\infty} \lambda^n E_{\text{pol}}^{(n)} \end{cases}. \tag{2.10}$$

Finally, general expressions for n-th correction to the interaction energy and wavefunction can be obtained by inserting Eq.(2.10) to (2.9) and comparing expressions at the same powers of λ:

$$\psi^{(n)} = -\hat{R}_0 \hat{V} \psi^{(n-1)} + \sum_{k=1}^{n-1} E_{\text{pol}}^{(k)} \hat{R}_0 \psi^{(n-k)}, \tag{2.11}$$

$$E_{\text{pol}}^{(n)} = \langle \psi^{(0)}|\hat{V}|\psi^{n-1}\rangle. \tag{2.12}$$

This approach is known as polarization perturbation theory or Rayleigh-Schrödinger perturbation theory. Although it correctly describes the asymptotic behavior of the interaction energy, polarization theory suffers from the lack of the exchange antisymmetry between monomer functions in Eq.(2.7). As a consequence, expansion in λ diverges for systems with more than three electrons [73–75]. This is a consequence of the fact that the fermionic ground state of the dimer is coupled with the continuum of the bosonic, Pauli-forbidden, states.

In order to circumvent this problem one may assume the 0-th order wavefunction in an antisymmetrized form, i.e. $\psi'^{(0)} = \hat{A}\psi^{(0)}$, with $\hat{A} = \frac{1}{N!}\sum_P (-1)^P \hat{P}$, $\hat{P}$ being the

N-object permutation operator. Although the new $\psi'^{(0)}$ is no longer the eigenfunction of $\hat{H}_0$, one may introduce the symmetry forcing by inserting appropriate projection operators into the perturbation equations. This approach leads to the symmetry-adapted perturbation theory, SAPT. Different SAPT formulations have been proposed which in general can be divided according to the symmetry forcing schemes applied into weak and strong symmetry forcing approaches [76]. In practice, the strong symmetry-forcing techniques are not applied due to their incorrect asymptotic behavior [77]. In the weak symmetry forcing the projection operator enters only in the energy expression, i.e. in Eq. (2.12). This leads to the symmetrized Rayleigh-Schrödinger (SRS) approach the main virtue of which are the proper asymptotic behavior and relatively easy implementation for many-electron systems.

One should note that apart from model systems, such as H_2 and He_2, SRS should be divergent. Nevertheless, the pragmatic approach following numerical empirical observations is that for most cases second-order SRS perturbation theory is able to recover the interaction energy to within few percent in the Van der Waals minimum region.

2.2   DFT-SAPT

In the presented Thesis we will focus on the DFT-SAPT method [9, 36]. Here one considers the partitioning of the Hamiltonian into the Kohn-Sham operators for the monomers $\hat{K}_X(X = A, B)$ and the interaction operator $\hat{V}$:

$$\hat{H} = \hat{K}_A + \hat{K}_B + \hat{V}, \tag{2.13}$$

thereby effectively neglecting the intramonomer correlation operators present in the many-body formulation of SAPT (MB-SAPT) [78] and taking into account only the lowest-order SAPT expressions. One should note, that in DFT-SAPT the intramonomer correlation effects are built-in *via* DFT description of the monomers. The first-order DFT-SAPT energy can be divided into the electrostatic and exchange-repulsion interaction energies:

$$E^{(1)} = \frac{\langle \psi^{(0)} | \hat{V} | \hat{\mathcal{A}} \psi^{(0)} \rangle}{\langle \psi^{(0)} | \hat{\mathcal{A}} \psi^{(0)} \rangle} = E_{\text{elst}}^{(1)} + E_{\text{exch}}^{(1)}. \tag{2.14}$$

The electrostatic energy corresponds to the classical picture of the interaction between the charges of the unperturbed monomers, whereas no classical interpretation of the exchange energy exists.

The second order energy is a sum of induction and dispersion components, taken together with their exchange counterparts:

$$E^{(2)} = E^{(2)}_{\text{ind}} + E^{(2)}_{\text{disp}} + E^{(2)}_{\text{exch-ind}} + E^{(2)}_{\text{exch-disp}}. \tag{2.15}$$

The induction energy can be interpreted as result of interaction between the permanent multiple moments on monomer B and the induced multipole moments on monomer A, and *vice versa*. Although the dispersion interaction does not have a classical counterpart, it is often interpreted as a stabilizing effect resulting from interaction between instantaneous multiple moments on both monomers. In DFT-SAPT one often includes an estimate of the higher-order energy terms, the so-called δ Hartree-Fock term defined as [79]:

$$\delta_{\text{HF}} = E_{\text{HF}} - \left(E^{(1)}_{\text{elst}}(\text{HF}) + E^{(1)}_{\text{exch}}(\text{HF}) + E^{(2)}_{\text{ind}}(\text{HF}) + E^{(2)}_{\text{exch-ind}}(\text{HF}) \right), \tag{2.16}$$

where E_{HF} denotes the supermolecular Hartree-Fock interaction energy, and the energy contributions come from the HF-based SAPT. This leads to the following decomposition of the interaction energy in DFT-SAPT, up to the second order in $\hat{V}$:

$$E_{\text{int}} = E^{(1)}_{\text{elst}} + E^{(1)}_{\text{exch}} + E^{(2)}_{\text{ind}} + E^{(2)}_{\text{disp}} + E^{(2)}_{\text{exch-ind}} + E^{(2)}_{\text{exch-disp}} + \delta_{\text{HF}}. \tag{2.17}$$

In the early days of DFT-SAPT, Hesselmann and Jansen [37, 38] showed that the correct asymptotic behavior of the exchange-correlation potential, $v_{xc}(\mathbf{r})$, is crucial for the quality of the first- and second-order energy components. Unfortunately, in spite of the correct asymptotic behavior of $v_{xc}(\mathbf{r})$, the results for the dispersion energy remained unsatisfactory. In 2003 Misquitta *et al.* [80] proposed a way of calculating dispersion energy using frequency-dependent density susceptibilities (FDDS) from time-dependent density-functional theory (TDDFT). This allowed to achieve a combination of both accuracy and computational efficiency which made DFT-SAPT the most widely used intermolecular perturbation theory in quantum chemistry [9].

Tuned long-range corrected functionals applied in SAPT

In this part of the Thesis we present incorporation and implementation of the LRC functionals in the DFT-SAPT method, i.e., the LRC-SAPT approach. First, we briefly give the motivation behind the LRC-SAPT approach. Next, we highlight the possible consequences of the delocalization error in SAPT. Furthermore, a brief outline of the LRC-SAPT performance with respect to HF-SAPT and DFT-SAPT approaches is given. The related publication with a detailed study of the method follows.

3.1   Introduction

Both proper asymptotic behavior of the xc potential $v_{xc}(\mathbf{r})$ as well as correct limiting behavior of the electron density were recognized as the essential prerequisites for good performance of DFT-SAPT [37, 38]. As explained in Chapter 1, the OT-LRC functionals were designed to meet the above mentioned criteria, which made them appealing to be adapted for SAPT.

The first attempt at LRC-SAPT was made by Cencek and Szalewicz [35, 81] who limited themselves to a set of four reference systems and pointed towards the need for further studies. The second work on LRC-SAPT by Lao and Herbert [82] provided a more thorough study covering the S22 [83], S66 and SS41 data sets. In their approach

33

the second-order energy contributions were calculated either in an approximate or empirical way. This made the method effective, but at the same time did not supply any information regarding the quality of the dispersion and induction energies obtained via FDDS.

The aim of the work presented in this Chapter was to conduct an evaluation of LRC-SAPT with second-order energy components obtained at the coupled level of theory, i.e., via FDDSs from TDDFT. Apart from providing a wider set of dimers than in the work of Cencek and Szalewicz [35, 81], we looked into the advantages of LRC-SAPT resulting from minimization of DE in OT-LRC functionals. Furthermore, the efficacy of different DFT-SAPT approaches was put in the context of general features of KS and GKS theory.

3.1.1   Asymptotic correction scheme in SAPT

It is important to recall that a correct asymptotic behavior of $v_{xc}(\mathbf{r})$ for large r is [17, 33]:

$$v_{xc}(r) \sim -\frac{1}{r} + \Delta_\infty, \tag{3.1}$$

where for DFAs that do not exhibit derivative discontinuities at integer numbers of electrons, termed continuum functionals, the limiting Δ_∞ value is:

$$\Delta_\infty = \mathrm{IP} + \varepsilon_{\mathrm{HOMO}}. \tag{3.2}$$

The first solution to the improper behavior of the xc potential that gained popularity in SAPT community was the asymptotic correction (AC) scheme [33, 34, 84]. In this approach one splices any semilocal potential in the bulk region with a potential decaying as $-1/r$. The proper Δ_∞ limit may then be assured either by shifting down the bulk part of v_{xc} [84], or equivalently by imposing the positive limit at infinity [33].

There exist several downsides to the AC potentials. The most important one results from the fact that they are not functional derivatives of any density functional of the xc energy. This results in the lack of unique definition of the exchange-correlation energy [85], which in turn causes its lack of the rotational and translational invariance [86, 87]. The practical consequences are spurious forces and torques preventing effective geometry optimizations [86], which probably contributed to the limited applications of

AC potentials in quantum chemistry [35].

However, the more serious problem from the point of view of SAPT methodology is that the AC potentials are *not* DE-free as long as the AC scheme involves semilocal LDA and GGA functionals [60, 88]. This may have direct impact on the quality of both first- and second-order energy contributions. Here I will show two examples of the flawed delocalization of electron density yielding incorrect electrostatic and exchange energies. An example concerning second-order response properties is described in details in Secs. III.A and III.B of the attached work [D1].

3.2 Results

3.2.1 Delocalization error in SAPT

Let us first consider a model system consisting of three collinearly arranged helium atoms with the net charge of +1, He_3^+ [6]. In order to visualize the presence of DE, we vary the interatomic distance R between the central and peripheral atoms, simultaneously tracing the Mulliken charge on the central atom. The results presented in Fig. 3.1 show that neither PBE0 nor PBE0AC manage to recreate the proper behavior of the FCI theory (see Ref. [6]), i.e. to localize the charge on the central atom. Instead, we observe a uniform delocalization of the electron density which will yield an erroneous electrostatic interaction with any other system. It is only the IP-tuned LC-ωPBE functional that captures the physics of the system ensuing proper electrostatic energy.

Next, let us look at a more realistic system: the *para*-nitroaniline (p-NA) molecule, which is a π-conjugated donor(amino)/acceptor(nitro) chromophore of a "push-pull" character. Sun and Autschbach [51] have investigated DE in this system and visualized its influence on the electron density by looking at the delocalization of the amine nitrogen π lone pair onto the aryl moiety. We take a different approach and use the fact that both electrostatic and exchange SAPT energy contributions are an excellent probe of the electron density distribution. For our study we chose a system of two p-NA molecules in an anti-parralel arrangement, close to the equilibrium geometry. Furthermore, from the family of twelve LC-ωPBEh functionals optimized for this systems [51] we chose two which vary in the total percent contribution of HF exchange,
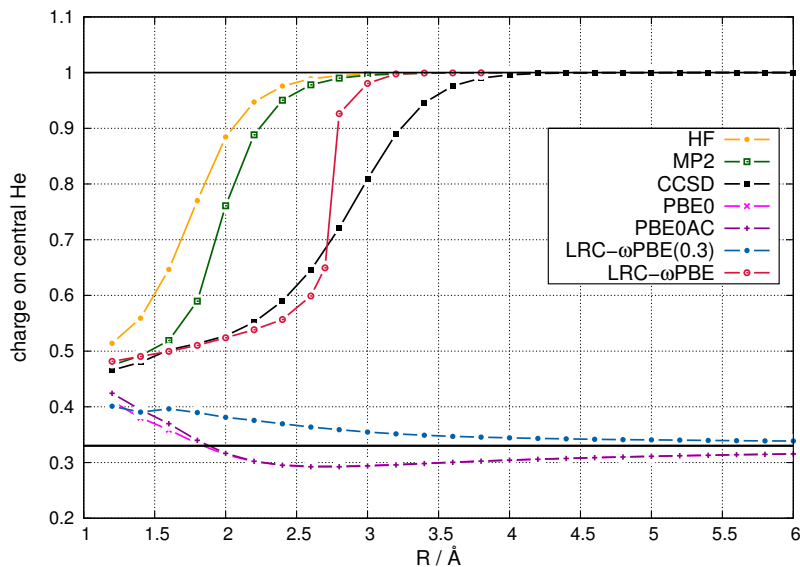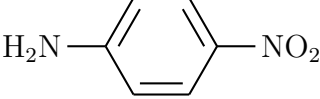
Figure 3.1: Mulliken charge on central He atom in He_3^+ as a function of the interatomic distance R calculated using HF, MP2, CCSD, PBE0, LRC-ωPBE(0.3) ($\omega = 0.3$ bohr^{-1}) and LRC-ωPBE (IP-tuned).

i.e., originating from both the short and the long-range exchange: LC-ωPBEh(63%) and LC-ωPBEh(26%). The corresponding optimized (ω, α) parameters are (0.05,0.622) for the first and (0.275,0.031) for the second. The results of SAPT calculations at different levels of theory, together with the values of the electric dipole moment of the monomer unit along the direction of the N-N axis, are presented in Table 3.1.[*]

The discrepancy between the DFT and benchmark CC results ranging from 12% to 49% in terms of $E^{(1)}$ and from 4% to 10% in terms of μ_z confirms that the p-NA dimer is a challenging system for DFT. The optimized LC-ωPBEh functionals constitute an improvement over other DFT-SAPT approaches, including PBE0AC. We observe that the lower percent of the total HF exchange in ωPBE(0.275,0.031) leads to an improvement of both $E^{(1)}$ contribution and the dipole moment with respect to the ωPBE(0.275,0.031) values.

---

[*]unpublished results

Table 3.1: First-order SAPT energy components of the interaction between two p-NA molecules arranged in an anti-parralel fashion. μ_z stands for z-component of the electric dipole moment. ωPBE(%HF) denote LC-ωPBEh functionals optimized in Ref. [51]. Above the results a single p-NA molecule is shown. All calculations employed def2-TZVP basis [89]. All energies given in kcal/mol.

SAPT	E_{elst}	$E_{\text{exch}}^{(1)}$	$E_{\text{tot}}^{(1)}$	μ_z [D]
HF	-3.37	2.07	-1.30	7.74
PBE0	-3.19	1.85	-1.34	7.61
PBE0AC	-3.23	1.99	-1.24	7.59
ωPBE(63%)	-3.07	1.61	-1.46	7.65
ωPBE(26%)	-2.93	1.92	-1.01	7.24
MP2	-2.82	2.05	-0.77	6.92
CCSD	-2.76	1.85	-0.90	6.96

3.2.2 A24 test results

Before moving to the performance test of different SAPT approaches we note that the LRC-SAPT method does not require any modification of the well-known expressions for energy contributions (see, e.g. Ref. [90]). However, one has to implement the right form of the Hessian matrices in order to calculate the second-order energy components *via* FDDSs [91]:

$$
\begin{aligned}
H_{ia,jb}^{(1)} &= (A+B)_{ia,jb} = (\epsilon_a - \epsilon_i)\delta_{ij}\delta_{ab} + 4(ia|jb) - \zeta\big((ij|ab) + (ib|aj)\big) \\
&\quad - (1-\zeta)\big((ij|ab)^{\text{LR}} + (ib|aj)^{\text{LR}}\big) + 4(ia|f_{xc}^{\text{SR}}|bj), \\
H_{ia,jb}^{(2)} &= (A-B)_{ia,jb} = (\epsilon_a - \epsilon_i)\delta_{ij}\delta_{ab} + \zeta\big((ib|aj) - (ij|ab)\big) \\
&\quad + (1-\zeta)\big((ib|aj)^{\text{LR}} - (ij|ab)^{\text{LR}}\big),
\end{aligned}
\tag{3.3}
$$

where ζ is the amount of HF-exchange admixture and $(ij|ab)^{\text{LR}}$ and $(ib|aj)^{\text{LR}}$ are the long-range two-electron Coulomb and exchange integrals, respectively.

In the attached work the accuracy of the LRC-SAPT and other DFT-SAPT approaches was analyzed using two data sets: the A24 data set of Hobza *et al.* [92] and DI6-04 set of Truhlar [93]. In order to briefly outline our findings, we concentrate on the results for the A24 set. Table 3.2 contains mean absolute errors (MAEs) and

Table 3.2: Mean absolute errors (MAEs) and root-mean-square deviations (RMSDs), in kcal/mol, for interaction energies of the A24 [92] data set, with respect to benchmarks computed at the CCSD(T)/CBS level. All SAPT results include the δE^{HF} correction.

MAE [kcal/mol]	PBE	PBEAC	PBE0AC	LRC-ωPBE	LRC-ωPBEh
A24	0.420	0.262	0.114	0.0752	0.0786
RMSD [kcal/mol]					
A24	0.619	0.471	0.162	0.088	0.095
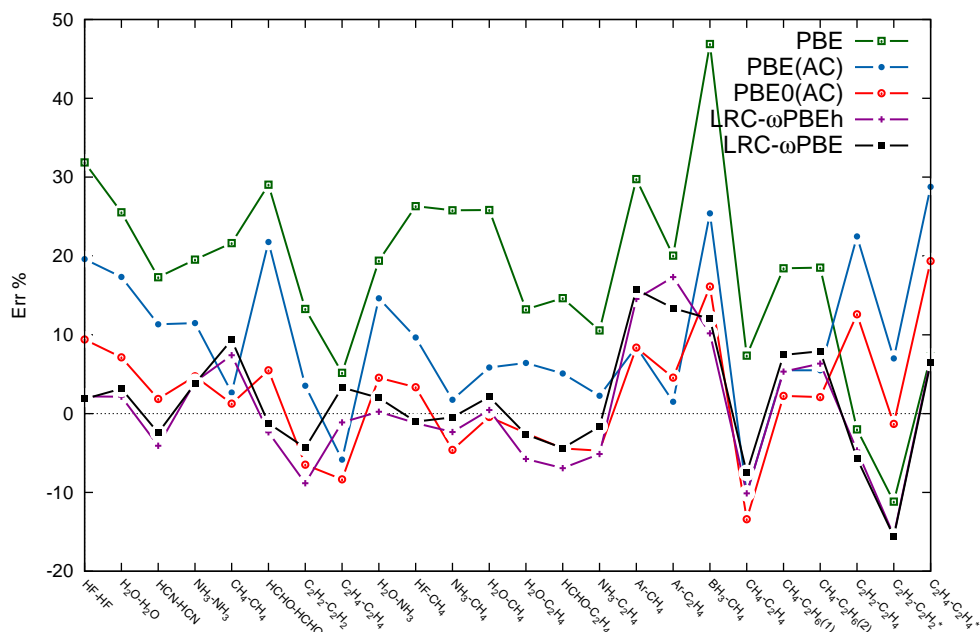
Figure 3.2: Percentage errors of DFT-SAPT total energies with respect to benchmark values (see the text for more information) for the A24 Set [92]. All SAPT results include the δE^{HF} correction.

root-mean-square deviations (RMSDs) for DFT-SAPT calculations, as compared to benchmark CCSD(T)/CBS energies.

We observe that moving from KS to GKS description of monomers,. i.e, from PBE to PBEAC to PBE0AC to LRC functionals, corresponds to a significant improvement in the accuracy of DFT-SAPT. For the A24 data set the optimally tuned LRC functionals perform better than the asymptotically corrected PBE0AC, which is the most popular DFA used in DFT-SAPT [9].

Additional information regarding performance of DFT-SAPT is achieved by looking at percentage errors of the DFT-SAPT total interaction energies (Fig. 3.2). Al-

though the observation of improvement on going from KS to GKS still holds, the results in Fig. 3.2 allow to see that the LRC-SAPT description leads to underbinding for the several dispersion-bound systems of the A24 data set ($CH_4 \cdots CH_4$, $CH_4 \cdots C_2H_6$, $Ar \cdots C_2H_4$). This may partially be attributed to the aug-cc-pVTZ basis set being too small to saturate the dispersion energy. Yet, a detailed analysis conducted in our work showed that response properties in LRC-SAPT may be underestimated in the case of systems for which the optimized functional exceeds ca. 50% of the HF exchange. Fortunately, this is true for a limited number of systems, such as rare gas monomers, characterized by large optimal ω values.

3.3   Related publication

The following publication [D1] contains an extended analysis of the impact of DE on DFT-SAPT, including examples regarding second-order response properties: static polarizabilities and isotropic C_6 coefficients of polyacetylenes. In particular, we prove that AC potentials show wrong scaling behavior with respect to the increasing particle size. Moreover, a thorough performance test of LRC-SAPT is conducted, with special attention paid to the behavior of dispersion energy in KS and GKS approaches. The role of short-range exchange in LRC-SAPT is also examined. Finally, the possible limitations of the LRC-SAPT approach are recognized and discussed.

Tuned range-separated hybrid functionals in the symmetry-adapted perturbation theory

Michał Hapka,[1] Łukasz Rajchel,[2,3] Marcin Modrzejewski,[1] Grzegorz Chałasiński,[1,4] and Małgorzata M. Szczęśniak[5]

[1]*Faculty of Chemistry, University of Warsaw, 02-093 Warsaw, Pasteura 1, Poland*
[2]*Faculty of Chemistry, University of Duisburg-Essen, Universitätsstraße 5, 45117 Essen, Germany*
[3]*Interdisciplinary Centre for Mathematical and Computational Modelling, University of Warsaw, 00-838 Warsaw, Prosta 69, Poland*
[4]*Department of Chemistry, Oakland University, Rochester, Michigan 48309-4477, USA*
[5]*Department of Chemistry, Oakland University, Rochester, Michigan 48309-4477, USA*

The aim of this study is to present a performance test of optimally tuned long-range corrected (LRC) functionals applied to the symmetry-adapted perturbation theory (SAPT). In the present variant, the second-order energy components are evaluated at the coupled level of theory. We demonstrate that the generalized Kohn-Sham (GKS) description of monomers with optimally tuned LRC functionals may be essential for the quality of SAPT interaction energy components. This is connected to the minimization of a many-electron self-interaction error and exemplified by two model systems: polyacetylenes of increasing length and stretching of He_3^+. Next we provide a comparison of SAPT approaches based on Kohn-Sham and GKS description of the monomers. We show that LRC leads to results better or comparable with the hitherto prevailing asymptotically corrected functionals. Finally, we discuss the advantages and possible limitations of SAPT based on LRC functionals. © *2014 AIP Publishing LLC*. [http://dx.doi.org/10.1063/1.4896608]

I. INTRODUCTION

Symmetry-adapted perturbation theory (SAPT) in its symmetrized Rayleigh-Schrödinger (SRS) formulation has become a successful method of calculating interaction energies in non-covalent molecular complexes.[1–5] In the most popular variant of SAPT, the description of monomers is provided by density functional approximations (DFAs). This approach is denoted as DFT-SAPT or SAPT(DFT).[6,7] For the latest review of the method, see the paper by Jansen.[5]

As has been recognized in the early days of the method, the proper asymptotic behavior of the exchange-correlation (xc) potential, v_{xc}, is crucial for DFT-SAPT.[8–11] In the case of the functionals that do not exhibit derivative discontinuities at integer numbers of electrons, so called continuum functionals, the behavior of the xc potential for large distances from the nuclei should be:[12,13]

$$v_{xc}(r) \sim -\frac{1}{r} + \Delta_\infty, \tag{1}$$

where Δ_∞ is the limit value of the potential at infinity and equals IP + ε_H [IP stands for the lowest ionization potential and ε_H is the Kohn-Sham (KS) eigenvalue of the highest occupied molecular orbital (HOMO)]. A solution that fulfills this condition is the asymptotic correction (AC) scheme.[13–15] Asymptotically corrected potentials provide an improved treatment of electron density and response properties essential for DFT-SAPT applications.[7,9–11] The AC method is based on combining a semilocal potential in the bulk region with a potential exhibiting proper long-range behavior in the asymptotic region of the density. The procedure referred to as "cutting and splicing" may employ differ-

ent continuous switching functions. Misquitta and Szalewicz combined the long-range Fermi-Amaldi expression with the connection scheme of Tozer and Handy.[11,13] Hesselmann and Jansen merged the LB94 potential from van Leeuwen and Baerends[16] with the PBE0[17,18] functional via the gradient-regulated seamless connection method of Grüning *et al.*[9,15] Finally, Misquitta proposed the use of the LB94 potential switched on by the function of Tozer and Handy.[19] All three flavors of the AC have recently been validated regarding their performance for molecular properties, energies of excitations to Rydberg states, and interaction energies in the paper of Cencek and Szalewicz.[20,21] In this work, as an alternative to ensuring the positive value at infinity (Eq. (1)), we employ the AC that shifts down the bulk part of v_{xc} by Δ_∞, while keeping the zero limit at infinity.

Two problems in applications of asymptotically corrected potentials should be mentioned. First, AC potentials belong to the class of the so-called "stray potentials," i.e., they are not functional derivatives of any density functional of the xc energy.[22,23] This prevents a unique definition of the exchange-correlation energy. Furthermore, energies from stray potentials lack the rotational and translational invariance.[23,24] Arguably, this is not a difficulty because monomer energies are not needed in SAPT. However, calculation of energy derivatives over the field or over fractional electron numbers is impossible and this, as we will argue, hinders checking the quality of the monomer description. Second, although asymptotically corrected potentials display the exact long-range behavior, the effects of many-electron self-interaction error (MSIE)[25,26] are *still* present if the AC scheme involves semilocal LDA and GGA functionals.[27] This manifests itself in erroneous dissociation of symmetric ion radicals[27] and

improper response to externally applied electric field in extended molecular systems.[28] The latter has been traced to the absence of the field-counteracting term[29–31] in the exchange potential of the underlying functional.[32–35]

The long-range corrected (LRC) functionals offer an alternative way of improving the asymptotic distance dependence[36–41] of v_{xc}. Moreover, the tuning of the range-separation parameter assures the proper limiting behavior of the electron density.[42,43] LRC functionals provide the xc potential in a straightforward manner, i.e., as a functional derivative $v_{xc} = \delta E_{xc}[\rho]/\delta\rho$, avoiding inconsistencies stray potentials are burdened with. Moreover, they allow for the minimization of MSIE,[44,45] and, as a consequence, reliable characterization of long-range-dependent properties including polarizabilities and hyperpolarizabilities of challenging π-conjugated systems.[36,44,46,47]

The applicability of long-range corrected functionals to DFT-SAPT was studied in two recent papers. Cencek and Szalewicz studied the performance of LRC-SAPT against a set of four reference systems for which benchmark first- and second-order energy contributions were available.[20] In the Erratum[21] to this paper, they show that the optimally tuned LRC functional affords *accurate* density for He. They further conclude that LRC functionals with optimally tuned range-separation parameter "perform not much worse than the best AC corrected functionals" and that further investigations are warranted.

Lao and Herbert conducted a more detailed study of the LRC-SAPT method.[48] Not only did they cover both S22[49] and S66[50] data sets for non-covalent interactions, but also constructed a new SS41 data set of benchmark energy components. In their approach, the second-order induction energy was treated at the uncoupled level of theory with only approximate treatment of orbital relaxation. Since the dispersion term calculated at the uncoupled level lead to unsatisfactory results, the authors replaced it with an empirical dispersion potential, the so-called SAPT(KS)+D approach.[51,52] Their conclusion was that the tuned LRC functionals provide quantitative predictions in DFT-SAPT, competitive with those obtained with the AC models. Furthermore, LRC-SAPT was in their view a step towards introduction of analytic gradients.[48]

The aim of this work is to present a performance test of LRC-SAPT with second-order energy components calculated at the coupled level of theory, i.e., via frequency-dependent density susceptibilities (FDDSs) from time-dependent DFT, on a wider set of dimers than in Ref. 20. We also provide a comparison of SAPT based on different DFT approaches and relate their efficacy to the features of Kohn-Sham (KS) and generalized Kohn-Sham (GKS) theory.[53,54]

The structure of this paper is as follows. In Secs. III A–III C, we reveal the weaknesses of the asymptotic correction scheme which are relevant to SAPT applications. In order to exemplify the effect of the missing field-counteracting term, we calculate static polarizabilities of polyacetylenes, similarly to Sekino *et al.*[28] In Sec. III C, on another model system, He_3^+, we demonstrate that when the electron distribution is examined, v_{xc}^{AC} may lead to the identically flawed delocalization of electron density as the underlying bulk semilocal xc functional.

Finally, in Sec. III D, a comparison with other DFT-SAPT schemes, namely, SAPT(PBE), SAPT(PBEAC), and SAPT(PBE0AC) is provided. In order to complement previous works on LRC-SAPT, we focus on total interaction energies for two sets of small van der Waals dimers, the A24 set of Hobza *et al.*[55] and DI6-04 set of Truhlar.[56] In particular, we address the behavior of the dispersion energy and recognize the possible limitations to the LRC-SAPT approach.

II. COMPUTATIONAL DETAILS

In DFT-SAPT, we calculate the interaction energy, E_{int}, as the sum of electrostatic $\left(E_{elst}\right)$, first-order exchange $\left(E_{exch}^{(1)}\right)$, second-order induction $\left(E_{ind}^{(2)}\right)$, and dispersion $\left(E_{disp}^{(2)}\right)$ energies as well as their exchange counterparts, exchange-induction $\left(E_{exch-ind}^{(2)}\right)$ and exchange-dispersion $\left(E_{exch-disp}^{(2)}\right)$:

$$E_{int} = E_{elst}^{(1)} + E_{exch}^{(1)} + E_{ind}^{(2)} + E_{exch-ind}^{(2)} + E_{disp}^{(2)}$$
$$+ E_{exch-disp}^{(2)} + \delta E^{HF}. \quad (2)$$

The last term, the so called δ Hartree-Fock term, approximately accounts for higher-order terms.[57] In our implementation, the second-order induction energy is computed using the coupled KS static response theory, and the dispersion energy via FDDSs from time-dependent DFT.

We chose a LRC functional composed of the PBE correlation and the short-range (SR) exchange ωPBE based on Henderson, Janesko, and Scuseria model of the exchange hole, LRC-ωPBE.[41] We support such selection by noting that this is a range-separated variant of the PBE functional which is thoroughly tested in the context of DFT-SAPT. The following range-separation scheme into short-range and long-range of the form is applied:

$$\frac{1}{r_{12}} = \frac{erfc(\omega r_{12})}{r_{12}} + \frac{erf(\omega r_{12})}{r_{12}}, \quad (3)$$

where erf and erfc stand for the error function and its complement, and ω is the range separation parameter. A further decomposition of SR exchange into Hartree-Fock (HF) and DFT parts is employed,

$$E_x^{SR} = \alpha E_{HF,x}^{SR} + (1-\alpha)E_{DFT,x}^{SR}. \quad (4)$$

In Sec. III D, we applied functionals with two different α values: 0.0 and 0.2, denoted as LRC-ωPBE and LRC-ωPBEh, respectively. In Sec. III E, α values from 0.0 to 0.6 were applied. The range-separation parameter, ω, was optimally tuned according to the IP-tuning procedure, i.e., by minimizing the difference between the negative of HOMO energy and the vertical ionization potential (IP):[58]

$$J_H^2(\omega_H) = \min_\omega \left(E(N-1) - E(N) + \varepsilon_H\right)^2, \quad (5)$$

where E denotes the self-consistent energy for N and $N-1$ electron systems and ε_H stands for energy of the HOMO orbital. The tuning procedure was carried out separately for each monomer in its dimer geometry.

All SAPT calculations were performed in the developer's version of the MOLPRO package.[59] Our implementation utilized a hybrid xc kernel composed of the short-range LDA

exchange kernel scaled by $(1 - \alpha)$, the LDA correlation kernel and the coupled Hartree-Fock kernel scaled by α. For both the A24 and DI6-04 data sets, the aug-cc-pVTZ basis set of Dunning *et al.* was applied.[60] The asymptotic correction scheme of Grüning *et al.* was applied to the PBE[17] and hybrid PBE0 functionals, yielding PBEAC and PBE0AC functionals, respectively.[15]

Dipole polarizabilities were calculated analytically in the cc-pVDZ basis set,[60] except for coupled-cluster with singles and doubles (CCSD) data where the finite-field (FF) method was employed. We confirmed the agreement between the FF and time-independent CCSD results utilizing the CCSD(3) model implemented in MOLPRO (for polyacetylenes up to four –C=C– units).[61,62] The geometries and IP-optimized range-separation parameters were taken from Ref. 58 (–C=C– distances reflect bond alternation). The polarizabilities were obtained with the following methods and program suites: MP2 and CCSD with MOLPRO,[59] PBE0 and PBE0AC with DALTON 2013,[63,64] and LRC-ωPBE with QCHEM.[65]

For the model He_3^+ system, the aug-cc-pVTZ basis set was chosen. The MP2 and CCSD calculations were performed in GAUSSIAN 09,[66] all other results were obtained with MOLPRO.

The A24 set of noncovalent complexes comprises small model systems selected in order to cover a wide spectrum of noncovalent interactions, i.e., hydrogen bonds, mixed electrostatics/dispersion, and dispersion-dominated interactions (including $\pi-\pi$ stacking).[55] The benchmark energies used to compare our SAPT results were based on the CCSD with perturbative triples extrapolated to complete basis set limit, CCSD(T)/CBS, with an additional correction for perturbative quadruples, CCSDT(Q).

To go beyond the interactions involving exclusively second-row atoms, an additional set of benchmark systems

was chosen. The DI6-04 basis set features six dipole interacting complexes containing third-row elements, sulfur and chlorine.[56] Benchmark geometries and energy values for DI6-04 were taken from Ref. 51, except for $(H_2S)_2$, whose geometry was reoptimized at the CCSD(T)/avtz level and the benchmark CCSD(T)/CBS value was obtained according to the expression of Halkier *et al.* with $X = 5$ (Eq. (4) of Ref. 67).

III. NUMERICAL RESULTS

Recently Tsai *et al.* conducted a comparison of the LRC and AC-based methods.[27] Their results demonstrate the superior performance of LRC functionals over the AC approach for a wide range of properties. In this work, we address the shortcomings of the AC scheme that should directly affect the SAPT terms, complementing the findings of Ref. 27. The shortcomings in question offer an indirect measure of the persistence of the self-interaction error. We emphasize that in the case of asymptotically corrected potentials, a direct test of the dependence of the energy with respect to fractional electron numbers[25] is impossible. This is due to the non-uniqueness of the AC energy, as stray potentials do not correspond to any density functional.

A. Polarizabilities of long chains

A known failure of local and semilocal DFAs is the catastrophic overestimation of polarizabilities and hyperpolarizabilities for long-chained molecules.[30,68] Several studies proved that LRC functionals can rectify this problem, at least qualitatively.[28,44,69–71] Figure 1 shows longitudinal static polarizabilities of polyacetylene chains up to $C_{24}H_{26}$ predicted by different levels of theory (the remaining components of the polarizability remain coherent within all the methods as shown in Table S1 of supplementary material[72,73]). The
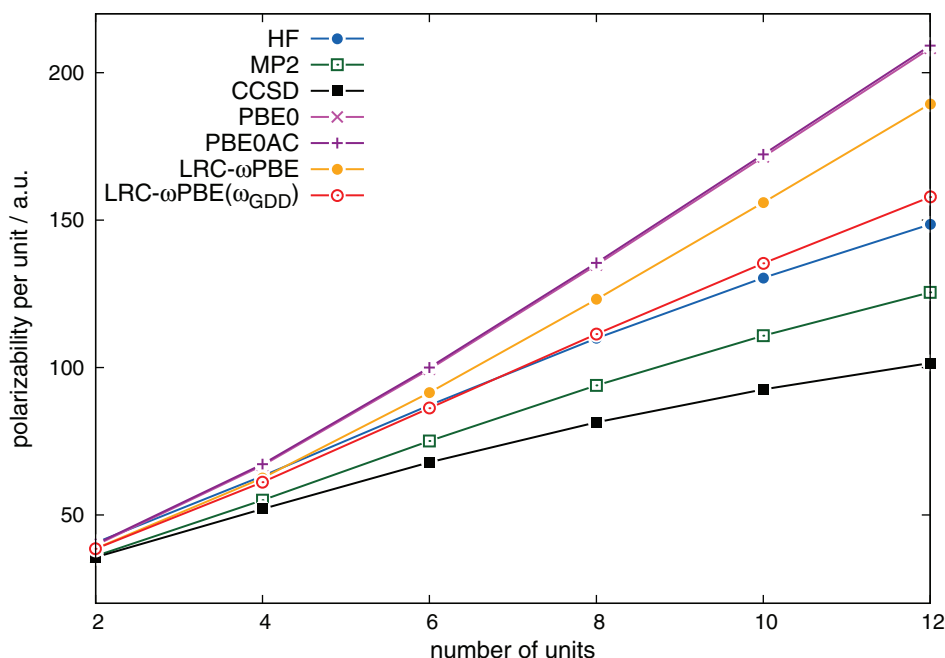

FIG. 1. Longitudinal dipole polarizabilities of polyacetylene per unit in a.u.: the number along the horizontal axis denotes the number of –C=C– units. The LRC-ωPBE and LRC-ωPBE(ω_{GDD}) stand for IP- and ω_{GDD}-optimized LRC-ωPBE functionals, respectively.

results show that PBE0 and PBE0AC fail identically, thus indicating the lack of the field-counteracting term. The same conclusion applies to the Casida-Salahub AC scheme, as observed by Sekino *et al.*[28] An overestimation in the linear response for long molecules should translate into inaccurate FDDSs and overestimated second-order induction and dispersion energy contributions in SAPT.

π-conjugated systems may pose a challenge for LRC-SAPT as well, as the IP-tuned ω values decrease rapidly with the chain length. This behavior was first observed by Körzdörfer *et al.* and attributed to the varying extent of the π-conjugated character of the system.[58] An alternative global-density-dependent (GDD) tuning procedure, termed ω_{GDD}, as proposed by Modrzejewski *et al.*[74] easily ameliorates this spurious behavior (Fig. 1). In this model, the optimal ω value is related to the average distance between the outer electron and an exchange hole. It is expected to lead to significantly improved response properties.

B. Isotropic C_6 coefficients of long chains

The lack of the field-counteracting term in the exchange potential should impact not only the static but also the dynamic response of the molecule. In particular, one expects incorrect behavior of dynamic polarizabilities at imaginary frequencies to yield systematically overestimated dispersion energy (see also Misquitta *et al.*).[75] In order to illustrate this effect we calculated isotropic C_6 coefficients for the interaction between two polyacetylene chains. The results presented in Table I follow the trends observed for longitudinal dipole polarizabilities: (i) the discrepancy between the DFA and CCSD reference values increases together with the chain length, (ii) PBE0AC constitutes *no improvement* over PBE0, and (iii) the optimally tuned CAM-B3LYP*[76] func-

TABLE I. Isotropic C_6 coefficients (in a.u.) of polyacetylene per unit, where n denotes the number of $-C=C-$ units. CAM-B3LYP* denotes the variation of standard functional with $\alpha = 0.19$, $\beta = 0.81$ and ω_{GDD}-tuned.

n	CCSD	HF	PBE	PBE0	PBE0AC	CAM-B3LYP*
2	389	391	409	401	399	391
4	918	968	1023	991	1004	949
6	1617	1763	2013	1896	1921	1751

tional shows similar n-dependence as HF values. We conclude that for extended systems with fluxional electron distributions, SAPT based on PBE, PBE0, and PBE0AC will yield overestimated dispersion energies.

C. Delocalization error

MSIE may adversely affect the distribution of the electron density. To demonstrate that AC does not cure the delocalization error of standard DFAs we applied it to the stretched He_3^+, a model system studied by Körzdörfer and Brédas.[45] In this collinear system, the intermolecular distance R between the central and peripheral atoms is varied from 1.2 to 7 Å. Figure 2 shows the variations of the charge on the central He as a function of R obtained by different methods. As evidenced by the full configuration interaction (FCI),[45] with increasing R the positive charge should localize on the central helium atom. Both PBE0 and PBE0AC, as well as an untuned LRC-ωPBE($\omega = 0.3$), lead to uniform delocalization of electron density over three atoms (Fig. 2). Such erroneous charge density will result in inaccurate electrostatic interaction energy with any other subsystem. By contrast, the IP-tuned LRC-ωPBE correctly assigns whole positive charge to the central He atom ensuing correct electrostatic energy.
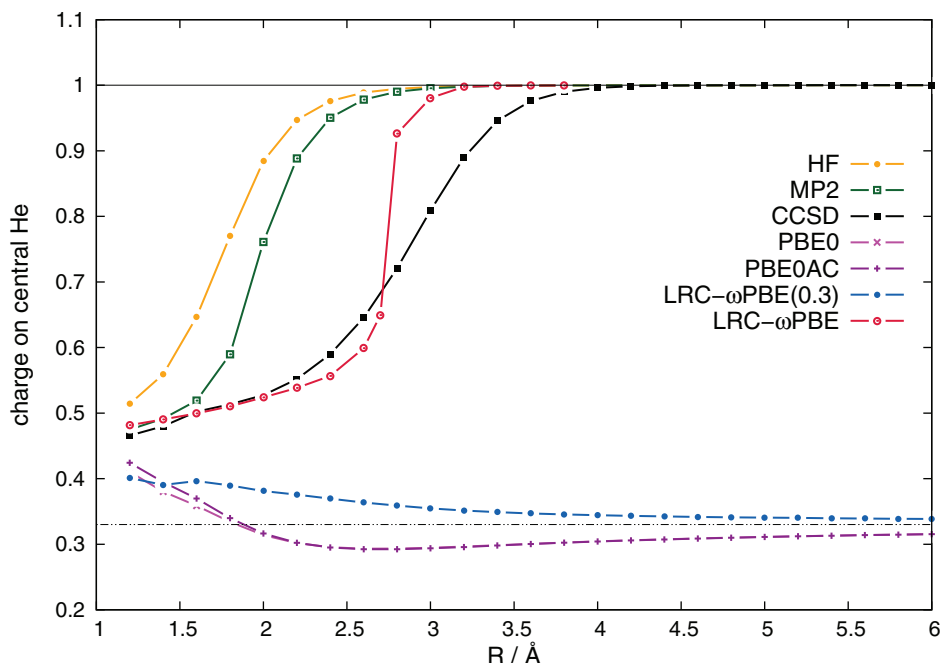

FIG. 2. Mulliken charge on central He atom in He_3^+ as a function of the interatomic distance R calculated using HF, MP2, CCSD, PBE0, LRC-ωPBE(0.3) ($\omega = 0.3$ bohr^{-1}), and LRC-ωPBE (IP-tuned).

TABLE II. Mean absolute errors (MAEs) and root-mean-square deviations (RMSDs), in kcal/mol, for interaction energies of the A24[55] and DI6-04[51,56] data sets, with respect to benchmarks computed at the CCSD(T)/CBS level. All SAPT results include the δE^{HF} correction.

	PBE	PBEAC	PBE0AC	LRC-ωPBE	LRC-ωPBEh
MAE [kcal/mol]					
A24	0.420	0.262	0.114	0.0752	0.0786
DI6-04	0.260	0.107	0.225	0.223	0.307
RMSD [kcal/mol]					
A24	0.619	0.471	0.162	0.088	0.095
DI6-04	0.290	0.121	0.268	0.262	0.345

The distortion of electrostatics due to the delocalization error can be expected for many chemically interesting systems, e.g., in molecular electronics.[77–79] To better appreciate the consequences to SAPT, let us recall the case of the tetrathiafulvalene diquinone anion (Q-TTFQ)$^-$ where Vydrov and Scuseria[77] demonstrated that LRC correctly localizes the negative charge on half of the molecule while both PBE and PBE0 erroneously delocalize the charge over the entire molecule. A SAPT(PBEAC/PBE0AC) calculation for this system as an interaction partner would no doubt be wrong.

D. A24 and DI6-04 test results

Having discussed challenges for DFT-SAPT applications, we now move to the performance test of different approaches to the method. In Table II, we present mean absolute errors (MAEs) and root-mean-square deviations (RMSDs) for DFT-SAPT calculations of the A24 and DI6-04 data sets, as compared to benchmark energies. The entries from the left to the right gradually move from a KS to a GKS description of monomers.

For the A24 data set, there is a clear improvement going from PBE to PBEAC to PBE0AC to LRC functionals, i.e., from KS to GKS description of monomers. We observe that optimally tuned LRC functionals stay in close agreement and outperform asymptotically corrected PBE0AC, considered as the functional of choice for the DFT-SAPT method.[5,80]

In the case of the dipole-bound systems in the DI6-04 data set, the situation is different, as the increased fraction of the HF exchange correlates with a considerable overbinding. There is a clear deterioration from PBEAC to PBE0AC and analogously from LRC-ωPBE to LRC-ωPBEh, with PBE0AC and LRC-ωPBE performing almost identically. Similar overbinding in DFT-SAPT was reported for dispersion dominated systems containing phosphorus, $(P_2)_2$ and $(PCCP)_2$, in Ref. 80.

An analysis of the SAPT energy components attributes this overbinding to the imbalanced reduction between $E_{\text{exch}}^{(1)}$ and $E_{\text{disp}}^{(2)}$ in GKS with respect to SAPT(PBEAC) (see Fig. S1 in the supplementary material[72]).

In Figs. 3 and 4, we provide percentage errors of the DFT-SAPT total interaction energies for systems of A24 and DI6-04 data sets, respectively. The underbinding observed for the several dispersion-bound systems of the A24 data set, i.e., CH$_4$$\cdots$CH$_4$, CH$_4$$\cdots$C$_2H_6$, Ar$\cdots$CH$_4$ and Ar$\cdots$C$_2$H$_4$ results from the aug-cc-pVTZ basis set being too small to saturate the dispersion interaction. Extending the basis set to aug-cc-pVQZ reduces the errors (not shown). One should bear in mind that the basis set error introduced by the application of aug-cc-pVTZ influences the overall comparison of the DFT-SAPT approaches. Nevertheless, a similar performance of LRC-SAPT and AC-SAPT in larger basis sets should hold, as shown in the work of Cencek and Szalewicz.[21]

Let us more closely examine the behavior of the dispersion energy in different realizations of DFT-SAPT. Williams

FIG. 3. Percentage errors of DFT-SAPT total energies with respect to benchmark values, $\Delta_\% = \frac{E_{\text{Ref}} - E_{\text{SAPT}}}{E_{\text{Ref}}} \times 100\%$ (see the text for more information) for the A24 Set.[55] All SAPT results include the δE^{HF} correction.
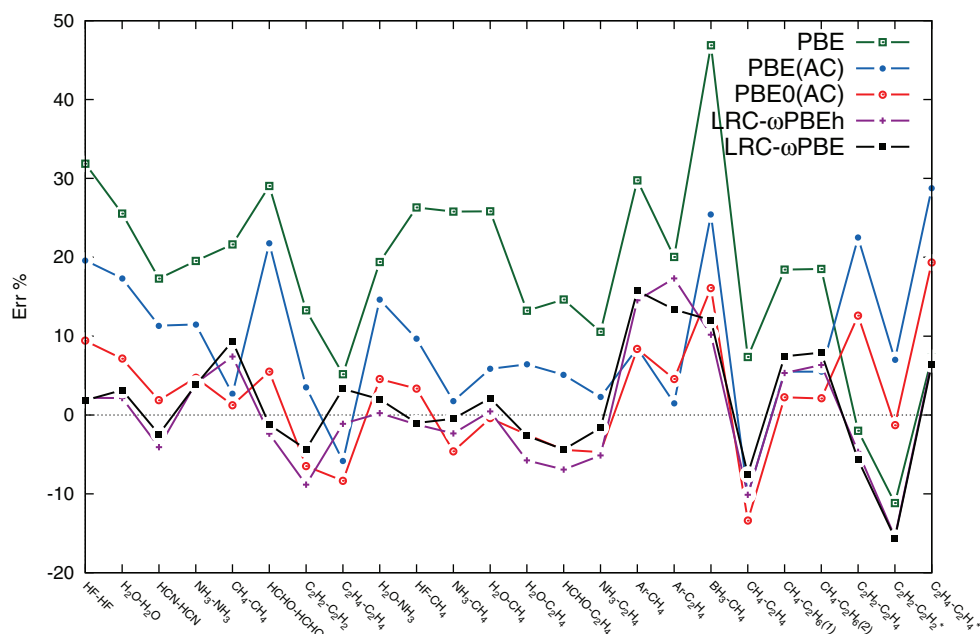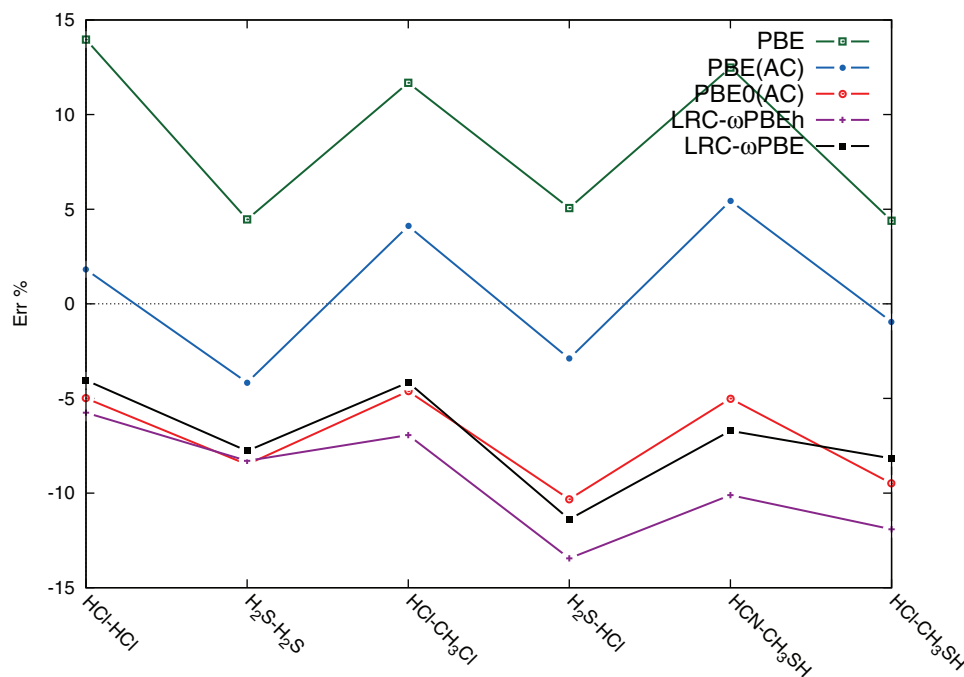
FIG. 4. Percentage errors of DFT-SAPT total energies with respect to benchmark values, $\Delta_\% = \frac{E_{\text{Ref}} - E_{\text{SAPT}}}{E_{\text{Ref}}} \times 100\%$ (see the text for more information) for the DI6-04 Set.[56] All SAPT results include the δE^{HF} correction.

and Chabalowski were first to notice a correlation between induction and dispersion terms and the gaps between occupied and virtual orbitals in the uncoupled second-order SAPT.[6,8] In the KS scheme, these differences are underestimated, which manifests itself in HOMO-LUMO (HL) gaps being significantly narrower than fundamental gaps. (We note that there is a difference in physical interpretation of HL gaps obtained from Kohn-Sham and Generalized Kohn-Sham approaches, see Refs. 81 and 82). In the GKS scheme, realized by hybrid and LRC functionals, HL gaps widen as a fraction of Hartree-Fock, the self-interaction-free exact-exchange term, is introduced.[83] In hybrid functionals, application of the AC ensures proper asymptotic behavior of the v_{xc} potential and shifts the HOMO level to match the vertical ionization potentials. This, however, is insufficient to raise LUMO to match HOMO of the negative ion because of the derivative discontinuity (DD). Consequently, even in asymptotically corrected hybrid functionals HL gaps remain too narrow. On the other hand, absorbing the DD by the optimal tuning procedure in LRC functionals leads to almost perfect correspondence between the HL orbital gaps and the (accurate) fundamental gaps from Δ self-consistent field (SCF) computations.[58,74,84,85]

In Fig. 5, we present correlation between the dispersion energy, $E_{\text{disp}}^{(2)}$, and HL gaps for homodimers from the A24 data set. As expected, a reduction of the dispersion interaction at the uncoupled level of theory follows a broadening of the HL gap from KS to AC KS and AC GKS to LRC GKS. A similar dependence is observed for the coupled treatment of dispersion (Fig. 5). It is expected that both KS and GKS formalisms would yield "exact" response properties, provided that the exact underlying (local or nonlocal) xc potentials and kernels in both theories were known and could

be calculated. Results presented in Fig. 5 reveal that the LRC description of orbital energies corresponds the observed underestimation of the dispersion energy in LRC-SAPT with respect to AC-SAPT and KS-SAPT methods (see Sec. III E. and Table S1 in the supplementary material[72]). Still, the LRC functionals were shown to provide a reliable description of response properties,[27,86] such as static[28,44,69–71] and dynamic polarizabilities[20,46] which benefits the quality of dispersion energy at the coupled level of SAPT.[87,88]

Nevertheless, systems characterized by large ω values pose a particular challenge for LRC-SAPT, as exemplified by dimers containing rare-gas atoms. Increasing the total fraction of HF exchange too much may distort the balance in error compensation between correlation and exchange functionals, resulting in the incorrect behavior of the energy contributions.[89,90] We show this by plotting the first-order, $E^{(1)} = E_{\text{elst}} + E_{\text{exch}}$, and dispersion, $E_{\text{disp,tot}}^{(2)} = E_{\text{exch-disp}}^{(2)} + E_{\text{disp}}^{(2)}$ energies, for the Ar…CH$_4$ and CH$_4$…CH$_4$ complexes (see Fig. 6). The first-order contributions remain in excellent agreement between SAPT(PBE0AC) and LRC-SAPT, indicating that the tuned ω values yield good electron densities. The problem lies in the dispersion energy, which in the case of LRC-SAPT acquires a more HF-like character, leading to the observed underbinding.

Previous studies of the LRC-SAPT method focused on He$_2$ and Ne$_2$ dimers as the simplest representatives of dispersion-bound systems.[20,48] Though excellent agreement with benchmark values was found for He$_2$, the results for the neon dimer were less satisfactory. Lao and Herbert interpret this as the problem of unsaturated dispersion interaction for the Ne$_2$ system. However, this could not be the case in the work of Cencek and Szalewicz who calculated the second-order energy contributions at the coupled
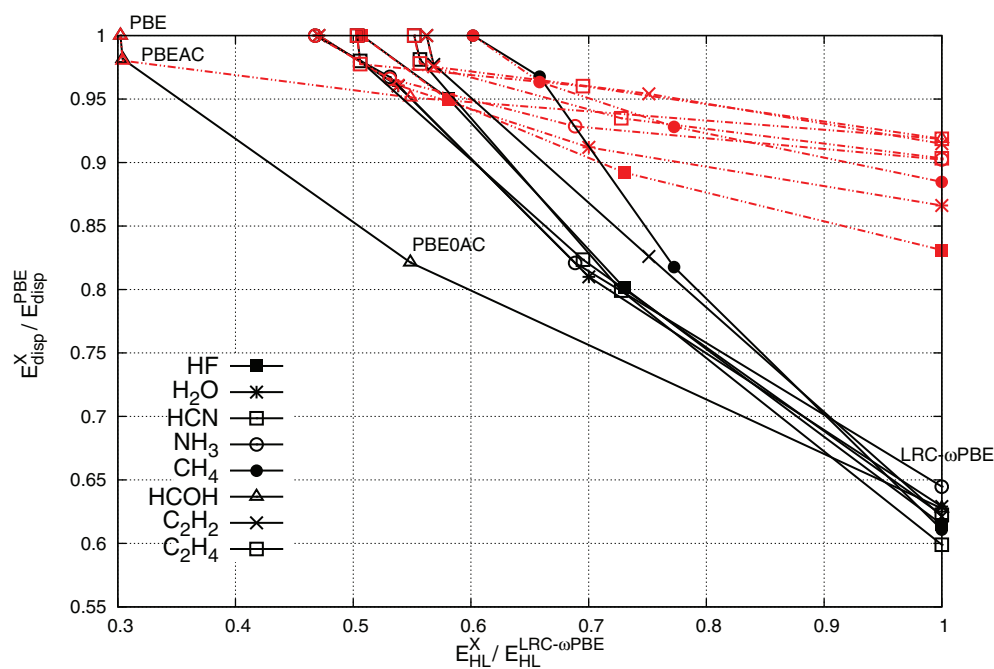
FIG. 5. Correlation between the dispersion energy at uncoupled (black) and coupled (red) levels of theory and the HOMO-LUMO gaps (E_{HL}) for eight homodimers from the A24 data set. For each monomer the HL gap were normalized to 1 with respect to the LRC-ωPBE value, whereas $E_{disp}^{(2)}$ were normalized to 1 with respect to the PBE value. X in the E_{HL}^X and E_{disp}^X labels denotes different functionals (PBE, PBEAC, PBE0AC, LRC-ωPBE). Functional labels are visualized for the HCOH dimer.

level of theory in a large basis set. Our results provide the following explanation: due to the large ω value, the dispersion energy becomes significantly shifted towards the Hartree-Fock limit, as seen in the Ar...CH$_4$ system (Fig. 6). For He$_2$, this shift toward Hartree-Fock fortuitously improves the result with respect to the full CI benchmark, whereas the opposite is true for Ne$_2$ (see Fig. S2 in the supplementary material[72]).

E. Water dimer

In this section, we examine the role of the short-range HF exchange in LRC-SAPT in hydrogen-bonded systems as exemplified by the water dimer. The data in Table III have been recomputed in the geometry of Ref. 91 to match that used by Cencek and Szalewicz.[20] We intend to demonstrate that the accurate performance of the LRC method extends to a
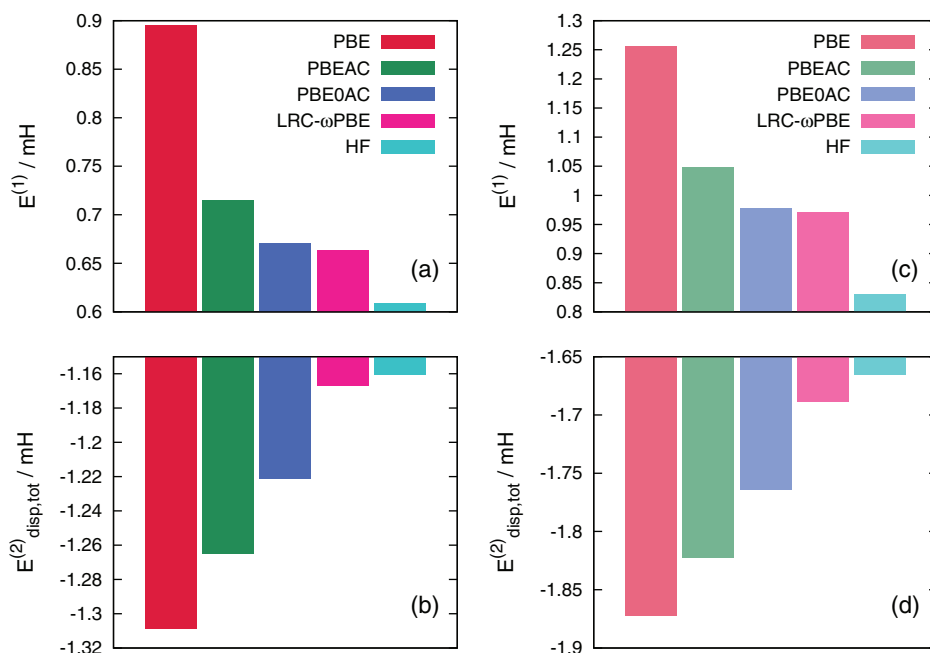
FIG. 6. First-order energy, $E^{(1)} = E_{\text{elst}} + E_{\text{exch}}$, and dispersion energy, $E_{\text{disp,tot}}^{(2)} = E_{\text{disp}}^{(2)} + E_{\text{exch-disp}}^{(2)}$ in different SAPT approaches. Panels (a) and (b) show results for the Ar... CH$_4$ complex, and panels (c) and (d) refer to the CH$_4$...CH$_4$ complex.

TABLE III. The SAPT energy components (in kcal/mol) of water dimer in its minimum structure[a] using PBEAC, PBE0AC, and a family of LRC functionals with varying short-range HF exchange. Basis set is aug-cc-pVTZ. SAPT(CCSD) reference results are computed in the same geometry and basis set. The δE^{HF} amounts to -0.940 kcal/mol; this contribution is not included in the sum of the SAPT terms, E_{int}. $\Delta_\%$ stands for the percentage error with respect to the reference value. %HF denotes the total fraction of the HF (see text), HL stands for HOMO-LUMO gap, and μ for a dipole moment.

SAPT level	α	%HF	$E_{elst}^{(1)}$	$E_{exch}^{(1)}$	$E_{ind}^{(2)}$	$E_{exch-ind}^{(2)}$	$E_{disp}^{(2)}$	$E_{exch-disp}^{(2)}$	E_{int}	$\Delta_\%$	HL/eV	μ/D
CCSD[b]			-8.125	7.953	-3.599	2.171	-3.046	0.6095	-4.037			
PBEAC		0	-8.019	8.592	-3.739	2.336	-3.078	0.630	-3.277	18.8	7.16	1.80
PBE0AC		25	-8.116	8.032	-3.532	2.150	-2.925	0.586	-3.805	5.7	9.35	1.86
$\omega = 0.498$	0.0	27	-8.395	8.075	-3.446	2.061	-2.793	0.555	-3.943	2.3	13.33	1.95
0.453	0.1	33	-8.362	8.019	-3.440	2.062	-2.792	0.555	-3.959	1.9	13.27	1.94
0.403	0.2	38	-8.327	7.939	-3.427	2.056	-2.789	0.554	-3.995	1.0	13.21	1.94
0.346	0.3	44	-8.291	7.824	-3.403	2.038	-2.782	0.551	-4.063	-0.7	13.14	1.93
0.280	0.4	50	-8.258	7.662	-3.358	1.998	-2.767	0.545	-4.178	-3.5	13.05	1.93
0.201	0.5	56	-8.230	7.436	-3.279	1.922	-2.742	0.533	-4.359	-8.0	12.95	1.93
0.101	0.6	62	-8.214	7.138	-3.146	1.790	-2.699	0.515	-4.616	-14.3	12.80	1.94
HF		100	-8.405	7.071	-3.044	1.670	-2.647	0.494	-4.862	14.4	14.57	1.99

[a]Minimum structure of the CC-pol-8s potential, see Table 5 of Ref. 91.
[b]No cumulant effects (see Ref. 92 and 93) in the first-order and the induction-exchange effects are included.

much wider class of IP-tuned functionals with variable short-range HF exchange. To this end we present a family of LRC-ωPBEα functionals [Eq. (3)] that increase the total percentage of the HF exchange (%HF) so as to gradually morph into the SAPT based on HF monomers. We recall that α denotes the constant fraction of HF in the functional. To avoid basis set issues, the SAPT(CCSD)[92–94] reference values have been recomputed in the same basis set as the other SAPT data in the table.

The total fraction of the HF for a given geometry, i.e., originating from both long- and short-range exchange, was calculated in three steps. First, the full functional was applied saving the vectors. In the second and third step, we performed no-SCF calculations starting from the saved vectors, with the DFT and HF exchange switched off, respectively.

As shown in Table III, the LRC-ωPBEα functionals afford total interaction energies in very good agreement with the reference data for a wide range of α values from 0 to 0.4. This range corresponds to the total percentage of HF from 27% to 50%. Above 50% E_{int} begins to drop and quickly becomes HF-like. We have discussed similar deterioration in rare gas dimers above. The first-order exchange energy decreases gradually as the %HF rises. By contrast, the dispersion energy experiences a drop in binding between PBE0AC and LRC with $\omega = 0.498$ despite nearly equal %HF (25% vs. 27%). Superficially, this drop can be rationalized by the increase in the HL gaps. More fundamentally, it can be attributed to the transition into monomers being described fully within GKS.

In the water dimer, as well as in the other studied dimers, the dispersion energy obtained in LRC functionals systematically underbinds compared to PBE0AC. The underbinding is partially offset by the less repulsive exchange-dispersion term. The LRC dispersion also departs from the SAPT(CCSD) benchmark by -8%. Cencek and Szalewicz[21] report a similar departure of -7.6% in aug-cc-pVQZ basis set. Although such a dispersion is less accurate, one may argue that this is the price one pays for the removal of the delocalization error within the monomers.

IV. CONCLUSIONS

LRC functionals have led to significant improvements over regular semilocal functionals in the description of a number of ground-state[47,85,95] and excited-state properties[96–99] that are relevant to the description of intermolecular forces. One should stress that these improvements were achieved, ultimately, as a result of the removal of MSIE. The SAPT formulation of the interaction energy relies on the quality of both types of properties. It is therefore pertinent to ask: what is the preferable DFT treatment of monomers to build SAPT theory on?

In this work, we examined the performance of SAPT built on GKS with optimally tuned LRC functionals. This treatment of monomers leads to the removal or the minimization of the effect of MSIE. This in turn corrects the erroneous delocalization of the ground-state density. As far as the excited-state properties are concerned, the optimized LRC functionals feature HL gaps being equal to fundamental gaps and a restored field-counteracting term in the v_{xc} potential. This in turn leads to an improved description of static and dynamic response properties. Our results show that the AC scheme does not overcome deficiencies of the underlying functional, such as spurious delocalization of density in He_3^+ and overestimated response, both static and dynamic, in π-conjugated chains. Thus, it is justifiable to expect that SAPT based on LRC functionals will be more predictive and of wider applicability than that based on the present AC schemes.

A comparison of the two approaches confirms that tuned LRC functionals yield results comparable or better than the best AC functional based on PBE0. Nevertheless, a detailed study of the water dimer reveals that PBE0AC energy components compare better with the SAPT(CCSD) values. To conclude, while the AC-SAPT interaction energy components taken separately are closer to the benchmarks, the total LRC-SAPT interaction energies are better than the AC-SAPT ones. One may infer from this observation that while AC-SAPT may provide better energy components, the cancellation of errors seems more evenly balanced within LRC-SAPT. Clearly,

a more thorough comparison with SAPT(CCSD) energies is necessary to explain the origin of the observed error cancellation in LRC-SAPT for its future applications.

Two main requirements of LRC-SAPT should be recognized. The first one is related to the strong dependence of SAPT terms on the value of range-separation parameter which makes optimization of ω with good precision a necessity.[20] For large molecular systems, combining LRC-SAPT with more effective functional tuning schemes, such as ω_{GDD},[74] is recommended. The second prerequisite is related to the applicability of the optimally tuned LRC functionals themselves.[36,77,100,101] Exceeding $\sim$50% of the HF exchange may distort the balance in error compensation between exchange and correlation within the functional, even in carefully tuned functionals. This happens in a limited number of cases, such as rare gases and other molecules with tightly bound electrons, where the optimal ω is exceptionally large, that is, the switch to HF exchange occurs at relatively short distances. This makes the interaction too HF-like.

ACKNOWLEDGMENTS

[1] B. Jeziorski, R. Moszyński, and K. Szalewicz, Chem. Rev. **94**, 1887 (1994).

[2] B. Jeziorski and K. Szalewicz, in "Intermolecular interactions by perturbation theory," *Encyclopedia of Computational Chemistry* (John Wiley & Sons, Ltd., 2002).

[3] K. Szalewicz, WIREs Comput. Mol. Sci. **2**, 254 (2012).

[4] E. G. Hohenstein and C. D. Sherrill, WIREs Comput. Mol. Sci. **2**, 304 (2012).

[5] G. Jansen, WIREs Comput. Mol. Sci. **4**, 127 (2014).

[6] A. Hesselmann, G. Jansen, and M. Schütz, J. Chem. Phys. **122**, 014103 (2005).

[7] A. J. Misquitta, R. Podeszwa, B. Jeziorski, and K. Szalewicz, J. Chem. Phys. **123**, 214103 (2005).

[8] H. L. Williams and C. F. Chabalowski, J. Phys. Chem. A **105**, 646 (2001).

[9] A. Heßelmann and G. Jansen, Chem. Phys. Lett. **357**, 464 (2002).

[10] A. Heßelmann and G. Jansen, Chem. Phys. Lett. **362**, 319 (2002).

[11] A. J. Misquitta and K. Szalewicz, Chem. Phys. Lett. **357**, 301 (2002).

[12] J. P. Perdew, R. G. Parr, M. Levy, and J. L. Balduz, Jr., Phys. Rev. Lett. **49**, 1691 (1982).

[13] D. J. Tozer and N. C. Handy, J. Chem. Phys. **109**, 10180 (1998).

[14] M. E. Casida and D. R. Salahub, J. Chem. Phys. **113**, 8918 (2000).

[15] M. Grüning, O. Gritsenko, S. Van Gisbergen, and E. Baerends, J. Phys. Chem. A **105**, 9211 (2001).

[16] R. Van Leeuwen and E. Baerends, Phys. Rev. A **49**, 2421 (1994).

[17] J. P. Perdew, K. Burke, and M. Ernzerhof, Phys. Rev. Lett. **77**, 3865 (1996).

[18] C. Adamo and V. Barone, J. Chem. Phys. **110**, 6158 (1999).

[19] A. J. Misquitta, "A symmetry-adapted perturbation theory based on density functional description of monomers," Ph.D. thesis (University of Delaware, 2004).

[20] W. Cencek and K. Szalewicz, J. Chem. Phys. **139**, 024104 (2013).

[21] W. Cencek and K. Szalewicz, J. Chem. Phys. **140**, 149902 (2014).

[22] R. van Leeuwen and E. J. Baerends, Phys. Rev. A **51**, 170 (1995).

[23] A. P. Gaiduk and V. N. Staroverov, J. Chem. Phys. **131**, 044107 (2009).

[24] R. Neumann, R. H. Nobes, and N. C. Handy, Mol. Phys. **87**, 1 (1996).

[25] P. Mori-Sánchez, A. J. Cohen, and W. Yang, J. Chem. Phys. **125**, 201102 (2006).

[26] A. Ruzsinszky, J. P. Perdew, G. I. Csonka, O. A. Vydrov, and G. E. Scuseria, J. Chem. Phys. **125**, 194112 (2006).

[27] C.-W. Tsai, Y.-C. Su, G.-D. Li, and J.-D. Chai, Phys. Chem. Chem. Phys. **15**, 8352 (2013).

[28] H. Sekino, Y. Maeda, M. Kamiya, and K. Hirao, J. Chem. Phys. **126**, 014107 (2007).

[29] X. Gonze, P. Ghosez, and R. W. Godby, Phys. Rev. Lett. **74**, 4035 (1995).

[30] B. Champagne, E. A. Perpète, S. J. A. van Gisbergen, E.-J. Baerends, J. G. Snijders, C. Soubra-Ghaoui, K. A. Robins, and B. Kirtman, J. Chem. Phys. **109**, 10489 (1998).

[31] S. Van Gisbergen, P. Schipper, O. Gritsenko, E. Baerends, J. Snijders, B. Champagne, and B. Kirtman, Phys. Rev. Lett. **83**, 694 (1999).

[32] P. Mori-Sánchez, Q. Wu, and W. Yang, J. Chem. Phys. **119**, 11001 (2003).

[33] A. Ruzsinszky, J. P. Perdew, G. I. Csonka, G. E. Scuseria, and O. A. Vydrov, Phys. Rev. A **77**, 060502 (2008).

[34] D. Varsano, A. Marini, and A. Rubio, Phys. Rev. Lett. **101**, 133002 (2008).

[35] T. Schmidt, E. Kraisler, L. Kronik, and S. Kümmel, Phys. Chem. Chem. Phys. **16**, 14357 (2014).

[36] H. Iikura, T. Tsuneda, T. Yanai, and K. Hirao, J. Chem. Phys. **115**, 3540 (2001).

[37] T. Yanai, D. P. Tew, and N. C. Handy, Chem. Phys. Lett. **393**, 51 (2004).

[38] O. A. Vydrov, J. Heyd, A. V. Krukau, and G. E. Scuseria, J. Chem. Phys. **125**, 074106 (2006).

[39] J.-W. Song, T. Hirosawa, T. Tsuneda, and K. Hirao, J. Chem. Phys. **126**, 154105 (2007).

[40] E. Livshits and R. Baer, Phys. Chem. Chem. Phys. **9**, 2932 (2007).

[41] T. M. Henderson, B. G. Janesko, and G. E. Scuseria, J. Chem. Phys. **128**, 194105 (2008).

[42] T. Stein, L. Kronik, and R. Baer, J. Chem. Phys. **131**, 244119 (2009).

[43] R. Baer, E. Livshits, and U. Salzner, Annu. Rev. Phys. Chem. **61**, 85 (2010).

[44] T. M. Henderson, A. F. Izmaylov, G. Scalmani, and G. E. Scuseria, J. Chem. Phys. **131**, 044108 (2009).

[45] T. Körzdörfer and J.-L. Brédas, "Organic electronic materials: Recent advances in the DFT description of the ground and excited states using tuned range-separated hybrid functional," Acc. Chem. Res. (published online).

[46] H. Sekino, Y. Maeda, and M. Kamiya, Mol. Phys. **103**, 2183 (2005).

[47] M. Kamiya, H. Sekino, T. Tsuneda, and K. Hirao, J. Chem. Phys. **122**, 234111 (2005).

[48] K. U. Lao and J. M. Herbert, J. Chem. Phys. **140**, 044108 (2014).

[49] P. Jurečka, J. Šponer, J. Černý, and P. Hobza, Phys. Chem. Chem. Phys. **8**, 1985 (2006).

[50] J. Rezác, K. E. Riley, and P. Hobza, J. Chem. Theory Comput. **7**, 2427 (2011).

[51] K. Pernal, R. Podeszwa, K. Patkowski, and K. Szalewicz, Phys. Rev. Lett. **103**, 263201 (2009).

[52] A. Hesselmann, J. Phys. Chem. A **115**, 11321 (2011).

[53] W. Kohn and L. J. Sham, Phys. Rev. **140**, A1133 (1965).

[54] A. Seidl, A. Görling, P. Vogl, J. Majewski, and M. Levy, Phys. Rev. B **53**, 3764 (1996).

[55] J. Řezáč and P. Hobza, J. Chem. Theory Comput. **9**, 2151 (2013).

[56] Y. Zhao and D. G. Truhlar, J. Chem. Theory Comput. **1**, 415 (2005).

[57] M. Jeziorska, B. Jeziorski, and J. Čížek, Int. J. Quantum Chem. **32**, 149 (1987).

[58] T. Körzdörfer, J. S. Sears, C. Sutton, and J.-L. Brédas, J. Chem. Phys. **135**, 204107 (2011).

[59] H.-J. Werner, P. J. Knowles, G. Knizia, F. R. Manby, M. Schütz *et al.*, "MOLPRO, version 2012.1, a package of *ab initio* programs," 2012, see http://www.molpro.net.

[60] T. H. Dunning, Jr., J. Chem. Phys. **90**, 1007 (1989).

[61] R. Moszyński, P. S. Żuchowski, and B. Jeziorski, Collect. Czech. Chem. Commun. **70**, 1109 (2005).

[62] T. Korona, M. Przybytek, and B. Jeziorski, Mol. Phys. **104**, 2303 (2006).

[63] K. Aidas, C. Angeli, K. L. Bak, V. Bakken, R. Bast, L. Boman, O. Christiansen, R. Cimiraglia, S. Coriani, P. Dahle, E. K. Dalskov, U. Ekström, T. Enevoldsen, J. J. Eriksen, P. Ettenhuber, B. Fernández, L. Ferrighi, H. Fliegl, L. Frediani, K. Hald, A. Halkier, C. Hättig, H. Heiberg, T.

Helgaker, A. C. Hennum, H. Hettema, E. Hjertenæs, S. Höst, I.-M. Høyvik, M. F. Iozzi, B. Jansík, H. J. A. Jensen, D. Jonsson, P. Jørgensen, J. Kauczor, S. Kirpekar, T. Kjærgaard, W. Klopper, S. Knecht, R. Kobayashi, H. Koch, J. Kongsted, A. Krapp, K. Kristensen, A. Ligabue, O. B. Lutnæs, J. I. Melo, K. V. Mikkelsen, R. H. Myhre, C. Neiss, C. B. Nielsen, P. Norman, J. Olsen, J. M. H. Olsen, A. Osted, M. J. Packer, F. Pawlowski, T. B. Pedersen, P. F. Provasi, S. Reine, Z. Rinkevicius, T. A. Ruden, K. Ruud, V. V. Rybkin, P. Sałek, C. C. M. Samson, A. S. de Merás, T. Saue, S. P. A. Sauer, B. Schimmelpfennig, K. Sneskov, A. H. Steindal, K. O. Sylvester-Hvid, P. R. Taylor, A. M. Teale, E. I. Tellgren, D. P. Tew, A. J. Thorvaldsen, L. Thøgersen, O. Vahtras, M. A. Watson, D. J. D. Wilson, M. Ziolkowski, and H. Ågren, WIREs Comput. Mol. Sci. **4**, 269 (2014).

[64] DALTON, a molecular electronic structure program, release DALTON2013.1 (2013).

[65] A. I. Krylov and P. M. Gill, WIREs Comput. Mol. Sci. **3**, 317 (2013).

[66] M. J. Frisch, G. W. Trucks, H. B. Schlegel *et al.*, GAUSSIAN 09 Revision d.01, Gaussian, Inc., Wallingford, CT, 2009.

[67] A. Halkier, W. Klopper, T. Helgaker, P. Jo, P. R. Taylor *et al.*, J. Chem. Phys. **111**, 9157 (1999).

[68] B. Champagne, E. A. Perpète, D. Jacquemin, S. J. A. van Gisbergen, E.-J. Baerends, C. Soubra-Ghaoui, K. A. Robins, and B. Kirtman, J. Phys. Chem. A **104**, 4755 (2000).

[69] D. Jacquemin, E. A. Perpéte, G. Scalmani, M. J. Frisch, R. Kobayashi, and C. Adamo, J. Chem. Phys. **126**, 144105 (2007).

[70] D. Jacquemin, E. A. Perpéte, M. Medved', G. Scalmani, M. J. Frisch, R. Kobayashi, and C. Adamo, J. Chem. Phys. **126**, 191108 (2007).

[71] P. A. Limacher, K. V. Mikkelsen, and H. P. Lüthi, J. Chem. Phys. **130**, 194114 (2009).

[72] See supplementary material at http://dx.doi.org/10.1063/1.4896608 for a brief description of SAPT energy components, range-separation parameter values.

[73] A. Karolewski, R. Armiento, and S. Kümmel, J. Chem. Theory Comput. **5**, 712 (2009).

[74] M. Modrzejewski, Ł. Rajchel, G. Chałasiński, and M. M. Szczęśniak, J. Phys. Chem. A **117**, 11580 (2013).

[75] A. J. Misquitta, J. Spencer, A. J. Stone, and A. Alavi, Phys. Rev. B **82**, 075312 (2010).

[76] J. V. Koppen, M. Hapka, M. M. Szczęśniak, and G. Chałasiński, J. Chem. Phys. **137**, 114302 (2012).

[77] O. A. Vydrov and G. E. Scuseria, J. Chem. Phys. **125**, 234109 (2006).

[78] S. N. Steinmann and C. Corminboeuf, J. Chem. Theory Comput. **8**, 4305 (2012).

[79] C. Sutton, T. Körzdörfer, V. Coropceanu, and J.-L. Brédas, J. Phys. Chem. C **118**, 3925 (2014).

[80] T. Korona, Mol. Phys. **111**, 3705 (2013).

[81] E. J. Baerends, O. V. Gritsenko, and R. van Meer, Phys. Chem. Chem. Phys. **15**, 16408 (2013).

[82] W. Yang, A. J. Cohen, and P. Mori-Sánchez, J. Chem. Phys. **136**, 204111 (2012).

[83] L. Kronik, T. Stein, S. Refaely-Abramson, and R. Baer, J. Chem. Theory Comput. **8**, 1515 (2012).

[84] T. Stein, H. Eisenberg, L. Kronik, and R. Baer, Phys. Rev. Lett. **105**, 266802 (2010).

[85] S. Refaely-Abramson, S. Sharifzadeh, N. Govind, J. Autschbach, J. B. Neaton, R. Baer, and L. Kronik, Phys. Rev. Lett. **109**, 226405 (2012).

[86] H. Sun and J. Autschbach, ChemPhysChem **14**, 2450 (2013).

[87] A. Heßelmann and G. Jansen, Chem. Phys. Lett. **367**, 778 (2003).

[88] A. J. Misquitta, B. Jeziorski, and K. Szalewicz, Phys. Rev. Lett. **91**, 033201 (2003).

[89] M. Seth, T. Ziegler, M. Steinmetz, and S. Grimme, J. Chem. Theory Comput. **9**, 2286 (2013).

[90] J. Koppen, M. Hapka, M. Modrzejewski, M. M. Szczęśniak, and G. Chałasiński, J. Chem. Phys. **140**, 244313 (2014).

[91] W. Cencek, K. Szalewicz, C. Leforestier, R. van Harrevelt, and A. van der Avoird, Phys. Chem. Chem. Phys. **10**, 4716 (2008).

[92] T. Korona, Phys. Chem. Chem. Phys. **10**, 6509 (2008).

[93] T. Korona, J. Chem. Phys. **128**, 224104 (2008).

[94] T. Korona, J. Chem. Theory Comput. **5**, 2663 (2009).

[95] E. R. Johnson, P. Mori-Sánchez, A. J. Cohen, and W. Yang, J. Chem. Phys. **129**, 204112 (2008).

[96] Y. Tawada, T. Tsuneda, S. Yanagisawa, T. Yanai, and K. Hirao, J. Chem. Phys. **120**, 8425 (2004).

[97] P. Mori-Sánchez, A. J. Cohen, and W. Yang, Phys. Rev. Lett. **100**, 146401 (2008).

[98] X. Zheng, A. J. Cohen, P. Mori-Sánchez, X. Hu, and W. Yang, Phys. Rev. Lett. **107**, 026403 (2011).

[99] T. Stein, L. Kronik, and R. Baer, J. Am. Chem. Soc. **131**, 2818 (2009).

[100] I. C. Gerber and J. G. Ángyán, Chem. Phys. Lett. **415**, 100 (2005).

[101] J.-D. Chai and M. Head-Gordon, J. Chem. Phys. **128**, 084106 (2008).

SAPT based on unrestricted Kohn-Sham orbitals for high-spin open-shell van der Waals complexes

In this chapter a SAPT formulation based on the spin-unrestricted Kohn-Sham description of the monomers (SAPT(UKS)) is concisely presented. We start with the motivation behind the development of SAPT(UKS). Next, a comparison with the previously introduced SAPT(ROKS) method is provided. Finally, we highlight SAPT(UKS) applications: from treatment of $^2\Pi$-state radicals to systems undergoing Penning Ionization reaction. The Chapter is accompanied with a related publication.

4.1 Introduction

The investigation of open-shell species remains a challenge in major areas of chemistry and physics, just to name atmospheric [94] and interstellar chemistry [95] or fundamental studies of reactions in the ultracold regime [96]. The challenge for theory comes from the fact that a reliable description of interactions involving radicals usually requires accounting for both static and dynamical correlation. The single-reference SAPT(UKS) method is dedicated to treat high-spin open-shell van der Waals complexes and is a step towards efficient inclusion of the dynamical correlation effects in this class of systems.

The first complete open-shell many-body SAPT based on restricted open-shell Kohn-

Sham formalism, SAPT(ROKS), was introduced by Żuchowski et $al.$ [97]. The SAPT(UKS) method presented in this Chapter was developed as an alternative, founded on unrestricted Kohn-Sham description of monomers. Computational chemists regard UKS and ROKS descriptions of single-reference open-shell systems while not identical, then largely equivalent. One should note, however, that the spin-restricted formalism is not uniquely defined, which leads to orbital energies having no interpretation within Koopmans' theorem. Additionally, according to Pople et $al.$, it is exclusively UKS that correctly captures the difference between the effective potentials in one-electron KS equations for α and β spinorbitals [98]. Thus, the SAPT(UKS) approach should be viewed as important and useful complementary to SAPT(ROKS).

4.2 Theory

Among the expressions for SAPT(UKS) energy contributions we focus on the exact first order exchange energy formula given in the atomic orbitals (AO) basis, as it has not previously been given in the literature:

$$
\begin{aligned}
E_{\text{exch}}^{(1)} = \text{Tr}\Big(&- \mathbf{P}_\alpha^A \mathbf{K}_\alpha^B - \mathbf{P}_\beta^A \mathbf{K}_\beta^B + \mathbf{T}_\alpha^A \mathbf{h}_\alpha^B + \mathbf{T}_\beta^A \mathbf{h}_\beta^B + \mathbf{T}_\alpha^B \mathbf{h}_\alpha^A + \mathbf{T}_\beta^B \mathbf{h}_\beta^A \\
&+ \mathbf{T}_\alpha^{AB} \mathbf{h}_\alpha^A + \mathbf{T}_\beta^{AB} \mathbf{h}_\beta^A + \mathbf{T}_\alpha^{AB} \mathbf{h}_\alpha^B + \mathbf{T}_\beta^{AB} \mathbf{h}_\beta^B \\
&+ \mathbf{T}_\alpha^{AB} \left(\mathbf{J}[\mathbf{T}_\alpha^B] - \mathbf{K}[\mathbf{T}_\alpha^B] \right) + \mathbf{T}_\beta^{AB} \left(\mathbf{J}[\mathbf{T}_\beta^B] - \mathbf{K}[\mathbf{T}_\beta^B] \right) \\
&+ \mathbf{T}_\alpha^{AB} \mathbf{J}[\mathbf{T}_\beta^B] + \mathbf{T}_\beta^{AB} \mathbf{J}[\mathbf{T}_\alpha^B] \\
&+ \mathbf{T}_\alpha^{AB} \left(\mathbf{J}[\mathbf{T}_\alpha^A] - \mathbf{K}[\mathbf{T}_\alpha^A] \right) + \mathbf{T}_\beta^{AB} \left(\mathbf{J}[\mathbf{T}_\beta^A] - \mathbf{K}[\mathbf{T}_\beta^A] \right) \\
&+ \mathbf{T}_\alpha^{AB} \mathbf{J}[\mathbf{T}_\beta^A] + \mathbf{T}_\beta^{AB} \mathbf{J}[\mathbf{T}_\alpha^A] \\
&+ \mathbf{T}_\alpha^A \left(\mathbf{J}[\mathbf{T}_\alpha^B] - \mathbf{K}[\mathbf{T}_\alpha^B] \right) + \mathbf{T}_\beta^A \left(\mathbf{J}[\mathbf{T}_\beta^B] - \mathbf{K}[\mathbf{T}_\beta^B] \right) \\
&+ \mathbf{T}_\alpha^A \mathbf{J}[\mathbf{T}_\beta^B] + \mathbf{T}_\beta^A \mathbf{J}[\mathbf{T}_\alpha^B] \\
&+ \mathbf{T}_\alpha^{AB} \left(\mathbf{J}[\mathbf{T}_\alpha^{AB}] - \mathbf{K}[\mathbf{T}_\alpha^{AB}] \right) + \mathbf{T}_\beta^{AB} \left(\mathbf{J}[\mathbf{T}_\beta^{AB}] - \mathbf{K}[\mathbf{T}_\beta^{AB}] \right) \\
&+ 2\mathbf{T}_\beta^{AB} \mathbf{J}[\mathbf{T}_\alpha^{AB}] \Big).
\end{aligned}
\tag{4.1}
$$

Here, $\mathbf{P}_\sigma^{\mathbf{X}}$ is the one-particle density matrix, $\mathbf{J}_\sigma^X \equiv \mathbf{J}[P_\sigma^X]$ and $\mathbf{K}_\sigma^X \equiv \mathbf{K}[P_\sigma^X]$ are the Coulomb and exchange matrices in the AO basis set, respectively. The definitions of the generalized Coulomb and exchange matrices, $\mathbf{J}[\mathbf{X}], \mathbf{K}[\mathbf{X}]$, as well as the $\mathbf{h}_\sigma^X$ and $\mathbf{T}_\sigma^{X/XY}$ matrices are given in the Appendix.

Moreover, in Ref. [D2] the expression for the exchange energy in the S^2 approximation, $E_{\text{exch}}^{(1)}(S^2)$, was given only in terms of molecular orbitals. It may therefore be elegant to supplement it with a generalized formula for $E_{\text{exch}}^{(1)}(S^2)$ in the AO basis. The derivation follows the one presented in Ref. [99] and leads to the following expression:

$$
\begin{aligned}
E_{\text{exch}}^{(1)}(S^2) = -\text{Tr}\Big(& \mathbf{P}_\alpha^A \overset{i}{\mathbf{K}}_\alpha^B + \mathbf{P}_\beta^A \overset{i}{\mathbf{K}}_\beta^B - (\mathbf{P}_\alpha^A \mathbf{S} \mathbf{P}_\alpha^B)^{\text{T}} (\overset{r}{\mathbf{J}}[\mathbf{P}_\alpha^B] + \overset{r}{\mathbf{J}}[\mathbf{P}_\beta^B] - \overset{i}{\mathbf{K}}[\mathbf{P}_\alpha^B]) \\
& - (\mathbf{P}_\beta^A \mathbf{S} \mathbf{P}_\beta^B)^{\text{T}} (\overset{r}{\mathbf{J}}[\mathbf{P}_\beta^B] + \overset{r}{\mathbf{J}}[\mathbf{P}_\alpha^B] - \overset{i}{\mathbf{K}}[\mathbf{P}_\beta^B]) - (\mathbf{P}_\alpha^A \mathbf{S} \mathbf{P}_\alpha^B)(\overset{l}{\mathbf{J}}[\mathbf{P}_\alpha^A] + \overset{l}{\mathbf{J}}[\mathbf{P}_\beta^A] - \overset{o}{\mathbf{K}}[\mathbf{P}_\alpha^A]) \\
& - (\mathbf{P}_\beta^A \mathbf{S} \mathbf{P}_\beta^B)(\overset{l}{\mathbf{J}}[\mathbf{P}_\beta^A] + \overset{l}{\mathbf{J}}[\mathbf{P}_\alpha^A] - \overset{o}{\mathbf{K}}[\mathbf{P}_\beta^A]) + (\mathbf{P}_\alpha^A \mathbf{S} \mathbf{P}_\alpha^B \mathbf{S} \mathbf{P}_\alpha^A)(\overset{r}{\mathbf{J}}[\mathbf{P}_\alpha^B] + \overset{r}{\mathbf{J}}[\mathbf{P}_\beta^B]) \\
& + (\mathbf{P}_\beta^A \mathbf{S} \mathbf{P}_\beta^B \mathbf{S} \mathbf{P}_\beta^A)(\overset{r}{\mathbf{J}}[\mathbf{P}_\beta^B] + \overset{r}{\mathbf{J}}[\mathbf{P}_\alpha^B]) + (\mathbf{P}_\alpha^B \mathbf{S} \mathbf{P}_\alpha^A \mathbf{S} \mathbf{P}_\alpha^B)(\overset{l}{\mathbf{J}}[\mathbf{P}_\alpha^A] + \overset{l}{\mathbf{J}}[\mathbf{P}_\beta^A]) \\
& + (\mathbf{P}_\beta^B \mathbf{S} \mathbf{P}_\beta^A \mathbf{S} \mathbf{P}_\beta^B)(\overset{l}{\mathbf{J}}[\mathbf{P}_\beta^A] + \overset{l}{\mathbf{J}}[\mathbf{P}_\alpha^A]) - (\mathbf{P}_\alpha^B \mathbf{S} \mathbf{P}_\alpha^A)^{\text{T}} \overset{o}{\mathbf{K}}[\mathbf{P}_\alpha^A \mathbf{S} \mathbf{P}_\alpha^B] - (\mathbf{P}_\beta^B \mathbf{S} \mathbf{P}_\beta^A)^{\text{T}} \overset{o}{\mathbf{K}}[\mathbf{P}_\beta^A \mathbf{S} \mathbf{P}_\beta^B] \Big).
\end{aligned}
$$

$$(4.2)$$

For definitions of the left/right Coulomb and inner/outer exchange matrices see the Appendix.

The remaining expressions for SAPT(UKS) energy contributions up to the second order are analogous to the ones given in the MO basis by Żuchowski *et al.* [97] and are presented in the attached work.

4.3 Results

4.3.1 SAPT(UKS) vs. SAPT(ROKS)

The comparison of SAPT(ROKS) and SAPT(UKS) approaches presented in Table 4.1 and Fig. 4.1 reveals a satisfactory agreement, with differences that amount to 5%. One should note, however, that inconsistent AC schemes were applied: gradient-regulated asymptotic correction (GRAC) in the case of SAPT(UKS) [34], and Fermi-Amaldi in the case of SAPT(ROKS) [33]. Although small, the spin contamination in UKS may also contribute to the observed discrepancy. A slightly better agreement is observed between SAPT(ROHF) and SAPT(UHF), with differences which do not exceed 4%. All DFT-based open-shell SAPT methods perform well with respect to the benchmark CCSD(T) values, the one exception being the He-NH dimer (see Ref. [97] for a detailed analysis).
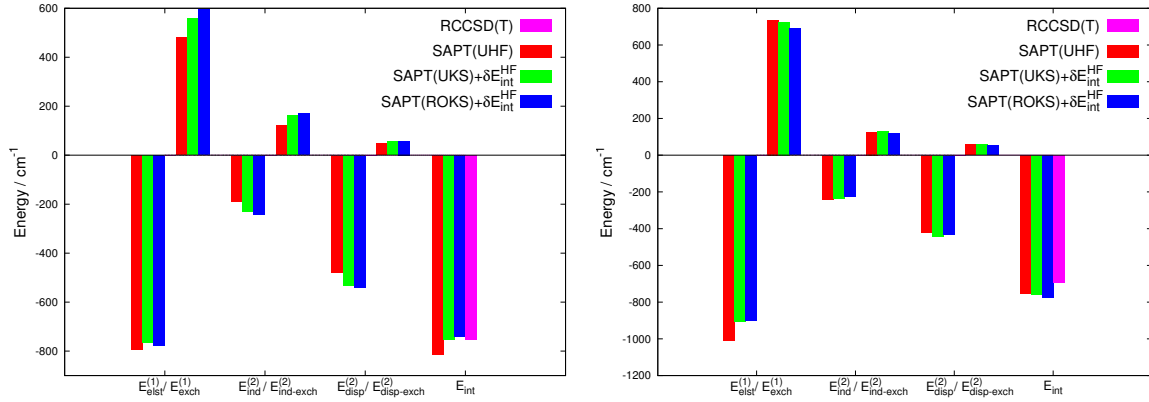
Figure 4.1: Comparison of SAPT energy contributions. Left: $H_2O\cdots HO_2(^2A)$, aug-cc-pVTZ + (322), right: $NH(^3\Sigma^-)$-$NH(^3\Sigma^-)$, aug-cc-pVQZ + (3322).

4.3.2   Rare gas atoms interacting with molecules in $^2\Pi$ electronic state

The first novel and useful application of SAPT(UKS) was the study of selected spatially degenerate states. We chose dimers comprising rare gas atoms interacting with molecules in $^2\Pi$ electronic state: $He\cdots OH$, $Ar\cdots OH$ and $Ar\cdots NO$. The results presented in Table 4.2 show that for all three systems SAPT(UKS) interaction energies are in excellent agreement with the reference CCSD(T) values. Moreover, we proved that SAPT(UKS) correctly captures the spatial degeneration arising from the interaction (see Fig. 1 and Tables V-VIII of Ref. [D2]). In Fig. 4.2 we visualize the effect of the state splitting for the $He\cdots OH(X^2\Pi)$ system.

Table 4.1: Interaction energies of the chosen open-shell systems within SAPT(UHF), SAPT(ROHF), SAPT(ROKS), SAPT(UKS) and RCCSD(T) approximations. Both SAPT(ROKS) and SAPT(UKS) results include the $\delta E_{\text{int}}^{\text{HF}}$ correction. All energies in cm^{-1}.

System	SAPT (UHF)	SAPT (ROHF)	SAPT (UKS)	SAPT (ROKS)	RCCSD(T)
$CN\cdots Ne$	-38.06	-40.07	-45.32	-43.88	-39.42
$NH\cdots NH$	-756	-767	-761	-774	-693
$H_2O\cdots HO_2$	-813	-813	-790	-776	-752
$He\cdots NH$	-20.65	-20.38	-26.98	-25.88	-19.83

Table 4.2: Interaction energies at global minima of the He$\cdots$OH($X^2\Pi$), Ar $-$ OH($X^2\Pi$) and Ar$\ldots$NO($X^2\Pi$) complexes. For details see Ref. [D2]. All energies in cm^{-1}

System	State	R [Å]	θ	SAPT(UHF)	SAPT(UKS)	UCCSD(T)
He–OH	A'	3.01	68.6	-36.97	-30.71	-30.02
Ar–OH	Π	3.65	0.0	-140.4	-144.2	-140.4
Ar–NO	A'	6.76	94.9	-111.0	-118.1	-115.9

Figure 4.2: SAPT(UKS) interaction energies of He$\cdots$OH($X^2\Pi$) system for A' and A'' symmetries

4.3.3   Further applications

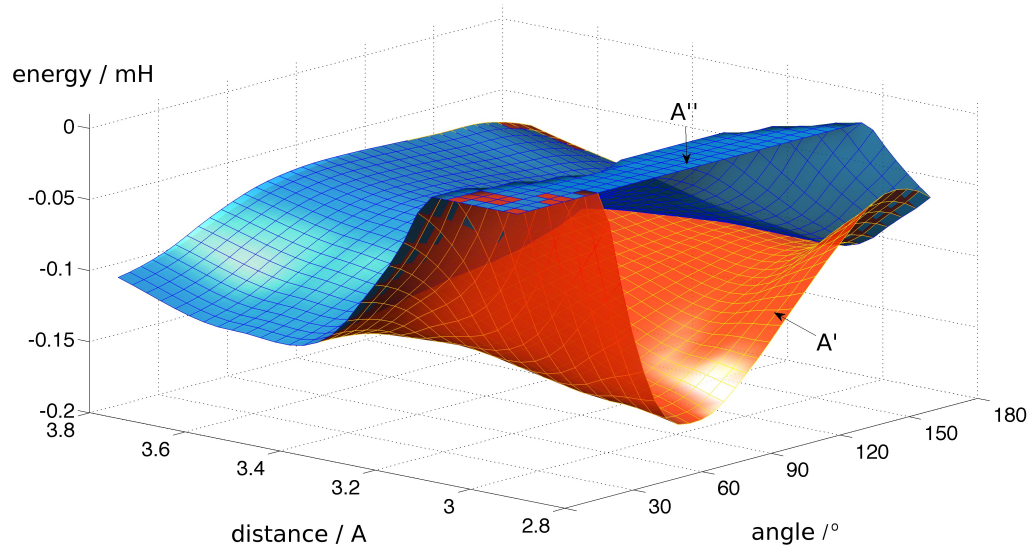Up to date, we have successfully used the SAPT(UKS) method in modelling of the Penning Ionization (PI) reaction [D6, D7, D8] and elucidation of the nature of the $CrH(X^6\Sigma^+)$-He bonding mechanism.

The works on PI reaction encompassed a combined coupled-cluster (CC) and SAPT study of $He(^3S)$-H_2, $He(^3S)$-Ar and $Ne(^3P)$-Ar systems [D6], as well as joint experimental and theoretical examination of $Ne(^3P)$-NH_3, $Ne(^3P)$-ND_3 [D7] and $He(^3S)$-NH_3 [D8] systems. We should stress that the description of the entrance channel of PI reaction requires treating electronic states of the A^*-B type, which are submerged in the continuum of states of the $(AB)^+ + e$ type. This is a serious difficulty for the supermolecular approach as the variational principle is expected to drive such states down either to the ground state, or one of the excited states or – because of the coupling with continuum states – to some delocalized state corresponding to the fragmentation into an ion, a molecule, and a free electron. In the aforementioned SAPT(UKS) studies we took advantage of the fact that SAPT ensures a fixed number of electrons at each monomer and is not prone to the variational collapse.

In Ref. [D6] we showed a good agreement between the SAPT and CC approaches. The obtained potentials were used to predict the positions of the shape resonances in low-energy scattering. We reported a satisfactory agreement with the state-of-the-art scattering experiment of Henson *et al.* [100]. In Refs. [D7, D8] I applied the SAPT(UHF) approach to calculate long-range dispersion and induction coefficients for the $Ne(^3P)$-NH_3, $Ne(^3P)$-ND_3 and $He(^3S)$-NH_3 systems. Moreover, SAPT was used to describe both global and local minima in the studied systems. The subsequent modelling of dynamics *via* multichannel quantum defect theory (MQDT) allowed for good reproduction of the experimental scattering results.

The PES of the $CrH(X^6\Sigma^+)$-He complex obtained at multi-reference configuration interaction including explicitly single and double excitations with a Davidson correction (MRCISD(+Q)) level of theory revealed unusually strong binding of the He atom in the collinear He–CrH arrangement: $3030cm^{-1}$ at $R_e = 3.75$ bohr (see Fig 4.3). SAPT(UKS) calculations for this dimer identified the presence of the so called "exchange cavity" – the diminished Pauli exchange accompanied by enhanced induction interaction on the
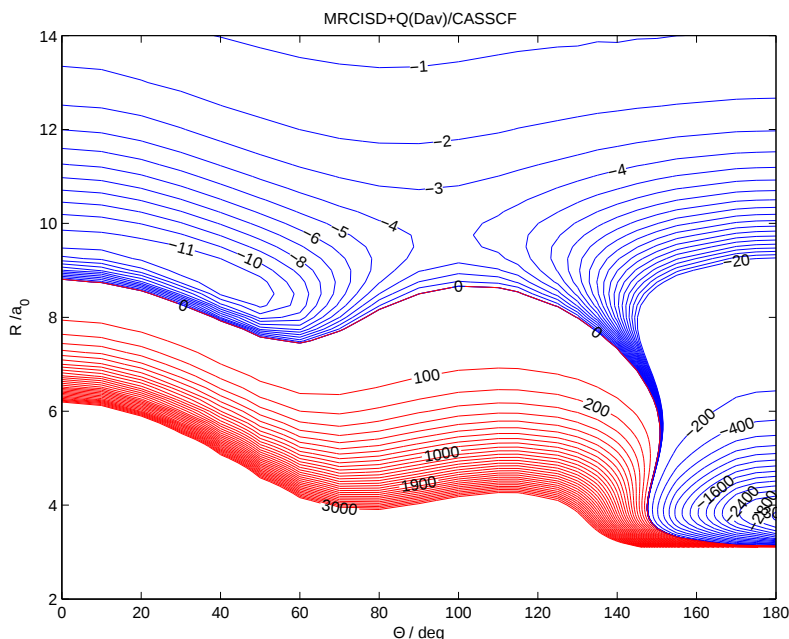
Figure 4.3: The MRCISD+Q(Dav) potential energy surface for the CrH($X^6\Sigma^+$)-He van der Waals complex. $\Theta = 180$ corresponds to He$\cdots$CrH arrangement.

chromium side of the CrH complex.[*] The presence of this phenomenon corresponds to the considerable dipole moment (3.512 D) of the CrH molecule. It is worth to mention, that we have recently observed a similar effect for the He-BeO($X^1\Sigma^+$) dimer – nominally a closed-shell but of some multi-configurational character [102].

4.4 Related publication

The attached publication [D2] supplements the findings included in this Chapter and provides a comprehensive presentation of the SAPT(UKS) method. First, introduced are all expressions for SAPT(UKS) energy contributions up to the second order in $\hat{V}$. Next follows a performance test of SAPT(UKS). Apart from a detailed analysis of the interaction energy components for the systems we analyzed in this Chapter, i.e., He-NH, H_2O-HO_2, He-OH, Ar-OH and Ar-NO, a special attention has been paid to two transition metal dimers: Au_2 ($^3\Sigma_u^+$) and Cr_2 ($^{13}\Sigma_g^+$). It is stressed that SAPT(UKS) is unsuited for effective core potentials. The role of spin contamination in SAPT(UKS) is briefly discussed. The final part contains remarks on possible future developments of

---

[*]see Figs. 7-9 in Ref. [101]

the SAPT(UKS) method.

Symmetry-adapted perturbation theory based on unrestricted Kohn-Sham orbitals for high-spin open-shell van der Waals complexes

Michał Hapka,[1,a)] Piotr S. Żuchowski,[2,b)] Małgorzata M. Szczęśniak,[3] and Grzegorz Chałasiński[1]

[1]*Faculty of Chemistry, University of Warsaw, 02-093 Warsaw, Pasteura 1, Poland*
[2]*Institute of Physics, Nicolaus Copernicus University, Grudziądzka 5, 87-100 Toruń, Poland*
[3]*Department of Chemistry, Oakland University, Rochester, Michigan 48309-4477, USA*

Two open-shell formulations of the symmetry-adapted perturbation theory are presented. They are based on the spin-unrestricted Kohn-Sham (SAPT(UKS)) and unrestricted Hartree-Fock (SAPT(UHF)) descriptions of the monomers, respectively. The key reason behind development of SAPT(UKS) is that it is more compatible with density functional theory (DFT) compared to the previous formulation of open-shell SAPT based on spin-restricted Kohn-Sham method of Żuchowski *et al.* [J. Chem. Phys. **129**, 084101 (2008)]. The performance of SAPT(UKS) and SAPT(UHF) is tested for the following open-shell van der Waals complexes: $He\cdots NH$, $H_2O\cdots HO_2$, $He\cdots OH$, $Ar\cdots OH$, $Ar\cdots NO$. The results show an excellent agreement between SAPT(UKS) and SAPT(ROKS). Furthermore, for the first time SAPT based on DFT is shown to be suitable for the treatment of interactions involving Π-state radicals ($He\cdots OH$, $Ar\cdots OH$, $Ar\cdots NO$). In the interactions of transition metal dimers $(^3\Sigma_u^+)Au_2$ and $(^{13}\Sigma_g^+)Cr_2$ we show that SAPT is incompatible with the use of effective core potentials. The interaction energies of both systems expressed instead as supermolecular UHF interaction plus dispersion from SAPT(UKS) result in reasonably accurate potential curves. © *2012 American Institute of Physics.* [http://dx.doi.org/10.1063/1.4758455]

I. INTRODUCTION

The open-shell interactions are of great importance to many areas of chemistry and physics, including reaction dynamics,[1–3] spectroscopy,[4,5] inelastic scattering,[6,7] cold-matter phenomena,[8,9] and many others. When the open-shell interactions lead to chemical reactions, the long-range forces play an important role in orienting the reactants as they approach the transition state.[10,11]

Compared to closed-shell interactions, the interactions involving open-shell species are not as well understood, and much more difficult to calculate reliably. Open-shell atoms or molecules, i.e., radical species, tend to be much more reactive than the closed-shell molecules. They can participate in fast, chain reactions, form reactive intermediates, and produce stable complexes.[12] Their chemical transformations, inelastic processes, and clustering properties are of key importance in atmospheric chemistry,[12,13] combustion,[14,15] interstellar chemistry,[16,17] and in physiology.[18] While these diverse aspects of radical reactivity have been exploited by chemists for many years, the fundamental understanding of these processes is only just beginning.

In *ab initio* studies of open-shell interactions, a wide range of computational methods have been employed that account for the dynamic and nondynamic electron correlation effects. This is because no single method is universally applicable in the studies of open-shell interactions. The most popular of them, multi-reference configu-ration interaction (MRCI), is not size-extensive and in the limit of separated monomers tends to some artificial, unphysical limit. In the long range, MRCI lacks sufficient numerical accuracy, and has improper asymptotic behavior which makes it impossible to extract van der Waals dispersion coefficients. Supermolecular methods based on the size-extensive complete active space perturbation theory (CASPT2 and CASPT3) suffer from the intruder-state problems, especially in the long-range region. The dispersion energy requires inclusion of triple excitations for its saturated description, and neither MRCI nor CASPT fully include them.

To the arsenal of methods for the study of open-shell interactions, Żuchowski *et al.*[19] have recently added the perturbation-theory based approach. This approach involves a generalization of the symmetry-adapted perturbation theory (SAPT), a well developed and robust method, to the treatment of the open-shell case. Developing open-shell SAPT is beneficial for the following reasons: (1) direct calculations of interaction components are the most accurate within SAPT; that entails the most reliable treatment of dispersion interaction and its anisotropy (2) basis set extension effects and BSSE can be effectively controlled (3) provided that the single reference method enables correct description of the monomers, problems with degeneracy, quasi-degeneracy, and in general multireference issues such as choosing active space and avoiding intruder states can be alleviated (4) the calculations may be performed at a potentially lower cost.

Although the SAPT method was first applied to H_2^+ in 1980,[20] the first many-electron implementation and application, based on the UHF formalism, appeared only in the

---
a)Electronic mail: hapka@tiger.chem.uw.edu.pl.
b)Electronic mail: pzuch@fizyka.umk.pl.

1990s.[21,22] However, this approach did not include any exchange corrections beyond the first order and relied on the uncoupled approximation of the dispersion term. For this reason it had to be applied together with the supermolecular method and its value was mainly of interpretational character. For a review of results obtained with this approach see Ref. 23. The first rigorous and complete open-shell many-body SAPT was published only recently by Żuchowski *et al.*[19] They introduced a SAPT formalism up to second order based on restricted open-shell Kohn-Sham (ROKS) together with restricted open-shell Hartree-Fock (ROHF) theory. The authors showed that for a class of dispersion- and electrostatic-bound dimers the performance of SAPT(ROKS) matches that of the coupled cluster singles and doubles with noniterative triples (RCCSD(T)), considered to be a "gold standard" method in quantum chemistry. To date, several applications of open-shell SAPT can be found in the literature.[24–32]

In this paper we present an alternative formulation of the perturbational energy expansion for the high-spin open-shell systems, founded on unrestricted Kohn-Sham and Hartree-Fock theories, which we will denote as SAPT(UKS) and SAPT(UHF), respectively.

The paper is organized as follows. In Sec. II, we describe the theory of SAPT(UKS) and provide working equations up to the second order in the intermolecular interaction operator. Section III contains the numerical results: comparison with previously studied systems,[19] results for studies of spatially degenerate states, and attempts to describe interactions in selected metal dimers. Section IV concludes the paper.

II. THEORY

A. Unrestricted Kohn-Sham equations with asymptotic correction

The Kohn-Sham spinorbitals (with $\sigma = \alpha$ or β) are eigenfunctions of the one-electron spin-dependent Kohn-Sham operator K^σ which reads,

$$K^\sigma = -\frac{1}{2}\nabla^2 + \sum_i \frac{Z_i}{|\mathbf{r}-\mathbf{r}_i|} + \int \frac{\rho^\alpha(\mathbf{r}')+\rho^\beta(\mathbf{r}')}{|\mathbf{r}-\mathbf{r}'|}d\mathbf{r}' + \frac{\delta E}{\delta\rho^\sigma(\mathbf{r})},$$
(1)

where the index i runs over nuclei of the molecule, Z_i and $\mathbf{r}_i$ denote, respectively, the atomic number and the position of nucleus i, E is the energy of the system, ρ^α and ρ^β denote alpha and beta spin densities, respectively. The last term in above equation denotes the exchange-correlation potential, which is the functional derivative of electronic energy with respect to the electron density of a given spin. There is a clear physical meaning of these equations: their solutions represent quasiparticles moving in an external potential determined by Coulomb forces and the exchange-correlation potential, which combines effects of the Pauli-exclusion together with the non-classical electronic correlation of electrons. In UKS the spinorbitals have different spatial parts for α and β electrons, which are K^α and K^β eigenfunctions, respectively.

In spin-restricted Kohn-Sham formulation,[33] the orbitals are no longer eigenfunctions of the separate K^α and K^β operators, but instead, the doubly occupied, singly occupied, and

unoccupied orbitals are defined by requiring that the single matrix of the following block form (below, c, o, and v labels denote the doubly occupied, singly occupied, and unoccupied orbitals),

$$\begin{pmatrix} \frac{1}{2}(K^\alpha+K^\beta)_{cc'} & K^\beta_{co} & \frac{1}{2}(K^\alpha+K^\beta)_{cv} \\ K^\beta_{oc} & \frac{1}{2}(K^\alpha+K^\beta)_{oo'} & K^\alpha_{ov} \\ \frac{1}{2}(K^\alpha+K^\beta)_{vc} & K^\alpha_{vo} & \frac{1}{2}(K^\alpha+K^\beta)_{vv'} \end{pmatrix}, \quad (2)$$

is diagonal.[33,34] On the one hand, the spin-restricted theory is easier to implement in SAPT, as it leads to fewer types of integrals between orbitals with the same spatial parts compared to spin-unrestricted theory. On the other hand, the spin-restricted formulation has the drawback of not being uniquely defined with the consequence of orbital energies having no interpretation within Koopmans' theorem.

It is thus clear that the spin-unrestricted Kohn-Sham theory should provide a complementary SAPT formulation for high-spin open-shell systems. Moreover, in the work of Pople *et al.*,[35] it has been argued that UKS is the only physically sound formulation of Kohn-Sham theory for systems with odd number of electrons. They claim that only UKS properly accounts for the difference between the effective potentials in one-electron KS equations for α and β spinorbitals. In contrast to ROKS, it also allows for description of local negative spin density (defined as a negative local value of $\rho_\alpha - \rho_\beta$).

It has been verified that standard LDA and GGA exchange-correlation functionals yield exchange-correlation potentials with wrong asymptotic behaviour, decaying faster than the correct $v^\sigma_{\text{xc}}(\mathbf{r}) \xrightarrow{r\to\infty} -\frac{1}{r}$ limit.[36] Following Hesselmann and Jansen,[37] to properly account for the asymptotic behavior of the exchange-correlation potential, we have applied the gradient-regulated asymptotic connection (GRAC) scheme of Grüning *et al.*[38] The GRAC variant used in this work is based on interpolation between the shifted GGA potential in the bulk region and the shifted LB potential[39] in the asymptotic region, with the interpolation function depending on the dimensionless gradient parameter $x(\mathbf{r}) = \frac{|\nabla\rho(\mathbf{r})|}{\rho^{4/3}(\mathbf{r})}$. Such a scheme leads to smooth asymptotically corrected potentials with an analytical representation that were shown to give improved vertical excitation energies and (hyper) polarizabilities.[38,40] The parameters used for GRAC were set to standard values: $\alpha = 0.05$, $\beta = 40$.

As the UHF/UKS single determinant is not an eigenfunction of the squared spin operator S^2, unrestricted Kohn-Sham and Hartree-Fock methods may suffer from spin symmetry contamination,[41] i.e., the UKS $\langle S^2\rangle$ might be different from $S(S+1)$. The standard formula for a system containing $N_\alpha + N_\beta$ electrons used in the present work to evaluate the $\langle S^2\rangle$ for the UHF wave function reads,

$$\langle S^2\rangle = \frac{N_\alpha - N_\beta}{2}\left(\frac{N_\alpha - N_\beta}{2} + 1\right) + N_\beta - \sum_{\bar{i}\bar{j}}^{\text{occ}}(S_{\bar{i}}^{\bar{j}})^2, \quad (3)$$

where $S_{\bar{i}}^{\bar{j}} = \langle \bar{i}|\bar{j}\rangle$ is the overlap integral between $\phi_{\bar{i}}\alpha$ and $\phi_{\bar{j}}\beta$ orbitals (for index convention see Sec. II B). One should note that Eq. (3) applied in UKS case yields $\langle S^2\rangle_{\text{NI}}$, i.e., $\langle S^2\rangle$ for the noninteracting system (NI). Wang *et al.*[42] have proposed evaluating $\langle S^2\rangle$ as an explicit functional of density within so

called exchange local spin density (XLSD) approximation. The work was later extended to general gradient approximation (GGA) by Cohen *et al.*[43] Their NI function was shown to be almost pure spin. They also showed that the UHF densities generally lead to a larger spin contamination than the UKS ones within the XLSD approximation.[43]

B. First-order SAPT energies

In this work the following index convention is used: indices marked with a tilde or an overbar refer to spinorbitals. The tilde marks the spin up spinorbitals, $\psi_{\tilde{k}} = \phi_{\tilde{k}}\alpha$, and the overbar the spin down spinorbitals, $\psi_{\bar{k}} = \phi_{\bar{k}}\beta$. σ denotes the general spin, either α or β. Greek letters ν, μ refer to the AO basis functions. Furthermore, $\tilde{i}$ and $\bar{i}$ ($\tilde{j}$ and $\bar{j}$) label the occupied spin-orbitals of monomer A(B), $\tilde{a}$ and $\bar{a}$ ($\tilde{b}$ and $\bar{b}$) label the virtual ones.

The first-order interaction energy in SAPT takes the form

$$E^{(1)} = \frac{\langle \Psi_A \Psi_B | V \mathcal{A} \Psi_A \Psi_B \rangle}{\langle \Psi_A \Psi_B | \mathcal{A} \Psi_A \Psi_B \rangle}, \quad (4)$$

with Ψ_X being the wave function of monomer X and V a intermolecular interaction operator. With a proper decomposition of the total antisymmetrizer $\mathcal{A}$, $E^{(1)}$ can be divided into an electrostatic and exchange contribution.[44,45] The electrostatic component is conveniently expressed in terms of electron density matrices of the monomers, ρ_X ($X = A, B$),[46]

$$E^{(1)}_{\text{elst}} = \int \rho_A(\mathbf{r})\tilde{v}(\mathbf{r}, \mathbf{r}')\rho_B(\mathbf{r}')d^3\mathbf{r}'d^3\mathbf{r}, \quad (5)$$

where the generalized interaction potential is defined as

$$\tilde{v}(\mathbf{r}, \mathbf{r}') = \frac{1}{|\mathbf{r} - \mathbf{r}'|} + v_A(\mathbf{r})\frac{1}{N_B} + v_B(\mathbf{r}')\frac{1}{N_A} + \frac{V_0}{N_A N_B}, \quad (6)$$

so that $V = \sum_i^{N_A} \sum_j^{N_B} \tilde{v}(\mathbf{r}_i, \mathbf{r}_j)$. N_X denotes the number of electrons in monomer X and V_0 is the constant internuclear repulsion term. By expanding the monomer densities in an atomic orbital (AO) basis set, Eq. (5) can be cast as follows:[47]

$$E^{(1)}_{\text{elst}} = \text{Tr}\left((\mathbf{P}^A_\alpha + \mathbf{P}^A_\beta)\mathbf{V}^B + (\mathbf{P}^B_\alpha + \mathbf{P}^B_\beta)(\mathbf{V}^A + \mathbf{J}^A_\alpha + \mathbf{J}^A_\beta) \right) + V_0, \quad (7)$$

where $\mathbf{P}^\mathbf{X}_\sigma$ is the one-particle density matrix, $\mathbf{V}^X$ the one-electron part of the electrostatic potential and $\mathbf{J}^X_\sigma \equiv \mathbf{J}[P^X_\sigma]$ the Coulomb matrix in the AO basis set.

In the case of a single-determinant wave function the first-order exchange energy can be expressed in terms of antisymmetrized products of one-particle density matrix. As previously noted,[19] the formula for the first-order exchange energy that takes into account all permutations of electrons between monomers[48] is, in fact, valid for any determinantal wave function and can be generalized to a case of high-spin one-determinantal wave function. In the AO basis it takes

the form[47]

$$\begin{aligned}
E^{(1)}_{\text{exch}} = \text{Tr}\Big(&-\mathbf{P}^A_\alpha \mathbf{K}^B_\alpha - \mathbf{P}^A_\beta \mathbf{K}^B_\beta + \mathbf{T}^A_\alpha \mathbf{h}^B_\alpha \\
&+ \mathbf{T}^A_\beta \mathbf{h}^B_\beta + \mathbf{T}^B_\alpha \mathbf{h}^A_\alpha + \mathbf{T}^B_\beta \mathbf{h}^A_\beta \\
&+ \mathbf{T}^{AB}_\alpha \mathbf{h}^A_\alpha + \mathbf{T}^{AB}_\beta \mathbf{h}^A_\beta + \mathbf{T}^{AB}_\alpha \mathbf{h}^B_\alpha + \mathbf{T}^{AB}_\beta \mathbf{h}^B_\beta \\
&+ \mathbf{T}^{AB}_\alpha \left(\mathbf{J}[\mathbf{T}^B_\alpha] - \mathbf{K}[\mathbf{T}^B_\alpha] \right) + \mathbf{T}^{AB}_\beta \left(\mathbf{J}[\mathbf{T}^B_\beta] - \mathbf{K}[\mathbf{T}^B_\beta] \right) \\
&+ \mathbf{T}^{AB}_\alpha \mathbf{J}[\mathbf{T}^B_\beta] + \mathbf{T}^{AB}_\beta \mathbf{J}[\mathbf{T}^B_\alpha] \\
&+ \mathbf{T}^{AB}_\alpha \left(\mathbf{J}[\mathbf{T}^A_\alpha] - \mathbf{K}[\mathbf{T}^A_\alpha] \right) + \mathbf{T}^{AB}_\beta \left(\mathbf{J}[\mathbf{T}^A_\beta] - \mathbf{K}[\mathbf{T}^A_\beta] \right) \\
&+ \mathbf{T}^{AB}_\alpha \mathbf{J}[\mathbf{T}^A_\beta] + \mathbf{T}^{AB}_\beta \mathbf{J}[\mathbf{T}^A_\alpha] \\
&+ \mathbf{T}^A_\alpha \left(\mathbf{J}[\mathbf{T}^B_\alpha] - \mathbf{K}[\mathbf{T}^B_\alpha] \right) + \mathbf{T}^A_\beta \left(\mathbf{J}[\mathbf{T}^B_\beta] - \mathbf{K}[\mathbf{T}^B_\beta] \right) \\
&+ \mathbf{T}^A_\alpha \mathbf{J}[\mathbf{T}^B_\beta] + \mathbf{T}^A_\beta \mathbf{J}[\mathbf{T}^B_\alpha] \\
&+ \mathbf{T}^{AB}_\alpha \left(\mathbf{J}[\mathbf{T}^{AB}_\alpha] - \mathbf{K}[\mathbf{T}^{AB}_\alpha] \right) \\
&+ \mathbf{T}^{AB}_\beta \left(\mathbf{J}[\mathbf{T}^{AB}_\beta] - \mathbf{K}[\mathbf{T}^{AB}_\beta] \right) \\
&+ 2\mathbf{T}^{AB}_\beta \mathbf{J}[\mathbf{T}^{AB}_\alpha] \Big). \quad (8)
\end{aligned}$$

The $\mathbf{K}^X_\sigma \equiv \mathbf{K}[P^X_\sigma]$ are the exchange matrices, whereas the generalized Coulomb and exchange matrices, $\mathbf{J}[X]$, $\mathbf{K}[X]$ are defined as follows:

$$J[X]_{\mu\nu} = \sum_{\lambda\sigma} X_{\lambda\sigma}(\mu\nu|\lambda\sigma),$$

$$K[X]_{\mu\nu} = \sum_{\lambda\sigma} X_{\lambda\sigma}(\mu\lambda|\sigma\nu). \quad (9)$$

The $\mathbf{h}^X_\sigma$ matrix is given as

$$\mathbf{h}^X_\sigma = \mathbf{V}^X + \mathbf{J}^X_\alpha + \mathbf{J}^X_\beta - \mathbf{K}^X_\sigma \quad (10)$$

and the $\mathbf{T}^{X/XY}_\sigma$ matrices back-transformed to the AO basis are computed as follows:

$$\mathbf{T}^X_\sigma = (\mathbf{C}^X_\sigma)^\dagger([\mathbf{S}_\sigma + \mathbf{1}]^{-1} - \mathbf{1})\mathbf{C}^X_\sigma,$$

$$\mathbf{T}^{XY}_\sigma = (\mathbf{C}^X_\sigma)^\dagger([\mathbf{S}_\sigma + \mathbf{1}]^{-1} - \mathbf{1})\mathbf{C}^Y_\sigma. \quad (11)$$

The $\mathbf{S}_\sigma$ stands for the matrix of overlap integrals between the occupied molecular orbitals of both monomers, $(\mathbf{S}_\alpha)^{\tilde{j}}_{\tilde{i}} \equiv S^{\tilde{j}}_{\tilde{i}} = \int \phi_{\tilde{i}}(\mathbf{r})\phi_{\tilde{j}}(\mathbf{r})d^3\mathbf{r}$.

By restricting the permutations of electrons between the monomers to transpositions only, one can derive the so called S^2 approximation to the exchange energy. The formula for $E^{(1)}_{\text{exch}}(S^2)$ in terms of molecular orbitals[46] reads,

$$E^{(1)}_{\text{exch}}(S^2) = (\omega^A_\alpha)^{\tilde{b}}_{\tilde{j}} S^{\tilde{j}}_{\tilde{i}} S^{\tilde{i}}_{\tilde{b}} + (\omega^A_\beta)^{\bar{b}}_{\bar{j}} S^{\bar{j}}_{\bar{i}} S^{\bar{i}}_{\bar{b}} + (\omega^B_\alpha)^{\tilde{a}}_{\tilde{i}} S^{\tilde{i}}_{\tilde{j}} S^{\tilde{j}}_{\tilde{a}}$$
$$+ (\omega^B_\beta)^{\bar{a}}_{\bar{i}} S^{\bar{i}}_{\bar{j}} S^{\bar{j}}_{\bar{a}} + v^{\tilde{a}\tilde{b}}_{\tilde{i}\tilde{j}} S^{\tilde{i}}_{\tilde{b}} S^{\tilde{j}}_{\tilde{a}} + v^{\bar{a}\bar{b}}_{\bar{i}\bar{j}} S^{\bar{i}}_{\bar{b}} S^{\bar{j}}_{\bar{a}}, \quad (12)$$

where

$$\omega^X_\sigma = \left[\mathbf{C}^X_\sigma \left(\mathbf{V}^X + \mathbf{J}^X_\alpha + \mathbf{J}^X_\beta \right) \mathbf{C}^X_\sigma \right]_{\text{occ,virt}} = \left[\mathbf{C}^X_\sigma \boldsymbol{\Omega}^X \mathbf{C}^X_\sigma \right]_{\text{occ,virt}} \quad (13)$$

and

$$v^{km}_{ln} = \int \phi_l(\mathbf{r})\phi_n(\mathbf{r}')\tilde{v}(\mathbf{r}, \mathbf{r}')\phi_k(\mathbf{r})\phi_m(\mathbf{r}')d^3\mathbf{r}d^3\mathbf{r}'. \quad (14)$$

We stress that Eq. (12) is valid only in the dimer-centered basis set (DCBS).[49] From now on we use the Einstein summation convention over repeated indices.

C. Second-order SAPT energies

In this section, we use the spinorbital formalism of Ref. 19 to give explicit expressions for the induction and dispersion energies in unrestricted Kohn-Sham SAPT formulation. For the dispersion energy we present the analytical formulation generalized for the unrestricted case.[50] In the implementation of the "electronic" Hessian matrices of the unrestricted TDKS equations we employed the local spin-density approximation of the exchange-correlation kernels.[19,51]

Both the induction and dispersion energies can be expressed in terms of frequency-dependent density susceptibility functions of the monomers (FDDSs, also referred to as response functions), $\alpha_A(\mathbf{r}, \mathbf{r}'|\omega)$ (defined, e.g., in Ref. 52). Those functions take either coupled or uncoupled form, leading to coupled or uncoupled formulation of second-order induction and dispersion terms. As the coupled FDDSs lead to substantially better results, they will be applied here. In the formalism of the TDHF/TDKS theory they take the following matrix form:

$$\mathbf{X}^X_{ia(\sigma),jb(\sigma')}(i\gamma) = \sum_p \frac{\gamma^X_p}{\gamma^2 + \left(\gamma^X_p\right)^2} \mathbf{U}^{X,\dagger}_{ia(\sigma),p} \mathbf{U}^X_{jb(\sigma'),p}, \quad (15)$$

where $\mathbf{U}^X$ are the eigenvectors and $\boldsymbol{\gamma}^X$ are eigenvalues of unrestricted TDHF/TDKS eigenequations (e.g., see Ref. 51). One can see that the FDDSs in the spin-unrestricted theories consist of four spin blocks, similarly to Eq. (27) of Ref. 19.

The general formula for the induction energy can be written as[19,52]

$$E^{(2)}_{\text{ind}}(A \leftarrow B) = \frac{1}{2} \int \int \omega^B(\mathbf{r})\, \alpha_A(\mathbf{r}, \mathbf{r}'|0)\omega^B(\mathbf{r}')\, \mathrm{d}^3\mathbf{r}\mathrm{d}^3\mathbf{r}' \tag{16}$$

with $(A \leftarrow B)$ denoting influence of monomer B on monomer A. By inserting the TDKS expressions for FDDS in (16) and summation of both $(A \leftarrow B)$ and $(B \leftarrow A)$ terms, we obtain

the matrix formulation of the induction energy,

$$E^{(2)}_{\text{ind}} = -\frac{1}{2}(\boldsymbol{\omega}^B)^T \mathbf{X}^A(0)\boldsymbol{\omega}^B - \frac{1}{2}(\boldsymbol{\omega}^A)^T \mathbf{X}^B(0)\boldsymbol{\omega}^A. \tag{17}$$

We note that vectors $\boldsymbol{\omega}^X$ consist of suitably ordered matrix elements of Eq. (13).

The most general expression for the dispersion energy in term of FDDSs is given by the Longuet-Higgins-type integral,[53,54]

$$E^{(2)}_{\text{disp}} = -\frac{1}{4\pi} \iiiint \int_{-\infty}^{+\infty} \frac{\alpha_A(\mathbf{r}_1, \mathbf{r}_2|i\omega)\alpha_B(\mathbf{r}_3, \mathbf{r}_4|i\omega)}{|\mathbf{r}_1 - \mathbf{r}_2||\mathbf{r}_3 - \mathbf{r}_4|}$$

$$\times \mathrm{d}\mathbf{r}_1\mathrm{d}\mathbf{r}_2\mathrm{d}\mathbf{r}_3\mathrm{d}\mathbf{r}_4\mathrm{d}\omega. \tag{18}$$

With the FDDS formulation in the TDHF/TDKS theory we can write the dispersion energy in a more transparent form

$$E^{(2)}_{\text{disp}} = -\sum_{p,q} \frac{\mathbf{D}^2_{p,q}}{\omega^A_p + \omega^B_q}, \tag{19}$$

where we introduced intermediate matrices,

$$\mathbf{E} = (\mathbf{U}^A)^{\mathrm{T}}\mathbf{J}^{AB},$$
$$\mathbf{D} = \mathbf{E}\mathbf{U}^B, \tag{20}$$

with $\mathbf{J}^{AB}$ denoting a matrix of properly ordered two-electron integrals, v^{km}_{ln}.

To derive second-order exchange terms one can apply the second-quantization[55] or density-matrix-based[46] formulation of exchange-dispersion and exchange-induction energies in the S^2 approximation. In second-quantization approach the overall numerical scaling is more expensive compared to density-matrix-based theory. The second-quantization approach is also *not* valid in monomer-centered basis sets. However, the implementation in such a case is significantly simpler, since we deal with much smaller amount of the 4-index molecular integrals also, with lower symmetry. Both second-quantization and density-matrix formalism were implemented leading to the same numerical results. Below, we present only expressions derived within the density-matrix formalism.

The exchange-induction energy is given by the following formula:

$$E^{(2)}_{\text{exch}-\text{ind}}(A \leftarrow B) = \frac{1}{2}\sum_\sigma \text{Tr}\big(\mathbf{t}^A_\sigma\mathbf{K}^B_\sigma + \mathbf{t}^A_\sigma\mathbf{S}\mathbf{P}^B_\sigma\mathbf{h}^A_\sigma + \mathbf{t}^A_\sigma\mathbf{J}_\sigma[\mathbf{O}_\sigma] - \mathbf{t}^A_\sigma\mathbf{K}[\mathbf{O}_\sigma] + \mathbf{P}^B_\sigma\mathbf{S}\mathbf{t}^A_\sigma\mathbf{h}^B_\sigma$$

$$- \mathbf{P}^B_\sigma\mathbf{S}\mathbf{t}^A_\sigma\mathbf{S}\mathbf{P}^B_\sigma\boldsymbol{\Omega}^A - \mathbf{P}^B_\sigma\mathbf{S}\mathbf{O}_\sigma\mathbf{J}_\sigma\big[\mathbf{t}^A_\sigma\big] - \mathbf{O}_\sigma\mathbf{S}\mathbf{t}^A_\sigma\boldsymbol{\Omega}^B - \mathbf{t}^A_\sigma\mathbf{S}\mathbf{O}^{\mathrm{T}}_\sigma\boldsymbol{\Omega}^B$$

$$+ \mathbf{P}^B_\sigma\mathbf{S}\mathbf{t}^A_\sigma\mathbf{K}_\sigma[\mathbf{O}_\sigma] + \mathbf{t}^A_\sigma\mathbf{S}\mathbf{P}^B_\sigma\mathbf{K}^{\mathrm{T}}_\sigma[\mathbf{O}_\sigma]\big) + \frac{1}{2}\text{Tr}\big(\mathbf{t}^A_\beta\mathbf{J}_\alpha[\mathbf{O}_\alpha] + \mathbf{t}^A_\alpha\mathbf{J}_\beta[\mathbf{O}_\beta]$$

$$- \mathbf{P}^B_\alpha\mathbf{S}\mathbf{O}_\alpha\mathbf{J}_\beta\big[\mathbf{t}^A_\beta\big] - \mathbf{P}^B_\beta\mathbf{S}\mathbf{O}_\beta\mathbf{J}_\alpha\big[\mathbf{t}^A_\alpha\big]\big), \tag{21}$$

where the coupled induction amplitudes are

$$\big[\mathbf{t}^A_\alpha\big]^{\tilde{i}}_{\tilde{a}} = \mathbf{X}^A_{i\tilde{a},\tilde{i}'\tilde{a}'}(0)\big[\boldsymbol{\omega}^B_\alpha\big]^{\tilde{i}'}_{\tilde{a}'}, \tag{22}$$

back-transformed to the AO basis, $\mathbf{S}$ stands for the AO overlap matrix, $\mathbf{O}_\sigma = \mathbf{P}^A_\sigma\mathbf{S}\mathbf{P}^B_\sigma$, and $\boldsymbol{\Omega}^X$ is defined in Eq. (13).

The second-order exchange-dispersion energy contribution in the $\alpha\alpha$ case takes the form,

$$
E^{(2)}_{\text{exch}-\text{disp},\alpha\alpha}(S^2) = -\tau_{\tilde{i}\tilde{a},\tilde{j}\tilde{b}}\big[-v^{\tilde{a}'\tilde{b}'}_{\tilde{i}\tilde{j}} S^{\tilde{b}}_{\tilde{a}'} S^{\tilde{a}}_{\tilde{b}'} + \big(v^{\tilde{a}\tilde{b}'}_{\tilde{i}'\tilde{j}} S^{\tilde{b}}_{\tilde{i}} - v^{\tilde{a}\tilde{b}'}_{\tilde{i}\tilde{j}} S^{\tilde{b}}_{\tilde{i}'}\big)S^{\tilde{i}'}_{\tilde{b}'} + \big(v^{\tilde{a}'\tilde{b}}_{\tilde{i}\tilde{j}'} S^{\tilde{j}}_{\tilde{a}} - v^{\tilde{a}'\tilde{b}}_{\tilde{i}\tilde{j}} S^{\tilde{a}}_{\tilde{j}'}\big)S^{\tilde{j}'}_{\tilde{a}'}
$$
$$
- \big(v^{\tilde{a}\tilde{b}}_{\tilde{i}'\tilde{j}'} + v^{\tilde{a}\tilde{b}}_{\tilde{i}\tilde{j}'} S^{\tilde{j}'}_{\tilde{i}'}\big)S^{\tilde{i}'}_{\tilde{j}} + v^{\tilde{a}\tilde{b}}_{\tilde{i}'\tilde{j}} S^{\tilde{i}'}_{\tilde{i}} S^{\tilde{j}'}_{\tilde{j}'} + \big((\boldsymbol{\omega}^A_\alpha)^{\tilde{b}}_{\tilde{j}'} S^{\tilde{a}}_{\tilde{j}} - (\boldsymbol{\omega}^A_\alpha)^{\tilde{b}}_{\tilde{j}} S^{\tilde{a}}_{\tilde{j}'}\big)S^{\tilde{i}'}_{\tilde{i}}
$$
$$
+ \big((\boldsymbol{\omega}^B_\alpha)^{\tilde{a}}_{\tilde{i}'} S^{\tilde{b}}_{\tilde{i}} - (\boldsymbol{\omega}^B_\alpha)^{\tilde{a}}_{\tilde{i}} S^{\tilde{b}}_{\tilde{i}'}\big)S^{\tilde{i}'}_{\tilde{j}} - (\boldsymbol{\omega}^B_\alpha)^{\tilde{a}'}_{\tilde{i}} S^{\tilde{a}}_{\tilde{a}'} S^{\tilde{a}}_{\tilde{j}} - (\boldsymbol{\omega}^A_\alpha)^{\tilde{b}'}_{\tilde{j}} S^{\tilde{a}}_{\tilde{b}'} S^{\tilde{b}}_{\tilde{i}}\big], \tag{23}
$$

and analogous expression holds for the $\beta\beta$ contribution. For the opposite $\alpha\beta$ spins, we have

$$
E^{(2)}_{\text{exch}-\text{disp},\alpha\beta}(S^2)
$$
$$
= -\tau_{\tilde{i}\tilde{a},\tilde{j}\tilde{b}}\big[-v^{\tilde{a}\tilde{b}'}_{\tilde{i}\tilde{j}} S^{\tilde{b}}_{\tilde{i}'} S^{\tilde{i}'}_{\tilde{b}'} - v^{\tilde{a}'\tilde{b}}_{\tilde{i}\tilde{j}} S^{\tilde{a}}_{\tilde{j}'} S^{\tilde{j}'}_{\tilde{a}'} + v^{\tilde{a}\tilde{b}}_{\tilde{i}\tilde{j}} S^{\tilde{j}'}_{\tilde{i}'} S^{\tilde{i}'}_{\tilde{j}} + v^{\tilde{a}\tilde{b}}_{\tilde{i}'\tilde{j}'} S^{\tilde{j}}_{\tilde{i}} S^{\tilde{i}'}_{\tilde{j}'}
$$
$$
- \big(\boldsymbol{\omega}^A_\beta\big)^{\tilde{b}}_{\tilde{j}} S^{\tilde{a}}_{\tilde{j}'} S^{\tilde{j}'}_{\tilde{i}} - \big(\boldsymbol{\omega}^B_\alpha\big)^{\tilde{a}}_{\tilde{i}} S^{\tilde{b}}_{\tilde{i}'} S^{\tilde{i}'}_{\tilde{j}}\big]. \tag{24}
$$

The uncoupled amplitudes $\tau_{ia(\sigma),jb(\sigma')}$ can be written in the form (for $\alpha\beta$ case),

$$
\tau_{\tilde{i}\tilde{a},\tilde{j}\tilde{b}} = \frac{v^{\tilde{a}\tilde{b}}_{\tilde{i}\tilde{j}}}{\epsilon_{\tilde{a}} + \epsilon_{\tilde{b}} - \epsilon_{\tilde{i}} - \epsilon_{\tilde{j}}}. \tag{25}
$$

Both exchange-dispersion implementations were positively verified against the closed-shell case. Following Ref. 52 we obtain the coupled exchange-dispersion formula by scaling the uncoupled term. Such estimation assumes the exchange-dispersion energy being proportional to the dispersion term,

$$
E^{(2)}_{\text{exch}-\text{disp}}(\text{cKS}) = E^{(2)}_{\text{exch}-\text{disp}}(\text{uKS}) \times \frac{E^{(2)}_{\text{disp}}(\text{cKS})}{E^{(2)}_{\text{disp}}(\text{uKS})}, \tag{26}
$$

where $E^{(2)}_{\text{disp}}(\text{cKS/uKS})$ denote terms obtained with the coupled and uncoupled Kohn-Sham FDDSs applied to Eq. (18).

D. Total interaction energies and effects beyond second order

The total interaction energy calculated with the SAPT(UKS) method takes the form,

$$
E^{\text{SAPT(UKS)}}_{\text{int}} = E^{(1)}_{\text{elst}}(\text{KS}) + E^{(1)}_{\text{exch}}(\text{KS}) + E^{(2)}_{\text{ind}}(\text{cKS})
$$
$$
+ E^{(2)}_{\text{exch}-\text{ind}}(\text{cKS}) + E^{(2)}_{\text{disp}}(\text{cKS}) + E^{(2)}_{\text{exch}-\text{disp}}(\text{cKS}), \tag{27}
$$

where KS denotes energy terms obtained with the Kohn-Sham orbitals and time-dependent Kohn-Sham response functions. All second-order terms are obtained at the coupled level of theory (denoted cKS).

We also present results obtained with the unrestricted Hartree-Fock wavefunctions,

$$
E^{\text{SAPT(UHF)}}_{\text{int}} = E^{(1)}_{\text{elst}}(\text{HF}) + E^{(1)}_{\text{exch}}(\text{HF}) + E^{(2)}_{\text{ind}}(\text{cHF})
$$
$$
+ E^{(2)}_{\text{exch}-\text{ind}}(\text{cHF}) + E^{(2)}_{\text{disp}}(\text{cHF}) + E^{(2)}_{\text{exch}-\text{disp}}(\text{cHF}). \tag{28}
$$

The total interaction energies calculated in (27) and (28) contain terms up to second order in V. Higher-order terms

can be estimated in SAPT(DFT) via applying the $\delta E^{\text{HF}}_{\text{int}}$ correction,[47,56,57]

$$
\delta E^{\text{HF}}_{\text{int}} = E^{\text{HF}}_{\text{int}} - \big(E^{(1)}_{\text{elst}}(\text{HF}) + E^{(1)}_{\text{exch}}(\text{HF})
$$
$$
+ E^{(2)}_{\text{ind}}(\text{HF}) + E^{(2)}_{\text{exch}-\text{ind}}(\text{HF})\big). \tag{29}
$$

The above formula relies on approximate extraction of the missing energy contributions from the supermolecular Hartree-Fock energy, $E^{\text{HF}}_{\text{int}}$. We intend to determine how effective the inclusion of this term will be for open-shell systems.

Because of the known problems of SAPT when ECP are employed,[58,59] in this work we also use a HF+dispersion hybrid approach, combining the HF supermolecular energies with either SAPT(UHF) or SAPT(UKS) dispersion contribution,[25,60]

$$
E_{\text{int}} = E^{\text{HF}}_{\text{int}} + E^{(2)}_{\text{disp}} + E^{(2)}_{\text{exch}-\text{disp}}. \tag{30}
$$

III. NUMERICAL RESULTS

In order to test the performance of the SAPT(UKS) approach we chose seven different van der Waals complexes, which we classify into three groups. The first group contains systems selected to compare the SAPT(UKS) and SAPT(ROKS) methods: a dispersion-bound dimer (He$\cdots$NH) and a dimer bound mainly by electrostatic forces (H$_2$O$\cdots$HO$_2$). The second group encompasses rare gas atoms interacting with molecules in $^2\Pi$ electronic states (He/Ar$\cdots$OH and Ar$\cdots$NO). We show that the SAPT(UKS) method allows for a proper description of both A' and A'' states in very good agreement with the coupled cluster reference values. Finally, the third group represents two weakly bound transition metal atom complexes (Au$_2$ ($^3\Sigma^+_u$) and Cr$_2$ ($^{13}\Sigma^+_g$)), treated at the SAPT level of theory with effective core potentials (ECP). We have used the asymptotically corrected[38] PBE0 density functional throughout the work,[61,62] as it is known to give the most accurate interaction energies for both the closed-shell and open-shell systems.[19,52] All the results were obtained with the dimer-centered basis set (DC$^+$BS) approach (the plus sign denoting the use of bond functions).

Next to the SAPT(UKS), we also present the SAPT(UHF) results, which may provide valuable insights into the nature of the energy contributions.

The total interaction energies are compared with the supermolecular unrestricted or spin-restricted CCSD(T) energies. Moreover, the electrostatic energy calculated with the CISD densities ($E^{(1)}_{\text{elst}}(\text{CISD})$) serves as a comparison to the

TABLE I. Total interaction energies of the chosen open-shell systems within SAPT(UHF), SAPT(ROHF), SAPT(ROKS), SAPT(UKS), and RCCSD(T) approximations. The SAPT(DFT) results include the $\delta E_{\text{int}}^{\text{HF}}$ correction. Geometries given in Ref. 19.

System	SAPT (UHF)	SAPT (ROHF)[a]	SAPT (UKS)	SAPT (ROKS)[a]	RCCSD(T)[a]
CN···Ne	−38.06	−40.07	−45.32	−43.88	−39.42
NH···NH	−756	−767	−761	−774	−693
H₂O-HO₂	−813	−813	−790	−776	−752
He···NH	−20.65	−20.38	−26.98	−25.88	−19.83

[a]Reference 19.

SAPT electrostatic contribution. The CISD wave functions were constructed from ROHF orbitals using the MATROP module in the MOLPRO package.[63]

All the formulas were implemented in the developer version of the MOLPRO package.

First we present a set of SAPT(UKS) interaction energies for four systems previously tested when introducing the SAPT(ROKS) approach by Żuchowski *et al.*[19] (see Table I). When comparing the two open-shell SAPT(DFT) methods one should note the use of the different asymptotic correction schemes: the GRAC scheme[38] in the present work versus the Fermi-Amaldi correction[64] in the previous studies.[19] This, together with the spin symmetry contamination present in UKS, may lead to discrepancies between both approaches. Both SAPT(ROKS) and SAPT(UKS) results in Table I include the $\delta E_{\text{int}}^{\text{HF}}$ correction.

The overall picture shows remarkable agreement between SAPT(ROHF) and SAPT(UHF) methods, with differences up to 4% in interaction energies. Similar performance is observed for SAPT based on Hartree-Fock, where discrepancies up to 5% are to be noted. It should be stressed that the open-shell SAPT(DFT) results agree well with the CCSD(T) benchmark values, except for the He···NH dimer.

In the next two subsections we will focus on the detailed analysis of selected complexes: He···NH and H₂O-HO₂. The remaining data are provided in the supplementary material.[65]

A. NH($^3\Sigma^-$)···He

The calculations for the NH radical in the $^3\Sigma^-$ state interacting with the helium atom followed the methodology of Refs. 19 and 66. We applied the aug-cc-pVQZ basis set[67–69] extended with a set of $3s3p2d2f1g$ bond functions.[19,70] The separation between the center of mass (COM) of NH and the He nucleus was $R = 6.3$ bohr. The angle between the line connecting the COM of NH and the He atom equaled 62°. The NH bond length was set to 1.95 bohr. This geometry is close to the global minimum geometry.[66] The reference interaction energy was obtained with the RCCSD(T) method. The SAPT components and total interaction energies are presented in Table II.

Comparison of the spin-unrestricted and spin-restricted results for NH···He (and similarly H₂O···O₂H of the next section) shows a general tendency that HF-based results are in closer agreement than the KS-based results. This difference is lesser in SAPT(UHF) and SAPT(ROHF) (up to 7%)

TABLE II. He···NH($^3\Sigma^-$) interaction energy components at the global minimum geometry (see the text). The basis set was aug-cc-pVQZ + $3s3p2d2f1g$. All energies in cm^{-1}.

	SAPT(UHF)	SAPT(ROHF)	SAPT(UKS)	SAPT(ROKS)
$E_{\text{elst}}^{(1)}$	−4.29	−4.49	−3.98	−4.71
$E_{\text{elst}}^{(1)}$(CISD)	−5.21			
$E_{\text{exch}}^{(1)}$	22.99	24.01	19.85	23.66
$E_{\text{ind}}^{(2)}$	−2.91	−2.96	−2.57	−2.87
$E_{\text{exch−ind}}^{(2)}$	1.27	1.35	1.03	1.20
$E_{\text{disp}}^{(2)\ \text{a}}$	−33.37	−35.92	−44.93	−48.39
$E_{\text{disp}}^{(2)\ \text{b}}$	−39.19	−39.71	−40.78	−42.80
$E_{\text{exch−disp}}^{(2)}$	1.48	1.42	1.35	1.63
E_{int}	−20.65	−20.38	−25.10	−23.88
$E_{\text{int}}+\delta E_{\text{int}}^{\text{HF}}$			−26.98	−25.88
$E_{\text{int}}^{\text{RCCSD}}$	−16.32			
$E_{\text{int}}^{\text{RCCSD(T)}}$	−19.83			
$\langle S^2 \rangle$	2.017	...	2.006	...

[a]Uncoupled.
[b]Coupled.

and larger for the SAPT(UKS) and SAPT(ROKS) (from 3% to 17%). The reason behind this tendency lies in different asymptotic correction schemes applied in the KS-based SAPT. Spin-contamination within the UKS method may also play a role.

Equally important is the detailed analysis of the UKS versus ROKS SAPT energy components. The electrostatic energy is underestimated by 24% with SAPT(UKS) and only by 9.6% with SAPT(ROKS), with respect to $E_{\text{elst}}^{(1)}$(CISD). However, applying the GRAC correction for SAPT(ROKS) results in electrostatic energy equal to −3.99 cm^{-1}, which cancels the difference with respect to the SAPT(UKS) result. The $\langle S^2 \rangle_{\text{NI}}$ with the value of 2.006 indicates a small spin contamination. The HF based results differ only by 4% for both electrostatic and exchange energies with $\langle S^2 \rangle$ substantially higher than in the UKS case (see Table II). The S^2 approximation to the exchange energy performs well, giving less than 1% deviation from the exact value.

The second-order induction and exchange-induction energies give small contribution to the total interaction energy, their values being even lower than the electrostatic energy.

The major energy contribution to E_{int} comes from the dispersion interaction. Here, the UKS and ROKS values are in close agreement. The exchange-dispersion energy is relatively small. We found that $\delta E_{\text{int}}^{\text{HF}}$ correction spoils the agreement between SAPT(UKS) and the reference RCCSD(T) interaction energies, similarly to the SAPT(ROKS) as shown in Refs. 19 and 71.

B. H₂O···HO₂(^2A)

The water molecule-hydroperoxide radical dimer serves as an example of a system bound mainly by electrostatic forces. The planar geometry was taken from Ref. 19 (see also supplementary material[65]). The basis set was aug-cc-pVTZ

TABLE III. Interaction energy components for $H_2O\cdots HO_2(^2A)$, aug-cc-pVTZ+ $3s3p2d$. Geometry given in Ref. 19. All energies in cm^{-1}.

	SAPT(UHF)	SAPT(ROHF)	SAPT(UKS)	SAPT(ROKS)
$E_{elst}^{(1)}$	-794	-794	-764	-778
$E_{elst}^{(1)}$(CISD)	-775			
$E_{exch}^{(1)}$	481	480	557	594
$E_{ind}^{(2)}$	-189	-188	-231	-243
$E_{exch-ind}^{(2)}$	121	120	163	171
$E_{disp}^{(2)\,a}$	-473	-476	-709	-720
$E_{disp}^{(2)\,b}$	-479	-478	-534	-541
$E_{exch-disp}^{(2)}$	48	47	56	58
E_{int}	-813	-813	-753	-739
$E_{int}+\delta E_{int}^{HF}$			-790	-776
E_{int}^{RCCSD}	-693			
$E_{int}^{RCCSD(T)}$	-752			
$\langle S^2 \rangle$	0.763	$\dots$	0.754	$\dots$

[a]Uncoupled.
[b]Coupled.

TABLE IV. Interaction energy components at the global minimum (the A' PES) of $He\cdots OH(X^2\Pi)$, aug-cc-pVTZ+ $3s3p2d2f1g$. $\theta = 0°$ corresponds to $OH\cdots Ar$ collinear arrangement. All energies in cm^{-1}.

	SAPT(UHF)	SAPT(UKS)
$E_{elst}^{(1)}$	-7.458	-9.888
$E_{elst}^{(1)}$(CISD)	-9.845	
$E_{exch}^{(1)}$	36.56	49.10
$E_{ind}^{(2)}$	-6.714	-7.668
$E_{exch-ind}^{(2)}$	2.496	3.547
$E_{disp}^{(2)\,a}$	-50.34	-72.98
$E_{disp}^{(2)\,b}$	-64.63	-66.32
$E_{exch-disp}^{(2)}$	2.780	3.048
E_{int}	-36.97	-28.18
$E_{int}+\delta E_{int}^{HF}$		-30.71
E_{int}^{RCCSD}	-24.66	
$E_{int}^{RCCSD(T)\,c}$	-30.02	
$\langle S^2 \rangle$	0.757	0.753

[a]Uncoupled.
[b]Coupled.
[c]Reference 72.

supplemented with $3s3p2d$ bond functions.[19,70] The results are presented in Table III.

For this system the agreement between SAPT(ROKS) and SAPT(UKS) is excellent with the differences ranging from 1.3% for coupled $E_{disp}^{(2)}$ to 6.2% for $E_{exch}^{(1)}$. At the Hartree-Fock level of theory we obtain virtually the same numbers, with discrepancies of 1 cm^{-1}. The total interaction energy agrees within a fraction of percent with the RCCSD(T) result, however it is due to fortuitous cancellation of errors: adding the δE_{int} term results in a few percent overbinding, still a reasonable result.

C. He$\cdots$OH($X^2\Pi$) complex

The PES for the He$\cdots$OH($X^2\Pi$) dimer was obtained by Lee *et al.*[72] and used as a reference in later works.[73] The electron configuration of OH in the ground state is $(1\sigma^2 2\sigma^2 3\sigma^2 1\pi^3)$, and gives rise to two states A' and A''. We have performed calculations for the global and local minima as described in Ref. 72. The OH equilibrium bond length was set to the experimentally determined value of 0.96966 Å.[74] The basis set was aug-cc-pVTZ with $3s3p2d2f1g$ bond functions placed in the middle between the COM of OH and the helium atom.[75] The SAPT(UKS) results for the global minimum geometry (A': R = 3.010 Å and $\theta = 68.6°$) are presented in Table IV. Total interaction energies for all the minima are given in Table V.

The importance of the intramonomer correlation effects is underscored by 24% difference between UKS and UHF electrostatic energy. We note that the DFT approach is in excellent agreement with the reference CISD value (only 0.4% discrepancy). Similarly the exchange energy is expected to be underestimated within the Hartree-Fock scheme.

The total induction component is small and contributes only 13% to the total interaction energy. Although the intramonomer correlation strongly affects the exchange-induction

energy and the PBE0 value differs by almost 30% from that of SAPT(UHF), the cancellation of the induction and exchange-induction components is similar for UHF and UKS approaches. For the dispersion energy, which is the main binding force in the He$\cdots$OH($X^2\Pi$) dimer, SAPT(UKS) and SAPT(UHF) give close results at the coupled level of theory (although the uncoupled values differ by more than 30%). The exchange-dispersion contribution quenches only 4.5% of the dispersion interaction.

The total SAPT interaction energy shows a remarkable agreement with the supermolecular RCCSD(T) values. The δE_{int}^{HF} correction accounts for 8% of the E_{int} and reduces the SAPT(UKS) error from 6.2% to 2.1% with respect to the reference values. Due to the aforementioned importance of the intramonomer correlation effects in this system, SAPT(UHF) performance is much worse and deviates by around 19% from the RCCSD(T) energy. For the two remaining minima of this system we observe a very good agreement with the supermolecular reference energies. SAPT(UHF) results agree with the SAPT(UKS) ones up to 2%.

In order to check the ability of the SAPT(UKS) method to correctly predict both states arising from the interaction of He with $^2\Pi$ systems we show a plot of the angular dependence for A' and A'' surfaces, compared with the RCCSD(T) data

TABLE V. Comparison of interaction energies at the minima on A' and A'' surfaces of He$\cdots$OH($X^2\Pi$) complex, aug-cc-pVTZ+ $3s3p2d2f1g$. $\theta = 0°$ corresponds to OH$\cdots$He collinear arrangement. All energies in cm^{-1}. A'' surface has minima for linear geometry (saddle points for A').

State	R [Å]	θ	SAPT(UHF)	SAPT(UKS)	RCCSD(T)[a]
A'	3.010	68.6	-36.97	-30.71	-30.02
Π	3.463	0.0	-27.16	-27.72	-27.06
Π	3.223	180.0	-23.49	-23.50	-21.79

[a]Reference 72.
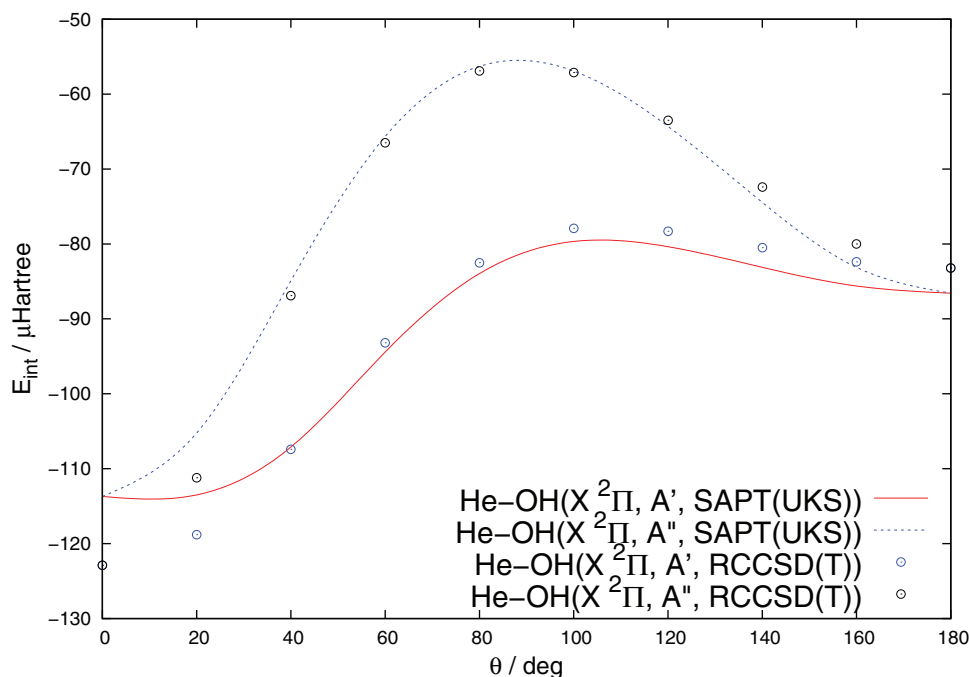
FIG. 1. θ-dependence of the SAPT(UKS) interaction energies of He$\cdots$OH($X^2\Pi$) system for A' and A'' symmetries, R = 3.5 Å. Comparison with RCCSD(T) points by Lee *et al.*[72]

(Fig. 1). We observe an excellent agreement with the reference values with largest deviations for the linear geometries.

D. Ar$\cdots$OH($X^2\Pi$) complex

The Ar$\cdots$OH($X^2\Pi$) dimer has been thoroughly studied in the past.[5] Important theoretical works concerning the electronic structure of the complex include Ref. 73, 76, and 77.

The aug-cc-pVQZ basis set extended with a $3s3p2d2f1g$ bond functions was applied.[73,75] The OH radical geometry was the same as for the He$\cdots$OH case. In Table VI we present

TABLE VI. Interaction energy components at the minimum of the Ar$\cdots$OH($X^2\Pi$) Π state complex: R = 6.9, $\theta=0°$, aug-cc-pVQZ + $3s3p2d2f1g$. $\theta = 0°$ corresponds to OH$\cdots$Ar collinear arrangement. All energies in cm^{-1}.

	SAPT(UHF)	SAPT(UKS)
$E_{\text{elst}}^{(1)}$	-54.28	-68.88
$E_{\text{elst}}^{(1)}$(CISD)	-60.96	
$E_{\text{exch}}^{(1)}$	258.37	297.07
$E_{\text{ind}}^{(2)}$	-136.1	-185.6
$E_{\text{exch-ind}}^{(2)}$	67.78	90.69
$E_{\text{disp}}^{(2)\,\text{a}}$	-251.0	-370.4
$E_{\text{disp}}^{(2)\,\text{b}}$	-276.3	-281.4
$E_{\text{exch-disp}}^{(2)}$	22.26	23.33
E_{int}	-139.26	-117.0
$E_{\text{int}}+\delta E_{\text{int}}^{\text{HF}}$		-144.2
$E_{\text{int}}^{\text{RCCSD(T)}\,\text{c}}$	-140.4	
$\langle S^2 \rangle$	0.757	0.753

[a]Uncoupled.
[b]Coupled.
[c]Reference 73.

results for the global minimum geometry (R = 6.9 bohr, $\theta = 0°$, which corresponds to the linear Ar-H-O atom arrangement). Table VII contains a comparison of total interaction energies for the remaining minima obtained in Ref. 73.

For all of the geometries the SAPT(UKS) electrostatic interaction agree well with the CISD reference values to within 10%. The induction term contributes relatively more to the binding energy than for He$\cdots$OH dimer. For the global minimum the coupled $E_{\text{disp}}^{(2)}$ damped by a few percent by the exchange-dispersion turns out to be the main binding force. The intramonomer correlation contribution to the dispersion energy is of the order of a few percent. The analysis of the remaining minima shows that SAPT(UHF) tends to overbind with respect to RCCSD(T) yielding errors as large as 40%. A more detailed analysis reveals that this results from underestimation of the $E_{\text{exch}}^{(1)}$ repulsion and overestimation of the dispersion attraction. Unlike in the global minimum, in the local minima the dispersion interaction is strongly affected by intramonomer correlation. The induction terms, due to the cancellation of errors, seem to be insensitive to this effect. The overall agreement of the SAPT(UKS) results with the reference data is very good with errors not exceeding 10%.

TABLE VII. Comparison of interaction energies at the minima on two surfaces of Ar – OH($X^2\Pi$), aug-cc-pVQZ+ $3s3p2d2f1g$. $\theta = 0°$ corresponds to OH$\cdots$Ar collinear arrangement. All energies in cm^{-1}.

State	R [a_0]	θ	SAPT(UHF)	SAPT(UKS)	RCCSD(T)[a]
Π	6.90	0.0	-140.4	-144.2	-140.4
A'	6.17	75.2	-217.6	-132.7	-137.5
Π	6.80	180.0	-110.4	-99.9	-91.8
A'	6.15	90.0	-217.9	-124.7	-131.7
A''	7.05	90.0	-106.4	-79.6	-71.2

[a]Reference 73.

TABLE VIII. Interaction energies at the minima on the A' and A'' surfaces of the Ar$\cdots$NO($X^2\Pi$) complex, aug-cc-pVTZ+ $3s3p2d$. $\theta = 0°$ corresponds to NO$\cdots$Ar collinear arrangement. All energies in cm^{-1}.

State	R [Å]	θ	SAPT(UHF)	SAPT(UKS)	UCCSD(T)[a]
A'	6.76	94.9	−111.0	−118.1	−115.9
A''	6.92	69.9	−108.9	−114.5	−111.0

[a]Reference 81.

E. Ar$\cdots$NO($X^2\Pi$) complex

Systems with NO($X^2\Pi$) molecule are particularly challenging, since the NO dipole moment is small (0.157 D) (Ref. 78) and sensitive to the method and basis set applied. Previous electronic structure studies on this complex include Refs. 79–81, as well as the most recent Refs. 82 and 83.

Similar to the case of the OH radical, the electron configuration of NO ($1\sigma^2 2\sigma^2 3\sigma^2 4\sigma^2 1\pi^4 5\sigma^2 2\pi^2$) gives rise to two states, $^2A'$ and $^2A''$ in the Ar$\cdots$NO dimer. In Table VIII we present results of the SAPT(UKS/UHF) calculations for the minima of the A' and A'' surfaces; and in Table IX the detailed SAPT(UKS) decomposition for the A'' minimum is shown. Geometries and reference energy values were taken from Ref. 81. The X NO equilibrium bond length was set to 1.5077 Å. We chose the aug-cc-pVTZ + $3s3p2d$ basis set.[66]

For both states the SAPT(UHF) and SAPT(UKS) results remain in a good agreement, showing that intramonomer correlation has a minor effect. For $E^{(1)}_{elst}$ and $E^{(1)}_{exch}$ terms the discrepancies are of the order of a few percent. The KS electrostatic energy deviates from CISD by more than 5% compared to almost 9% difference of SAPT(UHF).

F. Cr$_2$ ($^{13}\Sigma_g^+$)

A high-spin chromium dimer is an interesting system due to its importance in studies of the properties of dipolar ultracold quantum gases.[84,85] The van der Waals Cr$_2$ ($^{13}\Sigma_g^+$) com-

TABLE IX. Interaction energy components at the minimum of the Ar$\cdots$NO($X^2\Pi$) complex, (A'': R = 6.92, θ = 69.9°), aug-cc-pVTZ+ $3s3p2d$. $\theta = 0°$ corresponds to NO$\cdots$Ar collinear arrangement. All energies in cm^{-1}.

	SAPT(UHF)	SAPT(UKS)
$E^{(1)}_{elst}$	− 44.47	− 46.16
$E^{(1)}_{elst}$(CISD)	− 48.71	
$E^{(1)}_{exch}$	146.8	153.9
$E^{(2)}_{ind}$	− 46.10	− 49.35
$E^{(2)}_{exch-ind}$	44.96	48.98
$E^{(2)}_{disp}$ [a]	− 234.4	− 327.4
$E^{(2)}_{disp}$ [b]	− 225.0	− 231.2
$E^{(2)}_{exch-disp}$	15.01	14.92
E_{int}	− 108.8	− 108.9
$E_{int}+\delta E^{HF}_{int}$		− 114.5
$E^{UCCSD(T)}_{int}$ [c]	− 111.0	
$\langle S^2 \rangle$	0.796	0.754

[a]Uncoupled.
[b]Coupled.
[c]Reference 81.

plex poses a challenge for the SAPT methodology due to its $4s^1$ and $3d^5$ half-open shells.

Two sets of UHF+disp results are presented. In the first set (UHF + disp(TDHF)), we combine the UHF supermolecular energy with the dispersion contributions obtained at the cHF level of theory. The second set (UHF + disp(TDDFT)) takes advantage of the dispersion contributions calculated with the TDDFT response functions. In the previous study on this dimer,[25] an ROHF+disp formalism was applied. The calculations performed there were nonrelativistic and the large aug-cc-pVQZ basis set with bond functions was employed. In contrast, we have included the relativistic effects by using the Stuttgardt RSC ECP plus basis set[86,87] extended with $3s3p2d1f$ bond functions.[66] The results are shown in Fig. 2 and detailed data are provided in supplementary material.[65] The reference data include two sets previously given in Ref. 25—the nonrelativistic RCCSD(T), as well as scalar relativistic RCCSD(T) with the Douglas-Kroll-Hess integrals (denoted RCCSD(T)/DK). Additionally we enclose our results from the UCCSD(T) calculations performed with the Stuttgart ECP + $3s3p2d1f$ basis set.

The reference relativistic calculations employing effective core potentials (UCCSD(T)/ECP) and RCCSD(T)/DK show excellent agreement. However, the minimum geometry predicted by the two methods is slightly different. RCCSD(T)/DK gives the equilibrium distance of 6.18 bohr, while the RCCSD(T)/ECP methods leads to 6.25 bohr. The RCCSD(T)/ECP-predicted minimum is shallower, with the difference amounting to 5%.

The ROHF+disp(TDDFT) and UHF + disp(TDDFT) should be compared with dispersion originating from either SAPT(ROKS) or SAPT(UKS), respectively. The inclusion of relativistic effects in the UHF case leads to a deeper minimum at slightly shorter distance, 6.00 bohr versus 6.06 bohr in the ROHF method. This UHF + disp(TDDFT) minimum is overestimated by 3.4% compared to the RCCSD(T)/DK one and by over 8% when compared to the UCCSD(T)/ECP results. The shorter bond length in both hybrid SAPT approaches should be attributed to the neglect of the intramonomer electron correlation in the UHF method. The long range part of the potentials agrees to within 4% and is less attractive than the reference RCCSD(T) curve. The short-range region is significantly less repulsive in the UHF+disp(TDDFT) method. The spin contamination of chromium in UHF and UKS is smaller than 10^{-3}.

The hybrid UHF+disp(TDHF) results presented in Figure 2 clearly show that this approach gives a potential which is too attractive, with minimum at 5.9 bohr to deep by 27% with respect to RCCSD(T)/DK. It should be stressed that the UHF+disp(TDHF) result is in close agreement with the results of ROHF+disp(TDHF) of Ref. 25.

G. Au$_2$ ($^3\Sigma_u^+$)

The Au$_2$($^3\Sigma_u^+$) complex can be considered as the simplest model system of the aurophilic interaction between two Au(I) centers. The nature of the "aurophilicity" has been linked chiefly to the dispersion attraction between spherically symmetric (5d^{10}) Au(I).[88,89] However, only recently
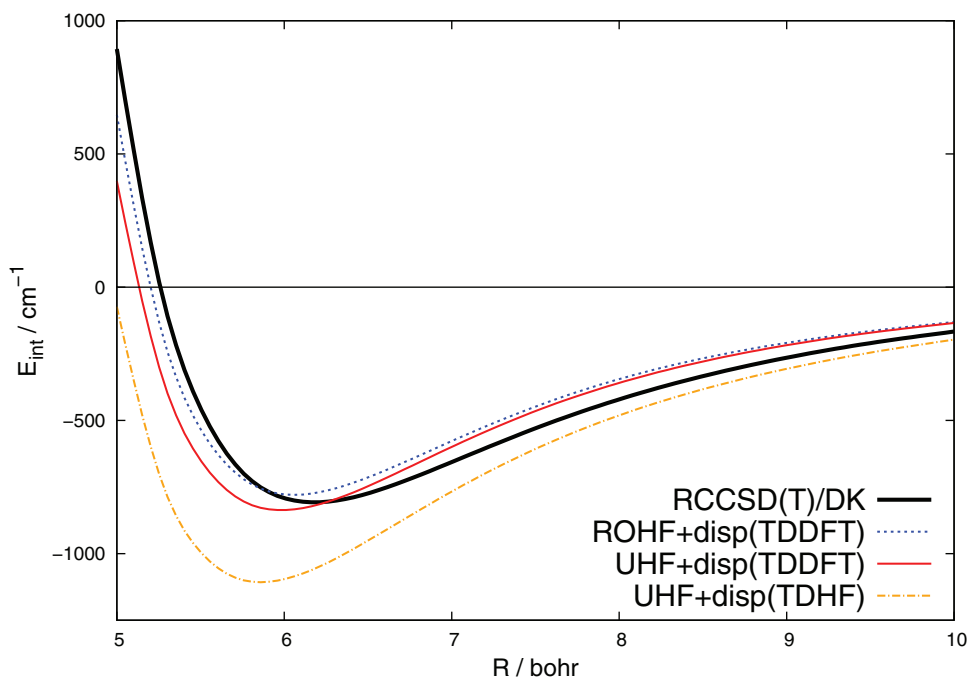
FIG. 2. The interaction potential for Cr_2 ($^{13}\Sigma_g^+$) with different methods. See the text for description of basis sets.

perturbative analysis of this important phenomenon has been performed.[59,89] In Ref. 59, the hybrid ROHF+disp(TDHF) method has been applied for a set of model Au(I)$\cdots$Au(I) bound systems. Here, we study the triplet Au_2 dimer with the unrestricted hybrid SAPT approach. In the description of gold atoms we applied a 19-electron, small core (1*s*-4*f*), relativistic effective core potential of Figgen *et al.*[90] The HF supermolecular energy was obtained with the aug-cc-pVTZ-PP basis set.[91] In the calculations of dispersion energy and supermolecular UCCSD(T) interaction energy we applied the aug-cc-pVQZ-PP basis set[91] (from which the more compact g and h orbitals were removed) extended with 3*s*3*p*2*d*2*f* bond functions.[66] The results for the global minimum geometry are given in Table X.

The supermolecular UCCSD(T) calculations within the described framework lead to the total interaction energy of 6.664 mH (4.182 kcal/mol) at $R_{\min}^e = 5.44$ bohr (2.88 Å). This is consistent with previous findings of Ref. 92: 6.854 mH (4.301 kcal/mol) at $R_{\min}^e = 5.42$ bohr (2.87 Å). The hybrid SAPT approach leads to overbinding of the triplet Au_2 dimer, with the global minimum energy of 8.760 mH (5.497 kcal/mol) obtained with the UHF+disp(TDHF) method and 7.799 mH (4.894 kcal/mol) in the UHF +disp(TDDFT) method. Similarly to the Cr_2 case, the predicted intermolecular distance is shorter with respect to the reference UCCSD(T) results and equals roughly 5.35 bohr. It is worth mentioning that the ROHF+disp(TDHF) calculations of Ref. 59 gave the binding energy of 4.36 (kcal/mol) at roughly $R_{\min}^e = 5.67$ bohr (3.00 Å) which is in excellent agreement with our saturated UCCSD(T) result. We note that the spin contamination for the Au atom is small and equals 0.752. The fact that UHF+disp methods recover the minimum geometry proves the Au dimer to be bound mainly by dispersion forces.

The SAPT energy decomposition (Table X) elucidates the problem with the second-order induction contribution dominating the total interaction energy due to the overpolarization of monomers. Adding the $\delta E_{\mathrm{int}}^{\mathrm{HF}}$ term not only fails to reproduce the minimum region, but gives a repulsive potential (37.40 mH at $R_{\min}^e$)—a problem that has already been noticed in Ref. 59. It should also be noted that for both Cr and Au dimers the S^2 approximation performs much worse in case of SAPT combined with ECP method, with differences of the order of 10% for minimum geometries (see supplementary material[65]).

TABLE X. Interaction energy components at the minimum geometry of Au_2 ($^3\Sigma_u^+$), aug-cc-pVQZ + 3*s*3*p*2*d*2*f*. All energies in mH.

	SAPT(UHF)	SAPT(UKS)
$E_{\mathrm{elst}}^{(1)}$	−57.76	−53.22
$E_{\mathrm{elst}}^{(1)}$(CISD)	−57.53	
$E_{\mathrm{exch}}^{(1)}$	63.51	60.38
$E_{\mathrm{ind}}^{(2)}$	−408.9	−348.8
$E_{\mathrm{exch-ind}}^{(2)}$	218.4	202.4
$E_{\mathrm{disp}}^{(2)\ \mathrm{a}}$	−34.56	−47.12
$E_{\mathrm{disp}}^{(2)\ \mathrm{b}}$	−28.40	−26.93
$E_{\mathrm{exch-disp}}^{(2)}$	8.519	8.007
E_{int}	−204.4	−158.2
$E_{\mathrm{int}}^{\mathrm{UHF+disp(TDHF)}}$	−8.760	
$E_{\mathrm{int}}^{\mathrm{UHF+disp(TDDFT)}}$	−7.799	
$E_{\mathrm{int}}^{\mathrm{UCCSD}}$	−3.904	
$E_{\mathrm{int}}^{\mathrm{UCCSD(T)}}$	−6.664	

^{a}Uncoupled.
^{b}Coupled.

IV. CONCLUSIONS

We have developed and implemented a SAPT formalism based on the UKS treatment of monomers. Its performance has been tested for seven representative high-spin open-shell van der Waals complexes divided into three groups. The first group contained systems that provided comparison with the previously developed SAPT(ROKS) approach.[19] SAPT(UKS) has proven to be of similar accuracy as SAPT(ROKS) and compared well with the reference supermolecular CCSD(T) values. In all of the tested complexes the spin symmetry breaking was small and neither in the case of SAPT(UKS) nor in SAPT(UHF) did seem to affect the results.

For the first time SAPT(DFT) has been applied to spatially degenerate states. We have focused on systems with molecules in $^2\Pi$ electronic states interacting with rare gas atoms. SAPT(UKS) reproduced the minima on both A' and A'' surfaces, the interaction energies remaining in excellent agreement with the reference CCSD(T) values. For He$\cdots$OH we have also obtained excellent results for the angular dependence of interaction energy for both surfaces.

We have also studied Cr and Au dimers with SAPT combined with ECP. In both cases SAPT(UHF/UKS) performed poorly—a result which agrees with previous studies applying SAPT to metal dimers.[93,94] Because of poor performance of SAPT for metals, amplified by the use of ECPs, we applied a UHF+disp method with different treatments of dispersion. For Cr$_2$ ($^{13}\Sigma_g^+$) we obtained good agreement with RCCSD(T)/DK results, whereas for Au$_2$($^3\Sigma_u^+$) the UHF+disp(TDDFT) gave minimum with 14.5% overbinding.

The SAPT(UKS) and SAPT(ROKS) methods should be useful for modeling interactions in complexes of open-shell nature particularly those composed of main-group atoms, without the need to account for relativistic effects. To be applicable for larger systems the density-fitting procedure[47,95,96] would be desirable. More work is necessary to make SAPT compatible with effective core potentials and other treatments of relativity and thus applicable to heavier elements including metals.

[1] K. Liu and A. Wagner, *The Chemical Dynamics and Kinetics of Small Radicals* (World Scientific, 1995), Vol. 6.

[2] D. Skouteris, D. E. Manolopoulos, W. Bian, H. J. Werner, L. H. Lai, and K. Liu, Science **286**, 1713 (1999).

[3] M. Qiu, Z. Ren, L. Che, D. Dai, S. Harich, X. Wang, X. Yang, C. Xu, D. Xie, and M. Gustafsson *et al.*, Science **311**, 1440 (2006).

[4] M. C. Heaven, Annu. Rev. Phys. Chem. **43**, 283 (1992).

[5] M. C. Heaven, Int. Rev. Phys. Chem. **24**, 375 (2005).

[6] H. Kohguchi, T. Suzuki, and M. H. Alexander, Science **294**, 832 (2001).

[7] B. C. Sawyer, B. K. Stuhl, M. Yeo, T. V. Tscherbul, M. Hummon, Y. Xia, J. Kłos, D. Patterson, J. M. Doyle, and J. Ye, Phys. Chem. Chem. Phys. **13**, 19059 (2011).

[8] P. F. Weck and N. Balakrishnan, Int. Rev. Phys. Chem. **25**, 283 (2006).

[9] L. P. Parazzoli, N. J. Fitch, P. S. Żuchowski, J. M. Hutson, and H. J. Lewandowski, Phys. Rev. Lett. **106**, 193201 (2011).

[10] P. J. Dagdigian, "Experimental studies of rotationally-inelastic state-resolved collisions of small molecular free radicals" in Ref. 1, pp. 315–364.

[11] R. T. Skodje, D. Skouteris, D. E. Manolopoulos, S. Lee, F. Dong, and K. Liu, Phys. Rev. Lett. **85**, 1206 (2000).

[12] S. Aloisio and S. Joseph, Acc. Chem. Res. **33**, 825 (2000).

[13] A. Galano, M. Narciso-Lopez, and M. Francisco-Marquez, J. Phys. Chem. A **114**, 5796 (2010).

[14] J. Warnatz, U. Maas, and R. W. Dibble, *Combustion: Physical and Chemical Fundamentals, Modeling and Simulation, Experiments, Pollutant Formation* (Springer-Verlag, 2006).

[15] J. D. Savee, O. Welz, C. A. Taatjes, and D. L. Osborn, Phys. Chem. Chem. Phys. **14**, 10410 (2012).

[16] W. Klemperer, Proc. Natl. Acad. Sci. U.S.A. **103**, 12232 (2006).

[17] J. Kłos and F. Lique, Mon. Not. R. Astron. Soc. **418**, 271 (2011).

[18] M. Valko, D. Leibfritz, J. Moncol, M. T. D. Cronin, M. Mazur, and J. Telser, Int. J. Biochem. Cell Biol. **39**, 44 (2007).

[19] P. S. Żuchowski, R. Podeszwa, R. Moszyński, B. Jeziorski, and K. Szalewicz, J. Chem. Phys. **129**, 084101 (2008).

[20] G. Chałasiński and K. Szalewicz, Int. J. Quantum Chem. **18**, 1071 (1980).

[21] S. M. Cybulski, R. Burcl, G. Chałasiński, and M. M. Szczęśniak, J. Chem. Phys. **103**, 10116 (1995).

[22] S. M. Cybulski, G. Chałasiński, and M. M. Szczęśniak, J. Chem. Phys. **105**, 9525 (1996).

[23] G. Chałasiński and M. M. Szczęśniak, Chem. Rev. **100**, 4227 (2000).

[24] S. Atahan, J. Kłos, P. S. Żuchowski, and M. H. Alexander, Phys. Chem. Chem. Phys. **8**, 4420 (2006).

[25] Ł. Rajchel, P. S. Żuchowski, J. Kłos, M. M. Szczęśniak, and G. Chałasiński, J. Chem. Phys. **127**, 244302 (2007).

[26] P. S. Żuchowski, Chem. Phys. Lett. **450**, 203 (2008).

[27] H. Cybulski, P. S. Żuchowski, B. Fernandez, and J. Sadlej, J. Chem. Phys. **130**, 104303 (2009).

[28] L. M. C. Janssen, G. C. Groenenboom, A. van der Avoird, P. S. Żuchowski, and R. Podeszwa, J. Chem. Phys. **131**, 224314 (2009).

[29] K. Patkowski, B. Jeziorski, and K. Szalewicz, J. Chem. Phys. **120**, 6849 (2004).

[30] W. Skomorowski and R. Moszyński, J. Chem. Phys. **134**, 124117 (2011).

[31] M. Bartolomei, E. Carmona-Novillo, M. Hernández, J. Campos-Martínez, and R. Hernández-Lamoneda, J. Comput. Chem. **32**, 279 (2011).

[32] G. Murdachaew, M. Valiev, S. M. Kathmann, and X.-B. Wang, J. Phys. Chem. A **116**, 2055 (2012).

[33] T. V. Russo, R. L. Martin, and P. J. Hay, J. Chem. Phys. **101**, 7729 (1994).

[34] Z. Rinkevicius, I. Tunell, P. Salek, O. Vahtras, and H. Agren, J. Chem. Phys. **119**, 34 (2003).

[35] J. A. Pople, P. M. W. Gill, and N. C. Handy, Int. J. Quantum Chem. **56**, 303 (1995).

[36] O. V. Gritsenko, P. R. T. Schipper, and E. J. Baerends, Chem. Phys. Lett. **302**, 199 (1999).

[37] A. Heßelmann and G. Jansen, Chem. Phys. Lett. **357**, 464 (2002).

[38] M. Grüning, O. V. Gritsenko, S. J. A. Van Gisbergen, and E. J. Baerends, J. Chem. Phys. **114**, 652 (2001).

[39] R. van Leeuwen and E. J. Baerends, Phys. Rev. A **49**, 2421 (1994).

[40] M. Grüning, O. V. Gritsenko, S. J. A. van Gisbergen, and E. J. Baerends, J. Chem. Phys. **116**, 9591 (2002).

[41] J. Baker, A. Scheiner, and J. Andzelm, Chem. Phys. Lett. **216**, 380 (1993).

[42] J. Wang, A. D. Becke, and V. H. Smith, Jr., J. Chem. Phys. **102**, 3477 (1995).

[43] A. Cohen, D. Tozer, and N. Handy, J. Chem. Phys. **126**, 214104 (2007).

[44] J. G. C. M. van Duijneveldt-van de Rijdt and F. B. van Duijneveldt, Chem. Phys. Lett. **17**, 425 (1972).

[45] K. Szalewicz, K. Patkowski, and B. Jeziorski, in *Intermolecular Forces and Clusters, Structure and Bonding*, edited by D. J. Wales (Springer-Verlag, Heidelberg, 2005), pp. 43–117.

[46] R. Moszyński, B. Jeziorski, and K. Szalewicz, J. Chem. Phys. **100**, 1312 (1994).

[47] A. Hesselmann, G. Jansen, and M. Schütz, J. Chem. Phys. **122**, 014103 (2005).

[48] B. Jeziorski, M. Bulski, and L. Piela, Int. J. Quantum Chem. **10**, 281 (1976).

[49] H. L. Williams, E. M. Mas, K. Szalewicz, and B. Jeziorski, J. Chem. Phys. **103**, 7374 (1995).

[50] A. Heßelmann and G. Jansen, Chem. Phys. Lett. **367**, 778 (2003).

[51] S. Hirata and M. Head-Gordon, Chem. Phys. Lett. **302**, 375 (1999).

[52] A. J. Misquitta, R. Podeszwa, B. Jeziorski, and K. Szalewicz, J. Chem. Phys. **123**, 214103 (2005).

[53] H. C. Longuet-Higgins, Discuss. Faraday Soc. **40**, 7 (1965).

[54] A. J. Misquitta, B. Jeziorski, and K. Szalewicz, Phys. Rev. Lett. **91**, 33201 (2003).

[55] R. Moszyński, B. Jeziorski, S. Rybak, K. Szalewicz, and H. L. Williams, J. Chem. Phys. **100**, 5080 (1994).

[56] J. Kłos, P. Żuchowski, Ł. Rajchel, G. Chałasiński, M. Szczęśniak, J. Chem. Phys. **129**, 134302 (2008).

[57] M. Jeziorska, B. Jeziorski, and J. Čížek, Int. J. Quantum Chem. **32**, 149 (1987).

[58] K. Patkowski and K. Szalewicz, J. Chem. Phys. **127**, 164103 (2007).

[59] R.-F. Liu, C. A. Franzese, R. Malek, P. S. Żuchowski, J. G. Ángyan, M. M. Szczęśniak, and G. Chałasiński, J. Chem. Theory Comput. **7**, 2399 (2011).

[60] R. Ahlrichs, R. Penco, and G. Scoles, Chem. Phys. **19**, 119 (1977).

[61] J. P. Perdew, K. Burke, and M. Ernzerhof, Phys. Rev. Lett. **77**, 3865 (1996).

[62] C. Adamo and V. Barone, J. Chem. Phys. **110**, 6158 (1999).

[63] H.-J. Werner, P. J. Knowles, G. Knizia, F. R. Manby, and M. Schütz *et al.*, MOLPRO, version 2010.1, a package of *ab initio* programs, 2010, see http://www.molpro.net.

[64] D. J. Tozer and N. C. Handy, J. Chem. Phys. **109**, 10180 (1998).

[65] See supplementary material at http://dx.doi.org/10.1063/1.4758455 for brief description of geometries and decomposition of interaction energies.

[66] H. Cybulski, R. V. Krems, H. R. Sadeghpour, A. Dalgarno, J. Kłos, G. C. Groenenboom, A. van der Avoird, D. Zgid, and G. Chałasiński, J. Chem. Phys. **122**, 094307 (2005).

[67] T. H. Dunning, Jr., J. Chem. Phys. **90**, 1007 (1989).

[68] R. A. Kendall, T. H. Dunning, Jr., and R. J. Harrison, J. Chem. Phys. **96**, 6796 (1992).

[69] D. E. Woon and T. H. Dunning, Jr., J. Chem. Phys. **100**, 2975 (1994).

[70] F. M. Tao and Y. K. Pan, J. Chem. Phys. **97**, 4989 (1992).

[71] K. Patkowski, K. Szalewicz, and B. Jeziorski, J. Chem. Phys. **125**, 154107 (2006).

[72] H. S. Lee, A. B. McCoy, R. R. Toczyłowski, and S. M. Cybulski, J. Chem. Phys. **113**, 5736 (2000).

[73] G. Paterson, S. Marinakis, M. L. Costen, K. McKendrick, J. Kłos, and R. Toboła, J. Chem. Phys. **129**, 074304 (2008).

[74] K. P. Huber and G. Herzberg, *Constants of Diatomic Molecules* (Van Nostrand Reinhold, New York, 1979).

[75] S. M. Cybulski and R. R. Toczyłowski, J. Chem. Phys. **111**, 10520 (1999).

[76] A. Degli Esposti and H. J. Werner, J. Chem. Phys. **93**, 3351 (1990).

[77] J. Klos, G. Chałasiński, M. T. Berry, R. A. Kendall, R. Burcl, M. M. Szczęśniak, and S. M. Cybulski, J. Chem. Phys. **112**, 4952 (2000).

[78] A. Hoy, J. Johns, and A. McKellar, Can. J. Phys. **53**, 2029 (1975).

[79] G. C. Nielson, G. A. Parker, and R. T. Pack, J. Chem. Phys. **66**, 1396 (1977).

[80] M. H. Alexander, J. Chem. Phys. **99**, 7725 (1993).

[81] M. H. Alexander, J. Chem. Phys. **111**, 7426 (1999).

[82] O. V. Ershova and N. A. Besley, J. Chem. Phys. **136**, 244313 (2012).

[83] H. Cybulski and B. Fernández, J. Phys. Chem. A **116**, 7319 (2012).

[84] A. Griesmaier, J. Werner, S. Hensler, J. Stuhler, and T. Pfau, Phys. Rev. Lett. **94**, 160401 (2005).

[85] J. Stuhler, A. Griesmaier, T. Koch, M. Fattori, T. Pfau, S. Giovanazzi, P. Pedri, and L. Santos, Phys. Rev. Lett. **95**, 150406 (2005).

[86] J. M. L. Martin and A. Sundermann, J. Chem. Phys. **114**, 3408 (2001).

[87] M. Dolg, U. Wedig, H. Stoll, and H. Preuss, J. Chem. Phys. **86**, 866 (1987).

[88] P. Pyykkö, Chem. Soc. Rev. **37**, 1967 (2008).

[89] J. Muñiz, C. Wang, and P. Pyykkö, Chem. Eur. J. **17**, 368 (2011).

[90] D. Figgen, G. Rauhut, M. Dolg, and H. Stoll, Chem. Phys. **311**, 227 (2005).

[91] K. A. Peterson and C. Puzzarini, Theor. Chim. Acta **114**, 283 (2005).

[92] D. Danovich and S. Shaik, J. Chem. Theory Comput. **6**, 1479 (2010).

[93] K. Patkowski, R. Podeszwa, and K. Szalewicz, J. Phys. Chem. A **111**, 12822 (2007).

[94] E. R. Sayfutyarova, A. A. Buchachenko, M. Hapka, M. M. Szczęśniak, and G. Chałasiński, Chem. Phys. **399**, 50 (2012).

[95] E. G. Hohenstein and C. D. Sherrill, J. Chem. Phys. **133**, 014101 (2010).

[96] E. G. Hohenstein and C. D. Sherrill, J. Chem. Phys. **132**, 184111 (2010).

PART II:
Applications

CHAPTER 5

DFT approach to gold-ligand interactions

In this Chapter we devise a dependable computational DFT treatment of gold-ligand interactions of the donor-acceptor type. We begin with a general diagnosis of the difficulties one encounters when describing donor-acceptor interactions in the Kohn-Sham formalism. Then, we propose a way to overcome these problems within the Generalized Kohn-Sham framework. Our approach is verified using a model aurophilic dimer and a series of gold-ligand complexes. The results for the $(HAuPH_3)_2$ and Au_4-SCN^- complexes presented in this Chapter encompass my main contribution to the reported research. The Chapter closes with a publication complementing the presented results.

5.1 Introduction

A proper description of gold-ligand interactions is one of the key prerequisites for computational studies of gold chemistry. These interactions underlie self-assembly processes on gold surface as well as self-assembly of aurophilic compounds and ligand-protected gold nanoparticles [103, 104]. The ability to model these systems *ab initio* is intrinsically related with the ongoing quest for control over nanosized gold systems, including hetero- and homogeneous catalysis [105], fine-tuning of emissive properties [106] or

advances in sensing and plasmonics [107].

Gold-ligand interactions are donor-acceptor (DA) interactions, also known as charge transfer interactions: gold in various oxidation states acts as a Lewis acid, while the accompanying ligand takes the role of a Lewis base. As proven by numerous examples in the literature (see, e.g. Refs. [108–111]), the reliable description of DA interactions is a considerable challenge for DFT. The reason behind this may be traced back to crucial problems of DFT itself: the presence of the delocalization error [108, 110] and lack of long-range correlation effects [109].

One of the consequences of the DE is the discrepancy between the HOMO-LUMO (HL) gaps and the fundamental gap, the latter defined as the difference between the ionization potential (IP) and electron affinity (EA) of the molecule [43, 112]. While the HOMO electrons become too loosely bound with respect to IP, the LUMO orbitals are lying too low with respect to EA (see the right panel in Fig. 1.2). This clearly distorts the electron flow in DA interactions: the electron donors give off partial charge too easily, whereas electron acceptors, in turn, are too eager to accept one.

Although the equivalence of the HOMO-LUMO gap and fundamental gap can never be assured in the Kohn-Sham picture, it may be achieved in the Generalized Kohn-Sham scheme due to the presence of the nonlocal, orbital dependent exchange [43]. Moreover, it has been shown that minimization of DE in optimally-tuned LRC functionals is a practical way of restoring the physical meaning of orbital energies in DFT [43].

The aim of the work presented in this Chapter was to test the capability of the optimally-tuned LRC functionals to describe DA interactions in gold-ligand systems. We wanted to verify whether DE-free interaction energy would properly account for IP of the electron donor and EA of the electron acceptor. Our model complexes comprised the Au_4 cluster (with gold atoms at 0 oxidation state) interacting with a series of small ligands: thiocyanate, benzenethiol, benzenethiolate anion, pyridine, and trimethylphosphine (see Fig. 5.1). The modest size of the systems allowed to obtain reference values at CCSD(T) level of theory. Finally, we wanted to verify the role of the dispersion energy in gold-ligand interactions.
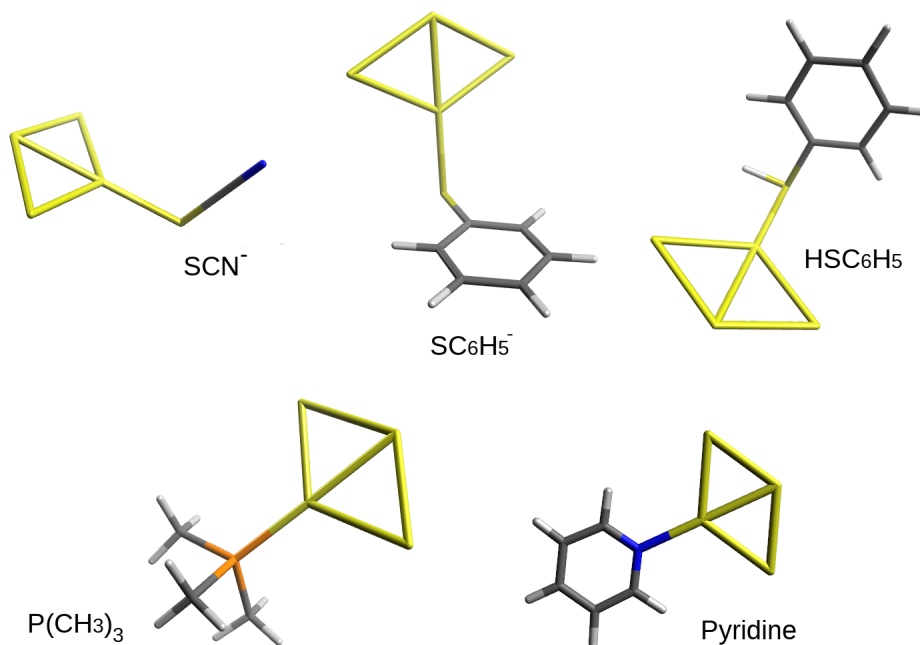
Figure 5.1: Geometries of the Au_4 complexes with five ligands: thiocyanate (SCN^-), benzenethiolate anion ($C_6H_5S^-$), benzenethiol (C_6H_5SH), pyridine (C_5H_5N) and trimethylphosphine ($P(CH_3)_3$).

5.2   Results

The idea of tuning the RS parameters for both donor and acceptor molecules brings us back to the problem of optimally-tuned functionals in supermolecular calculations (see Chapter 1, Sec. 1.2.1). Using different ω values for monomers would clearly violate size consistency, not to mention the question of choosing the proper value for dimer calculations. In order to avoid this, we proposed a two-step procedure employing functionals with a generalized error function ansatz (CAM). In the first step a two-parameter tuning is carried out separately for donor and acceptor molecules: the $J^2(\omega)$ functional (1.24) is minimized for six different values of the α parameter: 0.0, 0.1, 0.2, 0.3, 0.4, 0.5. This yields two classes of optimized functionals characterized by twelve sets of optimal (α, ω) parameters. For clarity, from now on we will refer to these functionals as LRC-ωPBEα. In the second step one chooses a parameter set common to both donor and acceptor, and consequently uses it for supermolecular calculations. In order to properly account for the missing long-rage dispersion contribution, we evaluated it through a $\frac{C_8}{R^8}$ term from the DFT-D3 method [113].

5.2.1   Aurophilic interactions

One may ask whether all optimized LRC-ωPBEα functionals predict identical interaction energies, in spite of different combination of the (α, ω) parameters. We address this question by examining an aurophilic homodimer of two HAuPH$_3$ molecules in a staggered configuration which excludes dipole-dipole interactions. The aurophilic interactions are weak noncovalent interactions classified "as the tendency of Au(I)-containing complexes to form short metal-metal contacts" [114]. As such, they constitute a challenge for correct description with DFT calculations [114, 115].

The interaction energies obtained with six different LC-ωPBEα are presented in Fig 5.2. We show that the results remain nearly constant irrespective not only of the optimized functional, but also of the intermolecular separation between the HAuPH$_3$ monomers – the observed discrepancies reach up to only 0.1 kcal/mol in the minimum region, and 3% on the repulsive wall. Furthermore, in Table 5.1 we present a comparison of our best performing LC-ωPBEα functional with the reference CCSD(T)/CBS results. As proven by Pyykkö and Zhao [116], the Hartree-Fock method misses the aurophilic stabilization and predicts the interaction to be solely repulsive. Our methodology shows that DE-free DFT already grasps at least some of the short-range intermolecular correlation and predicts -1.73 kcal/mol attraction between the monomers. This supplemented by a long-range dispersion contribution of -4.54 kcal/mol obtained by the C_8 term of the D3 method of Grimme [113] amounts to -6.27 kcal/mol which agrees well with the benchmark CCSD(T) value of -6.13 kcal/mol. As shown in the last column of Table 5.1, the dispersion energy from the LRC-SAPT method is clearly not compatible with the straightforward DE-free supermolecular approach. It is worthwhile to notice, that for this system B3LYP predicts an erroneous repulsive interaction of 1.6 kcal/mol.

Table 5.1: Interaction energy [kcal/mol] of the HAuPH$_3$ dimer at R = 3 Å separation calculated at different levels of theory.

HF	DFT (0.2,0.256)	Disp D3	DFT+D3	CCSD(T)/CBS	Disp DFT-SAPT
5.6	-1.73	-4.54	-6.27	-6.13	-13.0

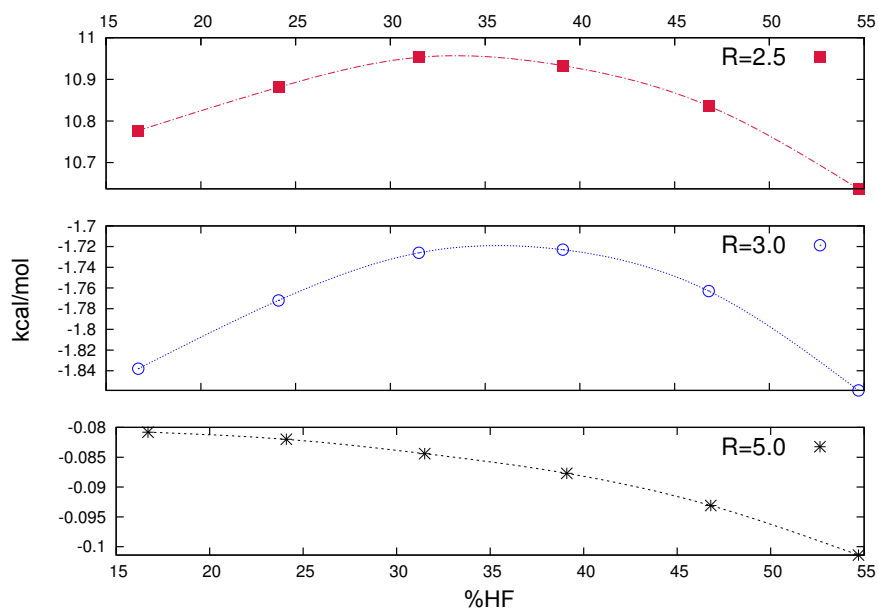Figure 5.2: Interaction energy [kcal/mol] of the $HAuPH_3$ dimer obtained with different OT-LRC functionals classified according to the total percent of the Hartree-Fock exchange. R denote different intermolecular distance between the $HAuPH_3$ monomers. Lines are added to guide the eye.
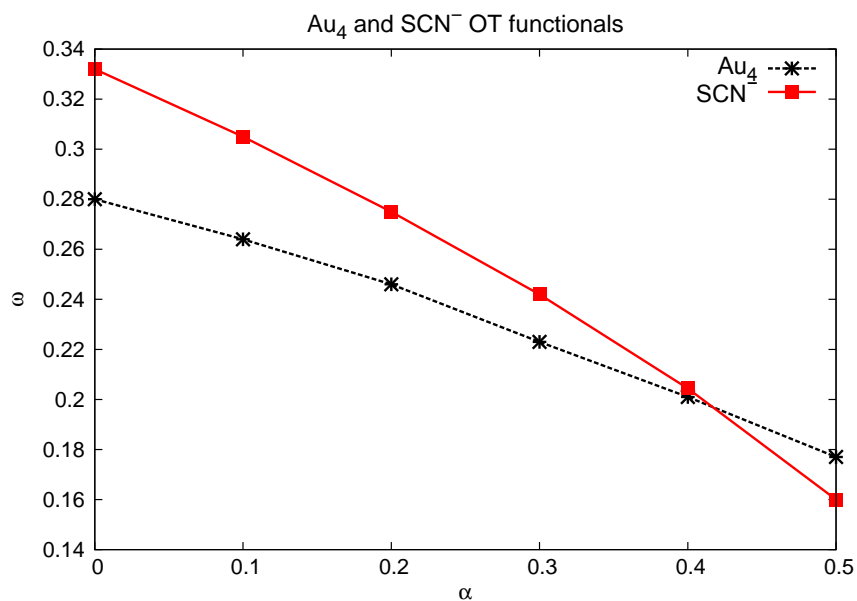

Figure 5.3: Optimized (α, ω) parameters for six $LC\omega PBE\alpha$ functionals for SCN^- (red) and Au_4 (black).

Table 5.2: Interaction energies [kcal/mol] and energy gaps [eV] between HOMO of SCN^- and LUMO of Au_4, denoted HO(D)-LU(A), for three LC-ωPBEα functionals.

(α, ω)	$(0.2, 0.275)$	$(0.3, 0.242)$	$(0.4, 0.204)$
E_{int}	-47.6	-47.1	-46.7
HO(D)-LU(A)	1.77	1.75	1.72
DFT + D3	-51.3	-50.8	-50.4
CCSD(T)		-52.9	

5.2.2 Optimized functionals of gold cluster-ligand complexes

Having validated the method for a representative Au(I)-Au(I) system, we now move to the model gold(0)-ligand complexes of donor-acceptor character. Herein we will focus on the Au_4-SCN^- dimer and follow the steps of the proposed supermolecular procedure. First, we carried out two-parameter optimization obtaining two classes of LC-ωPBEα functionals, presented in Fig 5.3. We then selected three functionals sharing a similar range of (α, ω) parameters. Their performance is compared in Table 5.2. We observe that the common range of the tuning parameters guarantees stable interaction energies, which – supplemented with dispersion energy from the D3 model – remain in close proximity to the benchmark CCSD(T) result. Moreover, the steady energy gap between HOMO of the donor and LUMO of the acceptor indicates that both IP of the donor and EA of the acceptor are correctly represented.

Fig. 5.4 summarizes the results obtained with the LRC-ωPBEα functionals for Au_4 interacting with five different ligands. A 3-5% agreement with the reference CCSD(T) values confirms that GKS is capable of a reliable description of charge transfer interactions, provided that the frontier molecular orbitals of the donor and acceptor molecules are conditioned to have physical interpretation matching their IP and EA, respectively. The results also show that adding the dispersion energy term on top of the DE-free energy is necessary to achieve a satisfactory agreement. However, the dispersion energy contribution to the binding is moderate in the selected system and reaches from 5% to 15%.
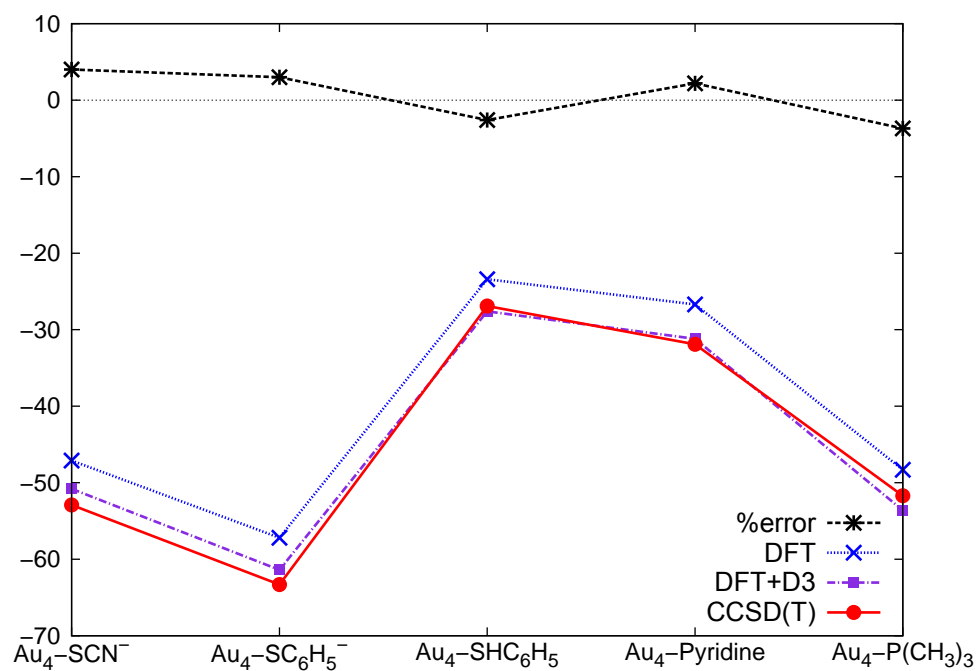
Figure 5.4: Interaction energies [kcal/mol] between Au_4 and five ligands with optimized LRC-ωPBEα functionals and CCSD(T). The %error stands for percentage error of the DFT-D3 method calculated as $\frac{E_{\text{CCSD(T)}} - E_{\text{DFTD3}}}{E_{\text{CCSD(T)}}} \times 100\%$

5.3   Related publication

The attached publication [D3] provides further insight into the nature of the studied complexes. Calculations with LDA, BP86, PBE0 reveal possible problems of the conventional approach resulting from wrong balance of the donor/acceptor properties. Furthermore, the consequences of the strong gold-benzenothiolate bonding are analyzed. Likewise, the difference in bonding of pyridine and trimethylphosphine to Au_4 is explained.

Density functional theory approach to gold-ligand interactions: Separating true effects from artifacts

Jessica V. Koppen,[1] Michał Hapka,[2] Marcin Modrzejewski,[2] Małgorzata M. Szczęśniak,[1,a)] and Grzegorz Chałasiński[2,1]
[1]*Department of Chemistry, Oakland University, Rochester, Michigan 48309, USA*
[2]*Faculty of Chemistry, Warsaw University, Pasteura 1, 02-093 Warszawa, Poland*

Donor-acceptor interactions are notoriously difficult and unpredictable for conventional density functional theory (DFT) methodologies. This work presents a reliable computational treatment of gold-ligand interactions of the donor-acceptor type within DFT. These interactions require a proper account of the ionization potential of the electron donor and electron affinity of the electron acceptor. This is accomplished in the Generalized Kohn Sham framework that allows one to relate these properties to the frontier orbitals in DFT via the tuning of range-separated functionals. A donor and an acceptor typically require different tuning schemes. This poses a problem when the binding energies are calculated using the supermolecular method. A two-parameter tuning for the monomer properties ensures that a common functional, optimal for both the donor and the acceptor, is found. A reliable DFT approach for these interactions also takes into account the dispersion contribution. The approach is validated using the water dimer and the $(HAuPH_3)_2$ aurophilic complex. Binding energies are computed for Au_4 interacting with the following ligands: SCN^-, benzenethiol, benzenethiolate anion, pyridine, and trimethylphosphine. The results agree for the right reasons with coupled-cluster reference values. © *2014 AIP Publishing LLC*. [http://dx.doi.org/10.1063/1.4885137]

I. INTRODUCTION

Interactions of gold clusters and surfaces with ligands are of great interest to chemistry for several reasons. These interactions are the key to the self-assembly of ligand-protected gold nanoparticles.[1,2] Ligand-protected gold nanoparticles are intensely investigated for their potential uses in sensing and plasmonics.[3] These interactions are also crucial to the unique catalytic properties of gold: e.g., in heterogeneous catalysis by nano-sized gold[4] and in homogeneous catalysis by gold compounds.[5] Finally, there is a need for the fundamental understanding of the rapidly developing field of the coordination chemistry of gold.[6,7] Study of gold-ligand interactions are the key to this understanding.

Gold-ligand interactions are examples of donor-acceptor (DA) interactions, sometimes referred to as charge transfer (CT) interactions, where gold in many oxidation states acts as Lewis acid and ligands mainly act as Lewis bases. Of course, it is possible for these roles to reverse.[8]

From the outset these interactions are surrounded by controversy regarding the necessity for and the meaning of the charge-transfer term in the partitioning of the interaction energy into physically meaningful components. For example, the symmetry-adapted perturbation theory (SAPT) has "no room" for the CT term[9] although there have been recent attempts to make such an accommodation.[10,11] Other partitioning schemes[12,13] distinguish between the polarization and charge-transfer contributions (the latter are sometimes referred to as orbital contributions). In the Reed and Wein-

hold scheme the CT terms are larger than the total interaction energies.[14]

There is considerable literature evidence that conventional density functional theory (DFT) methods have difficulties in dealing with DA interactions be it in main-group or in transition metal chemistry. A variety of causes for these problems have been presented in the literature. To name just a few, the Yang group pointed to localization error in common functionals as the reason behind large errors in thermochemistry of Diels-Alder cyclization and dimerization of Al complexes.[15] In a similar vein, Goerigk and Grimme constructed a separate database of test systems where the self-interaction error (SIE) is expected to be the problem.[16] Typical DA complexes ethylene-F_2 and NH_3-ClF figure prominently in this database. In a paradigm photovoltaic system, TTF-TCNQ, Sinni *et al.* brought to the fore the importance of the energy gaps between HOMO of the electron donor and LUMO of the electron acceptor to interactions and charge transfer in DA complexes.[17] They also identified another source of uncertainty in interaction results – the choice of an exchange functional. HOMO-LUMO gaps narrow considerably in complexes of base-donor and radical-acceptor, thereby exacerbating the problem of erroneous charge transfer in the ground state, as the work of Johnson *et al.* noted.[18] They attributed this problem to the lack of piecewise linearity of DFT energy of both donor and acceptor with respect to an addition and removal of fractional electrons.[19] The implications of SIE on the charge flow across the metal-ligand DA interface have been extensively discussed[20,21] (and references therein).

Steinmann *et al.* took a different view by arguing that the reason why DA interactions are challenging for the DFT

a)E-mail: bryant@oakland.edu

is that it does not properly account for dispersion.[22] While the importance of dispersion is unquestionable in π-π stacking DA interactions,[23,24] in DA complexes involving the σ*-acceptor halogen molecules Kozuch and Martin found that the addition of dispersion was not critical.[25] Our own results show that in addition to dispersion it is the many-electron SIE in conventional DFT methods artificially altering the donating and accepting abilities that contribute to the problem.[26]

In such circumstances a typical literature response is to examine dozens of different functionals for a particular type of interaction and recommend those that agree best with a benchmark of some sort. For metal-ligand complexes this strategy often results in some eye-popping spreads of binding energies. For example, Seth *et al.*[27] show wide variations in the binding energy of phosphine to the Grubbs II catalyst (Ru metal center): from 1/10 (BLYP[28]) to 1/2 (PBE0[29]) to a bizarre four times (LC-M06L) the experimental estimate. A several-functional compilation for AuCO[30] provides binding energies from 1/3 (M06-2X[31]) to 3/2 (PBE0) to over twofold overbinding by the favorites of the gold community: BP86,[32,33] PBE,[34] and PW91.[35] A similar, albeit narrower, comparison for Au-methylthiol[36] shows twofold disparity between PW91 (PBE) and B3LYP.[37] Arguably, with such uncertainty on every rung of DFT, the structural and energetical predictions of ligand protected gold nanoparticles could vary from functional to functional. Indeed, Häkkinen *et al.* observed that PBE and BLYP lead to different structures of $Au_{38}(SCH_3)_{24}$.[38] The predictions for ligand exchange reactions may also suffer. Therefore, benchmarking of these interactions with trustworthy methods is needed.

There are several reasons for the problems with computing gold-ligand DA interactions. The first one concerns a proper description of electron affinity (EA) and ionization potential (IP) of the acceptor and donor molecules.[39] Inaccuracies in the computational treatment of these quantities, such as, neglecting relativistic effects or insufficient account of correlation, particularly for gold, could lead to order of magnitude differences in binding energy. The second reason originates from the DFT treatment of these quantities (and is not specific to gold-ligand complexes). In an approximate Kohn-Sham (KS) scheme IP and EA are not related to KS frontier eigenvalues and often the magnitude of HOMO energy of the donor is smaller than its IP and the magnitude of LUMO energy of the acceptor is larger than its EA.[40] This mismatch alters a flow of charge between a donor and acceptor and poses a serious limitation on the application of DFT to metal-molecule interfaces.[20] An equivalent view of this problem involves a delocalization error, that is, the nonlinearity of DFT energy between the integer numbers of electrons.[41]

The Generalized Kohn-Sham (GKS) formalism involving range-separated hybrid functionals may help ameliorate some of these problems. The presence of nonlocal, orbital dependent exchange via the range-separation helps the HOMO and LUMO eigenvalues to acquire the meaning of IP and EA, respectively, and aids in absorbing the derivative discontinuity.[42] An optimal choice of the distance at which the long range is to commence may include setting the value of range separation parameter to satisfy the condition that a negative of the HOMO energy (ε_{HOMO}) equals IP[43] or evalu-

ating the average distance between an outer electron and its exchange hole.[44] Such tuning leads to two desirable properties of a functional: HOMO and LUMO of the GKS scheme become the IP and EA, respectively, and the functional gains the piecewise linear dependence with respect to fractional electrons. As the added benefit, the exchange-correlation (xc) potential acquires the proper asymptote. The tuning strategy dramatically improves the quality of CT excitations.[43] In this work we intend to show that it could be equally effective for the ground-state interactions involving partial electron transfer from a donor to an acceptor.

Our second aim is to apply the ideas of optimized range-separated functionals to the computations of gold-ligand interactions which are uncontaminated by what Johnson *et al.* call an artificial charge transfer.[18] Our models are sufficiently small to be validated by coupled-cluster singles, doubles, and perturbative triples (CCSD(T)) computations and include the interaction of Au_4 with common ligands such as pyridine, trimethylphosphine, SCN^-, and benzenethiolate and benzenethiol. They are representative of species used in the functionalization of gold clusters and surfaces. The aurophilic interactions,[6] important ingredients of the nanoparticle protection, will also be revisited in this context.

There exists substantial DFT (see Refs. 38 and 45–48 and references therein) and *ab initio*[49,50] literature on the subject of these and related interactions. The comparison of our results with these previous data will be discussed below.

II. COMPUTATIONAL DETAILS

The functionals used in the present work employ the range separation of the general form:

$$\frac{1}{r_{12}} = \frac{[\alpha + (1-\alpha)erf(\omega r_{12})]}{r_{12}} + \frac{(1-\alpha)erfc(\omega r_{12})}{r_{12}}, \quad (1)$$

where erf and erfc stand for the error function and its complement, and ω is the range separation parameter. This expression partitions the total exchange energy into short-range and long-range contributions. α defines the constant fraction of HF exchange in the short range. The functional employed in this work is composed of PBE correlation and the short-range exchange ωPBE based on Henderson, Janesko, and Scuseria (HJS) model of the exchange hole.[51] The choice of the DFT exchange functional is important in the context of DA interactions.[17] Too repulsive an exchange, such as B88,[32] makes interaction potentials too shallow, whereas an insufficiently repulsive one, such as PBE, makes interaction potentials artificially deep.[52,53] The exchange functional ωPBE based on HJS exchange hole is one of the most reliable in this regard.[54]

A two-parameter tuning[55] of this functional involves the optimization of ω to minimize the condition that $-\varepsilon_{HOMO}$ equals the (vertical) ionization potential[56]

$$J^2(\omega) = \min_\omega (E(N-1) - E(N) + \varepsilon_{HOMO})^2 \quad (2)$$

for six different values of $\alpha = 0.0, 0.1, 0.2, 0.3, 0.4, 0.5$. A similar family of optimized functionals was previously proposed in Refs. 57 and 58 recently employed in Ref. 59 Condition (2) imposes Janak's theorem that the exact functional

TABLE I. Water dimer DFT interaction energies without, E_{int}(DFT), and with D3 dispersion contribution (in kcal/mol) for the family of six LRC-ωPBEα optimized functionals (equilibrium geometry from Ref. 71; CP corrected values).

α	0	0.1	0.2	0.3	0.4	0.5
ω	0.503	0.457	0.408	0.351	0.285	0.207
%HF exchange	27.3	32.8	38.4	44.2	50.1	56.3
E_{int}(DFT)	−4.554	−4.552	−4.570	−4.613	−4.695	−4.830
E_{int}(DFT+D3)[a]	−5.09	−5.09	−5.10	−5.15	−5.23	−5.36
$1/\omega$ (Å)	1.052	1.158	1.297	1.508	1.857	2.556

[a]Equilibrium geometry dispersion contribution $E_{disp(8)}$ equals −0.533 kcal/mol.

satisfies.[60] The functionals will be denoted LRC-ωPBEα. The parameter ω, and indeed α as well, are system specific. This may create a problem for two different subsystems with different donor-acceptor abilities. The family of optimized functionals increases the likelihood that there will exist a parameter set common to both subsystems.

The optimized LRC-ωPBEα functionals can also be characterized (and referred to) by the *total* percent contribution of HF exchange, i.e., originating from both the short and the long-range, in the exchange energy. Such a contribution can be computed for a given geometry by performing three computations: first with the full functional and saving the vectors, then switching off the DFT and the HF exchange, respectively, and performing no-SCF calculations with the saved vectors.

A DFT interaction energy lacks the long-range dispersion component. It was computed through the C_8/R^8 term from the DFT-D3 approach of Grimme and coworkers[61] and denoted $E_{disp(8)}$. We used the same D3 parameters as for LC-ωPBE functional[62] of Vydrov and Scuseria. This choice has been justified in our recent work.[63]

All calculations employed aug-cc-pVTZ basis set[64] or its equivalent aug-cc-pVTZ-PP, which in the case of Au, combined the 19-electron effective core potential of Figgen *et al.*[65] with valence basis set of Peterson and Puzzarini[66]– all denoted avtz. Our CCSD(T) calculations were performed in the same avtz basis set as DFT except for one instance: In the complete basis set extrapolation (CBS) of (AuH-PH$_3$)$_2$ where both avtz and aug-cc-pVQZ (avqz) calculations were needed for the expression of Halkier *et al.*,[67]

$$E_{corr,\text{CBS}} = \frac{X^3}{X^3 - (X-1)^3} E_{corr,X}$$
$$- \frac{(X-1)^3}{X^3 - (X-1)^3} E_{corr,X-1}, \qquad (3)$$

where E_{corr} refers to CCSD(T) correlation energy and $X = 4$. The HF component of the CBS interaction energy was obtained without extrapolation in the avqz basis set.

The interaction energies were computed via the supermolecular method with the counterpoise correction (CP)[68] while holding the monomer geometries rigid. The monomer geometries of ligands were optimized using the B3LYP functional. The geometry of Au$_4$ was optimized within LC-ωPBE functional of Vydrov and Scuseria.[62] The calculations were performed using NWChem[69] and MOLPRO[70] program suites.

III. RESULTS AND DISCUSSION

A. The water dimer

To test the idea of tuned functionals for their suitability to provide interaction energies we first consider the water dimer since H$_2$O can be both an electron donor and acceptor. Other motivation stems from the recent observation of Ziegler, Grimme, and coworkers that the employment of range separation in the water dimer can lead to erratic results in the computed interaction energies.[27]

Table I shows the variations of the interaction energy with the optimized LRC-ωPBEα functionals. E_{int}(DFT+D3) values are very reasonable given the consensus value is −5.0 kcal/mol.[72] The variations in E_{int}(DFT) are very small in a wide range of the parameter space, e.g., its value varies only by 0.05 kcal/mol between $\alpha = 0$, $\omega = 0.503$ and $\alpha = 0.3$, $\omega = 0.351$. Furthermore, E_{int}(DFT) remains virtually independent of the total percentage of HF exchange (%HF) up to about 50%. Above that, the interaction energy begins to drop. This drop at larger %HF and small values of ω may have two causes: (i) $1/\omega$, i.e., the range of interaction described by the short-range exchange, becomes comparable with the length of the hydrogen bridge H—O; (ii) too high percentage of HF exchange may upset the balance between exchange and correlation within the functional. The main conclusion of this comparison is that with the help of optimized LRC-ωPBEα functionals we can obtain interaction energies which are nearly constant in a broad range of α and ω parameter space. Such interaction energies are free from delocalization error and remain physically sensible as long as the percentage of HF exchange (or $1/\omega$) is not too large.

B. Aurophilic interactions

To determine how these ideas apply to gold, as our second test case, we examine an aurophilic dimer of two HAu-PH$_3$ subunits arranged in a configuration that precludes electrostatic dipole-dipole interactions (Fig. 1(a)). There has been great deal of discussion in the literature about the origin of the aurophilic attraction attraction,[6,73–77] and to what degree DFT can be trusted in reproducing it. Other motivation follows from the work of Werner and collaborators who demonstrated the importance of ionic charge-transfer-type configurations in aurophilic bonding.[78]

The interaction energies for the aurophilic dimer are shown in Table II for the six optimized functionals. The E_{int}
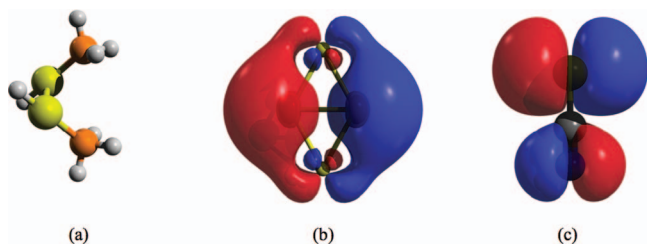
FIG. 1. (a) Configuration of aurophilic dimer (AuH-PH$_3$)$_2$. Geometry parameters are the same as in Ref. 76; (b) LUMO orbital of Au$_4$ (D$_{2h}$) is centered on two Au atoms on the shorter axis of the rhombus; (c) HOMO orbital of SCN$^-$.

TABLE III. Values of ω for the optimized LRC-ωPBEα functionals for Au$_4$ and for the five ligands.

			ω			
α	Au$_4$	SCN$^-$	SC$_6$H$_5^-$	SHC$_6$H$_5$	Pyridine	P(CH$_3$)$_3$
0	0.280	0.332	0.250	0.283	0.334	0.292
0.1	0.264	0.305	0.226	0.261	0.293	
0.2	0.246	0.275	0.200	0.236	0.250	0.242
0.3	0.223	0.242	0.171	0.208	0.216	
0.4	0.201	0.2044	0.134	0.177	0.183	
0.5	0.177	0.160	0.099	0.141	0.144	

values evaluated at the repulsive wall (R = 2.5 Å), near the minimum (R = 3.0 Å) and in the long range (R = 5.0 Å) remain nearly constant, to within 0.1 kcal/mol in the minimum, and to 3% on the repulsive wall. Let us recall that at the HF level the interaction is purely repulsive.[73] The present results show that the interaction energy, free from delocalization and BSSE errors, is *attractive* thus indicating the presence of a short-range intermolecular correlation contribution. The interaction energy still lacks the long-range dispersion contribution. This is estimated from D3 method of Grimme[61] to be −4.80 kcal/mol bringing the total binding energy to a reasonably good agreement with the CCSD(T) benchmark value of −6.13 kcal/mol. By comparison, Johnson's value of DFT+disp equals −5.59 kcal/mol.[77]

The frontier orbital energies of the HAu-PH$_3$ monomer and the HOMO-LUMO gap (E$_{LH}$), shown as a function of %HF in the optimized functionals, remain constant (see Fig. S1 in supplementary material). Upon the interaction, E$_{LH}$ narrows somewhat (by ∼1.3 eV at the minimum) and it too remains fairly constant as %HF increases (see Table II).

C. Optimized functionals of gold cluster-ligand complexes

The parameters for the six optimized LRC-ωPBEα functionals for Au$_4$ and five ligands are presented in Table III. Although the optimized parameters for Au$_4$ and the ligands are not the same, as required by the supermolecular method, there exists in each case an α and ω combination which is common or nearly so for Au$_4$ and each of the ligands.

The dependence of these functionals on fractional numbers of electrons in Au$_4$ is shown in Fig. 2. Functionals PBE0 and BP86 are included for comparison. It is seen that the optimized functionals show practically indistinguishable performance.

Figure 3 displays the eigenvalue variations of Au$_4$ (top) and SCN$^-$ (bottom) with optimized functionals. The two sets present an interesting contrast between molecules consisting of transitions metals and these of main-group atoms. In Au$_4$ only the three upper orbitals appear distinct while the lower, chiefly d-composed eigenvalues, form a band-like structure. By contrast, in SCN$^-$ the occupied orbitals are well separated (apart from degeneracy). In SCN$^-$ several occupied orbitals remain constant, whereas in Au$_4$ only the frontier orbitals remain so and the inner ones slope down as the functionals acquire more HF exchange (see. Refs. 57 and 58 for similar observations). The frontier orbitals, HOMO of the donor and the LUMO of the acceptor, are separated by a very small energy gap of ∼1.5 eV, so one expects a strong interaction.

D. Interaction energies of organo-sulfur ligands

SCN$^-$ ligand is a soft base which binds to a soft acid via its S end. The orientation of the monomers in the complex is determined by mutual alignment of high-lying HOMO of SCN$^-$ (π* maximally extended at S) and low-lying LUMO of Au$_4$ (see Figs. 1(b) and 1(c)). Consequently, the SCN$^-$ fragment and the other sulfur ligands are nearly perpendicular to the plane of Au$_4$. The interaction energies are shown in Table IV. The monomers were held fixed at their geometries and only the intersystem parameters R and θ were roughly

TABLE II. DFT interaction energies for (HAu-PH$_3$)$_2$ aurophilic dimer (in kcal/mol) in six optimized LRC-ωPBEα functionals (geometry from[78,76]; avtz basis set) at indicated distances. Values in parentheses include the D3 dispersion term. E$_{LH}$ (in eV) denotes the dimer HOMO-LUMO gap; R denotes Au-Au distance (in Å).

α	0.0	0.1	0.2	0.3	0.4	0.5
ω	0.303	0.282	0.256	0.231	0.2	0.164
%HF	16.7	24.1	31.5	39.1	46.8	54.7
E$_{int}$ (R = 2.5)	10.777	10.881	10.953	10.933	10.836	10.637
E$_{int}$ (R = 3)[a]	−1.838	−1.772	−1.726	−1.723	−1.763	−1.859
	(−6.64)	(−6.57)	(−6.53)	(−6.52)	(−6.56)	(−6.66)
E$_{HL}$ (R = 3)	8.11	8.11	8.09	8.09	8.08	8.06
E$_{int}$ (R = 5)	−0.0808	−0.0820	−0.0844	−0.0877	−0.0931	−0.1014

[a]Dispersion energy E$_{disp(8)}$ from D3[61] at this distance amounts to −4.80 kcal/mol. The CCSD(T)/CBS is −6.13 kcal/mol.
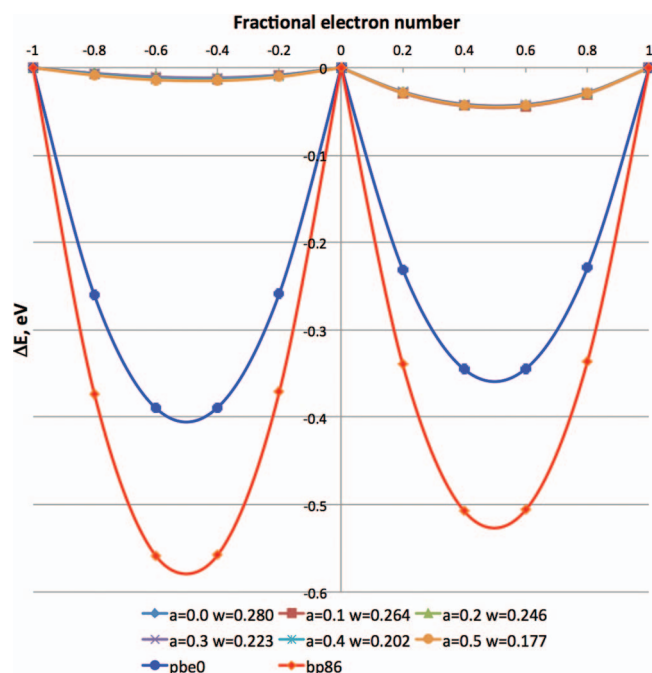
FIG. 2. The departure from the linear behavior of six optimized functionals, PBE0, and BP86 for Au$_4$. The left-most and the right-most sides represent the cation and the anion, respectively.

FIG. 3. Dependence of eigenvalues upon optimized functional: (top) in Au$_4$ (bottom) in SCN$^-$; MOs 15 and 14 are degenerate π^* HOMO orbitals.

optimized,[80] where R is the Au-S distance and θ denotes the angle between the shorter axis of Au$_4$ and S-C.

For the Au$_4$-SCN$^-$ interaction, Table IV shows the results for three LRC-ωPBEα functionals where the parameters for the donor and acceptor roughly overlap. The purpose of this comparison is to demonstrate that the results are fairly independent of the choice of optimized functional. Indeed, the binding energies remain stable with respect to the functional, similarly to the case of the water dimer (Table I). The interaction of this strength induces changes in electron density which manifests themselves in the opening of the HOMO-LUMO gap and a partial charge transfer from SCN$^-$ to Au$_4$ of 0.44e, according to Mulliken population analysis.

Let us assume for a moment that one electron is fully transferred to Au$_4$. In Au$_4^-$ one can isolate the interaction energy between one Au (^{2}S) atom on the shorter diagonal with
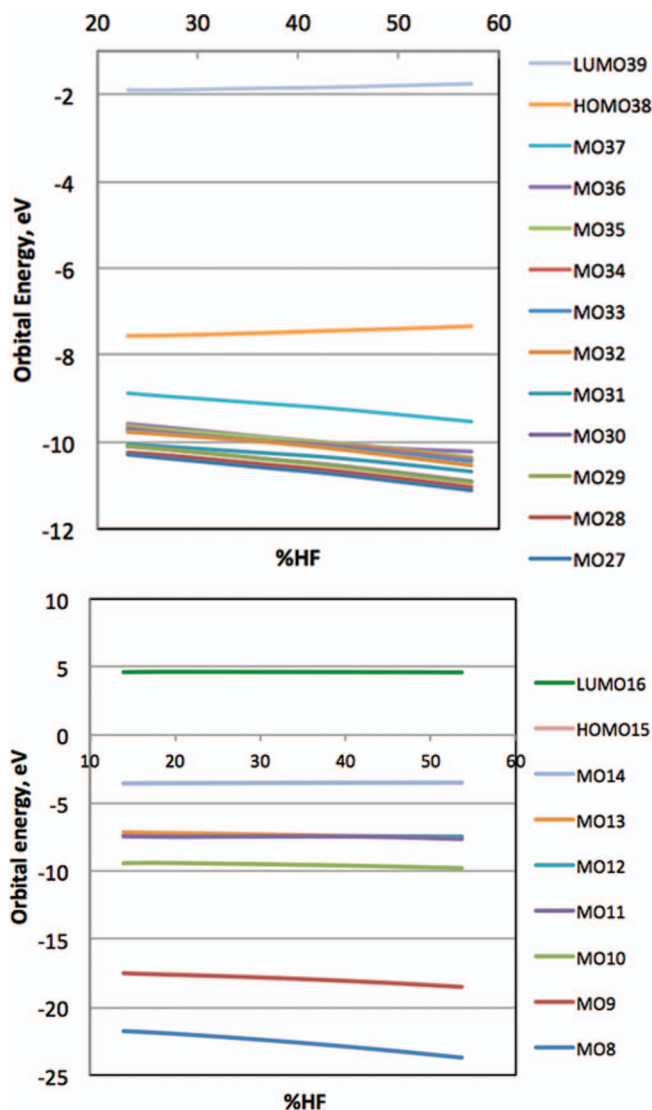
the Au$_3^-$, all considered in the geometry of Au$_4$. Such E$_{int}$ computed with TPSS/avtz amounts to -47.3 kcal/mol, i.e., the value closely resembling the interaction energy between Au$_4$ and SCN$^-$ in Table IV. The binding of S-C$_6$H$_5^-$ is some

TABLE IV. Interaction energies (kcal/mol) between Au$_4$ and five ligands with optimized LRC-ωPBEα functionals and CCSD(T). Orbital gaps are in eV. (R, θ) describes the intersystem geometry. D3 dispersion energy values are evaluated through the C$_8$ term (E$_{disp(8)}$).

Dimer (R, θ)	Functional				Interaction energy			
	α	ω	HO(D)-LU(A)	E$_{LH}$	DFT	CCSD(T)	E$_{disp(8)}$	DFT+disp
Au$_4$-SCN$^-$ (2.4, 105°)	0.2	0.275	1.77	5.93	-47.6	-52.9	-2.7	-50.3
	0.3	0.243	1.75	5.88	-47.1			-49.8
	0.4	0.2044	1.72	5.82	-46.7			-49.4
Au$_4$-SC$_6$H$_5^-$ (2.42, 100°)	0.0	0.250	0.27	5.45	-57.2	-63.3[a]	-4.2	-61.4
Au$_4$-SHC$_6$H$_5$ (2.48, 102°)	0.0	0.283	6.50	7.07	-23.7	-26.9[a]	-4.2	-27.9
	0.1	0.261	6.50	7.03	-23.4			-27.6
Au$_4$-pyridine (2.2, 0°)	0.2	0.250	7.88	6.23	-26.7	-31.9	-3.8	-30.5
Au$_4$-P(CH$_3$)$_3$ (2.3, 0°)	0.2	0.242	6.57	6.39	-48.3	-51.7	-5.3	-53.6

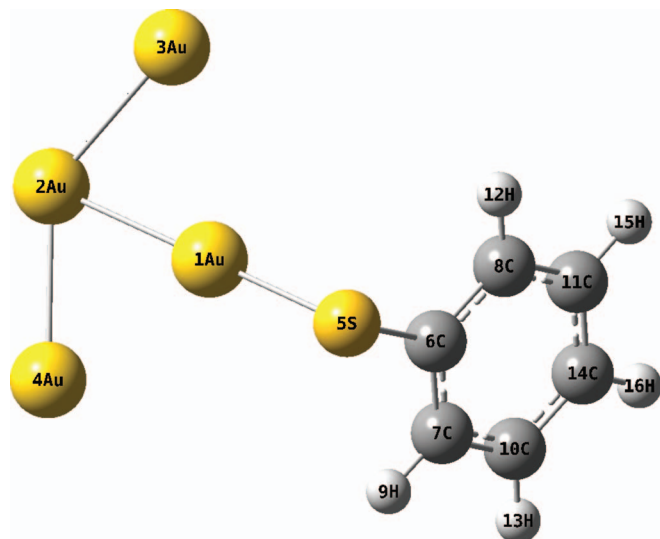[a]Calculation with frozen Au 5s orbitals; other systems include Au 5s in active space in CCSD(T).

FIG. 4. The relaxed geometry of the Au_4-$SC_6H_5^-$ complex: the distances are: S-Au1 = 2.309 Å, Au1-Au2 = 2.623 Å, Au1-Au4 = 2.905 Å, Au2-Au4 = 2.582 Å. The complex shows incipient separation into two units, Au_3^- + $AuSC_6H_5$.

10 kcal/mol stronger still. One can expect that such an interaction is capable of pulling out an Au atom from the Au_4 cluster. Indeed, as the geometry of Au_4-$SC_6H_5^-$ is allowed to fully relax, the complex begins to split into Au_3^- and Au-SC_6H_5 subunits (see Fig. 4). The ability of thiolates to etch Au atoms[38] or even a monoatomic nanowire[81] from Au_n clusters has been shown in the literature.

The neutral benzenethiol (PhSH) provides interesting context for the interactions of thiolates. The bonding between PhSH and Au_4 in two optimized functionals shows to be of intermediate strength (23.7–23.4 kcal/mol) with 4.2 kcal/mol coming from the D3 dispersion. This is again a complex in which thiol acts as an electron donor and gold as an acceptor. Although PhSH has been observed adsorbed on gold surface,[82] there is also a prevailing view that S-containing ligands are electron acceptors from gold (see, e.g., Ref. 38, 83). Let us examine if the full electron transfer is possible from Au_4 to PhSH. The energy gap to overcome would involve LUMO(thiol)-HOMO(Au_4) of 0.4 eV + 7.6 eV = 8 eV. This energy gap is certainly larger than LUMO(Au_4)-HOMO(thiol) of −1.9 eV + 8.4 eV = 6.5 eV. The energy balance in the first scenario can be partially offset by 5.8 eV originating from the interaction of ion pair separated by 2.48 Å, but this still leaves a 2.2 eV deficit. This scenario also calls for the formation of metastable $PhSH^-$ in a dissociative state PhS^- + H. We conclude that in the Au_4 + PhSH complex the thiol molecule can only act as an electron donor. To make it an electron acceptor would require a gold cluster with much lower IP (e.g., Au_n, n-odd, have lower IPs) or the dissociation of S-H. The latter issue has been extensively discussed in the literature.[36,45,47,46,82]

A less convoluted explanation takes into account that electrons tend to flow from a region of high chemical potential (low electronegativity) to a region of low chemical potential (high electronegativity). Both of these quantities are well defined within DFT.[84] The electronegativity $\chi = \frac{1}{2}$ (IP+EA)

= $-\mu$ can be described in the context of GKS using the HOMO and LUMO eigenvalues. The values listed above yield $\chi(Au_4)$ = 4.7 eV and χ(PhSH) = 4.4 eV, thus, indicating the direction of charge flow from PhSH to Au_4.

E. Interactions of pyridine and $P(CH_3)_3$ with Au_4

The remaining results in Table IV refer to the complexes of Au_4 with pyridine and trimethylphosphine. θ represents the angle between the short axis of Au_4 and the $C_2(C_3)$ axes of the ligands. Pyridine binds to Au_4 in the coplanar fashion and $P(CH_3)_3$ in a co-axial one. The optimized LRC-ωBPEα functionals for both complexes feature $\alpha = 0.2$. At this DFT level the interaction energy of pyridine is −26.7 kcal/mol, whereas that of $P(CH_3)_3$ is 21.6 kcal/mol stronger (Table IV). This difference cannot be explained by the differences in the IP of the donor alone as the IP of pyridine is 9.26 eV[85] (vertical IP from the present monomer calculations yields 9.72 eV), while the IP of $P(CH_3)_3$ is 8.12 eV[85] (vertical IP from our calculations yields 8.33 eV). The energy difference is due to the different character of the two upper-most occupied orbitals of the two complexes.

In Fig. 5 we compare the HOMO-1, HOMO, and LUMO orbitals of both ligands bound to Au_4. The HOMO-1 orbital of Au_4-pyridine shows a node between Au d-orbital and the N lone pair. In Au_4-$P(CH_3)_3$, the more extended lone pair on P envelops this node to overlap with the same-phase lobes of the d-orbital on the nearest Au. The HOMO orbital of Au_4-$P(CH_3)_3$ extends further from Au_4 toward P revealing hints of back-bonding.

In both complexes there is a strong enhancement of the dipole moment upon complex formation (4.6 D with pyridine and 4.2 D with $P(CH_3)_3$). A difference emerges from the Mulliken charge rearrangement. In the complex with pyridine there is a net transfer of 0.4e to Au_4. In the complex of $P(CH_3)_3$ a full electron is transferred to Au_4, but in a nonuniform way: the Au atom bound to P loses 0.86e, while the three remaining Au atoms gain 1.94e among them.

F. Comparison with standard functionals

To examine the performance of conventional DFT approaches in the treatment of the gold cluster-ligand
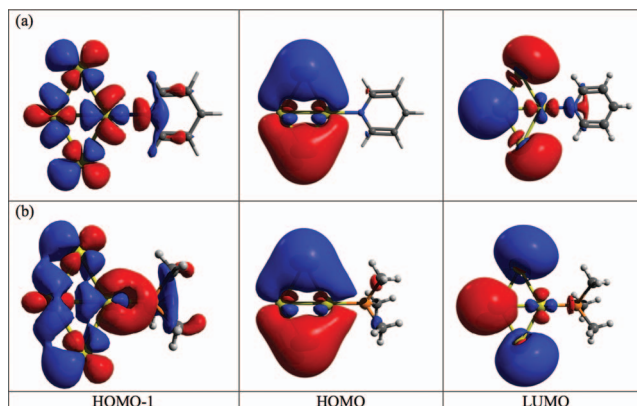

FIG. 5. Frontier orbitals of (a) Au_4-pyridine and (b) Au_4-$P(CH_3)_3$ complexes. Isosurfaces threshold is 0.02.

TABLE V. Comparison of interaction energies (kcal/mol) of Au_4-SCN^- and frontier eigenvalues (in eV) of SCN^- (D) and Au_4 (A) computed with conventional functionals.

Functional	E_{int}	HOMO(D)	LUMO(D)	HOMO(A)	LUMO(A)
LDA	− 65.8	− 0.37	2.67	− 5.95	− 4.91
BP86	− 51.8	− 0.30	2.55	− 5.76	− 4.70
PBE0	− 49.8	− 1.29	2.75	− 6.04	− 3.68
M06HF	− 44.9	− 4.22	2.23	− 8.07	− 1.88
ωB97X	− 47.8	− 3.54	2.99	− 7.57	− 1.84

interactions we compare in Table V the interaction energies of Au_4+SCN^- computed with functionals from increasing rungs: LDA, pure GGA, hybrid GGA,[86] meta GGA, and a standard range-separated ωB97X. The result of ωB97X closely matches the value from our optimized LRC-ωPBEα functionals in Table IV. This is the result of the gap between the donor HOMO and acceptor LUMO (1.7 eV) closely matching that of our optimized functionals. M06HF yields a weaker interaction which can be related to the increased LUMO(A)-HOMO(D) gap to 2.34 eV. By contrast, both PBE0 and BP86 which yield stronger binding, also provide negative LUMO(A)-HOMO(D) gaps, i.e., an incorrect balance of donor-acceptor properties of the constituents. The same is true, to the extreme, of the LDA result. Our conclusion is that even though BP86 and PBE0 results appear to agree with CCSD(T) (BP86: −51.8 kcal/mol; PBE0: −49.8 kcal/mol; CCSD(T): −52.9 kcal/mol), this apparent agreement is illusive as the underlying chemistry is wrong. Moreover, as seen in Fig. 2, both PBE0 and BP86 functionals strongly depart from a piecewise linearity of DFT energy with fractional electrons.

The recognition of the importance of frontier orbital gaps of donor and acceptor to the ability of DFT to describe correctly the ground state donor-acceptor binding and charge transfer is due to the seminal works on the TTF-TCNQ dimer.[17,87] The authors argued for the removal of many-electron SIE by increasing the percent HF in an xc functional. They observed that these frontier orbital gaps linearly correlate with %HF, thus allowing them to recommend the set percentage that prevents excessive ground-state charge transfer. By contrast, in our optimized functionals the HOMO(D)-LUMO(A) gaps are almost independent of the %HF. The restoration of the straight-line behavior of functionals with respect to fractional electrons due to such an optimization (see Fig. 2) prevents the artificial charge transfer and affords the DFT binding energies in good agreement with the wave function methods (see below) for the right reasons.

G. Comparison with CCSD(T)

The energetics from the optimized LRC-ωPBEα functionals can be compared to the CCSD(T) results obtained in the same basis set (see Table IV). Before performing this comparison, some accuracy issues concerning the CCSD(T) results for gold-ligand interactions should be clarified. The wave function methods, such as CCSD(T), are much more strongly dependent on the basis set than DFT methods are.

For example, our tests for Au_4-pyridine show that the difference in the binding energy obtained in vtz and avtz amounts to 4 kcal/mol in CCSD(T) but only 1 kcal/mol in the DFT method employed here. Therefore, obtaining a basis set saturated result in CCSD(T) would require a much larger basis set than DFT. A second issue concerns whether or not to correlate the outer-core 5s electrons of gold.[88] We tested the effect of correlating 5s electrons on the interaction energy on the Au_4-pyridine complex (since it contains the shortest intersystem bond). The effect again proved to be strongly basis set dependent amounting to ∼1 kcal/mol stabilization in vtz and 0.1 destabilization in avtz.

It should be stressed that MP2 cannot be reliably applied for these interactions (for reasons see Ref. 76) while SCS-MP2 can. For example, in Au_4-$P(CH_3)_3$ the MP2 approach yields 14 kcal/mol stronger binding than CCSD(T) of Table IV. On the other hand, SCS-MP2 overbinds only by 1.5–4 kcal/mol (see Table S1 in supplementary material[79]).

The CCSD(T) binding energies are between 3 and 5 kcal/mol stronger than our DFT values. We consider this a very reasonable result because the DFT interaction energy, while accounting for short-range intermolecular correlation, which provides the bulk of the bonding (see Ref. 50), neglects the non-local correlation contribution. The D3 dispersion results are shown in the penultimate column of Table IV. The dispersion term contributes a moderate 5%–15% to the interaction energy. The sum of DFT and dispersion contributions falls within a close range of CCSD(T).

H. Comparison with other results

Our result for benzenethiolate anion interacting with Au_4 indicates a strong bonding (DFT+disp in excellent agreement with CCSD(T)) of covalent nature because of vanishingly small HOMO(D)-LUMO(A) gap. Another way to achieve an analogous covalency would be by the interaction of benzenethiyl radical with odd-number Au_n clusters. Indeed, such a possibility was investigated by Pasteka *et al.*[50] between $CH_3S\bullet$ and a single Au atom on the singlet and triplet surfaces. Their all-electron scalar-relativistic Douglas-Kroll (DK) result for the singlet state bonding is −56.8 kcal/mol. A qualitative agreement with our result (anion with even-numbered cluster) is noteworthy. Among other conventional DFT studies[49,38,2] there is a consensus that the Au-S bond is stronger than an Au-Au bond. Kruger *et al.*[81] demonstrated that $CH_3S\bullet$ can pull a monoatomic gold wire from a gold surface. Häkkinen group showed that SR groups tend to etch gold atoms from Au_n clusters to form RS-Au-SR "staple" motives that protect the gold core. These results were obtained with PBE functional and 11-electron pseudopotential.

Our result for benzenethiol interacting with Au_4 indicates moderately strong bonding of about 28 kcal/mol (23.4–23.7 kcal/mol from DFT and 4.2 kcal/mol from dispersion). This is the interaction with the most significant dispersion contribution of 15%. By comparison, in a related system, recent work by Dufour *et al.*[46] using CAM-B3LYP[89] finds the binding of methanethiol with Au_{11} to be weaker (6 kcal/mol) but of the same nature, i.e., a DA complex with the thiol

acting as a donor. These authors also remark on the very strong sensitivity of the results to the choice of functional prior to choosing CAM-B3LYP.

Trimethylphosphine binds strongly to Au_4 at our DFT level by 48.3 kcal/mol plus 5.3 kcal/mol for dispersion. The literature value for the related systems includes Au-$P(CH_3)_3$ of Pasteka *et al.*[50] with binding of 22.6 kcal/mol (all electron DK). Goel *et al.* studied Au_4 bound to two and four $P(CH_3)_3$ ligands.[48] Their reported TPSS binding energies per bond are $\sim$43 kcal/mol in the former and 29 kcal/mol in the latter. The spread of binding energies in different functionals (as read from their graph) appears to be about 8 kcal/mol with PBE being the strongest and B3LYP being the weakest. They also find LDA to be an outlier overbinding by 15 kcal/mol compared to the rest.

IV. SUMMARY AND CONCLUSIONS

The results presented in this paper argue that GKS treatment is essential to the description of donor-acceptor bonds, in general, and gold-ligand interactions, in particular. Tuning the long-range corrected functionals within the GKS scheme ensures that the IP of the donor molecule and the EA of the acceptor molecule are correctly represented within the functional by the gap between the HOMO of the donor and the LUMO of the acceptor. However, one acknowledged problem is that different monomers may require different tuning parameters.[90] The two-parameter tuning for the monomer properties of the family of LRC-ωPBEα functionals help ensure the balanced treatment of the donating and accepting properties in these complexes. The optimized functionals also show nearly linear behavior of DFT energy with fractional electrons.

Hybrid functionals also belong to the GKS class.[91] However, these functionals do not guarantee that the gap between the HOMO(D) and LUMO(A) will be correctly represented. In fact, the PBE0 hybrid in our calculations for Au_4-SCN^- yields a negative gap. Previous work advocated the variation in the constant percent of exact exchange in hybrid functionals to match this gap. We believe that the (two-parameter) optimization of range-separated functionals is a better route to achieving this goal. Specifically, we showed the examples of homo-dimers where the HOMO-LUMO gaps are largely independent of the total percent of the HF exchange arising from both the short and long ranges in the total exchange.

The functionals that align frontier eigenvalues with IP and EA for donor-acceptor pairs are ideally suited for the predictions of the electron flow between a gold cluster or surface and ligands. A property which controls the flow, Mulliken electronegativity $\chi = 1/2$(IP+EA), is an average of IP and EA. In the case of a metal, χ corresponds to the position of the Fermi level whereas in the case of ligands, such as these studied in the present work, it is the middle of the E_{HL} gap.

A number of insights into the gold-ligand interactions were obtained. In a model aurophilic dimer bound only by the correlation effects, our optimized functionals yield the interaction energy in the range of -1.7 to -1.8 kcal/mol. This dimer (in this particular configuration) is purely repulsive at the HF level. Our attractive interaction, free from artifacts

masquerading as interaction energy, indicates the dimer is indeed bound by intermolecular correlation effects that are partially accounted for by the DFT. Together with the remaining D3 dispersion of $\sim$$-4.8$ kcal/mol our estimate is reasonably close to the CCSD(T)/CBS well depth of 6.13 kcal/mol.

In Au_4 interacting with a number of ligands (SCN^-, PhS^-, PhSH, pyridine, and $P(CH_3)_3$) monomer-optimized LRC-ωPBEα functionals have led to very sound binding energies. In combination with moderate contribution from the dispersion term, our values are in very good agreement with CCSD(T), i.e., 1-2 kcal/mol (pyridine, PhSH, PhS^-, and $P(CH_3)_3$) to up to 3 kcal/mol (SCN^-). It should be emphasized that the dispersion effect, as estimated by D3 method, contributes between 5% and 15% to the DA bonding in these systems. Benzenethiol forms a moderately strong DA bond with Au_4 of $\sim$28 kcal/mol with thiol acting the electron donor. The binding of the benzenethiolate anion is much stronger (over 60 kcal/mol) exceeding the Au-Au bonding strength. Trimethylphosphine interacts much more strongly with Au_4 than pyridine and benzenethiol.

The affinity of organo-sulfur ligands for gold stems from the larger variety of bonding situations from medium strength DA bonds of neutral thiols to strong coordinate bonds exhibited by negatively charged thiolates to covalent bonds of radical thiyls. We showed that the strength of thiolate bonding to gold cluster is capable of inducing an incipient transfer of gold atom from the cluster to ligand.

Our results for these ligands are consistent with other wave function predictions[50] and may serve as a platform for testing wide range of functionals. Such tests should take the dispersion energy into consideration.

[1]J. C. Love, L. A. Estroff, J. K. Kriebel, R. G. Nuzzo, and G. M. Whitesides, Chem. Rev. **105**, 1103 (2005).

[2]H. Häkkinen, Nat. Chem. **4**, 443 (2012).

[3]S. M. Morton, D. W. Silverstein, and L. Jensen, Chem. Rev. **111**, 3962 (2011).

[4]M. Haruta, Catal. Today **36**, 153 (1997).

[5]D. Gorin, B. Sherry, and F. D. Toste, Chem. Rev. **108**, 3351 (2008).

[6]P. Pyykkö, Angew. Chem., Int. Ed. **43**, 4412 (2004); Chem. Soc. Rev. **37**, 1967 (2008).

[7]H. Schmidbaur and A. Schier, Chem. Soc. Rev. **37**, 1931 (2008); **41**, 370 (2012).

[8]A. P. Woodham, G. Meijer, and A. Fielicke, J. Am. Chem. Soc. **135**, 1727 (2013).

[9]B. Jeziorski and W. Kolos, Int. J. Quantum Chem. **12** Suppl. 1, 91 (1977).

[10]A. J. Stone and A. J. Misquitta, Chem. Phys. Lett. **456**, 105 (2008).

[11]A. J. Misquitta, J. Chem. Theory Comput. **9**, 5313 (2013).

[12] K. Kitaura and K. Morokuma, Int. J. Quantum Chem. **10**, 325 (1976).

[13] R. Z. Khaliullin, E. A. Cobar, R. C. Lochan, A. T. Bell, and M. Head-Gordon, J. Phys. Chem. A **111**, 8753 (2007).

[14] A. E. Reed, L. A. Curtiss, and F. Weinhold, Chem. Rev. **88**, 899 (1988).

[15] E. R. Johnson, P. Mori-Sánchez, A. J. Cohen, and W. Yang, J. Chem. Phys. **129**, 204112 (2008).

[16] L. Goerigk and S. Grimme, J. Chem. Theory Comput. **7**, 291 (2011).

[17] G. Sini, J. S. Sears, and J.-L. Bredas, J. Chem. Theory Comput. **7**, 602 (2011).

[18] E. R. Johnson, M. Salamone, M. Bietti, and G. A. DiLabio, J. Phys. Chem. A **117**, 947 (2013).

[19] J. P. Perdew, R. G. Parr, M. Levy, and J. L. Balduz, Jr., Phys. Rev. Lett. **49**, 1691 (1982).

[20] A. Bilić, J. R. Reimers, and N. S. Hush, J. Chem. Phys. **122**, 094708 (2005).

[21] E. Fabiano, M. Piacenza, S. D'Agostino, and F. Della Sala, J. Chem. Phys. **131**, 234101 (2009).

[22] S. N. Steinmann, C. Piemontesi, A. Delachat, and C. Corminboeuf, J. Chem. Theory Comput. **8**, 1629 (2012).

[23] D. Kuchenbecker and G. Jansen, ChemPhysChem **13**, 2769 (2012).

[24] J. Aragó, J. C. Sancho-García, E. Ortí, and D. Beljonne, J. Chem. Theory Comput. **7**, 2068 (2011).

[25] S. Kozuch and J. M. L. Martin, J. Chem. Theory Comput. **9**, 1918 (2013).

[26] M. Modrzejewski, L. Rajchel, M. M. Szczesniak, and G. Chalasinski, J. Chem. Phys. **136**, 204109 (2012).

[27] M. Seth, T. Ziegler, M. Steinmetz, and S. Grimme, J. Chem. Theory Comput. **9**, 2286 (2013).

[28] P. M. Gill, B. G. Johnson, J. A. Pople, and M. J. Frisch, Chem. Phys. Lett. **197**, 499 (1992).

[29] C. Adamo and V. Barone, J. Chem. Phys. **110**, 6158 (1999).

[30] H.-C. Fang, Z. H. Li, and K.-N. Fan, Phys. Chem. Chem. Phys. **13**, 13358 (2011).

[31] Y. Zhao and D. G. Truhlar, Theor. Chem. Acc. **120**, 215 (2008).

[32] A. D. Becke, Phys. Rev. A **38**, 3098 (1988).

[33] J. P. Perdew, Phys. Rev. B **33**, 8822 (1986).

[34] J. P. Perdew, K. Burke, and M. Ernzerhof, Phys. Rev. Lett. **77**, 3865 (1996).

[35] J. P. Perdew and Y. Wang, Phys. Rev. B **45**, 13244 (1992).

[36] M. Askerka, D. Pichugina, N. Kuzmenko, and A. Shestakov, J. Phys. Chem. A **116**, 7686 (2012).

[37] P. J. Stephens, F. J. Devlin, C. F. Chabalowski, and M. J. Frisch, J. Phys. Chem. **98**, 11623 (1994).

[38] H. Häkkinen, M. Walter, and H. Gronbeck, J. Phys. Chem. B **110**, 9927 (2006).

[39] J. Granatier, M. Urban, and A. J. Sadlej, Chem. Phys. Lett. **484**, 154 (2010).

[40] T. Stein, H. Eisenberg, L. Kronik, and R. Baer, Phys. Rev. Lett. **105**, 266802 (2010); L. Kronik, T. Stein, S. Refaely-Abramson, and R. Baer, J. Chem. Theory Comput. **8**, 1515 (2012).

[41] A. J. Cohen, P. Mori-Sánchez, and W. Yang, Science **321**, 792 (2008).

[42] W. Yang, A. J. Cohen, and P. Mori-Sánchez, J. Chem. Phys. **136**, 204111 (2012).

[43] T. Stein, L. Kronik, and R. Baer, J. Am. Chem. Soc. **131**, 2818 (2009).

[44] M. Modrzejewski, Ł. Rajchel, G. Chalasinski, and M. M. Szczesniak, J. Phys. Chem. A **117**, 11580 (2013).

[45] Y. Wang, N. S. Hush, and J. R. Reimers, J. Am. Chem. Soc. **129**, 14532 (2007).

[46] F. Dufour, B. Fresch, O. Durupthy, C. Chaneac, and F. Remacle, J. Phys. Chem. C **118**, 4362 (2014).

[47] B. M. Barngrover and C. M. Aikens, J. Phys. Chem. A **117**, 5377 (2013).

[48] S. Goel, K. A. Velizhanin, A. Piryatinski, S. Tretiak, and S. A. Ivanov, J. Phys. Chem. Lett. **1**, 927 (2010).

[49] D. Kruger, H. Fuchs, R. Rousseau, D. Marx, and M. Parrinello, J. Chem. Phys. **115**, 4776 (2001).

[50] L. F. Pasteka, T. Rajsky, and M. Urban, J. Phys. Chem. A **117**, 4472 (2013).

[51] T. M. Henderson, B. G. Janesko, and G. E. Scuseria, J. Chem. Phys. **128**, 194105 (2008).

[52] M. Kamiya, T. Tsuneda, and K. Hirao, J. Chem. Phys. **117**, 6010 (2002).

[53] E. D. Murray, K. Lee, and D. C. Langreth, J. Chem. Theory Comput. **5**, 2754 (2009).

[54] K. U. Lao and J. M. Herbert, J. Chem. Phys. **140**, 044108 (2014).

[55] M. Srebro and J. Autschbach, J. Phys. Chem. Lett. **3**, 576 (2012).

[56] T. Stein, L. Kronik, and R. Baer, J. Chem. Phys. **131**, 244119 (2009).

[57] S. Refaely-Abramson, S. Sharifzadeh, N. Govind, J. Autschbach, J. B. Neaton, R. Baer, and L. Kronik, Phys. Rev. Lett. **109**, 226405 (2012).

[58] T. Korzdorfer, R. M. Parrish, N. Marom, J. S. Sears, C. D. Sherrill, and J.-L. Bredas, Phys. Rev. B **86**, 205110 (2012).

[59] D. A. Egger, S. Weissman, S. Refaely-Abramson, S. Sharifzadeh, M. Dauth, R. Baer, S. Kümmel, J. B. Neaton, E. Zojer, and L. Kronik, J. Chem. Theory Comput. **10**, 1934 (2014).

[60] J. F. Janak, Phys. Rev. B **18**, 7165 (1978).

[61] S. Grimme, J. Antony, S. Ehrlich, and H. Krieg, J. Chem. Phys. **132**, 154104 (2010).

[62] O. A. Vydrov and G. E. Scuseria, J. Chem. Phys. **125**, 234109 (2006).

[63] M. Modrzejewski, G. Chalasinski, and M. M. Szczesniak, "Range-separated meta-GGA functional designed for noncovalent interactions" J. Chem. Theory Comput (submitted).

[64] Basis sets were obtained from Basis Set Exchange v1.2.2; K. L. Schuchardt, B. T. Didier, T. Elsethagen, L. Sun, V. Gurumoorthi, J. Chase, J. Li, and T. L. Windus, "Basis set exchange: A community database for computational sciences," J. Chem. Inf. Model **47**, 1045 (2007).

[65] D. Figgen, G. Rauhut, M. Dolg, and H. Stoll, Chem. Phys. **311**, 227 (2005).

[66] K. A. Peterson and C. Puzzarini, Theor. Chem. Acc. **114**, 283 (2005).

[67] A. Halkier, W. Klopper, T. Helgaker, P. Jørgensen, and P. R. Taylor, J. Chem. Phys. **111**, 9157 (1999).

[68] S. F. Boys and F. Bernardi, Mol. Phys. **19**, 553 (1970).

[69] M. Valiev, E. J. Bylaska, N. Govind, K. Kowalski, T. P. Straatsma, H. J. J. van Dam, D. Wang, J. Nieplocha, E. Apra, T. L. Windus, and W. A. de Jong, Comput. Phys. Commun. **181**, 1477 (2010).

[70] H. J. Werner, P. J. Knowles, G. Knizia, F. R. Manby, M. Schütz *et al.*, MOLPRO, version 2010.1, a package of *ab initio* programs, 2010, see http://www.molpro.net.

[71] Y. Zhao and D. G. Truhlar, J. Phys. Chem. A **109**, 5656 (2005).

[72] J. Řezáč and P. Hobza, J. Chem. Theory Comput. **9**, 2151 (2013).

[73] P. Pyykkö and Y. F. Zhao, Angew. Chem., Int. Ed. Engl. **30**, 604 (1991).

[74] E. O'Grady and N. Kaltsoyannis, Phys. Chem. Chem. Phys. **6**, 680 (2004).

[75] B. Assadollahzadeh and P. Schwerdtfeger, Chem. Phys. Lett. **462**, 222 (2008).

[76] R.-F. Liu, C. A. Franzese, R. Malek, P. S. Zuchowski, J. G. Angyan, M. M. Szczesniak, and G. Chalasinski, J. Chem. Theory Comput. **7**, 2399 (2011).

[77] A. Otero-de-la-Roza, Jo. D. Mallory, and E. R. Johnson, J. Chem. Phys. **140**, 18A504 (2014).

[78] L. Magnko, M. Schweizer, G. Rauhat, M. Schütz, H. Stoll, and H. J. Werner, Phys. Chem. Chem. Phys. **4**, 1006 (2002).

[79] See supplementary material at http://dx.doi.org/10.1063/1.4885137 for additional results on the dependence of HOMO and LUMO eigenvalues of AuH-PH$_3$ on %HF. The MP2 and SCS-MP2 results for Au$_4$-ligand complexes are also included.

[80] Intermolecular parameters were minimized in a smaller LANL2DZ(pd) basis set for large systems and in avtz for the smaller ones and using ωB97X functional.

[81] D. Kruger, H. Fuchs, R. Rousseau, D. Marx, and M. Parrinello, Phys. Rev. Lett. **89**, 186402 (2002).

[82] P. Maksymovych and J. T. Yates, Jr., J. Am. Chem. Soc. **130**, 7518 (2008).

[83] P. Maksymovych, O. Voznyy, D. B. Dougherty, D. C. Sorescu, and J. T. Yates, Jr., Prog. Surf. Sci. **85**, 206 (2010).

[84] R. G. Parr and W. Yang, *Density-Functional Theory of Atoms and Molecules* (Oxford University Press, Oxford, 1989).

[85] See http://webbook.nist.gov for NIST Chemistry WebBook.

[86] J.-D. Chai and M. Head-Gordon, J. Chem. Phys. **128**, 084106 (2008).

[87] V. Atalla, M. Yoon, F. Caruso, P. Rinke, and M. Scheffler, Phys. Rev. B **88**, 165122 (2013).

[88] 5s electrons show strong radial correlation with 6s electrons of Au atom as demonstrated in T. Zeng and M. Klobukowski, J. Chem. Phys. **130**, 204107 (2009).

[89] T. Yanai, D. Tew, and N. Handy, Chem. Phys. Lett. **393**, 51 (2004).

[90] A. Karolewski, L. Kronik, and S. Kümmel, J. Chem. Phys. **138**, 204115 (2013).

[91] A. Seidl, A. Görling, P. Vogl, J. A. Majewski, and M. Levy, Phys. Rev. B **53**, 3764 (1996).

Optical absorption spectra of gold clusters Au$_n$ (n = 4,6,8,12,20)

In this Chapter presented are optical absorption spectra of Au$_n$ clusters ($n = 4, 6, 8, 12, 20$) obtained within the framework of TDDFT. For the first time the long-range corrected xc functionals were applied to predict optical response in this class of systems. The Chapter opens with an introduction in which we recognize the challenge posed by TDDFT treatment of excited states in metal clusters – gold clusters in particular. Next, the energetic structure of the excited states of the Au$_6$ cluster is analyzed with different TDDFT approaches. A detailed examination of the Au$_4$ cluster follows. The results of TDDFT calculations are compared with the wave function linear response theory based on CCSD and with the experimental high-resolution spectra in low temperature Ne matrix.

In this Chapter I highlight my contribution to the presented work, namely studies of the Au$_6$ and Au$_4$ clusters. In the attached publication the Reader will find both an extension of the herein described results and a comprehensive analysis of the Au$_8$, Au$_{12}$ and Au$_{20}$ systems.

6.1   Introduction

Optical and electronic properties of gold nanoparticles are an area of active research due to their applications in imagining techniques, sensors, solar cells and catalysis [105, 117, 118]. The phenomenon underlying strong absorption of light for metallic nanostructures is known as the surface plasmon resonance. It is defined as a collective response of conduction electrons upon excitation by resonant wavelength of light. Remarkably, when the size of the Au cluster is limited to several atoms, the absorption changes and exhibits a molecule-like character [107].

The reliable prediction of the optical response of gold clusters requires a fully quantum treatment. Due to its advantageous computational scaling and the possibility to account for both electron correlation and relativistic effects, TDDFT became the method of choice for this class of systems. Nevertheless, a comparison of high-resolution spectra of neutral Ag$_n$ [119] and Au$_n$ [120, 121] clusters with TDDFT simulations revealed poor agreement when conventional LDA and GGA functionals were applied. In the case of Au$_n$ the predicted spectra displayed large number of spurious low-energy/low-intensity states and could not be attributed to a specific isomer [120, 121].

In their work on optical properties of the Ag$_n$ clusters Silverstein and Jensen [119] have shown that the LRC functionals lead to a substantial improvement over conventional GGAs and global hybrid functionals. Indeed, assuring the correct asymptotic behavior of the xc potential has previously been shown essential for the proper treatment of Rydberg and CT excitations [84, 122], as well as extended systems with fluxional charge distribution. However, the gold clusters constitute an even bigger challenge for TDDFT. This is because of the small $s - d$ separation in Au atoms which results in active participation of d-electrons in the electronic transitions and, in consequence, leads to high spectral density and an attenuation of oscillator strengths.

The aim of our work was to calculate absorption spectra of a number of Au$_n$ ($n = 4, 6, 8, 12$, and 20) clusters with selected LRC functionals and compare the results with the wave function excited states method equation-of-motion coupled cluster singles and doubles (EOM-CCSD). For the Au$_4$ and Au$_8$ we could provide additional comparison with the high-resolution spectra recorded at Ne matrix [121].

Apart from using the default parameters for the LRC functionals, we applied the so-called gap tuning, i.e. simultaneous enforcing of the Koopmans' theorem for both

N and $N + 1$ electron systems [4]:

$$J'^2(\omega) = \min_{\omega} \left\{ [\varepsilon_{\text{HOMO}}(N;\omega) + \text{IP}(N;\omega)]^2 + [\varepsilon_{\text{HOMO}}(N+1;\omega) + \text{IP}(N+1;\omega)]^2 \right\}. \quad (6.1)$$

The relativistic effects were taken into account via small-core ECP of Figgen *et al.* [123].

We note that in our calculations the spin-orbit coupling (SO) effects were neglected. In 2014 Anak *et al.* [124] performed TDDFT calculations with the spin-orbit coupling included within the statistical averaging of the model orbital potential (SAOP) [125]. Their results showed significant broadening and damping of the optical response for small clusters (Au_4, Au_6, Au_8), whereas for the Au_{20} cluster this effect was less pronounced. Nevertheless, the inclusion of SO effects did not explain the origin of the prominent transitions below 3 eV recorded in the experiment.

6.2 Results

6.2.1 Excited states of the Au_6 cluster

The absorption spectra of gold clusters recorded in cold Ne matrices revealed a high density of transitions within the 2-6 eV range [121]. In order to gain insight into the level structure behind this phenomenon, we calculated the lowest twelve vertical transitions for the Au_6 (D_{3h}) cluster. According to Ref. [126], the Au_6 cluster should exhibit a wide excitation gap. Although this has not been confirmed in the experiment – no Au_6 spectra were available – we chose this cluster as a starting point to determine the challenges behind optical response calculations in Au_n from the standpoint of energetics.

The data presented in Fig. 6.1 unveil consistent picture at both DFT and *ab initio* levels of theory: two multitudes of states separated by a gap of ca. 0.3 eV. The predicted position of the lowest excited state is similar in EOM-CCSD (3.3 eV) and all LRC functionals (ωB97X: 3.26 eV, CAM-B3LYP: 3.14 eV), whereas TPSS and B3LYP yield lower positions at 2.37 and 2.76 eV, respectively. While excitations from the HOMO orbital of $6s$ character contribute mainly to the lower group of the excited states, the excitations from orbitals of $5d$ character contribute to the upper group. Finally, the order of states varies between the DFT and EOM-CCSD approaches. All LRC functionals predict the lowest excited state of A_2 symmetry (dark state) followed by
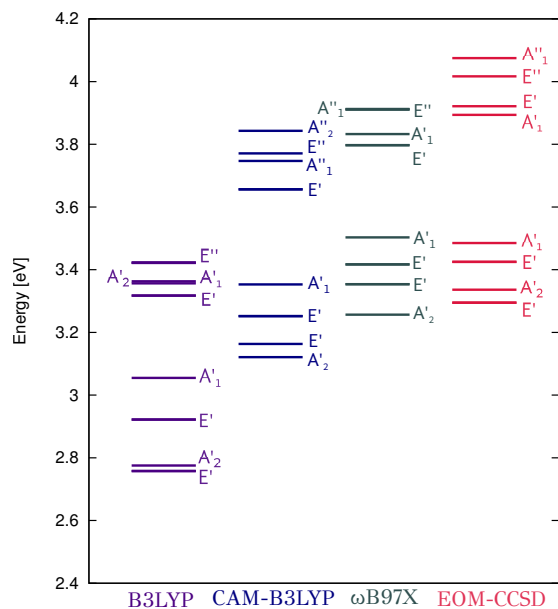
Figure 6.1: Comparison of the lowest-lying excited states of Au$_6$ (D$_{3h}$) from EOM-CCSD (marked in red) and DFT calculations in three designated xc functionals. All calculations were performed in the VDZ-PP basis set.

active E' state. By contrast, in EOM-CCSD that order is reversed.

6.2.2   The optical absorption spectrum of the Au$_4$ cluster

We now move to Au$_4$ – the smallest of the analyzed clusters. The cluster exhibits D_{2h} symmetry, as confirmed by geometry optimizations at all levels of theory. We start with comparing our *ab initio* EOM-CCSD results with the available experimental spectrum. In Fig. 6.2 we observe that the most intense transitions in the Ne matrix occur at 3.33, 3.73, 4.20 and 4.66 eV. The corresponding EOM-CCSD peaks are: the most intense transition at 3.25 eV of B$_{1u}$ symmetry (molecule lies on the yz plane), the trio of transition at 3.86, 4.60 and 4.85 eV of B$_{2u}$, B$_{1u}$ and B$_{2u}$ symmetries, respectively. The obtained agreement between the experiment and *ab initio* results is satisfactory, with the exception of the lowest-lying peak (2.73 eV) in the experimental spectrum. Interestingly, this transition corresponds to the second dark state of A$_g$ symmetry predicted by both CC and LRC calculations.

Next we compare the performance of the conventional hybrid B3LYP functional with its LRC version, i.e., the CAM-B3LYP functional and its asymptotically-corrected CAM-B3LYP* variant. We note that the original choice of the CAM parameters in

CAM-B3LYP was $\alpha = 0.19$ and $\beta = 0.46$ [24] which yields incorrect asymptote of the exchange potential [127]. Therefore, we also tested the corrected CAM-B3LYP* variant with $\beta = 0.81$.

In Fig. 6.2 we notice that the spectrum obtained with B3LYP shows different pattern of the transitions' intensities with respect to both EOM-CCSD and experiment. In particular, there is a significant decrease in the first B_{1u} peak and the most intense transition of B_{1u} symmetry appears at 4.52 eV. Moreover, B3LYP predicts several weakly active transitions at low energy below 3 eV. Surprisingly, although the application of range-separation in CAM-B3LYP removes the spurious low-lying transitions, the shape of the spectrum becomes even more bizarre. For CAM-B3LYP the first two peaks of B_{1u} and B_{1u} symmetries are split into two components of similar intensity. Also, the most intense peak now becomes the B_{2u} transition at 4.67 eV. It is only the fixing of the asymptotic behavior in CAM-B3LYP* that allows to rectify this erroneous behavior and provide good agreement with the EOM-CCSD results.

To better grasp the physics underlying the observed changes in the spectra following the introduction of range-separation, in Table 6.1 we gathered several different properties: vertical ionization potentials of the neutral Au_4 ($IP(N)$) and of the negative ion Au_4^- ($IP(N+1)$) obtained as ΔSCF, the negative of the HOMO eigenvalue ($-\varepsilon_{HOMO}$) of Au_4 and of Au_4^- ($-\varepsilon_{HOMO(N+1)}$). We recall that the difference, $IP(N)$-$IP(N+1) = E_g$, is the (vertical) fundamental gap, whereas the difference $\varepsilon_{LUMO}-\varepsilon_{HOMO} = E_{HL}$, is the HOMO-LUMO gap. We also remind that the two gaps may only be equal in the GKS framework [43].

We start with the comparison of the B3LYP and CAM-B3LYP*($\omega = 0.33$) results. Both functionals give similar $IP(N)$ and $IP(N+1)$, therefore also their fundamental gaps stay in good agreement. As one can expect, the discrepancy is manifested in the magnitude of the HOMO-LUMO gap: while in B3LYP E_g and E_{HL} differ by ca. 2 eV, in CAM-B3LYP*($\omega = 0.33$) the difference amounts only to 0.4 eV. This corresponds to a two orders of magnitude decrease in the J'^2 diagnostic: from 5.8 in B3LYP to 0.09 in CAM-B3LYP*.

In Table 6.1 we also present results for the optimally-tuned CAM-B3LYP* with the range-separation parameter ω equal to 0.25. Surprisingly, we found that the tuned functional predicts a mediocre spectrum, close to the one obtained with regular CAM-B3LYP (not shown). The tuning of the LC-ωPBE functional revealed a similar be-

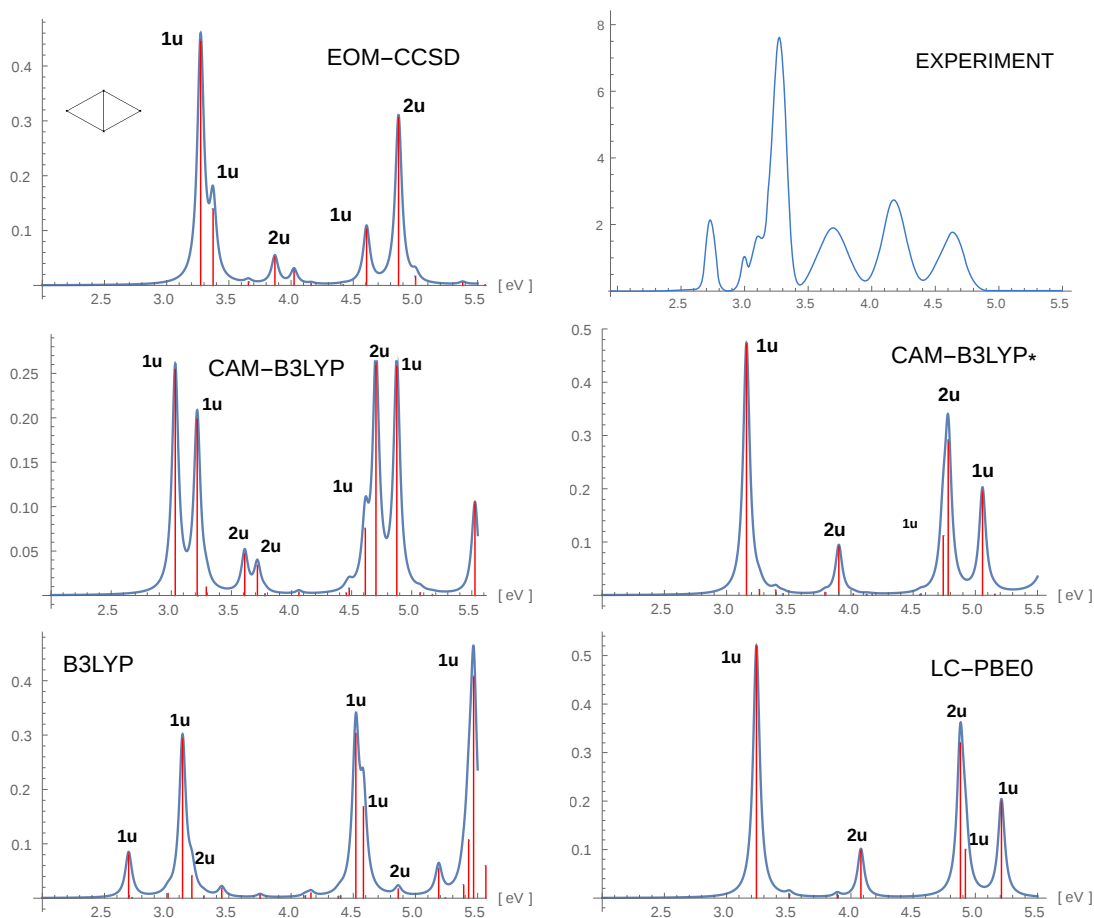Figure 6.2: Au$_4$ (D$_{2h}$): optical absorption spectra, theory vs. experiment. Vertical axes show oscillator strength. 1u and 2u denote excited state symmetries B$_{1u}$ and B$_{2u}$, respectively, of the D$_{2h}$ group. The experimental spectrum of Ref. [121] is redrawn from their Fig. 3. The spectral lines are broadened with a Lorentzian profile. All calculations were done in the aug-cc-pVTZ-PP basis.

Table 6.1: Energy characteristics of Au_4 (D_{2h}): the vertical ionization potential (IP) of the neutral cluster and its anion, orbital energies of the neutral and anion, HOMO-LUMO gap (E_{HL}) and fundamental gap (E_g) from different xc functionals. All energy values are in eV; J^2 in $(eV)^2$.

Energy [eV]	B3LYP	CAM-B3LYP* ω		LC-PBE0	Experiment
		0.33	0.25		
IP(N)	7.70	7.56	7.67	7.51	8.60
IP($N+1$)	2.31	2.20	2.28	2.11	2.67
-ε_{HOMO}	5.93	7.74	7.68	7.72	–
-$\varepsilon_{HOMO(N+1)}$	0.68	2.44	2.37	2.41	–
-$\varepsilon_{LUMO(N)}$	3.96	1.99	2.21	2.41	–
E_g	5.39	5.30	5.40	5.31	5.93
E_{HL}	1.99	5.75	5.47	5.91	–
J'^2	5.79	0.090	0.008	0.133	–

havior, i.e., poor performance of the optimally-tuned variant (see the attached work [D4]). However, we also recognized that the inclusion of the short-range HF exchange in the functional allows for substantial improvement of the spectra, as in the case of LC-PBE0 (see Fig. 6.2). Therefore, it is possible that for CAM-B3LYP a two-parameter (ω, α) tuning procedure [49] is necessary, in order to properly balance the short- and long-range admixture of the HF exchange.

6.3 Related publication

Further investigation of the Au_8, Au_{12} and Au_{20} clusters is presented in the attached publication [D4]. Apart from the DFAs presented in this Chapter, the performance of the TPSS [128], LC-TPSS [23] and ωB97X [129] xc functionals is tested. In particular, selected optical properties such as the position of the lowest excited state, the lowest optically bright excited state (the optical gap), the position of absorption maximum, and evolution of this properties as a function of geometry and cluster size are thoroughly examined.

Optical absorption spectra of gold clusters Au$_n$ (n = 4, 6, 8,12, 20) from long-range corrected functionals with optimal tuning

Jessica V. Koppen,[1] Michał Hapka,[2] Małgorzata M. Szczęśniak,[1] and Grzegorz Chałasiński[1,2,a)]

[1]*Department of Chemistry, Oakland University, Rochester, Michigan 48309, USA*
[2]*Faculty of Chemistry, University of Warsaw, Pasteura 1, 02-093 Warszawa, Poland*

Absorption UV spectra of gold clusters Au$_n$ (n = 4, 6, 8, 12, 20) are investigated using the time-dependent density functional theory (TDDFT). The calculations employ several long-range corrected xc functionals: ωB97X, LC-ωPBEh, CAM-B3LYP* (where * denotes a variant with corrected asymptote of CAM-B3LYP), and LC-ωPBE. The latter two are subject to first-principle tuning according to a prescription of Stein *et al.* [Phys. Rev. Lett. **105**, 266802 (2010)] by varying the range separation parameter. TDDFT results are validated for Au$_4$ and Au$_8$ against the equation-of-motion coupled cluster singles and doubles results and the experiment. Both long-range correction and the inclusion of a fixed portion of the exact exchange in the short-range are essential for the proper description of the optical spectra of gold. The ωB97X functional performs well across all studied cluster sizes. LC-ωPBEh, with parameters recommended by Rohrdanz *et al.* [J. Chem. Phys. **130**, 054112 (2009)], affords the best performance for clusters of n > 4. The optimally tuned CAM-B3LYP* features the range separation parameter of 0.33 for Au$_4$ and 0.25 for all the larger clusters. For LC-ωPBE the tuning procedure resulted in incorrect transition energies and oscillator strengths despite the fact that the optimized functional showed the accurate linear dependence on fractional electron numbers. Au$_n$ (n = 4, 6, 8) feature optical gaps above of 3 eV and Au$_{20}$ of ~2.9 eV. In Au$_{12}$ this gap narrows to ~2.1 eV. The calculated spectrum for Au$_{20}$ involves intensity being concentrated in only a few transitions with the absorption maximum at 3.5 eV. The intense 3.5 eV absorption is present in all cluster sizes of n > 4. The calculated HOMO-LUMO gaps for all cluster sizes are within 0.5 eV of the difference between the vertical ionization potential and electron affinity. The reasons for this and for the failure of conventional xc functionals for optical spectra of gold are discussed. © *2012 American Institute of Physics.* [http://dx.doi.org/10.1063/1.4752433]

I. INTRODUCTION

Properties of gold clusters reveal underlying periodicity as a function of cluster size. For example, the electron affinity of gold climbs from 2.3 eV for an atom to 4 eV for a 70-atom cluster in odd-even alternation due to closed- and open-shell structures as first showed by Smalley's group.[1] These oscillations are interspersed by "islands of stability" some of which are due to shell closings.[2] In small gold clusters such islands of stability occur for n = 2, 4, 6, 8, 12, 18, 20 as shown by photoelectron spectroscopy supported by theory.[3] For n = 4, 8, and 12 there is some experimental evidence for competing structures.[4] Nevertheless, a consensus has emerged that the neutral gold clusters tend to remain planar up to n = 12.[3,5]

Optical properties of gold clusters attract a great deal of interest for basic science reasons and for their potential nanotechnology applications (see, e.g., Ref. 6). One of the most interesting is the phenomenon of surface plasmon resonance, i.e., a strong UV absorption due to collective oscillations of conduction electrons in nanometer-sized cluster of gold. In small several-atom clusters gold absorption becomes molecule-like reflecting a well-defined electronic structure.[7,8]

One of the intriguing questions addressed by the studies of size-selected gold clusters is at what size the molecular-type electronic transitions evolve into a plasmon-like absorption (see, e.g., Refs. 9 and 10).

Optical spectra of size-selected small gold clusters have been recorded in the gas phase, matrix isolation, as ligand-encapsulated in solution (see, e.g., Ref. 11), or in a crystal phase.[12,13] The UV spectra of odd-numbered clusters Au$_n$ (n = 7–13) bound to one or two Xe atoms have been measured in photodepletion experiments by Collings *et al.*[14] whereas their anionic analogues by Gilb *et al.*[15] The high-resolution optical absorption spectra of a number of clusters n = 1–9 (except for n = 6) trapped in low-temperature Ne matrix have recently been reported by Lecoultre *et al.*[16] The spectra are sharper and more defined for even-number clusters, particularly for n = 4 and 8. Small clusters with ligand shells have also been observed in solution revealing UV spectra attributed to the gold core. For example, dendrimer encapsulated Au$_8$ in water solution reportedly displays a bright blue emission.[17] Another cluster, Au$_4$, was also dendrimer-encapsulated by another group and shown to fluoresce.[18] The optical spectrum of surfactant synthesized and resin isolated Au$_8$ has also been recently reported by Rath *et al.*[19] It reportedly served as a means of assigning the structure of this cluster. Most of the

---

a)Author to whom correspondence should be addressed. Electronic mail: chalbie@tiger.chem.uw.edu.pl.

137, 114302-1

solution-phase experiments provided fairly low-resolution UV spectra. By contrast, the low-temperature matrix-isolation spectroscopy and photodepletion experiments offered spectra of a higher resolution.

The calculations of UV absorption spectra of small gold clusters have employed linear-response time-dependent density functional theory (TDDFT) with exchange-correlation (xc) functionals mostly of local density approximation (LDA) type, but also of generalized gradient approximation (GGA) and hybrid. Several types of relativistic treatments have been employed including scalar-relativistic and spin-orbit pseudopotentials (PP), and scalar and two-component zero order regular approximation (ZORA).[20,21] Idrobo *et al.*[22] studied Au_n (n = 2–14, 20) using TDDFT theory based on LDA/PP. Castro *et al.* studied spin-orbit effects on TD-LDA spectra of clusters of different shape.[23] The experimental Ne matrix study[16] of Au_n for n = 1–5, 7–9 also included TDDFT/B3LYP and PBE[24]/PP simulations of the spectra. The calculated spectra, by the authors' own admission, agreed poorly with their measurements and so did the prior LDA results of Idrobo *et al.*[22] Simulations of UV depletion spectra of $Au_n^- Xe$ (n = 7–11) employed B3LYP/PP.[15] Several computational studies have been devoted to Au_{20}. Li *et al.*[25] were first to demonstrate that Au_{20} has the tetrahedral structure using Perdew-Wang (PW91)[26]/ZORA approach and measured its electron affinity by the photoelectron spectroscopy. Aikens and Schatz[27] employed Becke-Perdew (BP86)[28]/ZORA. Wu *et al.*[29] employed LB94, the asymptotically corrected model potential based on LDA[30] combined with ZORA. Calculations of Xie *et al.*[31] reported two sets of data: BP86/PP and B3LYP/PP with the LANL2 pseudopotential. The results of these studies paint a widely different picture of optical properties of Au_{20}. Without experimental results it is difficult to reconcile these differences.

The linear-response TDDFT has emerged as the method of choice for the treatment of excitation energies[32,33] in large systems and in clusters of a growing size.[34] Increasingly, several classes of excited states have been identified where TDDFT based on LDA and GGA xc funtionals appears to have problems. They include Rydberg states, whose poor description results from an artificially low ionization threshold.[35] Another class includes charge transfer (CT) excitations for which the xc functionals that do not incorporate the full Hartree-Fock (HF) exchange lead to the incorrect distance dependence.[36] This artifact leads to the appearance of spurious low-lying CT states in TDDFT calculations.[33,37] In the context of large systems, particularly with fluxional charge distributions, there appears to be yet another type of problem states. The π-π^* excited states in linear condensed acenes, which are polarized along the short axis, cannot be described accurately by conventional TDDFT method.[38] Such states were recently dubbed "charge-transfer in disguise" by Richard and Herbert[39] (see also Ref. 40). Metal clusters with their extended structures, polarizable charge distributions and high density of states could exemplify these problems with particular severity. Indeed recent study on silver clusters, Ag_n (with n = 4–20), reports the presence of a large number of spurious low-energy/low-intensity states in TDDFT calculations with conventional GGA xc functionals.[41]

Although these problems have seemingly different causes, a common remedy involves correcting the treatment of the inter-electron repulsion in the long range by gradually replacing the long-range part of the DFT exchange by the HF exchange. This approach referred to as long-range correction (LC) of an xc potential is implemented using the "range separation" of the Coulomb operator into short range and long range parts.[42] It restores the exact –1/r asymptote to the exchange potential as required for the proper treatment of Rydberg states. Long-range correction was shown to improve the predictability of the absorption spectra calculations of organic[43,44] and metallo-organic[45] chromophores and to improve dramatically the description of both typical CT excitations[46–48] as well as "disguised" ones.[39,40] In silver clusters the LC-TDDFT was found to eliminate the large number of the spurious CT states and led to a very good prediction of optical spectra of Ag_n clusters.[41] It is interesting if similar improvements can be seen in the treatment of the gold clusters.

The goal of this paper is to calculate absorption spectra of a number of Au_n (n = 4, 6, 8, 12, and 20) clusters with the range of LC functionals and compare the results with the wave function excited states method equation-of-motion coupled cluster singles and doubles (EOM-CCSD).[49] With the high-resolution experimental data for the selected clusters, n = 4 and 8, we also have a unique opportunity to gauge the computational results against matrix isolation data. It is not our aim to systematically evaluate xc functionals for their suitability in gold. Rather, we wish to identify attributes that the functionals should posses to correctly predict both the excitation energies and oscillator strengths. We are especially interested in the position of the lowest excited state, the lowest optically bright excited state (the optical gap), the structure of spectrum, i.e., the position of absorption maximum, and how these properties change as a function of geometry and cluster size.

II. METHOD

Compared to the work on Ag clusters the Au clusters bring about one significant complication—gold is arguably the most relativistic element in the Periodic Table.[5] In the present work the relativistic small-core (1s–4f) effective core potential of Figgen *et al.*[50] is used for 19 valence and outer-core $5s^2 5p^6 5d^{10} 6s$ electrons of Au. We employ the correlation consistent basis set of double-zeta quality optimized for this pseudopotential by Peterson and Puzzarini[51] (cc-pVDZ-PP, abbreviated VDZ-PP). Recent work by Olson and Gordon[52] showed that this combination correctly predicts the planarity of gold clusters up to Au_8 with CCSD(T). For the smallest cluster, Au_4, a more flexible correlation-consistent basis set aug-cc-pVTZ-PP[51] (AVTZ-PP) is employed.

The functionals used in the present work employ the range separation of the general form,

$$\frac{1}{r_{12}} = \frac{1 - [\alpha + \beta \cdot \mathrm{erf}(\omega r_{12})]}{r_{12}} + \frac{\alpha + \beta \cdot \mathrm{erf}(\omega r_{12})}{r_{12}}, \quad (1)$$

where erf stands for the error function, and ω is the range separation parameter. This expression partitions the total exchange energy into short-range and long-range contributions.

α and $\alpha+\beta$ define the fraction of HF exchange at $r_{12} = 0$ and $r_{12} = \infty$, respectively. We employ a one-parameter LC-ωPBE functional of Vydrov and Scuseria[53] as implemented in GAUSSIAN 09 (Ref. 54) which corresponds to setting $\alpha = 0$ and $\beta = 1$. The original CAM-B3LYP of Ref. 55 corresponds to the choice of $\alpha = 0.19$ and $\beta = 0.46$. In the course of this work we found it necessary to modify the asymptote of its exchange potential by setting $\beta = 0.81$. This variant is denoted CAM-B3LYP*. The functional ωB97X of Chai and Head-Gordon[56] also employs a small fraction of short-range HF exchange with $\alpha = 0.157706$, $\beta = 0.842294$ (see also Ref. 57). LC-ωPBEh proposed by Herbert's group involves a combination $\alpha = 0.2$ and $\beta = 0.8$.[48] It should be mentioned that LC-ωPBEh differs from LC-ωPBE mentioned above by not only including the short-range HF exchange but also by different short-range DFT exchange (from different models of PBE exchange hole[60] and Ernzerhof and Perdew,[61] respectively). Finally, the LC correction of Iikura *et al.*[62] was also applied to LDA and TPSS[63] pure functionals corresponding to $\alpha = 0$, $\beta = 1$.

There are a number of ways of finding the optimal value of range separation parameter. In CAM-B3LYP, $\omega = 0.33$ has been optimized for ground state properties[55] and so has been the value $\omega = 0.4$ in LC-ωPBE.[53] In the latter, the recent work on excited states of organic molecules recommends the use of $\omega = 0.20$.[43] On the other hand, the parameters ω and α (with $\alpha + \beta = 1$) in ωB97X and LC-ωPBEh have been optimized for both the ground and excited state properties yielding $\omega = 0.3$ and $\omega = 0.2$, respectively. While the strategy of finding the all-encompassing functional has a great deal of merit, there is also another school of thought advocating optimizing ω for individual systems. We will examine how well ωB97X and LC-ωPBEh with previously optimized range separation parameter will perform for gold and across all its cluster sizes. With LC-ωPBE and CAM-B3LYP* we will also explore the idea of "first-principles" tuning of these functionals as recommended by Stein *et al.*[64] In their procedure the range separation parameter ω is optimized by minimizing the following condition:

$$J'^2(\omega) = [\varepsilon_{HOMO}(N; \omega) + IP(N; \omega)]^2 + [\varepsilon_{HOMO}(N + 1; \omega) + IP(N + 1; \omega)]^2, \tag{2}$$

where IP denote the vertical ionization potentials for the neutral (N) and anionic (N+1) cluster and ε_{HOMO} denote the energies of the highest occupied molecular orbital (HOMO) for each. J'^2 value measures how well the Koopmans' theorem of the generalized Kohn-Sham (GKS) scheme (see, e.g., Ref. 65) is satisfied for both N and N+1 electron systems. In several recent works this strategy has resulted in very good predictions of excitation gaps of challenging chromophores,[66] optical rotation,[67] and charge-transfer "in disguise" excitations.[40]

The vertical singly excited states are computed using time-dependent DFT. For comparison purposes EOM-CCSD is employed for selected clusters with the same basis sets and effective core potentials as used in DFT calculations. The calculations are performed using the following program suites: GAUSSIAN 09,[54] NWChem 6.1,[68] and MOLPRO 2010.1.[69]
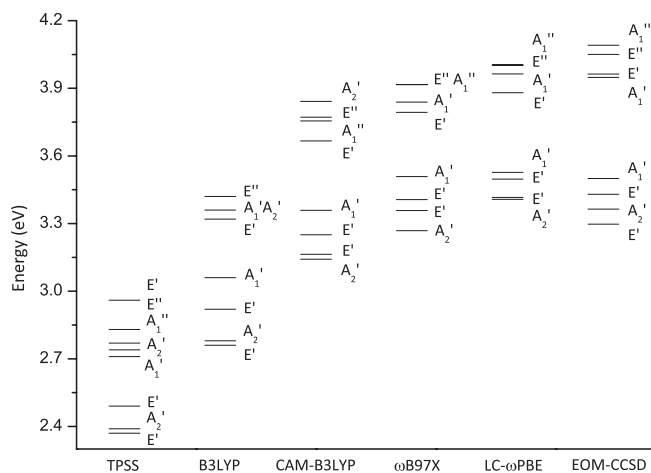

FIG. 1. Comparison of the lowest-lying excited states of Au$_6$ (D$_{3h}$) from EOM-CCSD and DFT calculations in five designated xc functionals. All calculations employ VDZ-PP basis set.

III. RESULTS AND DISCUSSION

A. Excited states of the Au$_6$ cluster

We begin with the discussion of the Au$_6$ cluster. There are no experimental UV matrix spectra for this cluster, but the analysis of Ref. 3 indicates that this is a "magic" cluster with a wide excitation gap. Thus, it can serve as a suitable model system for assessing the challenges of excited states calculations in gold clusters from the standpoint of energetics. Au$_6$ has D$_{3h}$ symmetry and its geometry was reoptimized in each of the DFT approaches as well as in CCSD. The lowest twelve vertical transitions from these ground-state optimized geometries are compared in Fig. 1. The level structure is similar in all cases: two groups of highly dense states separated by a gap of about 0.3 eV. The lowest excited state in the EOM-CCSD calculation is located at about 3.3 eV. A similar gap is obtained in ωB97X (3.27 eV) and in LC-ωPBE (3.41 eV) and a slightly lower one in CAM-B3LYP (3.14 eV). By contrast, in TPSS and B3LYP the lowest excited states lie about 2.37 and 2.76 eV above the ground state. However, the level structure retains a faint similarity to the other four. The lower group of excited states involves excitations primarily from the HOMO of Au$_6$ (e$'$) which has a large component of 6s orbitals and the upper group of states involves excitations from 5d-composed orbitals.

In all the long-range corrected functionals the lowest excited state is A$_2'$ (dark state) followed by very close-lying E$'$ to which there is the most intense transition. In EOM-CCSD calculation the most intense transition occurs at 3.425 eV to the second E$'$ state (see Fig. 1). A comparison of the absorption spectrum from EOM-CCSD and two selected LC functionals is shown in Fig. S1 of the supplementary material.[70]

B. The optical absorption spectrum of the Au$_4$ cluster

The equilibrium Au$_4$ cluster is of D$_{2h}$ symmetry as shown by all the studied xc functionals as well as CCSD. The small size of this cluster allows us to employ a larger basis set AVTZ-PP. The high-resolution spectrum of the
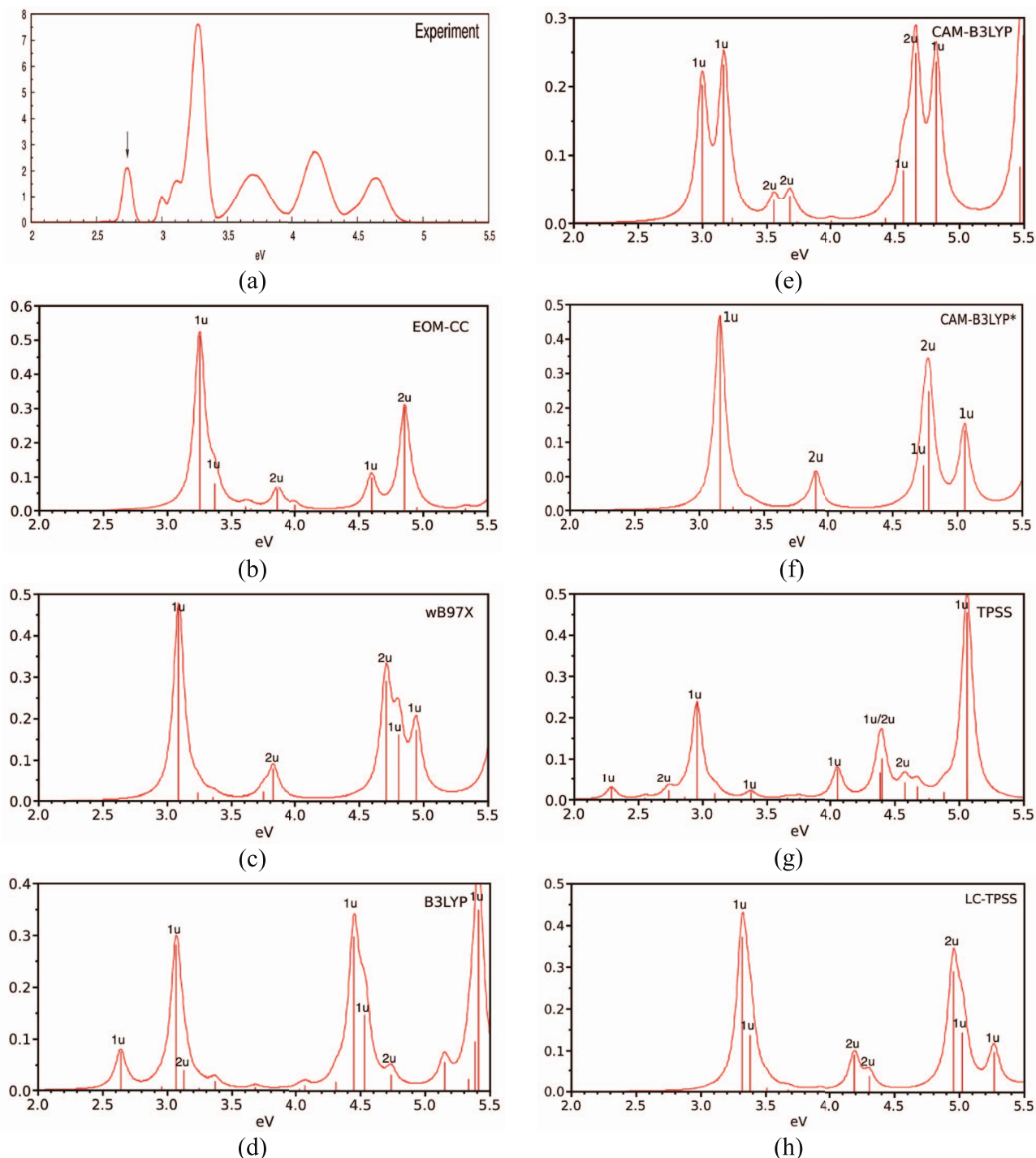
FIG. 2. Absorption spectra of the Au_4 (D_{2h}) cluster calculated with (b) EOM-CCSD and (c-h) indicated xc functionals with AVTZ-PP basis set. Vertical axes show oscillator strength. 1u and 2u denote excited state symmetries B_{1u} and B_{2u}, respectively, of the D_{2h} group. The experimental spectrum (a) of Ref. 16 is redrawn from their Fig. 3. The spectral lines are broadened with 0.05 eV H-W Lorentzian.

matrix-isolated Au_4 cluster[16] shows the most intense absorption peak at 3.33 eV along with a trio of less intense, broader peaks at 3.73, 4.20, and 4.66 eV (see Fig. 2(a)). The dendrimer-encapsulated cluster absorbs at 3.96 eV.[18]

The computed spectra are shown in Fig. 2 where they are compared with the high-resolution matrix experiment. The authors of the experiment[16] report that their spectra could only be recorded to 5.5 eV, so this is the upper limit that is shown in our results. The EOM-CC/AVTZ-PP calculations show the first intense peak at 3.254 eV corresponding to B_{1u} transitions

(molecule lies on the yz plane). There is a trio of weaker transition at 3.86, 4.60, and 4.85 eV corresponding to the B_{2u}, B_{1u}, and B_{2u} symmetries, respectively. The B_{1u} transitions are polarized along the longer axis whereas B_{2u} are polarized along the shorter one of the Au_4 rhombus. It is worth noting that B_{1u} is much more intense than B_{2u}. This fact is exploited below in the assessment of functionals. The agreement between the EOM-CC and experimental spectra is quite good except of the low-energy transition marked by an arrow in Fig. 2(a), which will be discussed at the end of this section.

TABLE I. Energetic characteristics of Au$_4$ (D$_{2h}$): the vertical ionization potential (IP) of the neutral cluster and its anion, orbital energies of the neutral and anion, HOMO-LUMO gap (E$_{HL}$) and fundamental gap (E$_g$) from different xc functionals. All energy values are in eV; J$'^2$ in (eV)^2.

| Energy (eV) | LC-ωPBE ω | | | | | LC-PBE0 | CAM-B3LYP* ω | | TPSS | LC-TPSS | ωB97X |
	0.4	0.35	0.30	0.25	0.2		0.33	0.25			
IP(N)[a]	7.30	7.38	7.47	7.57	7.68	7.51	7.56	7.67	7.74	7.43	7.44
IP(N+1)[b]	1.96	2.01	2.07	2.14	2.22	2.11	2.20	2.28	2.31	2.06	2.03
-ε_{HOMO}(N)	7.61	7.60	7.58	7.53	7.42	7.72	7.74	7.68	5.46	7.79	7.55
-ε_{HOMO}(N+1)	2.35	2.33	2.29	2.23	2.11	2.41	2.44	2.37	0.27	2.50	2.21
-ε_{LUMO}(N)	1.57	1.69	1.85	2.06	2.34	1.81	1.99	2.21	4.39	1.65	1.88
E$_g$[c]	5.26	5.27	5.29	5.30	5.31	5.31	5.30	5.40	5.18	5.29	5.34
E$_{HL}$	6.04	5.91	5.73	5.46	5.08	5.91	5.75	5.47	1.07	6.14	5.67
J$'^2$	0.250	0.154	0.061	0.010	0.084	0.133	0.092	0.009	9.330	0.320	0.042

[a]Experiment: 8.60 eV, Ref. 74.
[b]Experimental electron affinity: 2.667 ± 0.05 eV, Ref. 1.
[c]Experiment: 5.93 eV.

In the remainder of Fig. 2 we compare and contrast the long-range corrected and uncorrected functionals. The functional ωB97X shows similar pattern to EOM-CC: no active transitions below 3 eV and higher intensity of the B$_{1u}$ over the B$_{2u}$ transition. Two functionals that are not LC-corrected, B3LYP and TPSS, show completely different patterns: several weakly active transitions at low energy below 3 eV and the sharp decrease in the first intense B$_{1u}$ peak.

Let us now consider the following progression from a hybrid, B3LYP, through LC-corrected CAM-B3LYP, to asymptotically corrected CAM-B3LYP* functional (Fig. 2(d)–2(f)). CAM-B3LYP represents a slight improvement over B3LYP (disappearance of the lowest energy peak) but the spectrum is still quite odd. Namely, the first main B$_{1u}$ peak splits into two components (3.00 and 3.17 eV) of nearly equal intensity and so does the second peak (3.56 and 3.68 eV). Furthermore, the B$_{2u}$ feature at 4.67 eV becomes the most intense in the 2–5 eV region. CAM-B3LYP* (applied at the same CAM-B3LYP optimized geometry) fixes these problems leading to much better agreement with EOM-CC.

The second example involves TPSS and its variant, LC-TPSS, resulting from the application of the LC correction[62] with ω = 0.47 as optimized in Ref. 71. TPSS provides the most unlike spectrum of those displayed in Fig. 2. The LC correction brings it to a reasonably close agreement with EOM-CC.

To understand what happens to the properties of Au$_4$ as a consequence of the LC correction, the following computed properties are assembled in Table I: vertical ionization potentials of the neutral Au$_4$ (IP(N)) and of the negative ion Au$_4^-$ (IP(N+1)) obtained as ΔSCF, the negative of the DFT eigenvalue (-ε_{HOMO}) of Au$_4$ and of Au$_4^-$ (-ε_{HOMO}(N+1)). The difference, IP(N)-IP(N+1) = E$_g$, is the so-called (vertical) fundamental gap whereas the difference, $\varepsilon_{LUMO} - \varepsilon_{HOMO}$ = E$_{HL}$, is referred to as the HOMO-LUMO gap. The two gaps are not expected to equal[72] because of the functional derivative discontinuity.[73]

Let us begin with case of TPSS. The results of Table I show that TPSS and LC-TPSS lead to very similar values of IP(N) and also to similar values of IP(N+1). Consequently,

the E$_g$ values are also similar in both functionals and both are close to experiment by less than 1 eV. The differences appear when we examine orbital energies. In LC-TPSS the -ε_{HOMO} energy is reasonably close to IP(N); in TPSS these quantities differ by ~2 eV. Similarly, -ε_{HOMO}(N+1) is reasonably close to IP(N+1) in LC-TPSS, whereas it differs by 2 eV in TPSS. The difference between E$_g$ and E$_{HL}$ is particularly telling. While applying the LC correction to TPSS increases E$_{HL}$ by about 5 eV, the fundamental gaps remain almost the same. In LC-TPSS E$_{HL}$ nearly equals E$_g$, in TPSS E$_{HL}$ is smaller then E$_g$ by 4 eV. Furthermore, E$_{HL}$ in TPSS is 0.2 eV smaller than the energy of the first excited state, which is dominated by the HOMO-LUMO excitation. This, in light of Ref. 66, does not comport with a quasi-electron-quasi-hole picture of this excitation.

The value of the range-separation parameter in LC-TPSS mentioned above has been empirically optimized.[71] There is also a great deal of recent interest in the "first-principles" tuning of the value of the range separation parameters, such as by the minimization of the expression in Eq. (2). The value of J$'^2$ is listed in Table I for a number of functionals.

To further examine merits of tuning functionals, the same energetical quantities underlying Eq. (2) have been computed as a function ω in the LC-ωPBE functional (Table I). The E$_{HL}$ gap decreases rapidly with the lowering of ω. This is largely due to rapid change in the LUMO energy, which is the most sensitive to ω. J$'^2$ shows the minimum for ω = 0.25, roughly speaking. It is interesting to examine how this minimization of J$'^2$ correlates with the appearance of the spectrum of Au$_4$ (see Fig. 3). The evolution of the spectrum (Fig. 3) shows that B$_{1u}$ absorption at 3.2–3.3 eV remains well defined and most intense for ω > 0.35—in agreement with EOM-CC. At $\omega \leq 0.35$ this peak begins to split into two and to lose intensity. The high-energy region of the spectrum also appears to deteriorate. The second signature absorption, B$_{2u}$ around 4.8 eV, remains almost unchanged but it becomes surrounded by an increasing number of low intensity B$_{1u}$ transitions. If one were to choose the value of ω on the basis of the apparent agreement of the LC-ωPBE spectrum with EOM-CC, the choice would be ω = 0.4. However, according to Table I, the
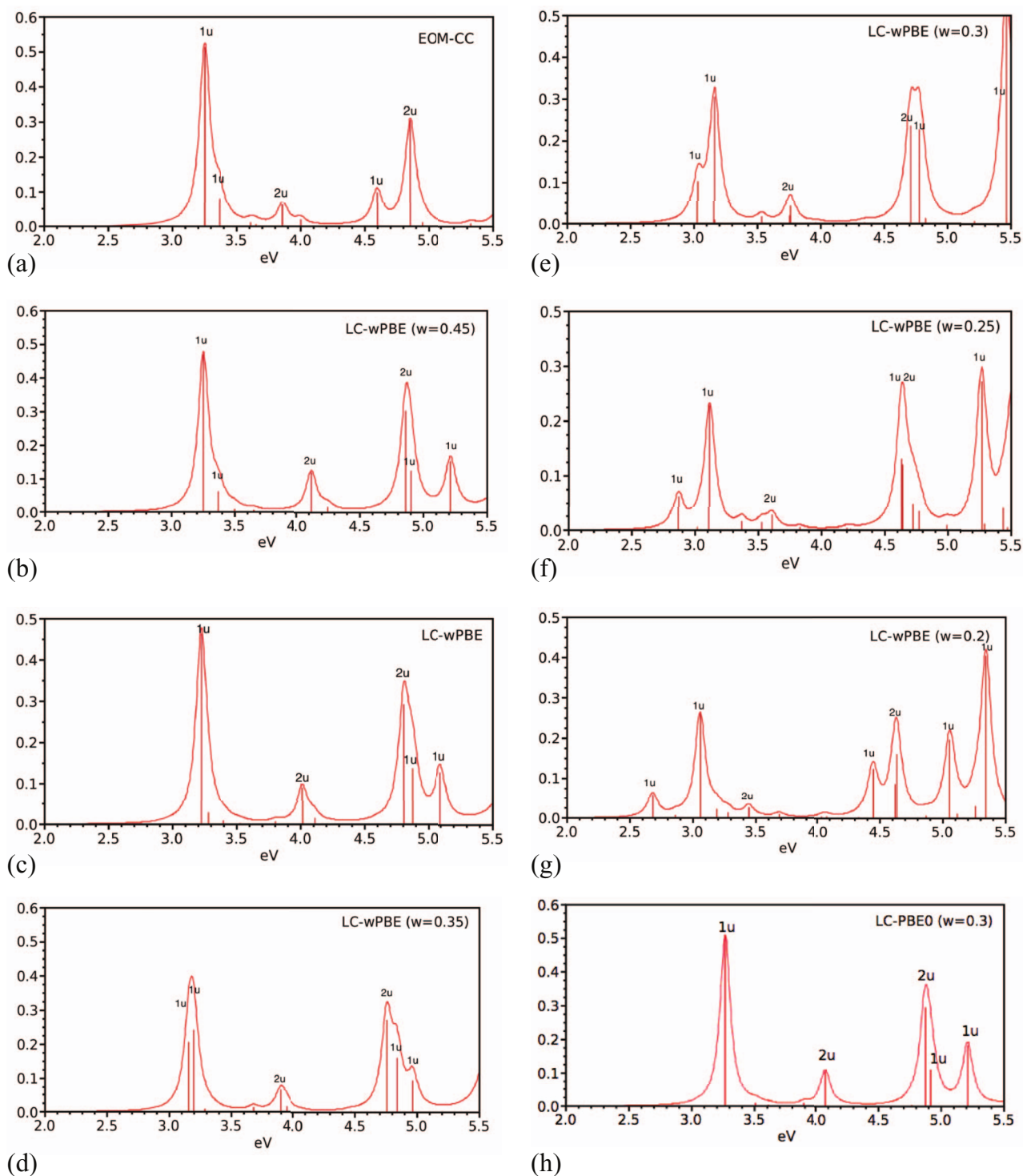
FIG. 3. Dependence of the Au$_4$ spectrum on the range separation parameter in LC-ωPBE (b-g) (the original LC-ωPBE is shown in (c) and corresponds to $\omega = 0.4$; and (h) in LC-PBE0 (for definition see the text). (a) shows EOM-CC spectrum. Spectra (b-h) obtained in the LC-ωPBE ($\omega = 0.4$) optimized geometry. The spectral lines are broadened with 0.05 eV H-W Lorentzian.

choice of ω that minimizes the J'^2 value is equal to 0.25. Actually, $-\varepsilon_{HOMO}(N)$ crosses IP(N) at a slightly different value than $-\varepsilon_{HOMO}(N+1)$ and IP($N+1$). Furthermore, at this ω, the value of E_{HL} becomes almost equal to E_g thus "absorbing" most of the derivative discontinuity. Despite satisfying these conditions, the spectrum for $\omega = 0.25$ functional (Fig. 3(f)) is incorrect compared to EOM-CC as it is cluttered with spu-

rious transitions particularly of B$_{1u}$ type. Is this a symptom of nonlinearity of the functional between the integral electron numbers[75] in Au$_4$?

The test for detecting the presence of the delocalization/localization error involves the determination of how the total energy behaves between the integer values of electron numbers. In the exact functional this dependence should be
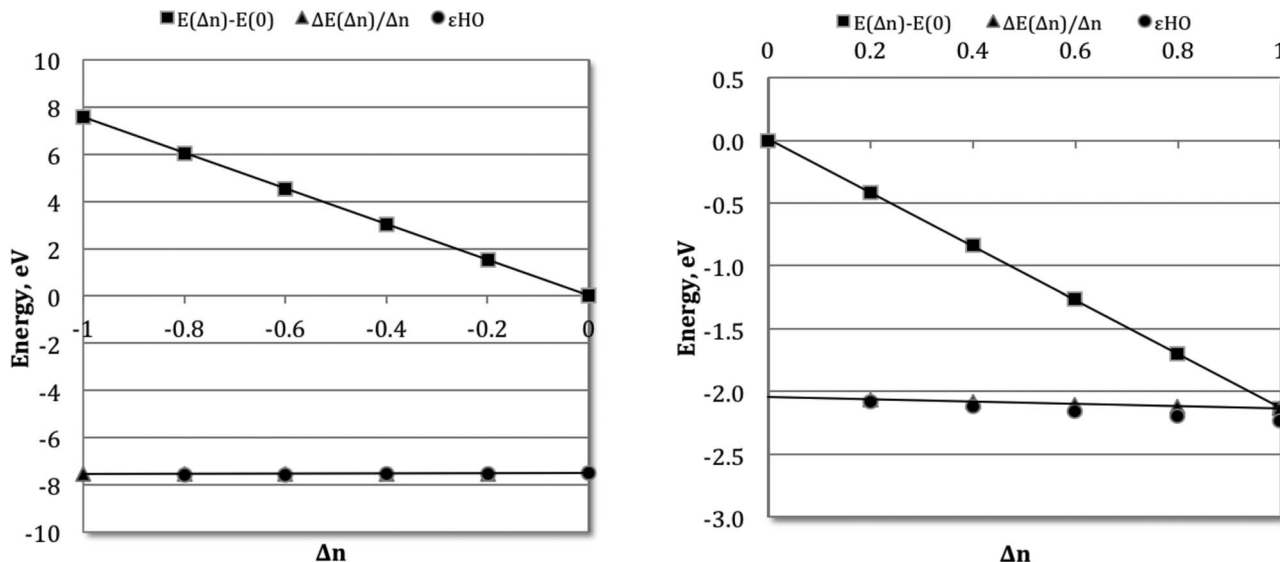
FIG. 4. Dependence of the total energy of Au_4 on the fractional electron numbers within the optimized LC-ωPBE ($\omega = 0.25$) functional: left panel - cation to neutral; right panel - neutral to anion. Calculations use aug-cc-pVTZ-PP basis set.

linear from the cation to the neutral and from the neutral to the anion, showing a discontinuity in the first derivative at the neutral. Departures from the linear behavior with respect to fractional electron numbers indicate presence of the delocalization/localization error.[75–77]

For Au_4, Fig. 4 presents the dependence of the total energy E on fractional electron number Δn for $-1 < \Delta n < 0$ (cation to neutral) and $0 < \Delta n < +1$ (neutral to anion) in the optimized functional LC-ωPBE ($\omega = 0.25$). $E(\Delta n) - E(0)$ varies linearly with the fractional charge for both cation to neutral and neutral to anion segments showing a discontinuity in the first derivative at the neutral. Also plotted is the derivative $dE(\Delta n)/d(\Delta n)$ and the HOMO energy for both situations. For the accurate functional $dE(N)/dN|_{N-|\Delta n|} = IP(N)$ for $-1 < \Delta n < 0$ and $dE(N)/dN|_{N+\Delta n} = IP(N+1)$ for $0 < \Delta n < +1$. IP(N) and IP(N+1), in turn, should be equal to $-\varepsilon_{HOMO}$ of the neutral and anion, respectively. As seen in Fig. 4 these relationships are almost exactly satisfied in the examined functional as per Janak's theorem.[78] We conclude that the reasons for the failure of the optimized functional are not related to these errors.

Interestingly, a greatly improved spectrum can be obtained by switching to a LC functional with the constant fraction of the HF exchange. To this end one can apply the LC correction to the hybrid functional PBE0.[79] This functional was first proposed for excited-state calculations by Rohrdanz and Herbert[80] with the choice of $\omega = 0.3$, $\alpha = 0.25$, and $\beta = 0.75$ (denoted LC-PBE0; not to be confused with LC-ωPBEh used later on). The LC-PBE0 spectrum (Fig. 3(h)) shows very good agreement in excitation energies and oscillator strengths with the EOM-CC result. It is noteworthy that it increases the value of J'^2 parameter (0.13 vs. 0.009 for LC-ωPBE (0.25)).

With regard to the CAM-B3LYP results, we showed above that adjusting its β parameter to 0.81 resulted in a dramatic improvement of the Au_4 spectrum (see Figs. 2(e) and 2(f)). This improvement was associated with one order of

magnitude decrease in J'^2: from 0.8 in CAM-B3LYP to 0.09 in CAM-B3LYP*. One might wonder if optimal tuning of this functional by varying the range separation parameter (while keeping α and β unchanged) would result in further improvement of the spectral predictions. Surprisingly, the answer is no. The optimized variant of CAM-B3LYP* with $\omega = 0.25$ (see Table I) leads to an equally poor spectrum as the original CAM-B3LYP shown in Fig. 2(e).

The list of recommended functionals and their results for the key transitions in Au_4 is shown in Table II. A common element in the featured functionals that include a short-range HF exchange is that their ω value is 0.3–0.33. If they do not, as in the case of LC-ωPBE, ω should be larger and the standard $\omega = 0.4$ is satisfactory. All calculations predict two dark states in the region below 3 eV. The second of them, A_g, closely corresponds to the low-intensity peak seen in the experimental spectrum at 2.80 eV (see in Fig. 2(a) marked by arrow). The optimized LC-ωPBE($\omega = 0.25$) reproduces only the first dark state (at 1.39 eV) followed by the *three more* dark states and the first active one at 2.87 eV as shown in Fig. 3(f).

To conclude, applying the LC correction leads to the lowering of J'^2 and to improved agreement of the spectrum with EOM-CC compared to the uncorrected functional. In the case

TABLE II. Comparison of the key transitions in the spectrum of Au_4 (D_{2h}). The results of the recommended functionals are compared with EOM-CC. CAM-B3LYP* denotes $\alpha = 0.19$ and $\beta = 0.81$ combination. The numbers in parentheses denote the value of range-separation parameter. The HOMO-LUMO excitation is marked in boldface.

Method	1st dark (B_{3g})	2nd dark (A_g)	B_{1u}	B_{2u}	B_{2u}
EOM-CC	**1.50**	2.72	3.25	3.86	4.86
LC-ωPBE (0.4)	**1.52**	2.63	3.23	4.02	4.81
ωB97X	**1.38**	2.62	3.09	3.83	4.71
CAM-B3LYP*	**1.41**	2.64	3.16	3.90	4.78
LC-PBE0 (0.3)	**1.47**	2.75	3.24	4.02	4.84

of CAM-B3LYP, adjusting β to correct the asymptote of the potential results in both better agreement of the computed spectrum with EOM-CC and lowered J'^2. In the series of LC-ωPBE functionals with varied ω, the minimization of J'^2 does not lead to a better appearance of the spectrum, although it leads to an almost complete elimination of the delocalization error. However, adding a constant fraction of the short-range HF exchange, as in the case of LC-PBE0, leads to a dramatic improvement.

C. The optical absorption spectrum of the Au$_8$ cluster

The calculations in this section were performed with the VDZ-PP basis set. The geometry of Au$_8$ was optimized at the CCSD level of theory and with several DFT approaches showing the D$_{4h}$ (Diagram 1) isomer to be consistently more stable than C$_{2v}$, in full accord with previous studies.[3,52] The optimized parameters of D$_{4h}$ structure show small variations among the methods (see Table S1 of the supplementary material[70]).

Diagram 1: D$_{4h}$ and C$_{2v}$ structures of Au$_8$ cluster.
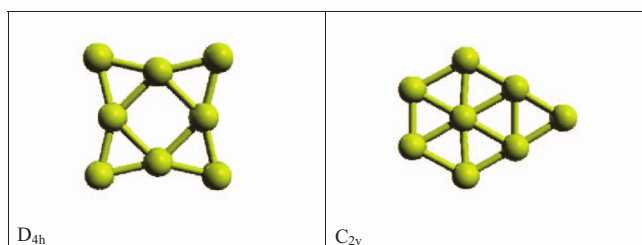
The experimental spectrum[16] (Fig. 5(a)) is highly structured and contains prominent transitions at 3.23, 3.69, 4.17, and 4.69 eV. There are also two low-energy features: a broader peak at 2.66 eV and a sharp and narrow doublet at 2.91/2.97 eV (marked by arrows). The experiment of Zheng *et al.*[17] shows the absorption of dendrimer-encapsulated Au$_8$ at 3.22 eV. The calculated optical spectrum of Au$_8$ as obtained from various methods is presented in Figs. 5 and 6, and S2 of the supplementary material.[70]

EOM-CC predicts the first bright state at 3.29 eV of the E$_u$ symmetry followed by a sequence of strong transitions at 3.64 and 4.52 eV and some weaker ones near 5 eV. All of them are of the E$_u$ symmetry except for one very faint A$_{2u}$ transition at 4.49 eV. All intense peaks thus correspond to the transition moment vectors lying on the cluster plane. The lowest dark excited state is at 2.67 eV and it is of A$_{2g}$ symmetry. One should mention that the ground state, reference CCSD wave function has some doubles' character as indicated by the D1 diagnostic[81] value around 0.076. This may increase a likelihood of low-lying doubly excited states, which typically entail much larger errors. Our additional calculations employing non-singles initial guesses did not detect any such states.

LC-corrected functionals yield spectra with similar general characteristics as EOM-CC. First, no active transitions appear below 3 eV. Second, the pattern of dominant transitions and their oscillator strengths resembles that of the EOM-CC spectrum. The functionals featured in Fig. 5 match these characteristics most accurately. LC-ωPBEh with parameters
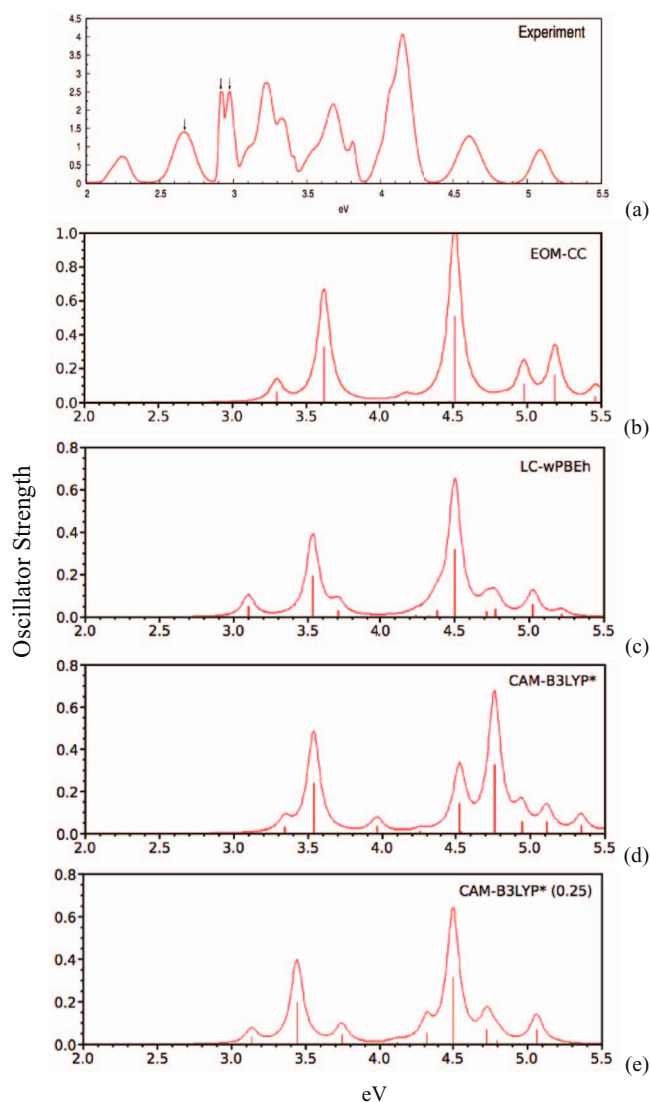

FIG. 5. The optical spectrum of Au$_8$ (D$_{4h}$) from (a) experiment (Ref. 16), (b) EOM-CC, (c-e) LC-DFT. The LC-ωPBEh spectrum (c) is computed at the LC-ωPBE optimized geometry. The basis set is VDZ-PP. The spectral lines are broadened with 0.05 eV H-W Lorentzian.

recommended by Herbert's group ($\omega = 0.2$ and $\alpha = 0.20$, $\beta = 0.80$)[48] leads to a very good agreement with EOM-CC for the three key transitions. Two variants of CAM-B3LYP* are worthy of mention: the one with $\omega = 0.25$ is nearly as good as LC-ωPBEh whereas the one with the original $\omega = 0.33$ value differs somewhat in the most intense transition region that splits into two peaks. The latter result is strikingly similar to the spectrum obtained by using ωB97X (not shown). Incidentally, both functionals have a similar value of the range separation parameter (0.33 and 0.3, respectively). To further elaborate on this observation we apply the LC correction to three pure functionals from three different rungs: LDA, GGA, and meta-GGA. The results are shown in Fig. S2 of the supplementary material.[70] It appears that the resulting spectra look very much alike regardless of the type of functional if the value of ω is the same.

The corresponding energetic characteristics of the featured functionals are displayed in Table III along with the LC-ωPBE functional with the varied ω parameter. The two
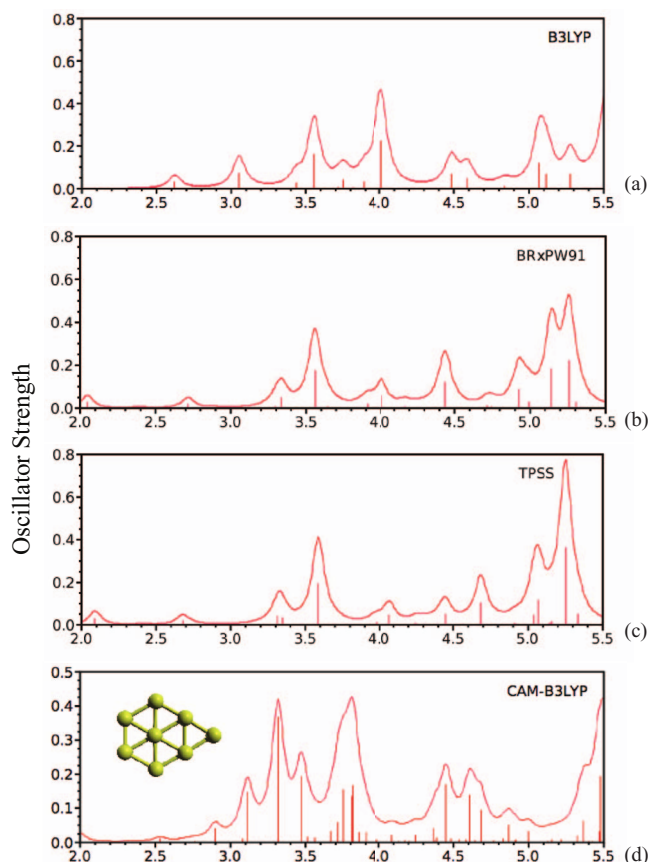
FIG. 6. A comparison of optical spectra of Au_8 (D_{4h}) (a-c) in three functionals B3LYP, BRxPW91, and TPSS with (d) Au_8 (C_{2v}) from CAM-B3LYP. The spectral lines are broadened with 0.05 eV H-W Lorentzian. The units on the abscissa are eV.

TABLE IV. Comparison of the key transitions in the spectrum of Au_8 (D_{4h}). The results of the recommended functionals are compared with EOM-CC. The calculations were performed in optimized geometries of LC-ωPBE(0.40), CAM-B3LYP, and ωB97X, respectively. CAM-B3LYP* denotes combination $\alpha = 0.19$ and $\beta = 0.81$. The numbers in parentheses denote the values of the range-separation parameter. The HOMO-LUMO excitation is marked in boldface.

Method	1st dark	2nd dark	1st active	Medium	Most intense
EOM-CC	**2.67**	2.81	3.29	3.64	4.52
LC-ωPBEh (0.20)	2.51	**2.67**	3.10	3.53	4.50
CAM-B3LYP*(0.25)	2.64	**2.69**	3.14	3.44	4.50
CAM-B3LYP* (0.33)	**2.79**	2.87	3.34	3.53	4.53/4.76
ωB97X (0.30)	**2.78**	2.91	3.36	3.53	4.50/4.75

(see Fig. S3(e) of the supplementary material[70]) is strongly red-shifted and its intensity is decreased by one half compared to LC-ωPBEh (Fig. 5(c)). The CAM-B3LYP*($\omega = 0.2$) spectrum is also red-shifted by ~0.2 eV compared to CAM-B3LYP*($\omega = 0.25$) (Fig. 5(e)) but without the intensity loss.

The recommended functionals and their results for the key transitions in Au_8 are listed in Table IV. The common characteristic of recommended functionals is the inclusion of a short-range HF exchange. The functionals with ω of 0.33/0.3 describe better the low-energy part of the spectrum than the region of the most intense peak. The ones with ω of 0.2–0.25 do just the opposite: reproduce the most intense transition accurately but underestimate the lower-energy part of the spectrum (although not by much). All calculations predict two dark states in the region below 3 eV of A_{2g} symmetry. One of them is the HOMO-LUMO transition (numbers marked in boldface in Table IV). By comparison, the "optimal" functional LC-ωPBE (0.25) correctly reproduces only the HOMO-LUMO transition (2.65 eV) as its second dark state. Its first dark state appears lower, at 2.3 eV, whereas its first bright state occurs at 2.88 eV. The data for Au_8 (Table III) and Au_4 (Table I) show that this functional not only satisfies nearly perfectly the Koopmans' theorem for both the neutral and the anion, but also shows linear behavior with

best performers in Fig. 5, LC-ωPBEh and CAM-B3LYP*($\omega = 0.25$), have very low values of $J'^2 - 0.01$ and 0.02 eV^2, respectively. We also include in Table III the two optimized functionals for which the J'^2 parameter has been minimized: LC-ωPBE($\omega = 0.25$) and CAM-B3LYP*($\omega = 0.2$). However, in both cases the optimization results in misrepresentation of spectral features. The LC-ωPBE ($\omega = 0.25$) spectrum

TABLE III. Energetic characteristics for Au_8 (D_{4h}): the vertical ionization potential of the neutral (IP(N)) and negative ion (IP(N+1)), frontier orbital energies, HOMO-LUMO gap (E_{HL}) and fundamental gap (E_g) from different xc functionals and their dependence on the range separation parameter ω. All energy values are in eV; J'^2 is expressed in (eV)^2.

Energy (eV)	LC-ωPBE				LC-ωPBEh	CAM-B3LYP*			ωB97X
	ω					ω			
	0.4	0.35	0.30	0.25		0.33	0.25	0.20	
IP(N)[a]	8.14	8.17	8.21	8.23	8.11	8.26	8.28	8.26	8.06
IP(N+1)[b]	2.02	2.09	2.18	2.28	2.21	2.23	2.35	2.42	2.09
-ε_{HOMO}	8.41	8.38	8.34	8.26	8.11	8.45	8.36	8.22	8.20
-ε_{HOMO} (N+1)	2.39	2.40	2.42	2.42	2.32	2.48	2.49	2.45	2.30
-ε_{LUMO}	1.69	1.81	1.97	2.17	2.13	2.02	2.24	2.40	1.91
E_g[c]	6.12	6.08	6.03	5.94	5.90	6.03	5.94	5.84	5.96
E_{HL}	6.72	6.58	6.37	6.09	5.98	6.42	6.12	5.82	6.29
J'^2	0.208	0.143	0.074	0.019	0.010	0.098	0.024	0.003	0.066

[a]Experiment: 8.65 eV, Ref. 74.
[b]Experimental value of electron affinity: 2.764 ± 0.05, Ref. 1.
[c]Experiment: 5.89 eV.

respect to fractional electron numbers (see Sec. II). So what can be wrong? Since in both Au_4 and Au_8 this functional predicts very accurately only the inactive HOMO-LUMO transition leaving the remaining ones seriously off, our hypothesis is that in LC-ωPBE the tuning procedure optimizes primarily the frontier orbitals leaving the remaining ones in the wrong place energetically. A recent work of Refaely-Abramson *et al.*[82] clearly confirms this hypothesis by showing that with $\alpha = 0$ a group of localized inner orbitals may be incorrectly ordered even with the optimally tuned ω parameter. This problem is rectified by including a fixed portion of the HF exchange in the short range, i.e., by setting $\alpha > 0$, as evidenced by a good performance of LC-ωPBEh ($\omega = 0.20$, $\alpha = 0.2$).

The results for non-LC corrected functionals are shown in Figs. 6(a) to 6(c). In addition to B3LYP and TPSS we also show results for a functional combining the Becke-Roussel (BRx)[83] exchange with the PW91 correlation. The reason for considering this particular exchange potential is that it has the correct asymptotic behavior of exchange energy density.

All three functionals show active transitions below 3 eV, albeit the faint ones, in sharp contrast to the EOM-CC spectrum. Nevertheless, they correctly predict the 3.6 eV transition. One interesting aspect of the BRxPW91 spectrum is that it also predicts a 4.5 eV transition although less intense than the one at 3.6 eV. Both BRxPW91 and TPSS, however, predict the first, HOMO-LUMO dominated, excited state as lying above the E_{HL} gap.

It is instructive to compare the present results (Table IV) with those of the TD-LDA study.[22] The LDA calculations predict the lowest bright state at much lower energy of 1.96 eV, a large number of low-intensity transitions followed by a strong absorption at 3.32 eV.

At this juncture, we should address the discrepancies between the experimental spectrum in Fig. 5(a) and EOM-CC as well as the LC-corrected functionals. The 2.66 eV and 2.91/2.97 eV features marked by the arrows in the experimental spectrum roughly correspond to dark A_{2g} states in the EOM-CC spectrum (at 2.67 and 2.81). Another discrepancy concerns the transition around 3.2–3.3 eV. In the experiment this transition is very intense, whereas in EOM-CC and the LC-corrected functionals it is comparatively weak. One possibility may involve the C_{2v} isomer, the presence of which was mentioned in the work of Rath *et al.*[19] involving the resin-stabilized Au_8. Although energetically unfavorable by 0.5–0.6 eV (see Table V), this isomer's spectrum shown in Fig. 6(d) from CAM-B3LYP features an intense transition around 3.2–3.3 eV. At higher energies, however, the spec-

trum becomes highly unstructured and band-like; hardly the match for the well structured experimental spectrum. The most intense experimental transition at 4.17 eV corresponds to the 4.5 eV peak in EOM-CC, LC-ωPBEh(0.2) and CAM-B3LYP*(0.25). The difference of 0.3 eV is sizable but not out of bounds given the neglect of spin-orbit coupling.[23, 84]

To further compare the optical properties of both isomers one can compare the sum rules for oscillator strengths in both geometries with different functionals. The Thomas-Reiche-Kuhn sum rule states that the sum of oscillator strengths for excitations from the ground state should sum-up to the total number of electrons (e.g., in an atom). The sums of oscillator strengths are shown in Table V. One can see that ωB97X and LC-ωPBE($\omega = 0.4$) give the values of *about* 8. This means that the Au_8 cluster may be viewed (approximately) as an 8-electron superatom in the spirit of shell model.[2] This description is better for D_{4h} symmetry and is highly sensitive to the quality of functional. It is noteworthy that the sum falls short of 8 electrons in LC-ωPBE with $\omega = 0.25$ thus indicating the oscillator strength losses at small ω. By contrast, adjusting the asymptote of CAM-B3LYP raises the sum from 6.6 to 8.1.

D. The optical absorption spectrum of Au₁₂

The three long-range corrected functionals, LC-ωPBE, ωB97X, and CAM-B3LYP, predict the Au_{12} cluster to form a D_{3h} structure in agreement with previous studies.[3, 85] Based on the conclusions of Sec. III C we computed the optical absorption spectra of Au_{12} with the following functionals: ωB97X, two variants of CAM-B3LYP* with $\omega = 0.33$ and 0.25, and LC-ωPBEh ($\omega = 0.20$, $\alpha = 0.20$, $\beta = 0.80$). Unfortunately, EOM-CC calculations were beyond our capabilities. The results are shown in Fig. 7.

The four considered functionals are in nearly quantitative agreement with one another in the spectral predictions. The lowest bright state is located at much lower energies than in the smaller clusters and followed by a gap of $\sim$1 eV to a characteristic trio of intense features separated by about 0.4–0.5 eV (we will refer to them as A, B, and C). All transitions are to E' states. Therefore, as in the other planar clusters, all absorptions are cluster plane-polarized. The characteristic transitions are tabulated in Table VI.

The first dark state lies much lower than in Au_4 and Au_8: at $\sim$1.3 eV, and the E_{HL} gap is also narrower. The transition energies shown in Table VI agree to within 0.1 eV among each other and the intensities are also very similar with the

TABLE V. Properties of Au_8 cluster in two different geometries D_{4h} and C_{2v}. Relative energy describes the energy difference between the two conformers. f_{0i} denotes oscillator strength of a transition from 0 to i state; sum over 200 states.

Functional:	B3LYP		CAM-B3LYP		LC-ωPBE(0.4)		ωB97X	
Geometry:	C_{2v}	D_{4h}	C_{2v}	D_{4h}	C_{2v}	D_{4h}	C_{2v}	D_{4h}
Relative energy, eV	0.502	0	0.588	0	0.626	0	0.637	0
$\sum_i f_{0i}$	3.2	4.3	5.8	6.6[a]	7.6	8.3[b]	7.4	8.1

[a]For CAM-B3LYP* the sum is 8.1.
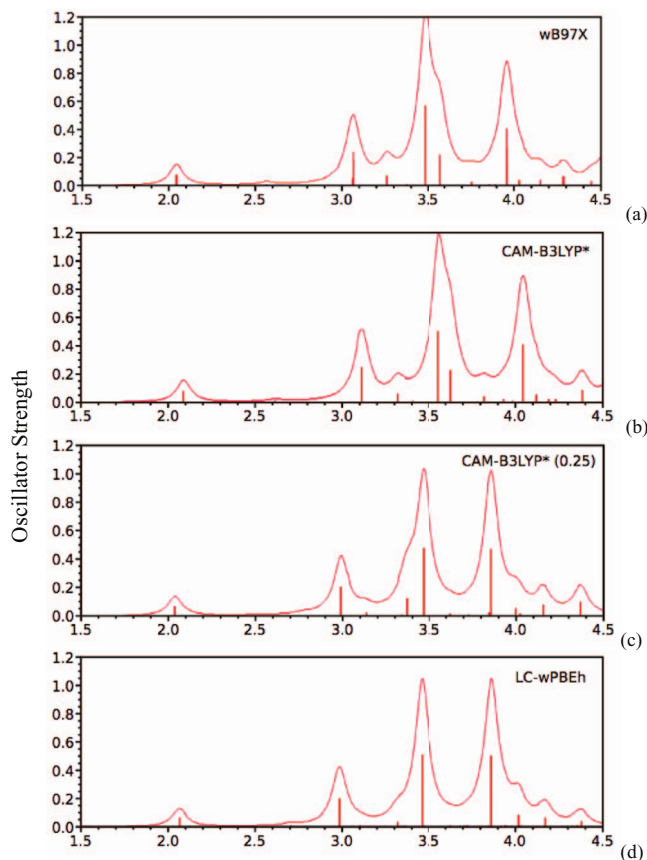[b]For $\omega = 0.25$ the sum is 6.49 (see spectrum in Fig. S3 (e)).

FIG. 7. Calculated spectrum of Au_{12} with the four LC corrected functionals: CAM-B3LYP* involves modified parameter $\beta = 0.81$; LC-ωPBEh involves $\omega = 0.2$, $\alpha = 0.2$, $\beta = 0.8$. Calculations use VDZ-PP basis set. The spectral lines are broadened with 0.05 eV H-W Lorentzian. The units on the abscissa are eV.

TABLE VI. Comparison of the key transitions and the HOMO-LUMO gaps (E_{HL}) for Au_{12} (D_{3h}) in the functionals featured in Fig. 7. All values are in eV.

Functional	1st dark (A_2')	1st active	A	B	C	E_{HL}
ωB97X	1.31	2.05	3.07	3.49	3.96	4.75
CAM-B3LYP*	1.32	2.09	3.11	3.56	4.04	4.84
CAM-B3LYP*(0.25)	1.27	2.04	2.99	3.47	3.86	4.63
LC-ωPBEh	1.30	2.07	2.99	3.46	3.87	4.54
LC-ωPBE(0.35)	1.32	2.13	3.08	3.55	3.94	4.91

only one intense feature at 2.76 eV of comparable oscillator strength to our values.

E. Optical absorption spectrum of Au_{20}

The calculations for Au_{20} are performed in the T_d geometries optimized within each of the three functionals: LC-ωPBE(0.40), ωB97X, and CAM-B3LYP. A sample of LC functionals with their energetics is surveyed in Table VII.

In view of findings for Au_4 and Au_8 the desirable characteristics for the predictions of the Au_{20} spectrum are seen in ωB97X, CAM-B3LYP* with $\omega = 0.25$ and LC-ωPBEh. The remaining surveyed functionals have either too large values of J'^2 or too large fundamental gaps or both. The optimization of CAM-B3LYP* has led to $\omega = 0.20$ and J'^2 value of 0.07 eV^2.

The computed spectra are shown in Fig. 8. The LDA spectrum from the work of Idrobo *et al.*[22] is included for comparison. All transitions are of T_2 symmetry. The key transitions are summarized in Table VIII.

Our predicted spectra differ dramatically in appearance from the results of previous LDA computations (Fig. 8(e)).[22] The LDA spectrum contains large number – indeed a near continuum – of low intensity transitions. By contrast, our results consistently predict the intensity being concentrated in only a few transitions with one very intense peak (marked C) around 3.5–3.6 eV. The majority of other symmetry-allowed transitions have either zero or near zero oscillator

exception of the B peak which consists of two transitions in ωB97X and CAM-B3LYP* (see Fig. 7).

Present results can be compared with the LDA findings of Idrobo *et al.*[22] who also determined the D_{3h} structure to be the most stable. Their computation predicts the lowest bright state at 1.63 eV, a large number of very weak transitions and

TABLE VII. Energetic characteristics for Au_{20} (T_d): the vertical ionization potential of neutral (IP(N)) and anion (IP(N+1), frontier orbital energies, HOMO-LUMO gap (E_{HL}), and fundamental gap (E_g) from different xc functionals. The parameters of LC-ωPBEh are $\omega = 0.20$ and $\alpha = 0.20$, $\beta = 0.80$; asterisk denotes $\alpha = 0.19$ and $\beta = 0.81$ combination. The parameters in parentheses denote values of range separation parameter. All energy values are in eV; J'^2 is expressed in $(eV)^2$.

| | LC-ωPBE | | | CAM-B3LYP* | | | | |
| | ω | | | ω | | | | |
Energy (eV)	0.40	0.35	LC-ωPBEh	0.33	0.25	ωB97X	LC-TPSS(35)	LC-LDA(35)
IP(N)[a]	8.42	8.41	7.19	7.47	7.47	7.32	8.66	8.96
IP(N+1)[b]	1.91	1.97	2.06	2.07	2.17	1.97	1.80	2.10
$-\varepsilon_{HOMO}(N)$	7.67	7.64	7.47	7.90	7.81	7.71	7.86	8.20
$-\varepsilon_{HOMO}(N+1)$	2.24	2.26	2.22	2.32	2.36	2.20	2.19	2.46
$-\varepsilon_{LUMO}(N)$	1.61	1.70	1.92	1.85	2.01	1.76	1.91	2.24
E_{HL}	6.06	5.94	5.54	6.06	5.79	5.94	5.95	5.97
E_g[c]	6.51	6.44	5.13	5.40	5.30	5.35	6.86	6.87
J'^2	0.648	0.672	0.101	0.248	0.146	0.193	0.653	0.600

[a]Experiment: 7.82 eV, Ref. 74.
[b]Experimental value of vertical electron affinity: 2.751 eV, Ref. 25.
[c]Experiment: 5.07 eV.

TABLE VIII. Comparison of key transitions in the spectrum of Au_{20} (T_d). The calculations were performed in optimized geometries of LC-ωPBE(0.40), CAM-B3LYP, and ωB97X, respectively. CAM-B3LYP* denotes a combination $\alpha = 0.19$ and $\beta = 0.81$. The numbers in parentheses denote the value of range-separation parameter.

Method	1st dark	A	B	C
ωB97X	2.58	2.93	3.37	3.57
CAM-B3LYP*	2.57	2.96	3.44	3.67
CAM-B3LYP*(0.25)	2.53	2.85	3.28	3.50
LC-ωPBEh(0.20)	2.41	2.74	3.21	3.44

strengths. The near continuum of low-intensity states in previous TDDFT calculations employing both LDA[22] and GGA[27] functionals appears to be an artifact of these functionals as first observed by Silverstein and Jansen[41] for the Ag_n clusters.

A comparison between the CAM-B3LYP*(0.33) and CAM-B3LYP*(0.25) results indicates that lowering ω from 0.33 to 0.25 shifts the spectrum 0.1–0.2 eV toward low energy. The CAM-B3LYP*(0.25) spectrum is in very good agreement with that of LC-ωPBEh although the latter has noticeably lower intensity. The optimized CAM-B3LYP(ω = 0.2) functional resulted in deterioration of the spectrum. The LC functionals featured in Fig. 8 and Table VIII predict on average the first active transition around 2.87 eV and the first dark state around 2.54 eV.

There are several previous investigations of the Au_{20} cluster and its optical spectrum by TDDFT.[22,25,27,29] The differences between them and our present results are not limited to absorption near-continuum discussed above. LDA and pure GGA functionals also tend to shift the absorption peaks toward low energies. Let us compare the position of the two characteristic peaks: the first active, weak peak (marked A) and the first intense one (marked C). All previous studies predict them at much lower energies. LDA calculation[22] produces the weak one at 1.85 eV, and the strong one at 2.78 eV. BP86 calculation[27] finds the former at about 1.9 eV and the latter at 2.89 eV. A hybrid functional B3LYP does better: the A peak is at 2.369 eV as reported by Xie *et al.*[31] (unfortunately the second one was not reported in their work). Most similar, albeit still on the low energy side of our values, are the LB94 results predicting the A peak at 2.355 and the C peak at 3.20 eV.[29]

Another issue where our results differ from previous findings for Au_{20} concerns the HOMO-LUMO gap. In our featured functionals E_{HL} is quite close to the fundamental gap E_g, the value of which has been determined experimentally to be about 5 eV. The literature values of E_{HL} most often mentioned are GGA results in the range of 1.8–1.9 eV (see Ref. 86 for a compilation of E_{HL} values). The calculations employing hybrid functionals which tend to increase these gaps[47] provide somewhat larger values of 2.93 using B3LYP[31] or 3.1 eV using PBE0.[87] These values are still smaller by some 2 eV compared to the LC-corrected results presented here. This apparent discrepancy can be explained on the basis of recent works which elucidate the issue of energy gaps in DFT.[66,73] The view of the HOMO-LUMO gap corresponding in magnitude to the fundamental gap emerges from GKS theory whereas
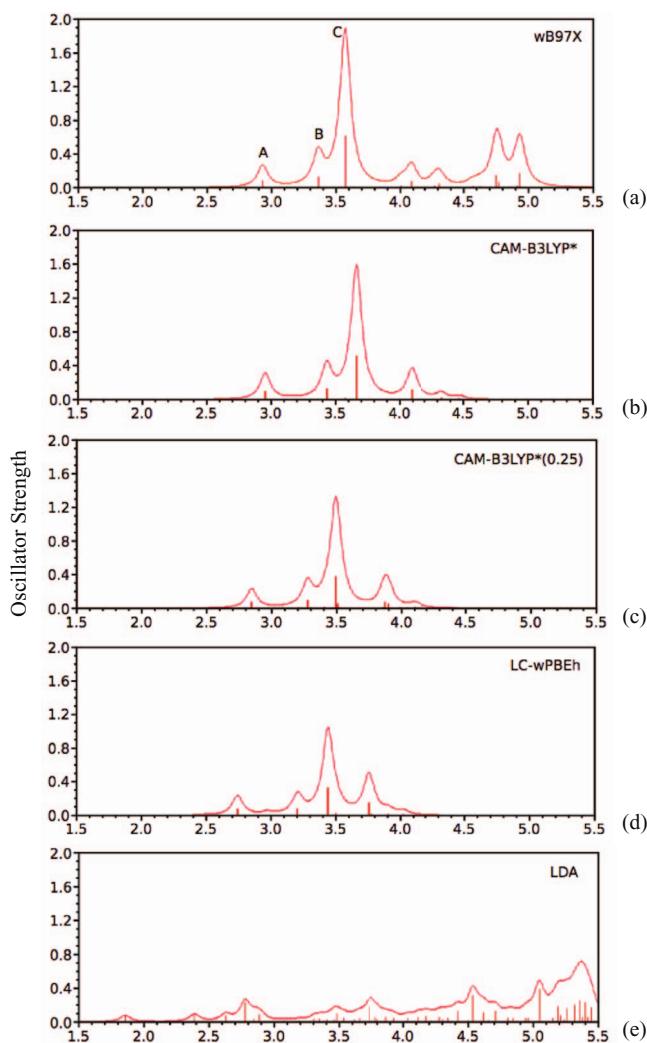

FIG. 8. Absorption spectrum of Au_{20} (T_d) in three indicated functionals. (a) ωB97X spectrum was calculated with 200 excited states; (b)-(c) spectra were calculated with 100 excited states; (d) spectrum was calculated with 80 excited states; (e) LDA spectrum is redrawn from the data of Ref. 22. The lines are broadened by 0.05 eV H-W Lorentzian. The units on the abscissa are eV.

the view of E_{HL} gap being close to the first vertical excitation in TDDFT arises from the conventional KS theory. One should bear in mind that the latter fails to correctly predict the excitation energies of excited states with charge-transfer character.

In summary, we predict Au_{20} having rather wide HOMO-LUMO gap (within 0.5 eV of the fundamental gap), the optical gap of ~2.87 eV, and the position of the first dark state at ~2.5 eV. These predictions of course neglect the effects of spin-orbit coupling. The spin-orbit coupling, according to Wang *et al.*,[25] may reduce the value of E_{HL} by about 0.37 eV.

IV. SUMMARY AND CONCLUSIONS

In this work we performed TDDFT calculations of the optical absorption spectra of Au_n clusters where n = 4, 6, 8, 12, and 20. The results of TDDFT simulations were compared for Au_4 and Au_8 with the wave function linear response theory based on CCSD and with the experimental high-resolution

spectra in low temperature Ne matrix. Several variants of LC functionals were compared with conventional xc functionals such as TPSS and B3LYP.

Conventional functionals applied in the calculations of excited states of gold clusters fail on two levels. First, as shown by the example of Au_6 (Fig. 1) the excited states are systematically shifted downward in energy making the gap to the first excited state much too small compared to EOM-CC. Second, the intensity pattern resulting from these functionals is incorrect as indicated by the incorrect ratio of oscillator strengths of B_{1u} vs. B_{2u} transitions in Au_4, as well as in a diffusion of intensity over too many active transitions, as shown in Au_4, Au_8, and Au_{20}.

Applying the long-range correction to these functionals induces dramatic changes in the spectra including widening of the optical gaps, removing spurious active transitions and bringing the excitation energies into a qualitative agreement with EOM-CC. For more quantitative agreement, we used the J'^2 parameter, the value of which gauges how well the Koopmans' theorem is obeyed for a neutral cluster and its negative ion by a particular functional. Generally, the smaller the value of J'^2 the better the agreement with the EOM-CC spectrum. However, there are some caveats here. In the case of CAM-B3LYP* reducing J'^2 to the 0.01–0.1 size was sufficient; seeking the minimum value resulted in a worsening of the spectra. It is possible that at this point a two-parameter optimization (ω and α), as recently proposed by Srebro and Autschbach,[88] would be more successful. The second caveat concerns the LC-ωPBE functional where the minimization of J'^2 by varying ω did not result in a superior spectrum. In Au_4 and Au_8 this "optimal" functional, LC-ωPBE ($\omega = 0.25$), led to incorrect transition energies except for the one dominated by a HOMO-LUMO excitation and dramatic losses of intensity (see Fig. S3 of the supplementary material[70]) as well as the sums of oscillator strengths in Au_8, (see Table V). Since this functional behaves like the exact functional with respect to fractional electron numbers (see Fig. 4) we suggest that the optimization of ω in LC-ωPBE affects only the frontier orbitals, the view shared with recent work of Refaely-Abramson *et al.*[82] However, an inclusion of constant fraction of the HF exchange in the context of LC-functional led to a dramatic improvement of spectra. It should be emphasized that the other LC-functionals with values of J'^2 at or below 0.1 eV^2 can be considered for all practical purposes optimally tuned in the sense advocated by Baer and co-workers.[64,66,89] In summary, there are two main factors that determine accurate spectral prediction for gold: the magnitude of range-separation parameter and whether or not an LC correction is applied to a hybrid functional.

Some further general observations based on the data in Tables I, III, and VII can be made. Larger values of ω result in the blueshift of the spectra whereas the small values in the redshift. One can notice that the computed vertical ionization potentials differ from the experimentally measured values. The disagreement is larger for Au_4 ($\sim$1 eV) and smaller for Au_8 and Au_{20}. This observation contrasts the Au_n clusters with the Ag_n ones, where a very good agreement between ΔSCF and experimental values of IP with LC-functionals was reported.[41] From this we can infer that the problem

may be related to the neglect of the spin-orbit effects. On the positive side, the errors appear to cancel out to a certain degree in the calculation of fundamental gaps. Consequently, our computed fundamental gaps are within $\sim$0.5 eV of the experimental values.

The computed vertical electron affinities are underestimated compared to experiment when the LC correction is applied. Generally, LC-ωPBEh and variants of CAM-B3LYP* perform better than ωB97X. By contrast, previous LDA and GGA calculations report very good predictions of electron affinities of gold clusters.[3,22,25] It appears that this underestimation is the price one pays for raising the LUMO energy upon adding the HF exchange.

The range separation parameter is somewhat size-dependent. Within the same type of functional, such as CAM-B3LYP*, a larger (standard) value of 0.33 is better suited for small molecule-like Au_4, whereas a smaller value of 0.25 is more suitable for larger clusters such as Au_{20}. In LC-ωPBEh the range separation parameter of 0.2 (with $\alpha = 0.2$, $\beta = 0.8$) is appropriate for cluster sizes n = 8, 12, and 20. However, for Au_4 a better spectrum was obtained with LC-PBE0 with $\omega = 0.3$ (with $\alpha = 0.25$, $\beta = 0.75$). On the intuitive level this size dependence makes a great deal of sense since $1/\omega$ has the meaning of distance at which the HF exchange becomes necessary and this tends to increase with the delocalization of orbitals over the larger range. The performance of ωB97X across all cluster sizes is very similar to that of CAM-B3LYP* which is not surprising since they have similar ω values (0.3 vs. 0.33).

In all well-performing LC functionals the magnitude of E_{HL} was comparable to the experimental fundamental gaps for reasons discussed above. As shown in Tables II, IV, VI, and VIII these functionals afford internally consistent and verifiable through EOM-CC predictions of the lowest, typically dark, excited state as well as the first bright state. The evolution of the energy gap to the first excited state and the optical gap as a function of the cluster size is displayed in Fig. 9.

The gaps to the first dark state are particularly narrow in Au_4 and Au_{12} while the largest one occurs in Au_6. Let us compare these observations with insights based on jellium-like model.[4] Based on an analysis of angular momentum of
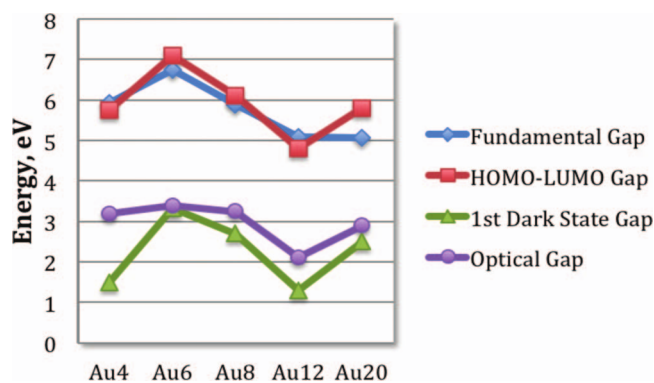

FIG. 9. Evolution of energy gaps as a function of cluster size in Au_n: The values of HL, optical, and the first dark state gaps are obtained as averages of computed results from Tables II, IV, VI, and VIII, respectively. The fundamental gap (IP-EA) values are from experiment (IP,[74] EA[1,25]).

"jellium" electrons, Häkkinen and co-workers advanced a one electron level diagram of a planar quantum dot for gold (see Ref. 4 and references therein). This model predicts a shell closing at n = 6. Our result is in full agreement with this prediction. The next shell closing according to their model should occur for n = 12. However, our results suggest that this is unlikely as Au_{12} has low-lying excited states. Rather, Au_8 appears to be a better candidate for shell closing due to its wider excitation gap and the 8-electron "superatom" character.

According to our calculations all clusters display molecule-like absorption spectra with well-defined features. With the exception of Au_{12} no active transitions are found below 3 eV (2.9 eV in Au_{20} case). Clusters with n = 6, 8, 12, 20 regardless of their shape and symmetry show an intense absorption around 3.5 eV. In Au_4 the corresponding transition occurs at 3.3 eV.

[1] K. J. Taylor, C. L. Pettiette-Hall, O. Cheshnovsky, and R. E. Smalley, J. Chem. Phys. **96**, 3319 (1992).

[2] W. A. de Heer, Rev. Mod. Phys. **65**, 611 (1993).

[3] H. Häkkinen, B. Yoon, U. Landman, X. Li, H. J. Zhai, and L. S. Wang, J. Phys. Chem. A **107**, 6168 (2003).

[4] H. Häkkinen, Chem. Soc. Rev. **37**, 1847 (2008).

[5] P. Pyykkö, Chem. Soc. Rev. **37**, 1967 (2008); P. Pyykko, Angew. Chem., Int. Ed. **43**, 4412 (2004).

[6] J. Lermé, B. Palpant, B. Prevel, E. Cottancin, M. Pellarin, M. Treilleux, J. L. Vialle, A. Perez, and M. Broyer, Eur. Phys. J. D **4**, 95 (1998).

[7] R. Sardar, A. M. Funston, P. Mulvaney, and R. W. Murray, Langmuir **25**, 13840 (2009).

[8] S. M. Morton, D. W. Silverstein, and L. Jensen, Chem. Rev. **111**, 3962 (2011).

[9] E. Cottancin, G. Celep, J. Lermé, M. Pellarin, J. R. Huntzinger, J. L. Vialle, and M. Broyer, Theor. Chem. Acc. **116**, 514 (2006).

[10] N. Durante, A. Fortunelli, M. Broyer, and M. Stener, J. Phys. Chem. C **115**, 6277 (2011).

[11] L. D. Menard, S. P. Gao, H. P. Xu, R. D. Twesten, A. S. Harper, Y. Song, G. L. Wang, A. D. Douglas, J. C. Yang, A. I. Frenkel, R. G. Nuzzo, and R. W. Murray, J. Phys. Chem. B **110**, 12874 (2006).

[12] M. Zhu, C. M. Aikens, F. J. Hollander, G. C. Schatz, and R. Jin, J. Am. Chem. Soc. **130**, 5883 (2008).

[13] M. M. Alvarez, J. T. Khoury, T. G. Schaaff, M. N. Shafigullin, I. Vezmar, and R. L. Whetten, J. Phys. Chem. B **101**, 3706 (1997).

[14] B. A. Collings, K. Athanassenas, D. Lacombe, D. M. Rayner, and P. A. Hackett, J. Chem. Phys. **101**, 3506 (1994).

[15] S. Gilb, K. Jacobsen, D. Schooss, F. Furche, R. Ahlrichs, and M. M. Kappes, J. Chem. Phys. **121**, 4619 (2004).

[16] S. Lecoultre, A. Rydlo, C. Felix, J. Buttet, S. Gilb, and W. J. Harbich, J. Chem. Phys. **134**, 074302 (2011).

[17] J. Zheng, C. Zhang, and R. M. Dickson, Phys. Rev. Lett. **93**, 077402 (2004).

[18] M. L. Tran, A. V. Zvyagin, and T. Plakhotnik, Chem. Commun. **2006**, 2400.

[19] S. Rath, S. Nozaki, D. Palagin, V. Matulis, O. Ivashkevich, and S. Maki, Appl. Phys. Lett. **97**, 053103 (2010).

[20] S. Faas, J. G. Snijders, J. H. van Lenthe, E. van Lenthe, and E. J. Baerends, Chem. Phys. Lett. **246**, 632 (1995).

[21] F. Wang, T. Ziegler, E. van Lenthe, S. van Gisbergen, and E. J. Baerends, J. Chem. Phys. **122**, 204103 (2005).

[22] J. C. Idrobo, W. Walkosz, S. F. Yip, S. Ogut, J. Wang, and J. Jellinek, J. Phys. Rev. B **76**, 205422 (2007).

[23] A. Castro, M. A. L. Marques, A. H. Romero, M. J. T. Oliveira, and A. Rubio, J. Chem. Phys. **129**, 144110 (2008).

[24] J. P. Perdew, K. Burke, and M. Ernzerhof, Phys. Rev. Lett. **77**, 3865 (1996).

[25] J. Li, X. Li, H. J. Zhai, and L. S. Wang, Science **299**, 864 (2003).

[26] J. P. Perdew, J. A. Chevary, S. H. Vosko, K. A. Jackson, M. R. Pederson, D. J. Sing, and C. Fiolhais, Phys. Rev. B **46**, 6671 (1992).

[27] C. M. Aikens and G. C. Schatz, J. Phys. Chem. A **110**, 13317 (2006).

[28] A. D. Becke, Phys. Rev. A **38**, 3098 (1988); J. P. Perdew, Phys. Rev. B **33**, 8822 (1986).

[29] K. Wu, J. Li, and C. Lin, Chem. Phys. Lett. **388**, 353 (2004).

[30] R. van Leeuwen and E. J. Baerends, Phys. Rev. A **49**, 2421 (1994).

[31] R. H. Xie, G. W. Bryant, J. Zhao, T. Kar, and V. H. Smith, Jr., Phys. Rev. B **71**, 125422 (2006).

[32] M. E. Casida, J. Mol. Struct.: THEOCHEM **914**, 3 (2009).

[33] A. Dreuw and M. Head-Gordon, Chem. Rev. **105**, 4009 (2005).

[34] P. Elliott, F. Furche, and K. Burke, in *Excited States from Time-Dependent Density Functional Theory*, edited by K. B. Lipkowitz and T. R. Cundari (Wiley, Hoboken, NJ, 2009), Vol. 26, pp. 91–165.

[35] M. E. Casida and D. R. Salahub, J. Chem. Phys. **113**, 8918 (2000).

[36] D. J. Tozer, J. Chem. Phys. **119**, 12697 (2003).

[37] A. W. Lange, M. A. Rohrdanz, and J. M. Herbert, J. Phys. Chem. B **112**, 6304 (2008).

[38] M. Parac and S. Grimme, Chem. Phys. **292**, 11 (2003).

[39] R. M. Richard and J. M. Herbert, J. Chem. Theory Comput. **7**, 1296 (2011).

[40] N. Kuritz, T. Stein, R. Baer, and L. Kronik, J. Chem. Theory Comput. **7**, 2408 (2011).

[41] D. M. Silverstein and L. Jensen, J. Chem. Phys. **132**, 194302 (2010).

[42] A. Savin, in *Recent Developments and Applications of Modern Density Functional Theory*, edited by J. M. Seminario (Elsevier, Amsterdam, 1996), pp. 327–357.

[43] D. Jacquemin, V. Wathelet, E. A. Perpete, and C. Adamo, J. Chem. Theory Comput. **5**, 2420 (2009).

[44] D. Jacquemin, E. A. Perpete, G. E. Scuseria, I. Ciofini, and C. Adamo, J. Chem. Theory Comput. **4**, 123 (2008).

[45] R. Kobayashi and R. D. Amos, Chem. Phys. Lett. **420**, 106 (2006).

[46] Y. Tawada, T. Tsuneda, S. Yanagisawa, T. Yanai, and K. Hirao, J. Chem. Phys. **120**, 8425 (2004).

[47] Z. L. Cai, M. J. Crossley, J. R. Reimers, R. Kobayashi, and R. D. Amos, J. Phys. Chem. B **110**, 15624 (2006).

[48] M. A. Rohrdanz, K. M. Martins, and J. M. Herbert, J. Chem. Phys. **130**, 054112 (2009).

[49] J. F. Stanton and R. J. Bartlett, J. Chem. Phys., **98**, 7029 (1993); T. Korona and H. J. Werner, J. Chem. Phys. **118**, 3006 (2003).

[50] D. Figgen, G. Rauhut, M. Dolg, and H. Stoll, Chem. Phys. **311**, 227 (2005).

[51] K. A. Peterson and C. Puzzarini, Theor. Chem. Acc. **114**, 283 (2005).

[52] R. M. Olson and M. S. Gordon, J. Chem. Phys. **126**, 214310 (2007).

[53] O. A. Vydrov and G. E. Scuseria, J. Chem. Phys. **125**, 234109 (2006).

[54] M. J. Frisch, G. W. Trucks, and H. B. Schlegel *et al.*, GAUSSIAN 09, Revision B.01, Gaussian, Inc., Wallingford, CT, 2010.

[55] T. Yanai, D. P. Tew, and N. C. Handy, Chem. Phys. Lett. **393**, 51 (2004).

[56] J. D. Chai and M. Head-Gordon, J. Chem. Phys. **128**, 084106 (2008).

[57] The dispersion-corrected variant of this functional, ωB97XD, (Ref. 58) is currently not parametrized for gold. Nonetheless, our results show that the ωB97X functional reproduces very well the well depth of aurophilic interactions (Ref. 59).

[58] J. D. Chai and M. Head-Gordon, Phys. Chem. Chem. Phys. **10**, 6615 (2008).

[59] R.-F. Liu, C. A. Franzese, R. Malek, P. S. Zuchowski, J. G. Angyan, M. M. Szczesniak, and G. Chalasinski, J. Chem. Theory Comput. **7**, 2399 (2011).

[60] T. M. Henderson, B. G. Janesko, and G. E. Scuseria, J. Chem. Phys. **128**, 194105 (2008).

[61] M. Ernzerhof and J. P. Perdew, J. Chem. Phys. **109**, 3313 (1998).

[62] H. Iikura, T. Tsuneda, T. Yanai, and K. Hirao, J. Chem. Phys. **115**, 3540 (2001).

[63] J. Tao, J. P. Perdew, V. N. Staroverov, and G. E. Scuseria, Phys. Rev. Lett. **91**, 146401 (2003).

[64] T. Stein, H. Eisenberg, L. Kronik, and R. Baer, Phys. Rev. Lett. **105**, 266802 (2010).

[65] A. J. Cohen, P. Mori-Sanchez, and W. Yang, Chem. Rev. **112**, 289 (2012).

[66] L. Kronik, T. Stein, S. Refaely-Abramson, and R. Baer, J. Chem. Theory Comput. **8**, 1515 (2012).

[67]M. Srebro and J. Autschbach, J. Chem. Theory Comput. **8**, 245 (2012).

[68]M. Valiev, E. J. Bylaska, N. Govind, K. Kowalski, T. P. Straatsma, H. J. J. van Dam, D. Wang, J. Nieplocha, E. Apra, T. L. Windus, and W. A. de Jong, Comput. Phys. Commun. **181**, 1477 (2010).

[69]H. J. Werner, P. J. Knowles, F. R. Manby, M. Schütz *et al.*, MOL-PRO, version 2010.1, a package of *ab initio* programs, 2010, see http://www.molpro.net.

[70]See supplementary material at http://dx.doi.org/10.1063/1.4752433 for additional results for the clusters Au_6, Au_8, and Au_{20}.

[71]J. W. Song, T. Hirosawa, T. Tsuneda, and K. Hirao, J. Chem. Phys. **126**, 154105 (2007).

[72]J. P. Perdew and M. Levy, Phys. Rev. Lett. **51**, 1884 (1983); Phys. Rev. B **56**, 16021 (1997).

[73]W. Yang, A. J. Cohen, and P. Mori-Sánchez, J. Chem. Phys. **136**, 204111 (2012).

[74]C. Jackschath, I. Rabin, and W. Schulze, Ber. Bunsenges. Phys. Chem. **96**, 1200 (1992).

[75]P. Mori-Sánchez, A. J. Cohen, and W. Yang, Phys. Rev. Lett. **100**, 146401 (2008).

[76]O. A. Vydrov, G. E. Scuseria, and J. P. Perdew, J. Chem. Phys. **126**, 154109 (2007).

[77]T. Tsuneda, J. W. Song, S. Suzuki, and K. Hirao, J. Chem. Phys. **133**, 174101 (2010).

[78]J. F. Janak, Phys. Rev. B **18**, 7165 (1978).

[79]C. Adamo and V. Barone, J. Chem. Phys. **110**, 6158 (1999).

[80]M. A. Rohrdanz and J. M. Herbert, J. Chem. Phys. **129**, 034107 (2008).

[81]C. L. Janssen and I. M. B. Nielsen, Chem. Phys. Lett. **290**, 423 (1998); T. J. Lee, Chem. Phys. Lett. **372**, 362 (2003).

[82]S. Refaely-Abramson, S. Sharifzadeh, Ni. Govind, J. Autschbach, J. B. Neaton, R. Baer, and L. Kronik, preprint arXiv:1203.2357v3 (2012).

[83]A. D. Becke and M. R. Roussel, Phys. Rev. A **39**, 3761 (1989).

[84]A. Devarajan, A. Gaenko, and J. Autschbach, J. Chem. Phys. **130**, 194102 (2009).

[85]We extended this comparison to the negative ion, Au_{12}^-, whose two isomers D_{3h} and C_{2v} were benchmarked with TPSS in M. P. Johansson, A. Lechtken, D. Schooss, M. M. Kappes, and F. Furche, Phys. Rev. A **77**, 053202 (2008). ωB97X optimization confirmed the energy difference between them (our value -0.316 eV vs. their value -0.34 eV).

[86]E. S. Kryachko and F. Remacle, Int. J. Quantum Chem. **107**, 2922 (2007).

[87]M. P. Johansson, D. Sundholm, and J. Vaara, Angew. Chem., Int. Ed. **43**, 2678 (2004).

[88]M. Srebro and J. Autschbach, J. Phys. Chem. Lett. **3**, 576 (2012).

[89]R. Baer, E. Livshits, and U. Salzner, Annu. Rev. Phys. Chem. **61**, 5 (2010).

A study of weak interactions affecting the conformation of gold(I) complexes with 2-Mercapto-4-methyl-5-thiazoleacetic acid ligands

In this Chapter we present a joint experimental and theoretical study of three gold(I) complexes $[\text{Au}(\text{H}_2\text{-}mmta)_2]\text{Cl}\cdot3\text{H}_2\text{O}$ (**1**), $\text{Na}_3[\text{Au}(mmta)_2]\cdot6\text{H}_2\text{O}$ (**2**) and $\text{Na}_3[\text{Au}(mmta)_2]\cdot10.5\text{H}_2\text{O}$ (**3**) ($\text{H}_2\text{-}mmta$ = 2-Mercapto-4-methyl-5-thiazoleacetic acid) in which the Au(I) centre is incorporated either in cationic or anionic units of the $[\text{Au}(\text{SR})_2]^{+/-}$ type depending on the protonation state of the ligand. All structures were characterized by single crystal X-ray analysis and found to exhibit unsupported aurophilic interactions leading to the formation of dimeric $[\text{Au}_2(\text{H}_2\text{-}mmta)_4]^{2+}$ and $[\text{Au}_2(mmta)_4]^{6-}$ species. By applying several *ab initio* interpretative techniques we examine the character of the intermolecular interactions stabilizing the eclipsed arrangement of the aurophilic dimers. The results given in this Chapter have been accepted for publication [D5].

7.1   Introduction

Gold thiolates are a fascinating group of compounds. They found applications as antiarthritic drugs and are being studied as potential anti-parasitic and anticancer agents [130, 131]. They are also at the centre of gold nanoparticles' research as commonly used stabilizing agents [132–134]. Finally, they are recognized for their tunable luminescent

7. A STUDY OF WEAK INTERACTIONS AFFECTING THE CONFORMATION OF GOLD(I)
COMPLEXES WITH 2-MERCAPTO-4-METHYL-5-THIAZOLEACETIC ACID LIGANDS

112

properties [135, 136].

In gold *bisthiolato* complexes the Au(I) centre may be incorporated either in cationic or anionic unit of the $[Au(SR)_2]^{+/-}$ type depending on the nature of the ligand [137]. Furthermore, both types of units can aggregate through ligand-unsupported aurophilic bonding [137–144].

So far, among gold *bisthiolato* compounds the salts of the $M^+[Au(SCN)_2]^-$ type attracted most attention. It has been shown that change in the size and flexibility of the cationic environment influences the dimensionality and range of the aurophilic contacts. This, in turn, has significant impact on the emissive properties of the crystalline solids [135, 145, 146].

In a recent paper Lim *et al.* [144] described two gold(I) salts exhibiting aurophilic bonding. Interestingly, in contrast to the trend observed for the $[Au(SCN)_2]^-$ aggregates, their $[Au(SCSN_3)_2]^-$ ($SCSN_3^- =$ 1,2,3,4-thiatriazole-5-thiolate anion), anions were arranged in an eclipsed geometry with the S-Au$\cdots$Au-S torsional angles of 2.02° and 4.11°. Similar arrangement, untypical of two-coordinate gold complexes with short Au$\cdots$Au distances [147, 148], was found in other gold bisthiolato complexes [138, 139, 141]. Clearly, a better understanding of the structural factors that determine the configuration of the aurophilic contact region could contribute to future control over the luminescent properties in this group of salts.

To gain insights into the properties of this group of salts we synthesized gold bisthiolato complexes in two charge states, cationic and anionic, both of which feature Au$\cdots$Au contacts. The compounds were analyzed by the X-ray diffraction technique revealing eclipsed conformations. Subsequently, based on their crystal structures we selected structural motifs that include aurophilic systems with a network of counterions and water molecules. The interactions within the selected motifs were analyzed by electronic structure methods and quantum interpretative techniques. The aim of these investigations was to obtain quantitative information on the noncovalent interactions in the contact region of aurophilic dimers with eclipsed structures and a qualitative picture of the bonding character in the intra- and interdimer space.

We chose 2-Mercapto-4-methyl-5-thiazoleacetic acid (H_2-*mmta*) as a stabilizing ligand. The complexes of thiazolidinethione's and thiazolethione's derivatives are known in gold chemistry (see, e.g. Refs. [140, 141, 149–151]). Moreover, both thiazolidine-2-thione and H_2-*mmta* have already been used in stabilizing structures with aurophilic

bonds [152, 153]. In the case to H$_2$-*mmta* a tetranuclear gold(I) complex exhibiting luminescence has been described [153]. Furthermore, H$_2$-*mmta* is unique in that it allows one to capture the Au(I) centres in two charge states depending on the protonation of the carboxylic group: deprotonation of COOH in the thiol form leads to anionic units, whereas the thione form with a protonated carboxylic group yields cationic units.

7.2 Experimental section

7.2.1 Materials

All chemicals and solvents used for the synthesis were obtained from commercial sources and were used as received, without further purification. The gold-containing reagent was HAuCl$_4$·xH$_2$O [49% Au]. Raman spectra of crystalline materials were recorded with a Nicolet Almega Dispersive Raman Spectrometer in the range 100-4000 cm^{-1}. The laser source wavelength used was 532 nm. The spectral resolution was about 2 cm^{-1} for all measurements.

7.2.2 Computational methods

The def2-TZVPP basis set was used throughout [89, 154], together with the relativistic small-core ($1s$-$4f$) effective core potential of Figgen *et al.* [123] All DFT and MP2 calculations were done in the developer version of the Molpro [13] program, the coupled cluster singles, doubles, and noniterative triples calculations using the domain based local pair-natural orbital (DLPNO-CCSD(T)) method were carried out in the Orca [155] program. The Quantum Theory of Atoms in Molecules (QTAIM) analysis was performed in the AIMAll program [156]. The Non Covalent Interactions (NCI) analysis was carried out with the NCIPLOT program [157, 158].

7.2.3 Synthesis

[Au(H$_2$-*mmta*)$_2$]Cl·3H$_2$O (**1**): A 0.56 mmol solution of H$_2$-*mmta* was prepared by dissolving 107 mg H$_2$-*mmta* in 4 ml of water:methanol (3:1) solution and stirred at 70°C for 10 min. The precipitate was removed and the supernatant mixed with 4 ml acidic 0.12 mmol water solution of HAuCl$_4$ (48.2 mg of HAuCl$_4$·xH$_2$O [49% Au], 3 ml H$_2$O

and 1 ml 38% HCl) yielding 14:3 H_2-$mmta$:$HAuCl_4$ molar ratio. The yellow solution was then stirred for 15 min at 70°C. After cooling acetonitrile was added until the precipitate was dissolved. The solution was filtered and dried for 24 hrs obtaining single, tiny colorless crystals of **1**. Raman [cm^{-1}]: 2926w, 2892w, 1614s, 1497vs, 1443s, 1396s, 1342vs, 1279s, 1198w, 1080s, 1019w, 931w, 692s, 620w, 556s, 473w, 403m, 355s, 302w, 266w, 216m, 160w.

$Na_3[Au(mmta)_2] \cdot 6H_2O$ (**2**) and $Na_3[Au(mmta)_2] \cdot 10.5H_2O$ (**3**): 0.02 ml of dimethyl sulfide (ρ = 0.846 g/ml) was added to a 0.16 mmol solution of $HAuCl_4$ (65.5 mg of $HAuCl_4 \cdot xH_2O$ [49% Au] in 2 ml MeOH), yielding 5:3 CH_3SCH_3:$HAuCl_4$ molar ratio, and stirred for 15 minutes at room temperature. The solution obtained by mixing 0.48 mmol H_2-$mmta$ (90.6 mg in 1.5 ml MeOH) with NaOMe (36.2 mg of Na in 2 ml MeOH) was added and stirred for 20 min. The murky solution was decanted and after storing at -20 °C for 72 h single plates of **2** could be isolated, whereas immediate evaporation on a glass plate under ambient conditions yielded single plates of **3**. Raman **2** [cm^{-1}]: 1682w, 1601s; 1548m; 1489s, 1452m, 1402m, 1366w, 1266m, 1226m, 1182m, 1029m, 1087m, 966w, 904m, 746w, 715w, 519w, 496w, 413w, 364w, 336w, 278w, 235w, 150w. Raman **3** [cm^{-1}]: 1618s; 1398s, 1377s, 1309s, 1264m, 1052w, 963w, 885m, 741w, 535w, 404w, 355w, 298w, 215w, 170w.

7.3   Results and discussion

All the obtained salts contain gold(I) dimers exhibiting Au$\cdots$Au interactions. While compound **1** encompasses protonated H_2-$mmta$ ligands, both **2** and **3** contain fully deprotonated ligands. Crystal data for $\mathbf{1} - \mathbf{3}$ are given in Table A.1 in the Appendix. Selected bond angles and distances are given in Table 7.1. Crystal data and structure refinement parameters of 2-Mercapto-4-methyl-5-thiazoleacetic acid are given in Tables A.2 and A.3 in the Appendix.

7.3.1   Crystal structure of [Au(H$_2$-$mmta$)$_2$]Cl·3H$_2$O

The asymmetric unit of compound **1** is composed of one $[Au(H_2$-$mmta)_2]^+$ cation accompanied by the Cl$^-$ anion and three water molecules (see Fig. 7.1). The Au1-S2 and Au1-S4 distances are 2.2873(15) Å and 2.2948(15) Å, respectively. The coordination to

Table 7.1: Selected bond lengths [Å], angles and torsion angles for compounds $\mathbf{1-3}$.

1			**2**		
Au1-S2	2.2948(15)	Au1-S1	2.294(2)	Au2-S21	2.297(2)
Au1-S4	2.2873(15)	Au1-S11	2.299(2)	Au2-S31	2.293(2)
S2-C1	1.702(5)	S1-C1	1.755(10)	S21-C21	1.750(10)
S4-C11	1.712(6)	S11-C11	1.749(9)	S31-C31	1.760(9)
N1-C1	1.337(7)	N1-C1	1.304(12)	N11-C11	1.287(12)
N2-C11	1.325(8)	N21-C21	1.306(12)	N31-C31	1.300(12)
Au1-Au1^{i}	3.3535(5)	Au1-Au2	3.1845(6)		
S4-Au1-S2	176.94(5)	S1-Au1-S11	178.92(9)	S31-Au2-S21	178.46(9)
C1-S2-Au1	103.47(19)	C1-S1-Au1	103.7(3)	C21-S21-Au2	102.7(3)
C11-S4-Au1	106.22(19)	C11-S11-Au1	104.6(3)	C31-S31-Au2	103.2(3)
Au1-S2-C1-S1	−3.6(4)	Au1-S1-C1-S2	−4.0(7)	Au2-S21-C21-S22	−17.5(6)
S3-C11-S4-Au1	−11.7(5)	S22-C21-S21-Au2	−17.5(6)	S32-C31-S31-Au2	−16.9(7)
S2-Au1-Au1^{i}-S4^{i}	−1.46(6)	S1-Au1-Au2-S21	19.33(9)	S11-Au1-Au2-S31	18.69(8)
S1-S2-S4-S3	2.20(5)	S2-S1-S11-S12	−46.32(9)	S22-S21-S31-S32	−52.48(9)
3					
Au1-S2	2.294(2)	S2-Au1-S2^{iii}	176.44(10)	Au1-S2-C1-S1	1.6(6)
S2-C1	1.720(8)	C1-S2-Au1	102.7(3)	S2-Au1-Au1^{ii}-S2^{ii}	−1.38(15)
N1-C1	1.316(11)			S1-S2-S2^{iii}-S1^{iii}	52.08(11)
Au1-Au1^{ii}	3.0936(9)				

Symmetry codes **1**: *i = −x, 1 − y, 1 − z; ii = 1 − x, 1 − y, 1 − z; iii = −1 + x, +y, +z;*
iv = +x, +y, −1 + z; v = −x, 1 − y, 2 − z; vi = +x, +y, 1 + z; vii = −x, 1 − y, 2 − z
2: *i = 2 − x, 2 − y, 1 − z, ii = 2 − x, 1 − y, 1 − z;* **3**: *i = −1/4 + x, −1/4 + y, 1 − z,*
ii = 3/4 − x, 3/4 − y, +z, iii = +x, 3/4 − y, 3/4 − z, iv = 3/4 − x, +y, 3/4 − z,
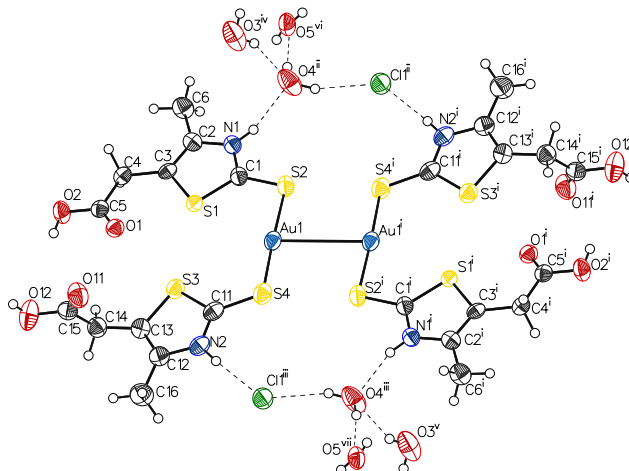*v = 1 − x, −1/4 + y, −1/4 + z.*

Figure 7.1: A drawing of a portion of the structure of $[Au(H_2\text{-}mmta)_2]Cl \cdot 3H_2O$ (**1**). Thermal ellipsoids are shown at the 50% probability. Symmetry codes: $i = -x, 1 - y, 1 - z$; $ii = 1 - x, 1 - y, 1 - z$; $iii = -1 + x, +y, +z$; $iv = +x, +y, -1 + z$; $v = -x, 1 - y, 2 - z$; $vi = +x, +y, 1 + z$, $vii = -x, 1 - y, 2 - z$.

Au(I) makes the S2-C1 and S4-C11 bonds of $1.702(5)\,\text{Å}$ and $1.712(6)\,\text{Å}$, respectively, slightly elongated with respect to the S2-C1 bond of $1.674(2)\,\text{Å}$ in the free $H_2\text{-}mmta$ (see Tab. A.3 in the Appendix). The coordination sphere of Au has a collinear arrangement with the S4-Au1-S2 angle of $176.94(5)°$.

Within the $[Au(H_2\text{-}mmta)_2]^+$ cations the heterocyclic $H_2\text{-}mmta$ rings adapt a *cis* conformation with the twist angle S1-S2-S4-S3 (on the S2-S4 line) equal to $2.20(6)°$. The *cis* conformation results in relatively short contact of $3.5478(18)\,\text{Å}$ between the S1$\cdots$S3 sulfur atoms. The contacts between the Au(I) center and the ring sulfur atoms are also notably short: Au1$\cdots$S1 is $3.3723(12)\,\text{Å}$ and Au1$\cdots$S3 is $3.5356(13)\,\text{Å}$. Moreover, the central $[Au(H_2\text{-}mmta)_2]^+$ moiety (excluding terminal carboxyl groups) is nearly coplanar with the torsion angles S1-C1-S2-Au1 and S3-C11-S4-Au1 equal to $-3.6(5)°$ and $-11.7(5)°$, respectively.

The $[Au(H_2\text{-}mmta)_2]^+$ cations form centrosymmetric dimers with the centre of inversion located at the midpoint of the Au(I)$\cdots$Au(I) line (Fig. 7.1). The dimers take an eclipsed geometry with the S2-Au1-Au1^i-S4^i torsion angle of $-1.46(6)°$. The distance between the aurophilic centers is $3.3535(5)\,\text{Å}$.

Apart from the Au(I)-Au(I) attraction, the $[Au(H_2\text{-}mmta)_2]^+$ monomers interact *via* two hydrogen bridges encompassing water molecules and chloride ions: [NH $\cdots$ OH $\cdots$ Cl$^-$ $\cdots$ HN]. Moreover, the carboxyl groups engage in intermolecular hydrogen bond
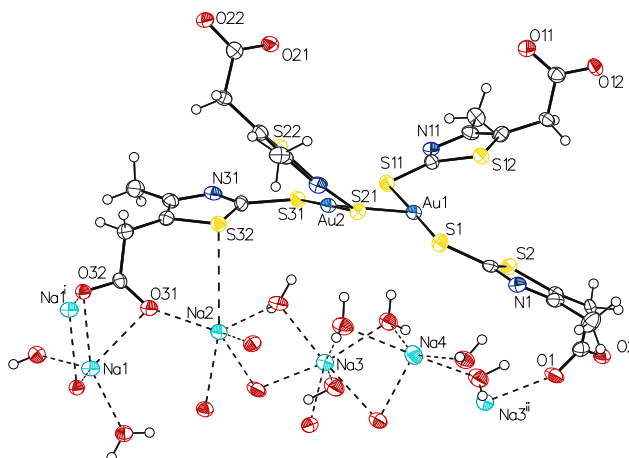
Figure 7.2: A drawing of a portion of the structure of $Na_3[Au(mmta)_2] \cdot 6H_2O$ (**2**). Thermal ellipsoids are shown at the 50% probability. Only selected sodium cations are shown. Symmetry codes: $i = 2 - x,\ 2 - y,\ 1 - z$, $ii = 2 - x,\ 1 - y,\ 1 - z$.

network comprising water molecules and Cl^- anions (see Table A.4 and Fig. A.1 in the Appendix). The network supports a parallel stacking of the dimers which are separated by ca. 3.4 Å. The coordination sphere of the chloride ions contains three H_2O molecules and one heterocyclic amide group.

7.3.2 Crystal structure of $Na_3[Au(mmta)_2] \cdot 6H_2O$ and $Na_3[Au(mmta)_2] \cdot 10.5H_2O$

In structures **2** and **3** the gold atoms are coordinated by two deprotonated *mmta* ligands which yields negatively charged monomers, $[Au(mmta)_2]^{3-}$ (see Figs. 7.2 and 7.3). The Au coordination spheres are linear with the S-Au-S angles and the Au-S bonds ranging from 176.44(10)° to 178.92(9)°, and from 2.293(2) Å to 2.299(2) Å, respectively. Similar to **1**, the S-C bonds formed by the Au-ligating sulfur atoms are elongated with respect to the free acid and fall within the $1.749(9) - 1.760(9)$ Å range. The N1-C1 bond in **3** and analogous N-C bonds in **2** range from 1.286(12) Å to 1.316(11) Å. The corresponding N1-C1 bonds in **1** and in the free ligand are longer: 1.337(7) Å and 1.341(3) Å, respectively.

In contrast to **1**, the heterocyclic rings in the $[Au(mmta)_2]^{3-}$ units of **2** and **3** display a *gauche* arrangement. In **2** the first appropriate twist angle S2-S1-S11-S12 (on the S1-Au1-S11 line) is $-46.32(9)°$, whereas the second S22-S21-S31-S32 (on the S21-Au2-S31
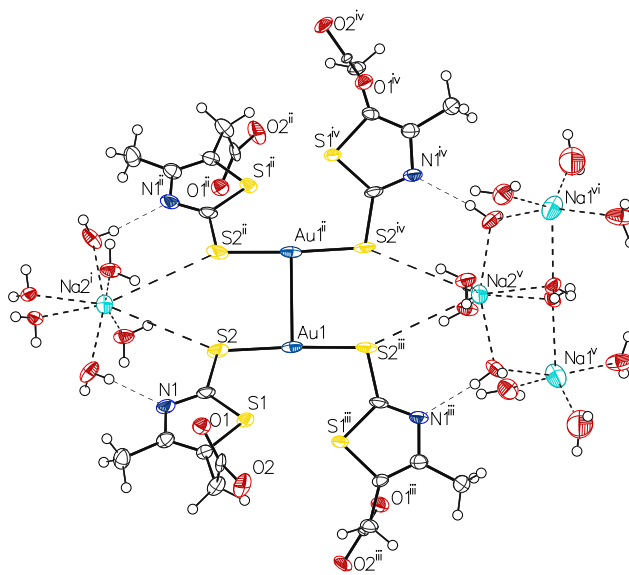
Figure 7.3: A drawing of a portion of the structure of $Na_3[Au(mmta)_2] \cdot 10.5H_2O$ (**3**). Thermal ellipsoids are shown at the 50% probability. Only selected sodium cations of the helical motif are shown. Symmetry codes: $i = -1/4 + x, -1/4 + y, 1 - z$, $ii = 3/4 - x, 3/4 - y, z$, $iii = x, 3/4 - y, 3/4 - z$, $iv = 3/4 - x, y, 3/4 - z$, $v = 1 - x$, $-1/4 + y, -1/4 + z$.

line) is $-52.48(9)°$. In **3** the analogous twist angle $S1$-$S2$-$S2^{iii}$-$S1^{iii}$ (on the $S2$-$Au1$-$S2^{iii}$ line) is $52.08(11)°$. Moreover, the *mmta* rings within the $[Au(mmta)_2]^{3-}$ anion are also somewhat twisted on the C-S bond (S refers to the Au-ligating sulfur atom). The respective torsion angles in **2** are $S12$-$C11$-$S11$-$Au1$, $S2$-$C1$-$S1$-$Au1$, $S22$-$C21$-$S21$-$Au2$ and $S32$-$C31$-$S31$-$Au2$ equal to $-11.9(7)°$, $-4.0(7)°$, $-17.5(6)°$ and $-16.9(7)°$, respectively. In **3** it is $S1$-$C1$-$S2$-$Au1$ equal to $1.6(6)°$.

In **2** the contacts between the heterocyclic sulfur atoms within the $[Au(mmta)_2]^{3-}$ anion, $S2 \cdots S12$ and $S22 \cdots S32$, amount to $3.958(3)$ Å and $4.034(3)$ Å, respectively. In **3** the analogous contact $S1 \cdots S1^{iii}$ is equal to $3.799(4)$ Å. The $Au \cdots S$ contacts within the units remain in the $3.30 - 3.39$ Å range.

The $[Au(mmta)_2]^{3-}$ monomers self-assemble in aurophilic dimers with the $Au(I) \cdots Au(I)$ distances of $3.1845(6)$ Å in **2** and $3.0936(9)$ Å in **3**. In **2** the dimer is asymmetric, whereas in **3** the center of the dimer is located on crystallographic special position (Wyckoff $8b$ notation) with site symmetry D_2. The dimers take an eclipsed arrangement: in **2** the respective torsion angles are $S1$-$Au1$-$Au2$-$S21$ and $S11$-$Au1$-$Au2$-$S31$

equal to 19.33(9)° and 18.69(8)°, respectively, in **3** it is S2-Au1-Au1^{ii}-S2^{ii} equal to 1.38(15)°. In **3** the Au-ligating S2 sulfur atoms facing each other enter the coordination sphere of the sodium cation forming a S2$\cdots$Na2^i contact of 3.877(5) Å.

Both **2** and **3** display π-π contacts: in **2** the π-π interactions link the dimers in a *tail-to-tail* fashion and propagate in the direction of the *b* axis, whereas in **3** the double π-stacking occurs along the *a* axis (see Tab. A.5 and Figs. A.2 and A.3 in the Appendix for details). In **2** the sodium cations are surrounded by oxygen atoms from the carboxylate anions and water molecules. In **3** the sodium cations are surrounded by water molecules forming helical structure along the *a* axis with six Na$^+$ per turn, whereas the carboxylate ions interact only with the solvating water molecules. We note that water molecules constituting the helical structure observed in **3** display a significant disorder.

7.3.3 Theoretical results

What is the nature of the noncovalent interactions contributing to the stability of the eclipsed conformation in the observed aurophilic dimers? To answer that question we selected three structures from compounds **1**, **2** and **3**, respectively, which we will refer to as (structural) motifs. This allows for reducing the computational cost and treat the intermolecular interactions stabilizing the chosen structures in a detailed manner. Our study embraced several quantum interpretative techniques: QTAIM [159, 160], NCI [157, 158] and Natural Bond Orbitals (NBO) [161, 162] analysis. The calculations were done on crystal geometries within the framework of Kohn-Sham theory utilizing PBE0 [163, 164] and MCSh [165, 166] functionals. The MCSh is a hybrid meta-GGA functional designed for accurate treatment of weak intermolecular interactions, therefore comparing its performance with the standard hybrid GGA PBE0 functional is of interest in the context of aurophilic structures. The dispersion interaction was included with the DFT-D3 method of Grimme *et al.* [113] and the revised many-body dispersion method (MBD) by Ambrosetti *et al.* [167].

The benchmark supermolecular interaction energies were calculated at the DLPNO-CCSD(T) level of theory [168, 169]. Moreover, we obtained results at the MP2 and spin-component scaled MP2 (SCS-MP2) [170] level of theory, which is a popular choice for calculations involving gold(I) complexes. The interaction energies were corrected

for the basis set superposition error using the standard counterpoise correction (CP)
[72].

The motif **1** is composed of two $[Au(H_2\text{-}mmta)_2]^+$ units, and two adjoining $[Cl^- \cdots$
$H_2O]$ fragments. In the case of **2** we did not include the sodium counterions because of
the complex pattern they form in the stabilization of the carboxylate groups. Instead,
2 consists of two $[Au(mmta)_2]^{3-}$. Finally, **3** encompasses two $[Au(H\text{-}mmta)_2]^-$ (where
H-$mmta$ denotes the ligand with carboxyl groups) and two $[Na^+ \cdots 5 H_2O]$ fragments
(see Fig. A.4 in the Appendix for visualization of **1**-**3**).

We begin by analyzing the strength of the intermolecular interactions between dif-
ferent components of motifs **1** and **3** in which the effect of the counterion stabilization
can be estimated. Taking into consideration the structure of **1** and **3** we distinguish
the binding energy of the complex (E_{complex}), the interaction energy of the charged
aurophilic dimers and the accompanying ions ($E_{\text{int}}^{\text{c}-\text{ions}}$), as well as the intermolecular
repulsion between the charged aurophilic dimers themselves ($E_{\text{int}}^{\text{Au}-\text{dim}}$), see Table 7.2 for
definitions. Finally, we compare the dispersion energy contribution, $E_{\text{disp}}^{\text{Au}-\text{dim}}$, obtained
with the DFT-D3 and MBD methods. The results are presented in Table 7.2.
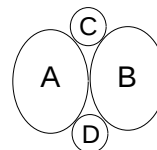
We first notice a remarkable agreement between the SCS-MP2 and the DLPNO-
CCSD(T) results. As expected, MP2 slightly overestimates the interaction energies.
Although the agreement between DFT and wave function methods is satisfactory, we
observe a slight overbinding in all DFT variants which can be traced to the overesti-
mation of the counterion stabilization effect $E_{\text{int}}^{\text{c}-\text{ions}}$. This effect is more pronounced in
3. The disagreement between different DFT approaches results from the D3 correction
overestimating the dispersion energy between the charged aurophilic units due to the
positive partial charge on gold atoms [171]. Finally, we recognize and recommend the
MCSh-MBD as a functional leading to the best DFT results.

The interaction energies given in Table 7.2 demonstrate that the binding of Cl^-/Na^+
and water molecules to the complex is crucial for the observed stabilization. We also
note the enhanced repulsion energy that accompanies the shortening of the distance
between the charged monomers in **3** with respect to **1**. This effect is compensated by
the stronger counterion attraction.

In order to further characterize the different $Au \cdots Au$ binding patterns in **1** − **3**,
we performed the QTAIM analysis. In all the structures we confirmed bond critical
points (BCP) indicating the presence of aurophilic interactions. In Table 7.3 given

Table 7.2: A schematic representation of the structure of **1** and **3**. Interaction energy components between different components of **1** and **3**. All interaction energies are given in kcal/mol and were calculated with the CP correction.

$$E_{\text{complex}} = E_{\text{ABCD}} - E_{\text{A}} - E_{\text{B}} - E_{\text{C}} - E_{\text{D}}$$

$$E_{\text{int}}^{\text{c}-\text{ions}} = E_{\text{ABCD}} - E_{\text{AB}} - E_{\text{CD}}$$

$$E_{\text{int}}^{\text{Au}-\text{dim}} = E_{\text{AB}} - E_{\text{A}} - E_{\text{B}}$$

(**1**)	E_{complex}	$E_{\text{int}}^{\text{c}-\text{ions}}$	$E_{\text{int}}^{\text{Au}-\text{dim}}$	$E_{\text{disp}}^{\text{Au}-\text{dim}}$
PBE0-D3	-209.1	-257.1	20.18	-6.48
PBE0-MBD	-205.3	-257.3	24.36	-2.30
MCSh-D3	-205.5	-252.8	19.68	-8.93
MCSh-MBD	-201.9	-254.7	25.18	-3.43
HF	-170.7	-232.9	34.72	
MP2	-208.4	-254.8	18.85	
SCS-MP2	-198.9	-249.0	22.62	
DLPNO-CCSD(T)	-200.0	-251.0	23.52	
(**3**)				
PBE0-D3	-216.7	-287.9	40.76	-6.46
PBE0-MBD	-212.6	-287.1	44.11	-2.56
MCSh-D3	-215.1	-286.4	40.94	-8.88
MCSh-MBD	-211.6	-287.8	45.90	-3.91
HF	-173.2	-263.1	59.14	
MP2	-207.1	-277.1	39.53	
SCS-MP2	-197.9	-272.7	44.36	
DLPNO-CCSD(T)	-199.8	-275.4	45.24	

are the topological parameters which characterize the obtained BCPs based on PBE0-D3 densities. The small values of the electron density at BCP, $\rho_c(r)$, together with small and positive values of its Laplacian at BCP, $\nabla^2 \rho_c(r)$, point towards a closed-shell type of interactions and fall within the range reported for the metallophilic interactions of group 11 so far [172–176]. The negative sign of the total energy density at BCP $H_c = G_c + V_c$, where G_c and V_c denote the kinetic and potential energy densities at BCP, respectively, indicates a stabilizing interaction with electron sharing [177]. This is reflected in the delocalization index $\delta(\text{Au,Au'})$ which provides the average number of electrons shared between (bonding) atoms at BCP [159]. The increase of both H_c and $\delta(\text{Au,Au'})$ with the shortening of the Au$\cdots$Au distance from **1** to **3** is a signature of the aurophilic interaction gaining a more covalent character. The behavior of the

Table 7.3: Electron charge density, $\rho_c(r)$, its Laplacian, $\nabla^2\rho_c(r)$, total energy density, $H_c(r)$, the ratio of the potential energy density (V_c) to the kinetic energy density G_c, $\frac{|V_c|}{G_c}$ and delocalization index, $\delta(Au,Au')$, at the Au$\cdots$Au BCP for structures $\mathbf{1}-\mathbf{3}$.

	r_{Au-Au}	$\rho_c(r)$	$\nabla^2\rho_c(r)$	$H_c(r)$	$\frac{|V_c|}{G_c}$	$\delta(Au,Au')$
1	3.354	0.016	0.039	-0.0004	1.04	0.189
2	3.184	0.022	0.054	-0.0011	1.07	0.233
3	3.093	0.026	0.063	-0.0020	1.11	0.289

$\frac{|V_c|}{G_c}$ ratio which allows one to distinguish between interactions of closed-shell ($\frac{|V_c|}{G_c} < 1$), intermediate ($1 < \frac{|V_c|}{G_c} < 2$) and covalent ($\frac{|V_c|}{G_c} > 2$) character [178–180] supports this observation and reveals the intermediate character of aurophilic interactions in terms of Bader analysis [174].

The QTAIM analysis also reveals some the weak interactions stabilizing the eclipsed conformation of the dimers. Figure 7.4 shows the BCPs and ring critical points (RCPs) identified in clusters **1** and **3** using PBE0-D3 density. In contrast to Lim *et al.* [144], for all structures we observe non-negligible interactions between the terminal S-atoms facing each other (e.g. S4$\cdots$S2^i in **1**). We notice, however, that these contacts in **1** − **3** salts are ca. 0.15 Å shorter than the ones observed by Lim *et al.*. The topological parameters of the BCPs ($\nabla^2\rho_c(r)$ in the range of 0.035-0.039, $H_c > 0$ and $\frac{|V_c|}{G_c} < 1$) classify those S$\cdots$S contacts as weak closed-shell interactions.

The variety of noncovalent interactions that contribute to the stabilization of the selected structures may be visualized based on the analysis of the electron densities and their reduced gradients $s(\rho)$. The reduced gradient reaches large positive values for regions far from the molecule corresponding to density tails and small positive values approaching zero for regions of both covalent bonding and noncovalent interactions. Mapping the regions of low $s(\rho)$ back to molecular space and examining the second derivatives of the density along the main axis of variation allows one to distinguish between different interactions in the low-density regime, including steric repulsion, hydrogen bonds and van der Waals interactions. This approach, termed NCI, was introduced by Johnson *et al.* [157, 158]. The color convention we use for the NCI analysis follows the work of Chaudret *et al.* [181]: *i*) blue for highly attractive weak interactions (such as hydrogen bonds) , *ii*) green for the weaker dispersion interactions (such as van der Waals), *iii*) red for repulsive interactions (such as steric clashes).
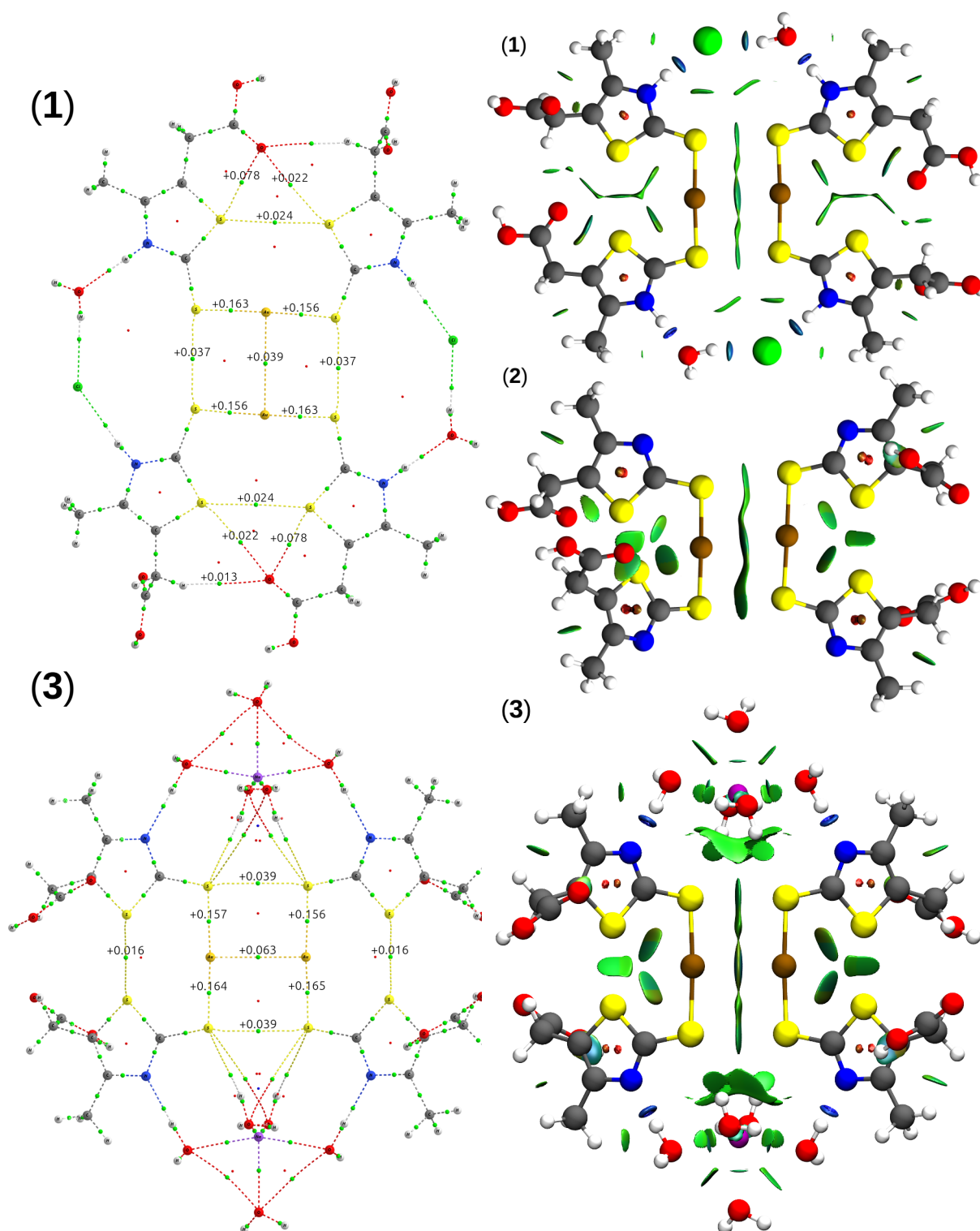
Figure 7.4: Molecular graph of **1** and **3** with BCPs marked as green spheres and RCPs marked as red spheres. The values denote $\nabla^2 \rho_c(r)$.

Figure 7.5: NCI analysis of the interactions in **1**, **2** and **3**. NCI surfaces correspond to $s = 0.45$ a.u. and a color scale of $-0.05 < \rho < 0.05$ a.u.

The results of NCI analysis are presented in Fig. 7.5. Several regions of inter-monomer interactions can be distinguished. In all the structures the eclipsed $(S\text{-}Au\text{-}S)_2$ junction exhibits regions corresponding to the attractive interactions of the $Au\cdots Au$, $S\cdots S$ and $Au\cdots S$ type. Importantly, the NCI method reveals that the shortening of the $Au\cdots Au$ distance from **1** to **3** is accompanied by the strengthening of the aurophilic interaction. This is manifested in the s versus ρ plots as the shift of the characteristic Au-Au peak towards more negative values which in the applied color convention amounts to bluish coloration of the solid green $Au\cdots Au$ isosurfaces (see Fig. A.4 in the Appendix) [182]. Furthermore, the evidence of the attractive $S\cdots S$ and $Au\cdots S$ contacts corresponds to the hypothesis [183] that the attractive dispersion interactions may outweigh the steric and Coulombic repulsion between the sulfur atoms.

In **1** and **3** visible are the dispersion interactions between the eclipsed dimers and the surrounding counterions and solvent molecules. The blue regions mark the hydrogen bonds bridging the monomers through the heterocyclic amine groups.

The intramonomer interactions can also be identified. In all the motifs there is a signature of the dispersion attraction between the Au(I) centers and the heterocyclic sulfur atoms. This could already be inferred from the range of the $Au\cdots S$ contacts that are smaller than the sum of their van der Waals radii (ca. 3.46 Å) [141, 184]. Furthermore, in **1** visible are the attractive $O1\cdots S1$ and $O1\cdots S3$ interactions. The regions of these interactions overlap with the BCPs predicted in the AIM picture (see Fig. 7.4). This shows that the carboxyl group directed towards the $S1\cdots S3$ contact additionally stabilizes the coplanar *cis* arrangement of the H_2-*mmta* rings in **1**. Finally, in the NCI picture the $S1\cdots S3$ contact in **1** and the corresponding $S\cdots S$ regions in **2** and **3** exhibit dispersion stabilization themselves.

As a final point we wish to address two effects stabilizing the *gauche* conformation in the crystal structure of compounds **2** and **3**. The first one is the stabilization due to the $\pi - \pi$ interactions between the rings of the neighboring dimers. The second one comes from the stabilization of the carboxylate groups either by the coordination with the Na^+ cations in **2**, or by hydrogen bonds with the surrounding water molecules in **3**. To estimate the $\pi - \pi$ contribution, we calculated the PBE0-D3 dispersion energy per one *mmta* pair in **2** and **3** obtaining -14.3 kcal/mol and -13.6 kcal/mol, respectively (see Fig. A.5 in the Appendix). The stabilization due to the presence of the counterions has previously been recognized in $Na_3[Au(S_2O_3)_2]\cdot 2H_2O$ [138, 139] and

$[(H_2O)_3Na][Au(SCSN_3)_2]$ [144]. We note that the *gauche* configuration has already been observed for other $[Au(SR)_2]$-complexes containing five- or six-membered heterocycles [141, 142, 144, 151, 184].

7.4   Conclusions

We presented three new gold(I) salts containing $[Au(H_2\text{-}mmta)_2]^+$ cations and $[Au(mmta)_2]^{3-}$ anions. The obtained compounds were characterized by means of X-Ray crystallography as gold(I) dimers – all of which exhibit aurophilic interactions. The aurophilic dimers adopt an eclipsed conformation which is uncommon for linear, two-coordinate gold complexes. [144] In order to better understand the intermolecular interactions stabilizing the eclipsed arrangement of the aurophilic dimers, we selected representative structural motifs of **1-3** for a more detailed *ab initio* investigation.

In each compound, by means of the NCI and QTAIM analyses, we identified several regions of weakly attractive intermolecular interactions. In particular, we found signatures of the dispersion interactions in the eclipsed S-Au-S contact region, which can be attributed partly to aurophilic attraction. The NCI analysis also revealed intramolecular dispersion interactions of the $Au(I)\cdots S$ type stabilizing both *cis* and *gauche* conformations of the *mmta* rings within the Au(I)-monomers. The *gauche* conformation of the $[Au(mmta)_2]^{3-}$ anions in **2** and **3** is moreover stabilized by crystal packing effects: the $\pi - \pi$ stacking and coordination of the carboxylate groups either by sodium cations or *via* hydrogen bonds with the water molecules. Based on the D3 model we estimated the dispersion contribution to the $\pi - \pi$ stacking to yield ca. -14 kcal/mol per one *mmta* pair.

The eclipsed geometry of the aurophilic dimers in compounds **1** and **3** is additionally stabilized by electrostatic and induction interactions with the surrounding counterions. Both DFT and *ab initio* calculations have shown that the Cl^--mediated stabilization in **1**, as well as the Na^+-mediated stabilization in **3** constitute the major contribution to the binding energy of the selected motifs and have a similar energetic effect. Nevertheless, no corresponding counterion support is observed in **2** or other dimeric $[Au(SR)_2]$ compounds containing five- or six-membered heterocycles. [141, 142, 144] Finally, the central eclipsed $(RS\text{-}Au\text{-}SR)_2$ motif is consistent for all of the presented compounds $\mathbf{1 - 3}$, irrespective of different counterion and crystal packing stabilization effects.

CHAPTER 8

Conclusions

In the presented Thesis advances in both theory and applications of DFT were reported. The theoretical developments involved introduction of two new SAPT formalisms based on Kohn-Sham description of monomers. New applications were focused on reliable DFT calculations of intermolecular interactions and optical response properties of gold complexes.

The most important achievements of my PhD Thesis:

1. I have implemented and tested the LRC-SAPT formalism with second-order energies calculated via FDDSs from TDDFT. I have shown that LRC xc functionals combined with SAPT yield results comparable or better with the asymptotically corrected functionals. Moreover, based on the studies of two model systems: polyacetylenes of increasing length and stretching of He_3^+, I have shown that minimization of the delocalization error in LRC-SAPT may be crucial for the quality of SAPT interaction energy components.

2. I have derived, implemented and tested a novel DFT-SAPT formulation based on urestricted Kohn-Sham formulation (SAPT(UKS)). The new method was compared to the SAPT(ROKS) approach introduced by Żuchowski *et al.* [97] showing a very good agreement.

3. I have presented several novel applications of SAPT(UKS): i) calculations of interactions involving Π-state radicals (He$\cdots$OH, Ar$\cdots$OH, Ar$\cdots$NO), ii) modelling of the systems undergoing Penning Ionization (PI) reaction (He*$\cdots$H$_2$, He*$\cdots$Ar, Ne*$\cdots$Ar, Ne*$\cdots$ND$_3$, He*$\cdots$NH$_3$), iii) clarification of the nature of the CrH(X$^6\Sigma^+$)$\cdots$He bonding mechanism.

4. I have participated in developing a reliable DFT computational treatment of gold-ligand interactions of the donor-acceptor character. We have devised a method allowing for a correct description of both the ionization potential of the electron donor and electron affinity of the electron acceptor. This is achieved by selecting an optimal LRC functional based on two-parameter tuning for the monomer properties. We have shown that, with the dispersion interactions properly taken into account, our approach leads to a very good agreement with respect to coupled-cluster reference values. My main contribution to the described work involved studies of the (HAuPH$_3$)$_2$ and Au$_4$-SCN$^-$ complexes presented in Chapter 5.

5. I have participated in the study of optical properties of gold clusters Au$_n$ ($n = 4$, 6, 8, 12, 20). Our work was the first to apply LRC xc functionals to the absorption UV spectra of this class of systems. We have proven that both inclusion of a fixed portion of the exact exchange and assuring correct asymptotics of the xc potential are vital for correct description of the optical response of gold. The results for the Au$_4$ and Au$_6$ clusters presented in Chapter 6 were my main contribution to the described research.

6. I have synthesized three new gold(I) complexes: [Au(H$_2$-$mmta$)$_2$]Cl$\cdot$3H$_2$O, Na$_3$[Au($mmta$)$_2$] $\cdot$6H$_2$O and Na$_3$[Au($mmta$)$_2$] $\cdot$10.5H$_2$O (H$_2$-$mmta$ = 2-Mercapto-4-methyl-5-thiazoleacetic acid). The obtained salts have been characterized via single crystal X-ray analysis and Raman spectroscopy. All structures exhibit unsupported aurophilic interactions leading to the formation of dimeric [Au$_2$(H$_2$-$mmta$)$_4$]$^{2+}$ and [Au$_2$($mmta$)$_4$]$^{6-}$ species. The experimental part was supplemented with a detailed theoretical analysis of the weak intermolecular interactions stabilizing the untypical eclipsed arrangement of the aurophilic dimers in **1**-**3**.

Appendix

A.1   Symbols and notation

In Chapter 2 the occupied orbital indices for monomer A and B are i and j, respectively, with the corresponding indices for virtual orbitals being a and b. Vectors $\mathbf{r}_i$ and $\mathbf{R}_\alpha$ denote electron and nuclei positions, respectively, and

$$\begin{cases} r_{ij} = |\mathbf{r}_i - \mathbf{r}_j| \\ R_{\alpha\beta} = |\mathbf{R}_\alpha - \mathbf{R}_\beta|. \end{cases} \tag{A.1}$$

The atomic units are used unless indicated otherwise.

A.2 $E_{\text{exch}}^{(1)}$ in SAPT(UKS): definitions

Below we give definitions of the quantities used in the expressions for the first-order exchange energy in its full form and using the S^2 approximation (see Chapter 4, Sec. 4.2).

We start with the generalized Coulomb and exchange matrices, $\mathbf{J}[\mathbf{X}], \mathbf{K}[\mathbf{X}]$:

$$\mathbf{J}[\mathbf{X}]_R^S = \sum_{PQ} X_Q^P (PQ|RS),$$

$$\mathbf{K}[\mathbf{X}]_R^Q = \sum_{PS} X_S^P (PQ|RS), \tag{A.2}$$

where

$$(PQ|RS) = \int \int \varphi_P^*(\mathbf{r}_1) \varphi_Q(\mathbf{r}_2) \frac{1}{r_{12}} \varphi_R^*(\mathbf{r}_1) \varphi_S(\mathbf{r}_2) d\mathbf{r}_1 d\mathbf{r}_2. \tag{A.3}$$

In the $E_{\text{exch}}^{(1)}(S^2)$ expression it is convenient to introduce generalized right and left Coulomb matrices:

$$\overset{r}{\mathbf{J}}[\mathbf{X}]_R^S = \sum_{R'S'} X_{S'}^{R'} (RS|v|R'S'),$$

$$\overset{l}{\mathbf{J}}[\mathbf{X}]_{R'}^{S'} = \sum_{RS} X_S^R (RS|v|R'S'), \tag{A.4}$$

and the generalized inner and outer exchange matrices:

$$\overset{i}{\mathbf{K}}[\mathbf{X}]_R^{S'} = \sum_{R'S} X_S^{R'} (RS|v|R'S'),$$

$$\overset{o}{\mathbf{K}}[\mathbf{X}]_{R'}^S = \sum_{RS'} X_{S'}^R (RS|v|R'S'). \tag{A.5}$$

In (A.4) and (A.5) the four-index integral of the form

$$(PQ|v|RS) = \int \int \varphi_P^*(\mathbf{r}_1) \varphi_Q(\mathbf{r}_2) v(\mathbf{r}_1, \mathbf{r}_2) \varphi_R^*(\mathbf{r}_1) \varphi_S(\mathbf{r}_2) d\mathbf{r}_1 d\mathbf{r}_2 \tag{A.6}$$

is used. The generalized interaction potential $v(\mathbf{r}_1, \mathbf{r}_2)$ is defined as:

$$\tilde{v}(\mathbf{r}_1, \mathbf{r}_2) = \frac{1}{|\mathbf{r}_1 - \mathbf{r}_2|} + v_A(\mathbf{r}_1) \frac{1}{N_B} + v_B(\mathbf{r}_2) \frac{1}{N_A} + \frac{V_0}{N_A N_B}, \tag{A.7}$$

so that $V = \sum_i^{N_A} \sum_j^{N_B} \tilde{v}(\mathbf{r}_i, \mathbf{r}_j)$. N_X denotes the number of electrons in monomer X and V_0 is the constant internuclear repulsion term. We note that the explicit form of the generalized Coulomb and exchange matrices in given in Appendix A of Ref. [99].

The $\mathbf{h}_\sigma^X$ matrix in (4.1) is given as

$$\mathbf{h}_\sigma^X = \mathbf{V}^X + \mathbf{J}_\alpha^X + \mathbf{J}_\beta^X - \mathbf{K}_\sigma^X \tag{A.8}$$

and the $\mathbf{T}_\sigma^{X/XY}$ matices backtransformed to the AO basis are computed as follows:

$$\begin{aligned}
\mathbf{T}_\sigma^X &= (\mathbf{C}_\sigma^X)^\dagger([\mathbf{S}_\sigma + \mathbf{1}]^{-1} - \mathbf{1})\mathbf{C}_\sigma^X \\
\mathbf{T}_\sigma^{XY} &= (\mathbf{C}_\sigma^X)^\dagger([\mathbf{S}_\sigma + \mathbf{1}]^{-1} - \mathbf{1})\mathbf{C}_\sigma^Y
\end{aligned} \tag{A.9}$$

The $\mathbf{S}_\sigma$ stands for the matrix of overlap integrals between the occupied molecular orbitals of both monomers, $(\mathbf{S}_\alpha)_{\tilde{i}}^{\tilde{j}} \equiv S_{\tilde{i}}^{\tilde{j}} = \int \varphi_{\tilde{i}}(\mathbf{r})\varphi_{\tilde{j}}(\mathbf{r})d^3\mathbf{r}$.

A.3 Data to accompany Chapter 7

A.3.1 X-ray crystallography

A selected single crystal was mounted in inert oil and transferred to the cold gas stream of the diffractometer. Diffraction data were measured with mirror monochromated CuKα or graphite monochromated MoKα radiation on an Oxford Diffraction κ-CCD Gemini A Ultra diffractometer. Cell refinement and data collection as well as data reduction and analysis were performed with the CRYSALIS$^{\text{PRO}}$ software [185]. Structures were solved by direct methods using the SHELXS-97 structure solution program and refined by full-matrix least-squares against F^2 with SHELXL-2014 [186] and OLEX2 [187] programs. All non-hydrogen atoms were refined with anisotropic displacement parameters. Hydrogen atoms were added to the structure model at geometrically idealized coordinates and refined as riding atoms. The crystal data and experimental parameters are summarized in Table A.1. CCDC1062294-1062297 contain the supplementary crystallographic data. These data can be obtained free of charge from The Cambridge Crystallographic Data Centre via www.ccdc.cam.ac.uk/data_request/cif.

Table A.1: Crystal data and data collection parameters for structures **1**-**3**.

	(**1**)	(**2**)	(**3**)
Compound reference	(**1**)	(**2**)	(**3**)
Chemical formula	$C_{12}H_{20}AuClN_2O_7S_4$	$C_{24}H_{44}Au_2N_4Na_6O_{20}S_8$	$C_{24}H_{61}Au_2N_4Na_6O_{29}S_8$
Formula Mass	664.96	1496.98	1658.12
Crystal system	Triclinic	Monoclinic	Orthorhombic
a/Å	6.4839(5)	11.8332(4)	11.14230(14)
b/Å	10.6956(8)	21.4246(8)	26.7990(3)
c/Å	16.2649(9)	18.7942(6)	38.4479(5)
α/°	79.106(6)	90	90
β/°	87.562(5)	91.843(3)	90
γ/°	75.111(6)	90	90
Unit cell volume/Å^3	1070.42(13)	4762.3(3)	11480.6(3)
Space group	$P\bar{1}$	$P2_1/n$	$Fddd$
No. of formula units per unit cell, Z	2	4	8
Radiation type	CuKα	CuKα	CuKα
Absorption coefficient, μ/mm^{-1}	18.046	15.905	13.386
No. of reflections measured	10803	35597	43130
No. of independent reflections	3806	8441	2551
R_{int}	0.0305	0.0589	0.0334
Final R_1 values ($I > 2\sigma(I)$)	0.0308	0.0469	0.046
Final $wR(F^2)$ values ($I > 2\sigma(I)$)	0.071	0.1066	0.1094
Final R_1 values (all data)	0.0356	0.0665	0.0466
Final $wR(F^2)$ values (all data)	0.074	0.1155	0.1096
Goodness of fit on F^2	1.129	1.125	1.375

Table A.2: Crystal data and data collection parameters for 2-Mercapto-4-methyl-5-thiazoleacetic acid H$_2$-*mmta*.

Compound reference	4
Chemical formula	$C_6H_7NO_2S_2$
Formula Mass	189.25
Crystal system	Monoclinic
$a/\text{Å}$	7.3214(6)
$b/\text{Å}$	14.1820(13)
$c/\text{Å}$	15.5197(10)
$\alpha/°$	90
$\beta/°$	95.774(7)
$\gamma/°$	90
Unit cell volume/Å^3	1603.3(2)
Space group	$I2/a$
No. of formula units per unit cell, Z	8
Radiation type	MoKα
Absorption coefficient, μ/mm^{-1}	0.61
No. of reflections measured	3825
No. of independent reflections	1816
R_{int}	0.0344
Final R_1 values ($I > 2\sigma(I)$)	0.0387
Final $wR(F^2)$ values ($I > 2\sigma(I)$)	0.0944
Final R_1 values (all data)	0.05
Final $wR(F^2)$ values (all data)	0.1017
Goodness of fit on F^2	1.08

Table A.3: The assymetric unit, selected bond lengths [Å] and angles for 2-Mercapto-4-methyl-5-thiazoleacetic acid.

S2-C1	1.674(2)
C1-S1	1.720(2)
C1-N1	1.341(3)
C2-C3	1.347(3)
S2-C1-S1	124.09(13)
N1-C1-S2	127.64(17)

Table A.4: Hydrogen bond network in **1**

D-H$\cdots A$	D-H (Å)	H$\cdots A$ (Å)	D$\cdots A$ (Å)	D-H$\cdots A$ (°)
N1-H1-O4[1]	0.85(5)	1.95(5)	2.774(6)	164(6)
N2-H2A-Cl1[2]	0.85(5)	2.31(5)	3.163(5)	176(6)
O2-H2-O3[3]	0.85(2)	1.73(3)	2.540(6)	159(8)
O12-H12-O5[4]	0.84(2)	1.84(3)	2.661(7)	164(8)
O3-H3A-O11	0.85(2)	2.09(8)	2.762(7)	135(9)
O3-H3B-O4	0.85(2)	2.17(3)	2.974(9)	158(8)
O4-H4C-O5[5]	0.85(2)	1.92(2)	2.763(6)	176(8)
O4-H4D-Cl1[6]	0.85(2)	2.31(4)	3.106(5)	157(9)
O5-H5A-Cl1	0.85(2)	2.21(2)	3.059(5)	177(6)
O5-H5B-Cl1[7]	0.85(2)	2.28(3)	3.107(5)	163(7)

Symmetry codes: [1] *1-x,1-y,1-z;* [2] *-1+x,+y,+z;* [3] *1+x,+y,+z;*
[4] *2-x,-y,2-z;* [5] *+x,-1+y,+z;* [6] *1-x,1-y,2-z;* [7] *2-x,1-y,2-z*
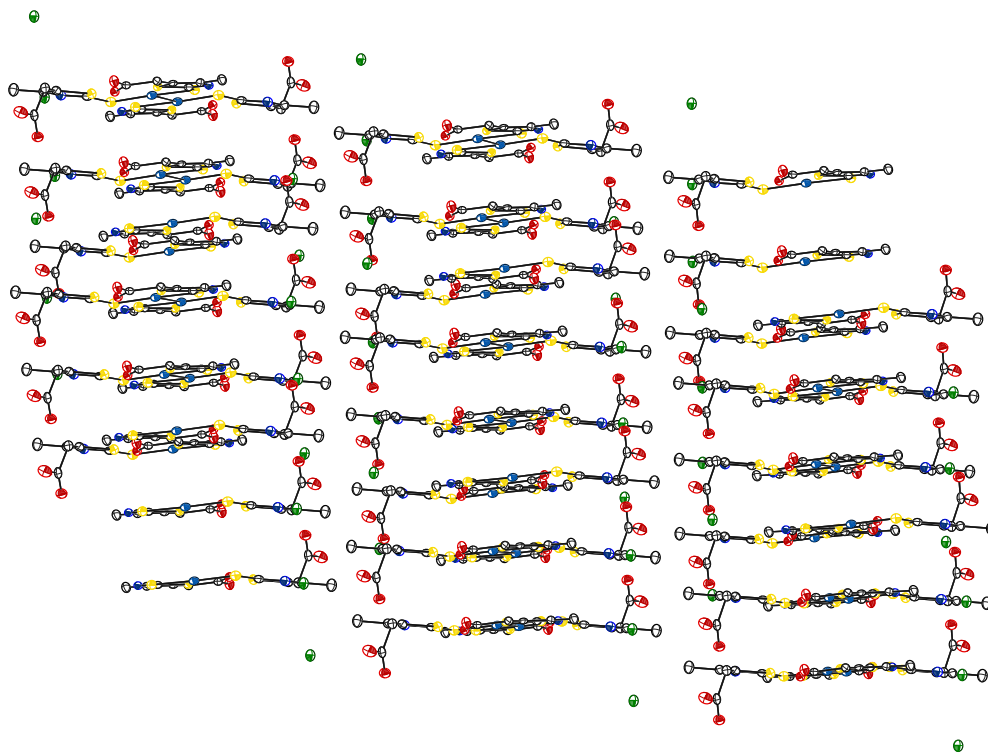
Figure A.1: A drawing of a portion of the structure of $[\text{Au}(\text{H}_2\text{-}mmta)_2]\text{Cl}\cdot3\text{H}_2\text{O}$ that shows the parallel stacking of the $[\text{Au}_2(\text{H}_2\text{-}mmta)_4]^{2+}$ dimers. Color code: Au - navy blue, S - yellow, O - red, N -blue, Cl$^-$ - green.
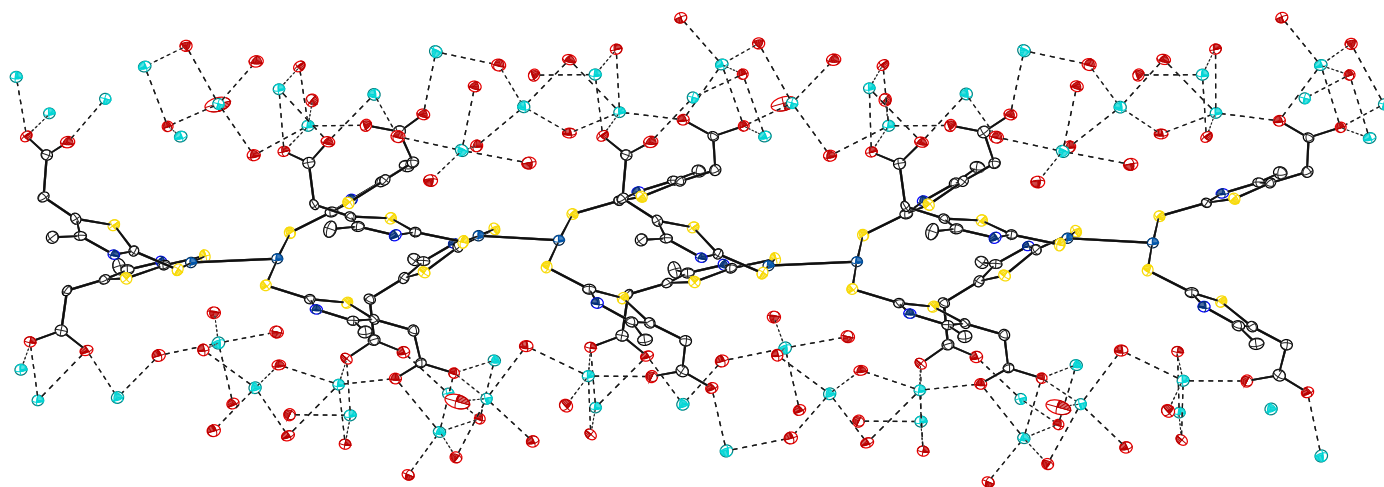
Figure A.2: A drawing of a portion of the structure of $Na_3[Au(mmta)_2]\cdot6H_2O$ that shows the $\pi-\pi$ stacking of the dimers along the b axis. Color code: Au - navy blue, S - yellow, O - red, N -blue, Na - cyan.
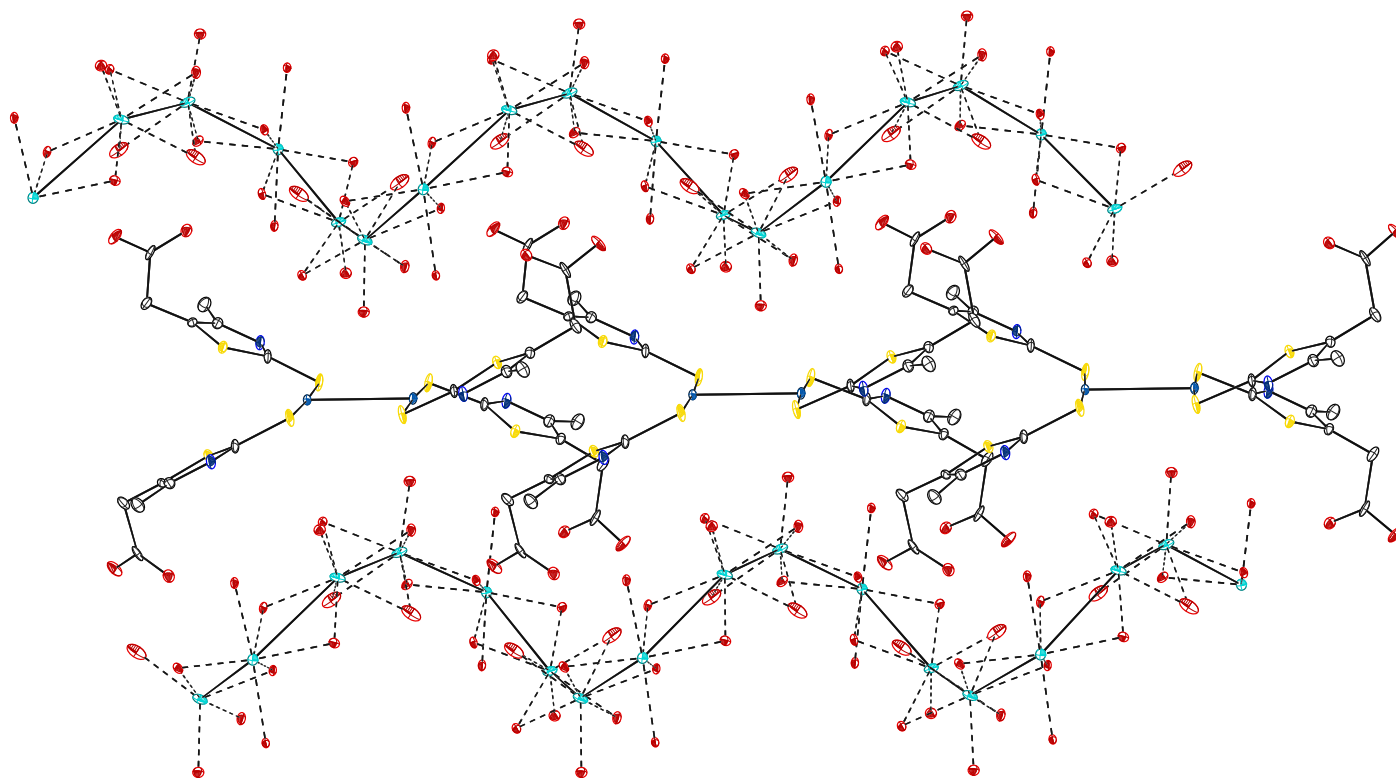

Figure A.3: A drawing of a portion of the structure of $Na_3[Au(mmta)_2]\cdot10.5H_2O$ that shows the $\pi-\pi$ stacking of the dimers along the a axis. The helical structure formed by sodium cations along the a axis is also presented. Color code: Au - navy blue, S - yellow, O - red, N -blue, Na - cyan.

Table A.5: Characteristic of $\pi - \pi$ stacking interactions in **2** and **3**. All distances given in Å, all angles given in degrees.

| **2**	
Plane 1	S2-C1-N1-C2-C3
Plane 2	S32-C31-N31-C32-C33
Plane 1 to plane angle	4.9(4)
Plane centroid to plane centroid distance	3.615(5)
Plane [1] to plane centroid distance	3.472(7)
Plane [2] to plane centroid distance	-3.529(7)
Plane 1	N21-C21-S22-C23-C22
Plane 2	N11-C11-S12-C13-C12
Plane 1 to plane angle	6.3(5)
Plane centroid to plane centroid distance	3.645(5)
Plane [1] to plane centroid distance	3.481(8)
Plane [2] to plane centroid distance	-3.502(7)
3	
Plane 1	S1-C1-N1-C2-C3
Plane 2	$(S1\text{-}C1\text{-}N1\text{-}C2\text{-}C3)^{i}$
Plane 1 to plane angle	3.4(3)
Plane centroid to plane centroid distance	3.635(6)
Plane [1] to plane centroid distance	-3.413(8)
Plane [1] to plane shift	1.250(15)

$i = 7/4 - x,\ 3/4 - y,\ +z$
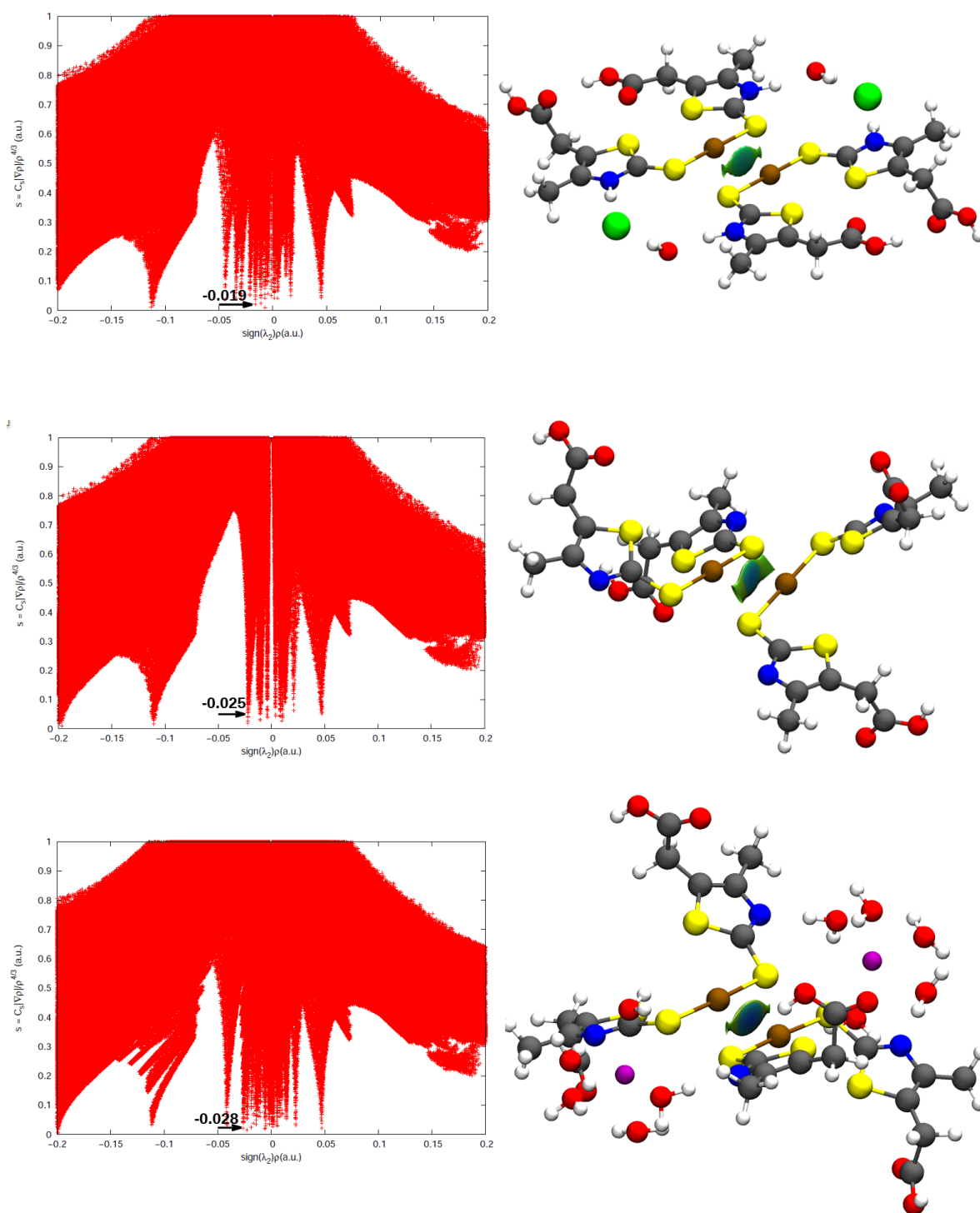
Figure A.4: Left: The reduced density gradient versus the electron density multiplied by the sign of the second Hessian eigenvalue. Marked are the peaks corresponding to the Au-Au interaction. Right: Gradient isosurfaces plotted in 1 Å radius around the midpoint of the Au-Au line with $s=0.5$ a.u.
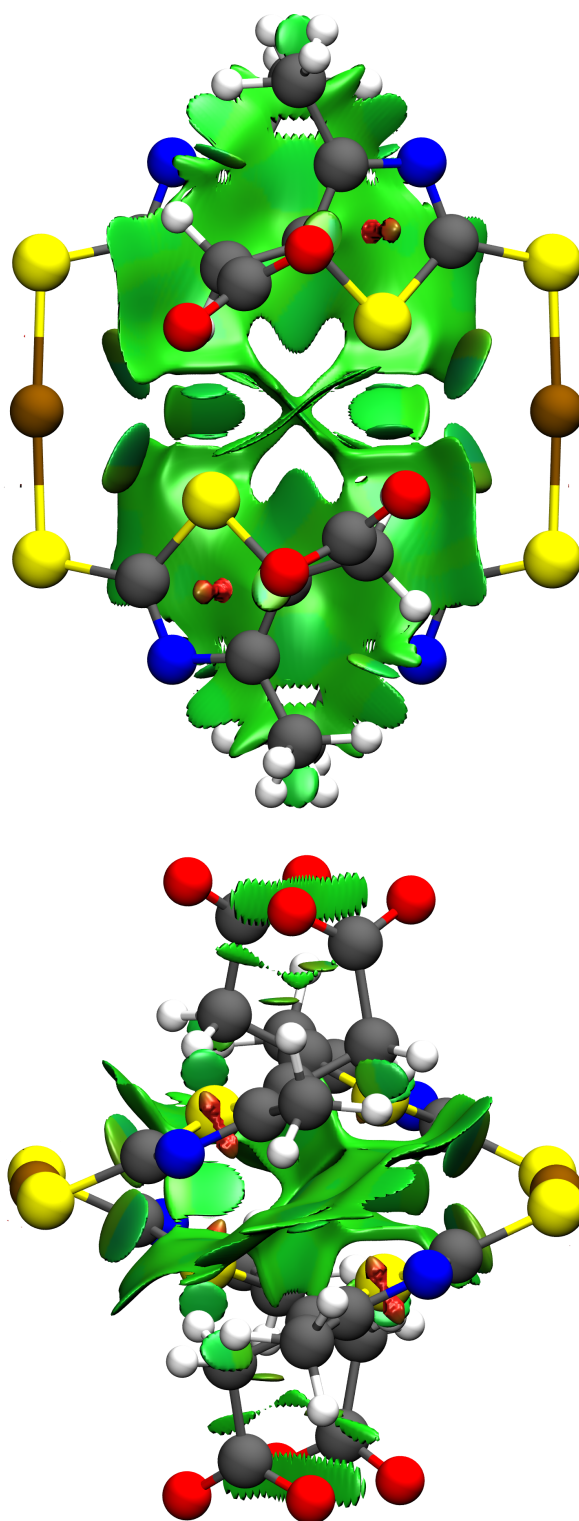
Figure A.5: Two views of NCI $\pi - \pi$ stabilization regions between the adjacent $[\text{Au}(mmta)_2]^{3-}$ monomers of **3** presented along the b and c axis. NCI surfaces correspond to $s = 0.5$ a.u. and a color scale of $-0.04 < \rho < 0.04$ a.u.

Bibliography

The results presented in this Thesis were published in the following papers:

[D1] M. Hapka, Ł. Rajchel, M. Modrzejewski, G. Chałasiński, and M. M. Szczęśniak, J. Chem. Phys. **141**, 134120 (2014).

[D2] M. Hapka, P. S. Żuchowski, M. M. Szczęśniak, and G. Chałasiński, J. Chem. Phys. **137**, 164104 (2012).

[D3] J. Koppen, M. Hapka, M. Modrzejewski, M. M. Szczęśniak, and G. Chałasiński, J. Chem. Phys. **140**, 244313 (2014).

[D4] J. V. Koppen, M. Hapka, M. M. Szczęśniak, and G. Chałasiński, J. Chem. Phys. **137**, 114302 (2012).

[D5] M. Hapka, M. Dranka, K. Orłowska, G. Chałasiński, M. M. Szczęśniak, and J. Zachara, Dalton Trans., (2015), DOI: 10.1039/C5DT01627D.

[D6] M. Hapka, G. Chałasiński, J. Kłos, and P. S. Żuchowski, J. Chem. Phys. **139**, 014307 (2013).

[D7] J. Jankunas, B. Bertsche, K. Jachymski, M. Hapka, and A. Osterwalder, J. Chem. Phys. **140**, 244302 (2014).

[D8] J. Jankunas, K. Jachymski, M. Hapka, and A. Osterwalder, J. Chem. Phys. **142**, 164305 (2015).

The full Bibliography:

[1] W. Kohn and L. J. Sham, Phys. Rev. **140**, A1133 (1965).

[2] A. D. Becke, J. Chem. Phys. **98**, 5648 (1993).

[3] P. J. Stephens, F. J. Devlin, C. F. Chabalowski, and M. J. Frisch, J. Phys. Chem. **98**, 11623 (1994).

[4] A. J. Cohen, P. Mori-Sánchez, and W. Yang, Chem. Rev. **112**, 289 (2012).

[5] K. Burke, J. Chem. Phys. **136**, 150901 (2012).

[6] T. Körzdörfer and J.-L. Brédas, Acc. Chem. Res. **47**, 3284 (2014).

[7] P. Mori-Sánchez, A. J. Cohen, and W. Yang, J. Chem. Phys. **125**, 201102 (2006).

[8] J. Autschbach and M. Srebro, Acc. Chem. Res. **47**, 2592 (2014).

[9] G. Jansen, WIREs Comput. Mol. Sci. **4**, 127 (2014).

[10] K. Pernal, R. Podeszwa, K. Patkowski, and K. Szalewicz, Phys. Rev. Lett. **103**, 263201 (2009).

[11] Ł. Rajchel, P. S. Żuchowski, M. M. Szczęśniak, and G. Chałasiński, Phys. Rev. Lett. **104**, 163001 (2010).

[12] R. Podeszwa and K. Szalewicz, J. Chem. Phys. **136**, 161102 (2012).

[13] H.-J. Werner, P. J. Knowles, G. Knizia, F. R. Manby, M. Schütz, P. Celani, T. Korona, R. Lindh, A. Mitrushenkov, G. Rauhut, K. R. Shamasundar, T. B. Adler, R. D. Amos, A. Bernhardsson, A. Berning, D. L. Cooper, M. J. O. Deegan, A. J. Dobbyn, F. Eckert, E. Goll, C. Hampel, A. Hesselmann, G. Hetzer, T. Hrenar, G. Jansen, C. Köppl, Y. Liu, A. W. Lloyd, R. A. Mata, A. J. May, S. J. McNicholas, W. Meyer, M. E. Mura, A. Nicklass, D. P. O'Neill, P. Palmieri, D. Peng, K. Pflüger, R. Pitzer, M. Reiher, T. Shiozaki, H. Stoll, A. J. Stone, R. Tarroni, T. Thorsteinsson, and M. Wang, MOLPRO, version 2012.1, a package of ab initio programs, 2012, see http://www.molpro.net.

[14] P. Pyykkö, Angew. Chem. Int. Ed. **43**, 4412 (2004).

[15] P. Pyykkö, Inorg. Chim. Acta **358**, 4113 (2005).

[16] P. Pyykkö, Chem. Soc. Rev. **37**, 1967 (2008).

[17] J. P. Perdew, R. G. Parr, M. Levy, and J. L. Balduz Jr, Phys. Rev. Lett. **49**, 1691 (1982).

[18] M. J. Allen and D. J. Tozer, J. Chem. Phys. **117**, 11113 (2002).

[19] P. Hohenberg and W. Kohn, Phys. Rev. **136**, B864 (1964).

[20] M. Levy, Phys. Rev. A **26**, 1200 (1982).

[21] A. Seidl, A. Görling, P. Vogl, J. A. Majewski, and M. Levy, Phys. Rev. B **53**, 3764 (1996).

[22] A. D. Becke, J. Chem. Phys. **98**, 1372 (1993).

[23] H. Iikura, T. Tsuneda, T. Yanai, and K. Hirao, J. Chem. Phys. **115**, 3540 (2001).

[24] T. Yanai, D. P. Tew, and N. C. Handy, Chem. Phys. Lett. **393**, 51 (2004).

[25] I. C. Gerber and J. G. Ángyán, Chem. Phys. Lett. **415**, 100 (2005).

[26] A. Savin and H.-J. Flad, Int. J. Quant. Chem. **56**, 327 (1995).

[27] A. Savin, in *Recent Developments and Applications of Modern Density Functional Theory*, Vol. 4 of *Theoretical and Computational Chemistry*, edited by J. Seminario (Elsevier, Amsterdam, 1996), pp. 327 – 357.

[28] T. Leininger, H. Stoll, H.-J. Werner, and A. Savin, Chem. Phys. Lett. **275**, 151 (1997).

[29] F. Furche, Phys. Rev. B **64**, 195120 (2001).

[30] S. Kümmel and L. Kronik, Rev. Mod. Phys. **80**, 3 (2008).

[31] R. Baer, E. Livshits, and U. Salzner, Ann. Rev. Phys. Chem. **61**, 85 (2010).

[32] R. Van Leeuwen and E. Baerends, Phys. Rev. A **49**, 2421 (1994).

[33] D. J. Tozer and N. C. Handy, J. Chem. Phys. **109**, 10180 (1998).

[34] M. Grüning, O. Gritsenko, S. Van Gisbergen, and E. Baerends, J. Phys. Chem. A **105**, 9211 (2001).

[35] W. Cencek and K. Szalewicz, J. Chem. Phys. **139**, 024104 (2013).

[36] H. L. Williams and C. F. Chabalowski, J. Phys. Chem. A **105**, 646 (2001).

[37] A. Heßelmann and G. Jansen, Chem. Phys. Lett. **357**, 464 (2002).

[38] A. Heßelmann and G. Jansen, Chem. Phys. Lett. **362**, 319 (2002).

[39] A. J. Misquitta and K. Szalewicz, Chem. Phys. Lett. **357**, 301 (2002).

[40] R. Baer and D. Neuhauser, Phys. Rev. Lett. **94**, 043002 (2005).

[41] E. Livshits and R. Baer, Phys. Chem. Chem. Phys. **9**, 2932 (2007).

[42] M. Modrzejewski, Ł. Rajchel, G. Chałasiński, and M. M. Szczęśniak, J. Phys. Chem. A **117**, 11580 (2013).

[43] L. Kronik, T. Stein, S. Refaely-Abramson, and R. Baer, J. Chem. Theory Comput. **8**, 1515 (2012).

[44] T. Körzdörfer, J. S. Sears, C. Sutton, and J.-L. Brédas, J. Chem. Phys. **135**, 204107 (2011).

[45] T. Stein, L. Kronik, and R. Baer, J. Am. Chem. Soc. **131**, 2818 (2009).

[46] S. Refaely-Abramson, S. Sharifzadeh, N. Govind, J. Autschbach, J. B. Neaton, R. Baer, and L. Kronik, Phys. Rev. Lett. **109**, 226405 (2012).

[47] T. Stein, L. Kronik, and R. Baer, J. Chem. Phys. **131**, 244119 (2009).

[48] T. Stein, H. Eisenberg, L. Kronik, and R. Baer, Phys. Rev. Lett. **105**, 266802 (2010).

[49] M. Srebro and J. Autschbach, J. Phys. Chem. Lett. **3**, 576 (2012).

[50] H. Sekino, Y. Maeda, M. Kamiya, and K. Hirao, J. Chem. Phys. **126**, 014107 (2007).

[51] H. Sun and J. Autschbach, ChemPhysChem **14**, 2450 (2013).

[52] A. J. Garza, O. I. Osman, A. M. Asiri, and G. E. Scuseria, J. Phys. Chem. B **119**, 1202 (2015).

[53] A. Karolewski, L. Kronik, and S. Kümmel, J. Chem. Phys. **138**, 204115 (2013).

[54] K. Garrett, X. Sosa Vazquez, S. B. Egri, J. Wilmer, L. E. Johnson, B. H. Robinson, and C. M. Isborn, J. Chem. Theory Comput. **10**, 3821 (2014).

[55] S. R. Whittleton, X. A. Sosa Vazquez, C. M. Isborn, and E. R. Johnson, J. Chem. Phys. **142**, 184106 (2015).

[56] P. Mori-Sánchez, A. J. Cohen, and W. Yang, Phys. Rev. Lett. **100**, 146401 (2008).

[57] W. Yang, Y. Zhang, and P. W. Ayers, Phys. Rev. Lett. **84**, 5172 (2000).

[58] W. Yang, A. J. Cohen, and P. Mori-Sánchez, J. Chem. Phys. **136**, 204111 (2012).

[59] O. A. Vydrov, G. E. Scuseria, and J. P. Perdew, J. Chem. Phys. **126**, 154109 (2007).

[60] C.-W. Tsai, Y.-C. Su, G.-D. Li, and J.-D. Chai, Phys. Chem. Chem. Phys. **15**, 8352 (2013).

[61] E. Runge and E. K. U. Gross, Phys. Rev. Lett. **52**, 997 (1984).

[62] M. Marques and E. Gross, Annu. Rev. Phys. Chem. **55**, 427 (2004).

[63] M. E. Casida, J. Mol. Struct. THEOCHEM **914**, 3 (2009).

[64] E. Gross, C. Ullrich, and U. Gossman, in *Density Functional Theory*, Vol. 337 of *NATO ASI Ser. B*, edited by E. Gross and R. Dreizler (Plenum, New York, 1994), pp. 149–71.

[65] E. Gross, J. Dobson, and M. Petersilka, in *Density Functional Theory II*, Vol. 181 of *Topics in Current Chemistry*, edited by R. Nalewajski (Springer, Berlin, 1996), pp. 81–172.

[66] R. van Leeuwen, Phys. Rev. Lett. **80**, 1280 (1998).

[67] L. Keldysh, Sov. Phys. JETP **20**, 1018 (1965).

[68] G. Vignale, Phys. Rev. A **77**, 062511 (2008).

[69] M. A. Marques, A. Castro, G. F. Bertsch, and A. Rubio, Computer Physics Communications **151**, 60 (2003).

[70] T. Burnus, M. A. Marques, and E. K. Gross, Phys. Rev. A **71**, 010501 (2005).

[71] C. Neidel, J. Klei, C.-H. Yang, A. Rouzée, M. J. J. Vrakking, K. Klünder, M. Miranda, C. L. Arnold, T. Fordell, A. L'Huillier, M. Gisselbrecht, P. Johnsson, M. P. Dinh, E. Suraud, P.-G. Reinhard, V. Despré, M. A. L. Marques, and F. Lépine, Phys. Rev. Lett. **111**, 033001 (2013).

[72] S. F. Boys and F. d. Bernardi, Mol. Phys. **19**, 553 (1970).

[73] G. Chałasiński, B. Jeziorski, J. Andzelm, and K. Szalewicz, Mol. Phys. **33**, 971 (1977).

[74] W. Kutzelnigg, J. Chem. Phys. **73**, 343 (1980).

[75] T. Cwiok, B. Jeziorski, W. Kołos, R. Moszyński, J. Rychlewski, and K. Szalewicz, Chem. Phys. Lett. **195**, 67 (1992).

[76] K. Szalewicz, K. Patkowski, and B. Jeziorski, in *Intermolecular Forces and Clusters II*, Vol. 116 of *Structure and Bonding*, edited by D. Wales (Springer, Berlin,Heidelberg, 2005), pp. 43–117.

[77] B. Jeziorski, K. Szalewicz, and G. Chałasiński, Int. J. Quantum Chem. **14**, 271 (1978).

[78] S. Rybak, B. Jeziorski, and K. Szalewicz, J. Chem. Phys. **95**, 6576 (1991).

[79] M. Jeziorska, B. Jeziorski, and J. Čížek, Int. J. Quant. Chem. **32**, 149 (1987).

[80] A. J. Misquitta, B. Jeziorski, and K. Szalewicz, Phys. Rev. Lett. **91**, 033201 (2003).

[81] W. Cencek and K. Szalewicz, J. Chem. Phys. **140**, 149902 (2014).

[82] K. U. Lao and J. M. Herbert, J. Chem. Phys. **140**, 044108 (2014).

[83] P. Jurečka, J. Šponer, J. Černỳ, and P. Hobza, Phys. Chem. Chem. Phys. **8**, 1985 (2006).

[84] M. E. Casida and D. R. Salahub, J. Chem. Phys. **113**, 8918 (2000).

[85] R. van Leeuwen and E. J. Baerends, Phys. Rev. A **51**, 170 (1995).

[86] A. P. Gaiduk and V. N. Staroverov, J. Chem. Phys. **131**, 044107 (2009).

[87] R. Neumann, R. H. Nobes, and N. C. Handy, Mol. Phys. **87**, 1 (1996).

[88] H. Sekino, Y. Maeda, and M. Kamiya, Mol. Phys. **103**, 2183 (2005).

[89] F. Weigend and R. Ahlrichs, Phys. Chem. Chem. Phys. **7**, 3297 (2005).

[90] A. Hesselmann, G. Jansen, and M. Schütz, J. Chem. Phys. **122**, 014103 (2005).

[91] Y. Tawada, T. Tsuneda, S. Yanagisawa, T. Yanai, and K. Hirao, J. Chem. Phys. **120**, 8425 (2004).

[92] J. Řezáč and P. Hobza, J. Chem. Theory Comput. **9**, 2151 (2013).

[93] Y. Zhao and D. G. Truhlar, J. Chem. Theory Comput. **1**, 415 (2005).

[94] J. C. Hansen and J. S. Francisco, Chem. Phys. Chem. **3**, 833 (2002).

[95] W. Klemperer, Proc. Natl. Acad. Sci. U. S. A. **103**, 12232 (2006).

[96] G. Quéméner and P. S. Julienne, Chem. Rev. **112**, 4949 (2012).

[97] P. S. Żuchowski, R. Podeszwa, R. Moszyński, B. Jeziorski, and K. Szalewicz, J. Chem. Phys. **129**, 084101 (2008).

[98] J. A. Pople, P. M. Gill, and N. C. Handy, Int. J. Quant. Chem. **56**, 303 (1995).

[99] T. Korona, J. Chem. Phys. **128**, 224104 (2008).

[100] A. Henson, S. Gersten, Y. Shagam, J. Narevicius, and E. Narevicius, Science **338**, 234 (2012).

[101] J. Kłos, M. Hapka, and G. Chałasiński, arXiv preprint arXiv:1312.4796 (2013).

[102] M. Hapka, J. Kłos, T. Korona, and G. Chałasiński, J. Phys. Chem. A **117**, 6657 (2013).

[103] J. C. Love, L. A. Estroff, J. K. Kriebel, R. G. Nuzzo, and G. M. Whitesides, Chem. Rev. **105**, 1103 (2005).

[104] K. Saha, S. S. Agasti, C. Kim, X. Li, and V. M. Rotello, Chem. Rev. **112**, 2739 (2012).

[105] M.-C. Daniel and D. Astruc, Chem. Rev. **104**, 293 (2004).

[106] V. Wing-Wah Yam and E. Chung-Chin Cheng, in *Photochemistry and Photophysics of Coordination Compounds II*, Vol. 281 of *Topics in Current Chemistry*, edited by V. Balzani and S. Campagna (Springer, Berlin Heidelberg, 2007), pp. 269–309.

[107] S. M. Morton, D. W. Silverstein, and L. Jensen, Chem. Rev. **111**, 3962 (2011).

[108] G. Sini, J. S. Sears, and J.-L. Brédas, J. Chem. Theory Comput. **7**, 602 (2011).

[109] S. N. Steinmann, C. Piemontesi, A. Delachat, and C. Corminboeuf, J. Chem. Theory Comput. **8**, 1629 (2012).

[110] E. R. Johnson, M. Salamone, M. Bietti, and G. A. DiLabio, J. Phys. Chem. A **117**, 947 (2013), pMID: 23323943.

[111] M. Seth, T. Ziegler, M. Steinmetz, and S. Grimme, J. Chem. Theory Comput. **9**, 2286 (2013).

[112] S. Refaely-Abramson, R. Baer, and L. Kronik, Phys. Rev. B **84**, 075144 (2011).

[113] S. Grimme, J. Antony, S. Ehrlich, and H. Krieg, J. Chem. Phys. **132**, 154104 (2010).

[114] A. Otero-de-la Roza, J. D. Mallory, and E. R. Johnson, J. Chem. Phys. **140**, 18A504 (2014).

[115] E. O'Grady and N. Kaltsoyannis, Phys. Chem. Chem. Phys. **6**, 680 (2004).

[116] P. Pyykkö and Y. Zhao, Angew. Chem., Int. Ed. Engl. **30**, 604 (1991).

[117] S. Eustis and M. A. El-Sayed, Chem. Soc. Rev. **35**, 209 (2006).

[118] T. L. Doane and C. Burda, Chem. Soc. Rev. **41**, 2885 (2012).

[119] D. W. Silverstein and L. Jensen, J. Chem. Phys. **132**, 194302 (2010).

[120] J. C. Idrobo, W. Walkosz, S. F. Yip, S. Öğüt, J. Wang, and J. Jellinek, Phys. Rev. B **76**, 205422 (2007).

[121] S. Lecoultre, A. Rydlo, C. Félix, J. Buttet, S. Gilb, and W. Harbich, J. Chem. Phys. **134**, 074302 (2011).

[122] M. J. G. Peach, P. Benfield, T. Helgaker, and D. J. Tozer, J. Chem. Phys. **128**, 044118 (2008).

[123] D. Figgen, G. Rauhut, M. Dolg, and H. Stoll, Chem. Phys. **311**, 227 (2005).

[124] B. Anak, M. Bencharif, and F. Rabilloud, RSC Adv. **4**, 13001 (2014).

[125] P. R. T. Schipper, O. V. Gritsenko, S. J. A. van Gisbergen, and E. J. Baerends, J. Chem. Phys. **112**, 1344 (2000).

[126] H. Häkkinen, B. Yoon, U. Landman, X. Li, H.-J. Zhai, and L.-S. Wang, J. Phys. Chem. A **107**, 6168 (2003).

[127] M. J. G. Peach, T. Helgaker, P. Salek, T. W. Keal, O. B. Lutnaes, D. J. Tozer, and N. C. Handy, Phys. Chem. Chem. Phys. **8**, 558 (2006).

[128] J. Tao, J. P. Perdew, V. N. Staroverov, and G. E. Scuseria, Phys. Rev. Lett. **91**, 146401 (2003).

[129] J.-D. Chai and M. Head-Gordon, J. Chem. Phys. **128**, 084106 (2008).

[130] M. Navarro, Coord. Chem. Rev. **253**, 1619 (2009).

[131] S. J. Berners-Price and A. Filipovska, Metallomics **3**, 863 (2011).

[132] H. Häkkinen, M. Walter, and H. Grönbeck, J. Phys. Chem. B **110**, 9927 (2006).

[133] H. Schmidbaur and A. Schier, Chem. Soc. Rev. **37**, 1931 (2008).

[134] B. M. Barngrover and C. M. Aikens, J. Phys. Chem. Lett. **2**, 990 (2011).

[135] R. K. Arvapally, P. Sinha, S. R. Hettiarachchi, N. L. Coker, C. E. Bedel, H. H. Patterson, R. Elder, A. K. Wilson, and M. A. Omary, J. Phys. Chem. C **111**, 10689 (2007).

[136] M. J. Katz, K. Sakai, and D. B. Leznoff, Chem. Soc. Rev. **37**, 1884 (2008).

[137] H. Schmidbaur and A. Schier, Chem. Soc. Rev. **41**, 370 (2012).

[138] R. Baggio and S. Baggio, J. Inorg. Nucl. Chem. **35**, 3191 (1973).

[139] H. Ruben, A. Zalkin, M. O. Faltens, and D. H. Templeton, Inorg. Chem. **13**, 1836 (1974).

[140] R. Usón, A. Laguna, M. Laguna, J. Jiménez, M. P. Gómez, A. Sainz, and P. G. Jones, J. Chem. Soc. Dalton Trans. 3457 (1990).

[141] S. Friedrichs and P. G. Jones, Z. Naturforsch., Teil B **59b**, 793 (2004).

[142] J.-X. Chen, W.-H. Zhang, X.-Y. Tang, Z.-G. Ren, H.-X. Li, Y. Zhang, and J.-P. Lang, Inorg. Chem. **45**, 7671 (2006).

[143] A. J. Fischmann and L. Spiccia, Dalton Trans. **40**, 4803 (2011).

[144] S. H. Lim, J. C. Schmitt, J. Shearer, K. R. England, M. M. Olmstead, and A. L. Balch, Dalton Trans. **43**, 13756 (2014).

[145] Z. Assefa, B. G. McBurnett, R. J. Staples, J. P. Fackler, B. Assmann, K. Anger-maier, and H. Schmidbaur, Inorg. Chem. **34**, 75 (1995).

[146] N. L. Coker, J. A. Krause Bauer, and R. Elder, J. Am. Chem. Soc. **126**, 12 (2004).

[147] S. S. Pathaneni and G. R. Desiraju, J. Chem. Soc., Dalton Trans. 319 (1993).

[148] K. M. Anderson, A. E. Goeta, and J. W. Steed, Inorg. Chem. **46**, 6444 (2007).

[149] S. Cronje, H. G. Raubenheimer, H. S. Spies, C. Esterhuysen, H. Schmidbaur, A. Schier, and G. J. Kruger, Dalton Trans. 2859 (2003).

[150] S. Friedrichs and P. G. Jones, Z. Naturforsch., Teil B **59b**, 49 (2004).

[151] P. G. Jones and S. Friedrichs, Acta Crystallogr., Sect. C: Cryst. Struct. Commun. **62**, m623 (2006).

[152] S. Friedrichs and P. G. Jones, Z. Naturforsch., Teil B **59b**, 1429 (2004).

[153] B.-C. Tzeng, W.-H. Liu, J.-H. Liao, G.-H. Lee, and S.-M. Peng, Cryst. Growth Des. **4**, 573 (2004).

[154] D. Andrae, U. Häussermann, M. Dolg, H. Stoll, and H. Preuss, Theor. Chim. Acta **77**, 123 (1990).

[155] F. Neese, Wiley Interdiscip. Rev.: Comput. Mol. Sci. **2**, 73 (2012).

[156] T. A. Keith, AIMAll (Version 14.10.27), 2014, TK Gristmill Software, Overland Park KS, USA.

[157] E. R. Johnson, S. Keinan, P. Mori-Sánchez, J. Contreras-García, A. J. Cohen, and W. Yang, J. Am. Chem. Soc. **132**, 6498 (2010).

[158] J. Contreras-García, E. R. Johnson, S. Keinan, R. Chaudret, J.-P. Piquemal, D. N. Beratan, and W. Yang, J. Chem. Theory Comput. **7**, 625 (2011).

[159] R. F. Bader, *Atoms in Molecules: A Quantum Theory* (Oxford University Press, Oxford, UK, 1990).

[160] C. F. Matta and R. J. Boyd, *An introduction to the quantum theory of atoms in molecules* (Wiley-VCH, New York, 2007).

[161] A. E. Reed and F. Weinhold, J. Chem. Phys. **78**, 4066 (1983).

[162] A. E. Reed, R. B. Weinstock, and F. Weinhold, J. Chem. Phys. **83**, 735 (1985).

[163] J. P. Perdew, K. Burke, and M. Ernzerhof, Phys. Rev. Lett. **77**, 3865 (1996).

[164] C. Adamo and V. Barone, J. Chem. Phys. **110**, 6158 (1999).

[165] M. Modrzejewski, M. Lesiuk, Ł. Rajchel, M. M. Szczęśniak, and G. Chałasiński, J. Chem. Phys. **137**, 204121 (2012).

[166] M. Modrzejewski, G. Chałasiński, and M. M. Szczęśniak, J. Chem. Theory Comput. **10**, 4297 (2014).

[167] A. Ambrosetti, A. M. Reilly, R. A. DiStasio, and A. Tkatchenko, J. Chem. Phys. **140**, 18A508 (2014).

[168] C. Riplinger and F. Neese, J. Chem. Phys. **138**, 034106 (2013).

[169] C. Riplinger, B. Sandhoefer, A. Hansen, and F. Neese, J. Chem. Phys. **139**, 134101 (2013).

[170] S. Grimme, J. Chem. Phys. **118**, 9095 (2003).

[171] A. Hansen, C. Bannwarth, S. Grimme, P. Petrović, C. Werlé, and J.-P. Djukic, ChemistryOpen **3**, 177 (2014).

[172] J. El-Bahraoui, J. Dobado, and J. Molina, J. Mol. Struct.: THEOCHEM **493**, 249 (1999).

[173] E. Colacio, F. Lloret, R. Kivekäs, J. Suárez-Varela, M. R. Sundberg, and R. Uggla, Inorg. Chem. **42**, 560 (2003).

[174] S. Dinda and A. G. Samuelson, Chem.–Eur. J. **18**, 3032 (2012).

[175] G. Mukherjee, P. Singh, C. Ganguri, S. Sharma, H. B. Singh, N. Goel, U. P. Singh, and R. J. Butcher, Inorg. Chem. **51**, 8128 (2012).

[176] Z.-F. Li, X.-P. Yang, L. Hui-Xue, and Z. Guo, Organometallics **33**, 5101 (2014).

[177] D. Cremer and E. Kraka, Angew. Chem. **23**, 627 (1984).

[178] S. Jenkins and I. Morrison, Chem. Phys. Lett. **317**, 97 (2000).

[179] E. Espinosa, I. Alkorta, J. Elguero, and E. Molins, J. Chem. Phys. **117**, 5529 (2002).

[180] P. R. Varadwaj and H. M. Marques, Phys. Chem. Chem. Phys. **12**, 2126 (2010).

[181] R. Chaudret, J. Contreras-García, M. Delcey, O. Parisel, W. Yang, and J.-P. Piquemal, J. Chem. Theory Comput. **10**, 1900 (2014).

[182] B. Pinter, L. Broeckaert, J. Turek, A. Růžička, and F. De Proft, Chem.– Eur. J.
20, 734 (2014).

[183] Y. Jiang, S. Alvarez, and R. Hoffmann, Inorg. Chem. 749 (1985).

[184] P. D. Akrivos, S. K. Hadjikakou, P. Karagiannidis, M. Gdaniec, and Z. Kos-
turkiewicz, Polyhedron **13**, 753 (1994).

[185] CRYSALIS^{PRO} Software system, Agilent Technologies, Oxford, UK, 2014.

[186] G. M. Sheldrick, Acta Crystallogr., Sect. A: Found. Crystallogr. **64**, 112 (2008).

[187] O. V. Dolomanov, L. J. Bourhis, R. J. Gildea, J. A. K. Howard, and H.
Puschmann, J. Appl. Cryst. **42**, 339 (2009).